SUPERSONIC CLUSTER BEAM DEPOSITION OF NANOALLOYS AND BIMETALLIC NANOSTRUCTURES FOR ENHANCED OXYGEN EVOLUTION REACTION

A Dissertation

Submitted to the Graduate School

of the University of Notre Dame

in Partial Fulfillment of the Requirements

for the Degree of

Doctor of Philosophy

by

Luca Ciambriello

Luca Gavioli, Co-Director

Svetlana Neretina, Co-Director

Ivano Alessandri, Co-Director

Sylwia Ptasinska, Co-Director

Graduate Program in Physics

Notre Dame, Indiana

April 2024

Università Cattolica Del Sacro Cuore
University of Notre Dame

Doctoral thesis

SUPERSONIC CLUSTER BEAM DEPOSITION OF NANOALLOYS AND BIMETALLIC NANOSTRUCTURES FOR ENHANCED OXYGEN EVOLUTION REACTION

Author:
Luca Ciambriello

Matricola:
4915894

Supervisors:
Prof. Luca Gavioli
Prov. Svetlana Neretina
Prof. Ivano Alessandri
Prof. Sylwia Ptasinska

A thesis submitted in fulfillment of the requirements for the degree of Doctor of Philosophy in the

International Doctoral Program in Science
Ciclo XXXV
Academic year 2022/2023

SUPERSONIC CLUSTER BEAM DEPOSITION OF NANOALLOYS AND BIMETALLIC NANOSTRUCTURES FOR ENHANCED OXYGEN EVOLUTION REACTION

Abstract

by

Luca Ciambriello

Making Hydrogen synthesized by electrochemistry the best alternative to fossil fuels requires to overcome the slow kinetic of the oxygen evolution reaction (OER) in the electrochemical cell. The state-of-the-art OER electrocatalysts, based on nanoalloyed materials, face two main challenges still hindering the large-scale development: 1) the optimization of the electrode morphology and 2) the achievement of the catalyst stability under industrial prolonged activity. This PhD dissertation tackles both issues by synthesizing, through Supersonic Cluster Beam Deposition, a novel NiFe nanoalloyed electrode of controllable morphology, applied as OER catalyst under prolonged operational conditions. An in-depth physical, chemical and electrochemical characterization is carried out through several microscopy and spectroscopy techniques. The electrochemical characterization is carried out as a function of the NiFe morphology and mass loading

within the $10\ ng/cm^2$ – $30\ \mu g/cm^2$ range. The data reveal that an excellent OER catalytic activity can be achieved, while the optimization of the NiFe morphology is accomplished by minimizing the NiFe mass loading without affecting the electrochemical efficiency. Conversely a procedure to stabilize the catalytic response in prolonged OER operation is proposed and correlated to chemical and morphological transformation of the electrode. These findings represent a crucial step towards the synthesis of affordable OER electrocatalysts in large-scale industrial applications.

In the physical and chemical characterization of the NiFe films, the optical spectroscopy plays a crucial role. To this aim a new home-made software for the quantitative analysis of the UV-VIS-NIR optical spectra is developed and also applied to other Au and Ag based plasmonic system. In this framework, an advanced fabrication technique (nanoimprinting lithography and dynamic templating combined with liquid/solid interface growth) is employed to synthesize arrays of Au crystalline structures with an enhanced optical and plasmonic response. The investigation of such synthesis method and the design of specific plasmonic structures, combined with a through optical characterization, represent an advancement in a wide range of applications including sensing and nanoelectronics.

CONTENTS

FIGURES

TABLES

ACKNOWLEDGMENTS

I would like to thank first of all my supervisors prof. Luca Gavioli, prof. Svetlana Neretina, prof. Ivano Alessandri, and prof. Sylwia Ptasinska for their fundamental role of mentorship in this journey. I learned from them not only a wide range of technical concepts, but also very important skills such as the scientific research approach, investigation, and the scientific communication. I thank in particular prof. Luca Gavioli also for founding the doctoral program "International PhD in Science", that allowed me and the other graduate students to experience collaborations between different research groups and to broaden our skills in different laboratories. I thank dr. Emanuele Cavaliere, dr. Irene Vassalini, and prof. Robert Hughes for their precious guidance and collaboration, that always resulted in a significant learning experience. I thank my colleagues, graduate students in Brescia and Notre Dame, with whom I shared daily routine moments, team-work and useful discussions. I am very grateful to my best friends from my undergraduate studies, Fabrizio, Guglielmo, Fabio, Francesco, Gianfranco, Alberto, who have continuously supported me also in my graduate degree. I thank my best friends I met in Brescia, Francesco, Puria, Gabriele for sharing daily conversations, dinners and entertainment. Thank you to Andrea, my Italian roommate in America, for sharing the travels and good food, and my friends in Notre Dame, Zach, Adnan, Aydin, Nandini, Oles, Brian for enjoying trips, celebrations and dinners.

A special acknowledgement goes to my family and my girlfriend Laura, who have always believed in me and have been the first supporters in this journey. I thank my mother, my father, my brother, and my grandmother for their persistent and precious advices and encouragement. I thank Laura for being by my side, for her fundamental support and cheering that allowed to bring out the best of myself.

CHAPTER 1:

INTRODUCTION

1.1 The role of H_2 in the energy system

The world's growth of the population and the production processes requires increasingly higher energy sources. Between 2017 and 2040 a 28% increment of the global energy demand is forecasted [1], opening fundamental questions on the sustainability of this formidable expansion.

Nowadays, more than 80% of the energy sources are represented by fossil fuels [2], whose unsustainability stems from their polluting effects and from the alteration of the atmosphere chemical composition with greenhouse gas emissions [3], besides their limited availability on the planet. As a consequence, in the past decades a big effort has been made to develop the use of renewable and environmentally friendly sources, such as solar, wind and geothermal power. In addition to the optimization of the harvesting techniques, the intermittence of these natural sources on a daily or annual time scales will represent a big issue in a society that requires a continuous energy delivery, requiring the development of storage systems [4].

In this framework, hydrogen can represent a powerful resource as energy carrier [4], [5]. Its production can be achieved electrochemically through the water splitting (WS), i.e. the dissociation of water molecules, by employing renewable energy sources when

available. Conversely, if combined with oxygen in fuel cells, it can release energy with just water byproducts. The major potential advantages of this energy stocking technique are on one side a complete sustainability, with no greenhouse gas emissions, and on the other side the large availability on earth in water supplies. Moreover, the three-time higher released energy per unit of mass (120 MJ/kg) with respect to conventional fuels (40 MJ/kg) make of H_2 the best alternative to fossil sources [4].

However, at the current state-of-the-art technological advancement, the WS process results two times more expensive than the extraction of conventional fuels, hindering a large-scale diffusion of H_2 in the market [2], [6]. As a consequence, nowadays, neither the H_2 is a sustainable process, as far as 95% of it is generated from fossil fuels [7], [8], nor it is used as energy reservoir, finding mainly direct applications in food processing, production of fertilizers and semiconductors manufacturing [4].

The great challenge consists then in the optimization of the WS process, in order to make the sustainable large-scale H_2 production affordable.

1.2 The electrochemical water splitting

The WS process consists in the electrochemical dissociation of the water molecule into gaseous H_2 and O_2 according to:

$$2H_2O \rightarrow 2H_2 + O_2 \tag{1-1}$$

In an electrochemical cell, the reaction (1-1) takes place through two half reactions, the hydrogen evolution reaction (HER) at the cathode:

$$2H_2O + 2e^- \rightarrow H_2 + 2OH^-$$

(1-2)

and the oxygen evolution reaction (OER) at the anode

$$4OH^- \rightarrow O_2 + 2H_2O + 4e^-$$

(1-3)

The thermodynamic value for the voltage required to carry out the overall WS reaction (1-1) is 1.23 V. However, since the two half reactions are 2- and 4- electron processes respectively, both OER and HER require separate catalysts in which the reactions evolve through intermediate steps. As a consequence, in a real electrochemical cell, the applied voltage required for the WS to take place (i.e. the WS activation potential V_{real}) will be determined by the activation potential of each intermediate step and will exceed the thermodynamical value according to [9]:

$$V_{real} = 1.23\,V + \bar{\eta}_{OER} + \bar{\eta}_{HER}$$

(1-4)

where $\bar{\eta}_{OER}$ and $\bar{\eta}_{HER}$ are the OER and HER activation overpotentials. These two quantities result from the cumulative energy required in each intermediate step of the half reactions and quantify the efficiency of the two half reaction catalysts. In particular, the OER mechanism, involving 4 electrons rather than 2 as for the HER, is characterized by the highest overpotential and represents the major contribution in the activation potential (4) [10]. As a consequence, OER represents the bottleneck of the overall WS process and a great effort has been made in the past decades in order to improve its catalysis through the design of a wide range of electrodes.

In order to have a better insight on the OER catalysis, each intermediate step of the process needs to be taken into account. In the following description, the voltage values are rescaled with respect to the reversible hydrogen electrode (RHE) potential reference. Furthermore, alkaline electrolytes, usually preferred in electrochemical cells with respect to more corrosive acidic environments [11], are considered. The commonly accepted pathway of the OER is the five steps process [12]:

$$* + OH^- \rightarrow *OH + e^- \quad \text{(a)}$$

$$*OH + OH^- \rightarrow H_2O + *O + e^- \quad \text{(b)}$$

$$*O + OH^- \rightarrow *OOH + e^- \quad \text{(c)}$$

$$*OOH + OH^- \rightarrow *O_2 + e^- \quad \text{(d)}$$

$$*O_2 \rightarrow * + O_2 \quad \text{(e)}$$

(1-5)

where * indicates an active site in the catalysts. This five-step process involves the subsequent formation of hydroxides (*OH), oxides (*O), oxy-hydroxides (*OOH), dioxides ($*O_2$) followed by the production of gaseous O_2. As represented schematically in [13] and reported in Figure 1-1, each step of the chain in equation (1-5) requires an activation energy that is determined by the catalyst chemical composition of the active site and in particular on the strength of the oxy-hydroxide bounds. The potential required to carry out the overall OER corresponds then to the maximum among the energies required in each of the five steps in (1-5).

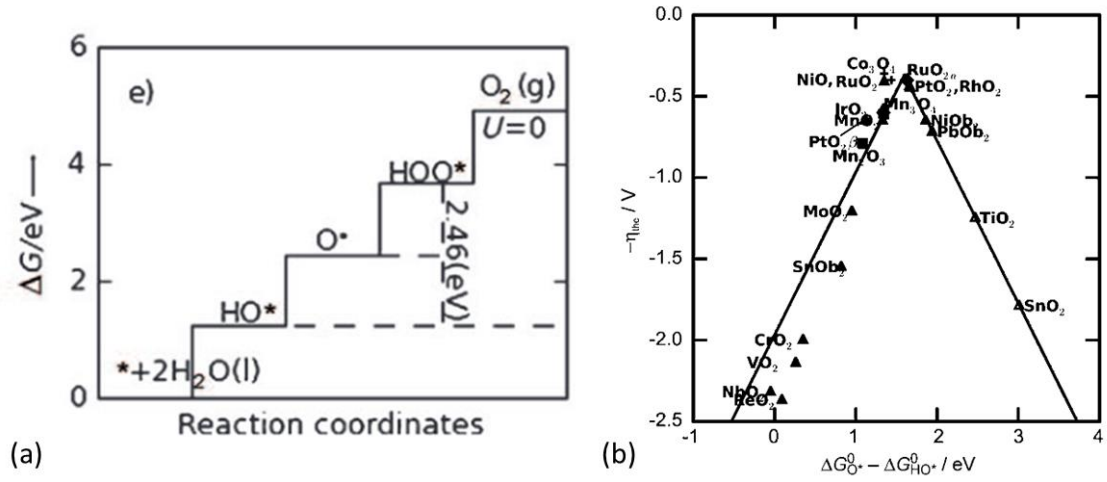

Figure 1-1. Both panels are adapted from [13]. (a) Each step of the OER catalysis contributing to the overpotential. (b) Volcano plot showing that the OER efficiency reaches a maximum for intermediate *O→ *OH reaction energy values around 1.6 eV

Interestingly, it was found that the two intermediate steps (1-5)b and (1-5)c are the most determining in the energy balance of the overall OER catalysis. Furthermore, the sum of the two energy gaps required by these two steps results to be roughly constant, independently of the active site type [13], [14]:

$$\Delta \mathrm{E}_{*OH\rightarrow *O} + \Delta \mathrm{E}_{*O\rightarrow *OOH} \sim 3.2 \pm 0.4\ eV \tag{1-6}$$

This relation implies that at least one of the two gaps must be necessary greater or equal to $1.6 \pm 0.2\ eV$ and, as a consequence, sets a lower bound for the OER overpotential given by $(1.6 - 1.23)\ V = 0.4 \pm 0.2\ V$. This implies that in each catalytic site, an overpotential of the order of 400 mV should always be expected in oxy-hydroxides mediated catalytic processes, while a greater value can occur when one of the two steps in equation (1-6) exceeds 1.6 V. In [13], the OER efficiency ($-\bar{\eta}_{OER}$) is reported as a function of $\Delta \mathrm{E}_{*OH\rightarrow *O}$ for a set of density functional theory (DFT) calculations on oxide based

compounds (Figure 1-1b). A clear dependence between these two quantities is visible, confirming that one of the two energy gaps in equation (3-6) is sufficient to describe the overall efficiency. The reaction is hindered for higher *OH binding energy (when $\Delta E_{*OH \rightarrow *O} > 1.6\,V$), while in the opposite case the OER is slown down by a greater amount of energy required by the *O→*OOH step, according to equation (3-6). The maximum around 1.6 V corresponds to an uniformly distributed activation energy between the two steps in (3-6).

1.3 Nanomaterials as OER catalysts.

The complexity of the OER process requires the design of efficient electrocatalysts to decrease the overpotential. In actual electrodes, the OER efficiency, is determined by the combination of two main factors:

1) the electrode chemical composition, that determines the efficiency of each single active site, parametrized by the OER activation overpotential $\bar{\eta}_{OER}$
2) the electrode morphology, that determines the number of active sites available for the catalytic process.

The electrode efficiency, determined by the convolution of the two effects above, is usually parametrized through the overpotential η_{10} at $10\,mA/cm^2$, i.e. the potential exceeding the thermodynamic value of 1.23 V required to carry out that current density per unit of electrode geometrical surface.

From the chemical viewpoint, noble metals such as Pt, Ir, Ru, and Pd, represent the state-of-the-art electrodes due to their good activity in both alkaline and acidic environments [15], with overpotentials as low as 320 mV (Ir-oxides) [16] and 345 mV (Ru-

oxides) [17]. Nonetheless, their scarce abundance on Earth prevents the development of such materials in practical applications. For this reason, in the past decades, some works have focused on the combination of such elements with more earth abundant compounds [15], [18], such as transition metals [19], polymers [20], and carbon [21] and sometimes trying to minimize the noble metal mass loading [19], [22].

Conversely, noble metal free electrodes based on transition metals are attracting an increasing interest, due to their promising electrochemical activity and their large availability on the planet [11], [23]. This remarkable OER response can be ascribed to the numerous possible oxidation states that these can easily form [9].

Furthermore, alloying more than one transition metals can considerably enhance the electrochemical performances. This effect is ascribed to the mechanism of the partial charge transfer (PCT). PCT consists in the slight modification of the oxidation state of each transition metal in an alloyed material, with respect to a pure electrode according to [24]:

$$S^z \rightarrow S^{z+\lambda} \tag{1-7}$$

where the initial oxidation state z of the active site S is shifted of a fractional quantity z. Such charge transfer, if properly tuned by specific alloying, can decrease the activation potentials in equations (1-5) and improve the OER efficiency. In several review papers, excellent catalytic properties are reported for bimetallic alloys such as Ni-Fe, Ni-Co, and Co-Fe compounds and their oxides, showing a typical overpotential at 10 mA/cm^2 in the 300-500 mV range [16], [23], [25], as also shown in Figure 1-2a for a set of Ni, Co, and Fe electrodeposited materials.

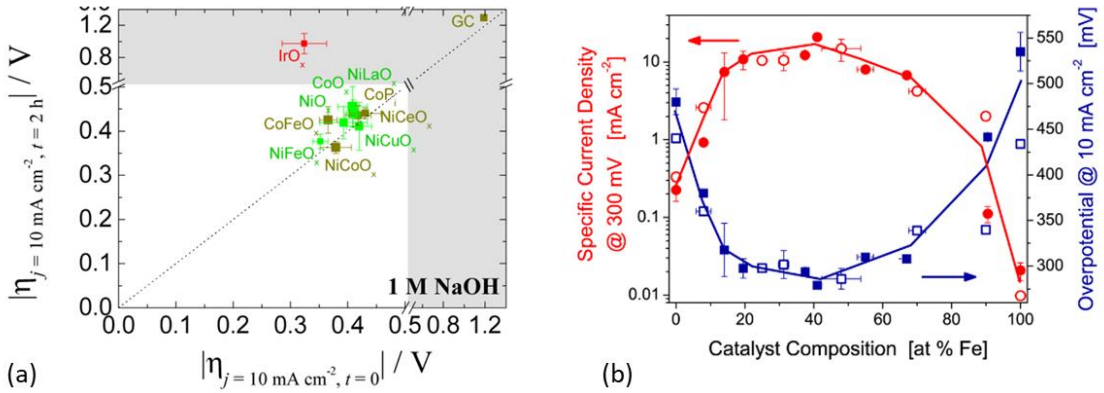

Figure 1-2. (a) from McCrory[16]. Overpotential at 10 mA/cm^2 for a set of electrodeposited transition metal alloys electrodes. On the y axis is also reported the overpotential after 2 hours OER working condition to evaluate the stability. (b) from [26]. OER efficiency in NiFe electrodeposited catalysts as a function of the Fe content.

Among the several transition metal alloyed electrodes, NiFe is one of the most promising from the viewpoint of earth abundancy (Fe is the 4th element and the Ni abundancy exceeds 50 ppm on the planet), as well as due to a particularly enhanced catalytic activity [27]. It was shown indeed that, in Ni based compounds, an inclusion of a Fe percentage as low as 10 % can result in a 100 time enhancement of the OER current [28]. A thorough investigation of the electrochemical response as a function of the Fe content showed that such high efficiency is retained between 10 and 70% alloying fraction [26], [28], [29], as shown in Figure 1-2b.

The high reactivity of both Ni and Fe in ambient air as well as in the alkaline environment of an electrochemical cell, implies the formation of a wide range of oxide and hydroxide states, depending on the synthesis process and on the electrode pretreatment before the application as catalysts. As outlined in recent reviews [27], [30], [31], [32], these differences in the oxidation level result in a wide variety of OER efficiencies, with overpotentials ranging between 200 and 400 mV.

In particular, NiFe hydroxides and oxy-hydroxides [32], [33], [34] have revealed a generally better efficiency than in other compounds, especially in the case of α-phase hydroxides [35] and layered double hydroxides (LDH) [27], [36], where a the ion exchange with the solution is facilitated by the layered structure. Overpotentials in the 200-350 mV range are reported in such cases [27], while an average slightly lower efficiency is revealed for NiFe oxides and spinels (250-400 range) [23], [27].

Despite the OER efficiency of a wide range of NiFe based materials has been investigated in several alloying fraction and oxidation conditions, the role of each active site in the catalytic process remains still unclear [30], [37]. In some works, the $Ni(OH)_2$ species are believed to play the predominant role as mediator in the OER activity [38]. However, it was pointed out that the formation of $Ni(OH)_2$ species in the electrode is not directly correlated to an enhancement of the OER current, but only serves as site for the Fe incorporation [33], while if converted into NiOOH result even detrimental for the catalysis [39]. Moreover, in oxy-hydroxide NiFe compounds [29] computational methods reported that Fe species act as principal active site, as a consequence of a modified Fe-O bound.

The second main factor affecting the OER catalytic efficiency is the electrode morphology. A composite structure at the micro- or nano- scale can increase the effective surface exposed to the electrolyte, also known as ElectroChemical Surface Area (ECSA), and the number of available active sites in reaction (1-4). This results in a decrease of the overpotential at 10 mA/cm^2 even though the single site efficiency is not altered.

In this framework, a wide plethora of NiFe structures have been explored recently. These were obtained through mechanical processes such as exfoliation [40], or chemical techniques, including dealloying [41] and morphological spontaneous modification under

electrochemical operation [42]. For instance, at the micron scale, structures as pores [43], holes and wires[44] revealed excellent OER catalytic properties with overpotentials as low as 190 mV. Comparable overpotentials were also obtained in nanoalloys, i.e. alloys confined in nanostructures, such as nanorods [42] and core/shell [45], cubes [46] (Figure 1-3a). In some cases, an increased active site exposure can also be achieved when hierarchical structures are characterized by a composite morphology both at the nano- and micro-scale (Figure 1-3b,c). It is the case of NiFe dendrites [41], [47] that can reach a current density of 10 mA/cm^2 at an overpotential as low as 180 mV.

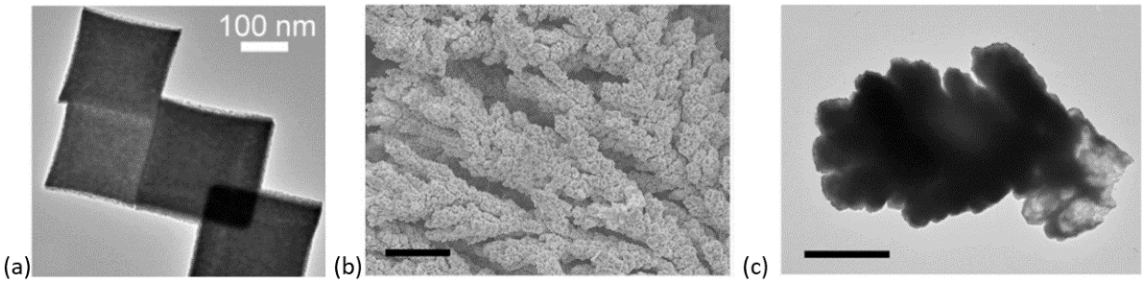

Figure 1-3. Examples of NiFe structures employed as catalysts: (a) nanostructures from [46] and hierarchical structures from [41] (b) (scale bar 10 μm) with a higher magnification view in (c) (scale bar 500 nm).

However, despite a variety of structures have been explored, a systematic investigation of the electrode's efficiency as a function of the material morphology has not yet been addressed. In most of the cases, the main challenge arises from the impossibility of controlling independently the electrode morphology and chemical composition during the synthesis. In such case the trends in the OER response result from a combination of the two factors and no clear morphology/catalysis dependence can be deduced [34], [48], [49].

1.4 Challenges in OER catalysis

In the state-of-the-art knowledge of the OER catalytic processes, a lot of progress has been made in the identification of the most efficient chemical composition, while the design of several structured morphologies has been proven to be effective but not yet investigated systematically. Furthermore, from the practical viewpoint of an industrial application, these electrodes are still unsatisfactory, because of the high manufacturing costs, as well as their poor stability under prolonged OER working conditions. We identify here two major challenges in the OER catalysts synthesis, that represent a crucial step towards a large-scale diffusion of the electrochemical WS.

1. The optimization of the morphology with the aim of reducing the synthesis cost
2. The improvement of the OER catalyst stability under prolonged working conditions.

1.4.1 Catalysts morphology

From the morphological viewpoint, a particular attention should be paid on a systematic investigation that aims to reduce the electrode synthesis costs, while keeping an excellent OER response. This can be accomplished by exploring different morphologies resulting from a variable NiFe mass loading on the electrode. In this framework the turnover frequency (TOF), i.e. the O_2 molar production rate normalized by the NiFe moles [27], is the most representative parameter that can quantify the balance between the electrode OER efficiency and the manufacturing cost [50].

In past work, this approach has been rarely addressed. The mass loading quantification was usually limited to the noble metal content in the electrodes, mainly Ir, in noble/noble [51], [52] and noble/non noble [19], [22], [53] metal compounds. This issue has been tackled for non-noble metals in very few cases. In the 0.5-10 mg/cm^2 mass loading range, an investigation on NiFe hexacyanoferrate electrodes revealed an increase of OER activity for 5 mg/cm^2 [54]. For electrodeposited transition metal oxides in the 0.1-100 $\mu g/cm^2$ mass loading range, an high dependence of the TOF values on the metal type was found, from 10 s^{-1} for CoFeO to 0.001 s^{-1} for MnO [55]. A substrate dependent electrochemical response was recorded instead for NiFe oxides (0.3-3.8 $nmol/cm^2$ density range [56]) and oxyhydroxides (1.5-20 $\mu g/cm^2$ [57]), as a consequence of a variable nanostructure adhesion and dispersion on the electrode surface. However, the OER activity/morphology correlation and the identification of an ideal mass loading range are still lacking.

1.4.2 Catalysts stability

The issue of stability plays a crucial role in the large-scale development of H_2 technology, as far as in industrial applications continuous or intermitted prolonged working conditions are required.

The state-of-the-art devices are still affected by a poor stability [58], [59], [60], determined by a wide range of mechanical, morphological and chemical transformation dependent on the type of prolonged activity under investigation [61]. Typically, the stability is tested through chronoamperometry or less frequently through prolonged cyclic

voltammetry [32], [62]. In the first case a fixed potential is applied while the current flowing in the cell is measured. Conversely, in cyclic voltammetry (CV), the applied potential is not constant but repeatedly scanned forward and backward in a given voltage range.

The most common source of electrode deactivation after prolonged activity is the corrosion [27], that can happen as a consequence of a mechanical exfoliation of the NiFe material from the electrode surface or through the progressive metal leaching in the electrolyte. This effect is highly affected by the material's morphology. For instance, in [63], crystalline structures revealed a worse stability with respect to amorphous structures of the same NiFe alloyed chemical composition, due to a less efficient OH^- ions absorption and active site formation.

Another limiting factor in the electrochemical stability is given by the O_2 bubble formation, that can cap a significant fraction of the electrode surface (up to 90%), reducing the active sites exposure to the electrolyte. Furthermore, the O_2 bubbles formation can also induce a mechanical exfoliation in nanostructured catalyst, as a consequence of an increase of the pressure inside the pores [61], [64], [65]. Moreover, in case of CV tests, a further transformation process was reported due to the application of a time dependent voltage. In such case, a critical voltage value is identified, such that for higher values the OER activity is accompanied by a degradation, while for lower potentials the electrode can recover the efficiency [39], [66]. The catalyst behavior in these two stages is associated respectively to a process of NiFe leaching in the electrolyte and redeposition on the electrode surface. The material stability and transformation is therefore determined by the alternation of these two opposite effects [67], [68], as well as by the dissolved ions in the electrolyte [39]. However,

the role of each Ni and Fe species in this mechanism are still under debate. In particular, though incorporation of Fe is commonly believed to be beneficial in the OER catalysis, in some cases its leaching revealed an improvement of the catalyst's surface reconstruction with an enhancement of the stability [69].

Despite the main causes of electrode degradation have been approximately classified, very few solutions to this problem have been proposed. A natural improvement of the electrode stability can be achieved during the OER activity if a Ni/Fe oxide/hydroxide coating forms spontaneously [70]. Nonetheless, in most of the cases, a C-based coating of the catalyst's surface is performed to prevent the material leaching in the electrolyte [31]. However, this technique increases significantly the manufacturing complexity and also limits the electrical conductivity [71].

This highlights the need for a better understanding of the degradation processes in OER catalysts and the identification of a stabilization procedure that can make this electrochemical process affordable from an industrial viewpoint.

1.5 The aim and overview of this work.

The aim of this dissertation is to improve the state-of-the-art nanoalloyed OER catalysts, by facing both the two major challenges that are preventing the large-scale development of such materials: the optimization of the electrode morphology and stability. In this framework, the results presented here can be classified in two parts:

- Investigation of NiFe nanoalloys as OER catalyst, involving the synthesis, characterization and modelling of the electrodes.

- Development of new experimental and data analysis technique in optical spectroscopy, useful to characterize electrodes and nanomaterials in general. A new, home-made software written in Python is developed with this aim. The application of such techniques to NiFe nanomaterials and plasmonic Au/Ag based systems is presented. In particular, in the latter case, a synthesis technique based on nanoimprinting lithography and dynamic templating is investigated in detail and analyzed from the optical viewpoint.

1.5.1 Development of new NiFe catalysts

We employed the Supersonic Cluster Beam Deposition (SCBD) to synthesize NiFe nanoalloyed electrodes (90%/10% Ni/Fe weight fraction) of variable morphology applied as OER electrocatalysts under prolonged operational conditions.

SCBD consists in a gas phase ablation of a bulk metal rod induced by an He gas pulse synchronized with an arc discharge, followed by the formation of alloyed nanoparticles that are then ballistically deposited onto the substrate [72], [73]. The process, carried out in vacuum, allows to tune the chemical composition of the nanoparticles, fixed to Ni/Fe at 90%/10% weight fraction in this work, as well as the nanoparticle mass loading on the substrate, through an in-situ quartz microbalance. The electrode OER efficiency was measured by performing cyclic voltammetry measurements in alkaline electrolyte, while its stability was tested through accelerated voltametric cycles and chronoamperometry of a duration up to 72 hours. The electrode chemical composition was monitored before and after the electrochemical application through X-ray photoelectron spectroscopy as well as spectrophotometry. A new home-made software (DEMON- Determination of Effective Multilayer Optical constants for Nanotechnology), written in Python, has been developed in this thesis to simulate and fit the optical reflectivity and transmittance (UV-VIS-NIR),

and correlate quantitatively the experimentally measured spectra to the material oxidation state and nanogranular morphology.

From the morphological viewpoint, the individual nanoparticles size, provided through atomic force microscopy (AFM) and transmission electron microscopy (TEM), is characterized by a three-modal distribution ranging from 0.4 nm to 2.8 nm. A wide range of electrode morphologies were investigated by depositing such NiFe nanoparticles in variable mass loadings in the 10 ng/cm^2- 30 $\mu g/cm^2$ range. For mass loadings lower than 1 $\mu g/cm^2$, the nanoparticles are sparse on the substrate, revealing their individual catalytic properties, while for increasingly higher density these aggregate and show a collective electrochemical behavior.

When the mass loading is sufficiently high (5-30 $\mu g/cm^2$), the nanoparticles assemble in thin nanogranular films (up to 90 nm thickness at 30 $\mu g/cm^2$), in which different bulk and surface electrochemical processes take place. A progressive oxidation and hydroxylation process occurs in all the film depth during the electrochemical operation, while the OER catalytic response is independent of the thickness and involves just the film surface. This suggests an excess of NiFe mass for loadings higher than 1-2 $\mu g/cm^2$, identifying the ultra-low loading range as the most promising strategy to reduce the synthesis complexity without affecting the OER efficiency. For lower NiFe deposited mass, an interesting trend results from the nanoparticle arrangement and interaction on the electrode surface. Between 200 ng/cm^2 and 1 $\mu g/cm^2$, the highest TOF value is reported (0.9 s^{-1}), while for lower nanoparticle densities a 20 times lower current per unit of NiFe mass is registered. This considerable drop can possibly result from the nanoparticle/substrate interaction and vanishes for higher mass loadings, when the

structures start to stack. This TOF/mass loading dependence allows to identify an ideal intermediate range (200 ng/cm^2 – 1 $\mu g/cm^2$), where an excellent catalytic efficiency (380 mV overpotential at 10 mA/cm^2) can be achieved with a minimized amount of NiFe active material. This represents a crucial step towards the optimization of the synthesis costs in nanogranular catalysts.

From the stability viewpoint, prolonged tests revealed different chemical and morphological transformations of the electrode during the OER activity. While in chronoamperometry the NiFe catalysts showed a monotonously decreasing efficiency, in cyclic voltammetry a promising morphology-dependent behavior was registered, that can be ascribed to a repeated process of NiFe leaching and redeposition. Below 200 ng/cm^2, the sparse nanoparticle efficiency increased during the test as a consequence of a possible process of rearrangement on the electrode surface. Conversely, for higher mass loadings, the morphological transformations determined the dissolution of a fraction of the NiFe active sites with an associated decrease in OER current density.

Through this mechanism, it was possible to device a cyclic voltammetry-based treatment to induce a solid electrode stability. Furthermore, this highlights a new route to achieve not only an excellent efficiency, but also better steady state performances than for the freshly synthesized electrode.

1.5.2 Development of new optical techniques and plasmonic materials

Optical spectroscopy represents an extremely powerful tool for the investigation of nanostructured materials. In this thesis it was employed in the OER catalysts characterization, as well as applied to other Ag and Au based plasmonic materials.

The advantages of this technique stem from the possibility of probing non-invasively the materials and by employing a more affordable instrumentation with respect to more sophisticated spectroscopic analyzers (X-ray photoelectron spectroscopy for instance). Furthermore, optical spectroscopy investigations are not only limited to the material's surface, but can also involve deeper regions, depending on the refractive index.

The effectiveness of this approach relies on a strong correlation between the measured optical spectra and the nanostructures morphology and chemical composition [74]. Plasmonic materials are a paradigmatic example, in which light can excite localized surface plasmon resonances (LSPR), i.e. collective excitation of electrons confined in the nanostructures [74], [75], [76]. For instance, largely different optical responses were measured in past works for thin Ag films of nominally equivalent thicknesses, due to the difference in their nanostructured morphologies determined by each synthesis process [75]. In order to extrapolate quantitative morphological and chemical parameters from the experimentally measured spectra, an optical modelling of the nanostructures shape, size and chemical composition and the gradient of these quantities along the film depth need to be taken into account. In literature, this complete optical modelling is still missing: films are often modelled as homogeneous layers [77], neglecting the nano-granularity or the surface roughness [78], [79], or sometimes ad hoc oscillators in the dielectric function are

added to reproduce the resonances with no correlation with physical/chemical properties [80], [81].

In this framework, in this thesis a new home-made software, DEMON (Determination of Effective Multi-layer Optical constant for Nanotechnology) written in Python, is elaborated to simulate and fit experimental reflectivity, transmittance, extinction and ellipsometry data in terms of morphological and chemical composition parameters. The films are modelled as a stack of multiple layers in order to take into account the variations of these properties along the film depth. In each layer a Bruggeman's model [82] is employed to calculate the optical response of nanostructures of variable size, shape and composition.

This approach was firstly applied to carry out a complete characterization of Ag films of variable thickness (5-60 nm) obtained by thermal evaporation, whose thickness dependent morphological parameters and effective dielectric function were extrapolated. Furthermore, in NiFe catalysts, the application of the DEMON software allowed to characterized the nanograin shape and on the degree of oxidation/hydroxylation across all the electrode depth, that could not be provided by surface analyses such as XPS and AFM.

In this framework, this thesis also tackles the synthesis and investigation of Au based plasmonic materials, in which the optical response is not only one of the most effective characterizing tools, but also a property needed in a wide range of applications, from sensing to optical coating.

The Au materials are obtained through a multi-step synthesis process, combining the dynamic templating (DT) and the liquid-solid solution growth (LSG) [83]. The first step (DT) consists in the formation of an array of Au crystal nanoparticles, all of them

sharing the same crystalline orientation induced by the underlying sapphire substrate. In the second stage (LSG), the nanoparticles are immersed in a growth solution, containing an Au salt and a reducing agent, and used as nucleation sites for the growth of larger crystalline structures. This technique allows to tune the structures shape and size, leading to controllable optical responses and LSPR resonances [84]. For instance, a wide range of architectures were designed recently through this technique, including array of nanostars [85], chiral structures with spiral geometry [86], and asymmetric bimetallic Janus particles [87] or hexagonal and triangular planar structures[83], [84], finding direct applications in plasmonics, surface enhanced Raman scattering, and catalysts [88].

The present work deals with the synthesis of hexagonal shaped 2D crystal array, achieved by properly tuning the chemical parameters in the LSG growth process. Firstly, the LSG growth process was investigated and optimized as a function of the reducing agent type and concentration, as well as of the exposure to light radiation of different wavelengths. In particular, the reducing agent concentration can affect significantly the Au structures growth rate and shapes. Conversely, the light radiation induces a two-fold mechanism: the enhancement of the Au reduction rate due to plasmonic excitations in the crystals and the mediation of the growth process by means of intermediates forming in the growth solution for blue and UV exposures.

Afterwards, the optimized synthesis process is applied to develop specific nano- and micro- structures. By combining 2D plate array growth with TiO_2 atomic layer deposition and milling, it was possible to synthesize asymmetric nanostructures, that embed a 5 nm nanogap. Such high control on the gap thickness could be achieved thanks to the formation of flat Au interfaces arising from the crystalline growth mode. This is

crucial in the development of molecular sensing, where narrow nanogaps are required to measure electrical conductivity of single molecules, and cannot be achieved in traditional nanomaterials, characterized by rough interfaces and a nanogranular composition [89].

The DT+LSG technique was also applied to the development of large area crystalline pads, obtained by merging adjacent 2D structures. During the growth, the Au plate array showed an evolving LSPR spectrum that was directly associated with the hexagon size increase, while the transition from isolated crystals to the formation of percolated conductive regions was monitored through resistivity measurements. In this way it was possible to achieve 10 μm sized single-crystal pads with an enhanced conductivity ($1.2 \pm 0.7\ 10^{-7} \Omega\, m$), resulting from the same crystalline orientation of the individual merging Au plates. This finds direct application in the development of nanoelectronics devices, also including the possibility of growing these structures in specific patterns.

Finally, a new methodology for the synthesis of plasmonic materials was proposed in this work, in which, instead of the DT step, the use of colloidal nanoparticles as Au seeds for the plate nucleation is investigated.

1.6 Summary

Chapter 2: introduces the experimental techniques employed in the synthesis and characterization of materials. A general description of the working principle is provided for each experimental setup, while their specific use and associated data analysis are reported in each of the following chapters.

Chapter 3: presents the optical spectroscopy techniques and the new home-made DEMON software for the data analysis, with a particular application to thermally evaporated Ag films. These techniques will be then used in the following chapters to characterize Au based plasmonic materials and OER electrodes.

In Chapter 4: the dynamic templating + liquid/solid solution growth is presented. The optimization of such synthesis technique is investigated as a function of the chemical composition of the growth solution and on the light radiation exposure. The application of such technique to the growth of large area conductive regions as well as nanogap embedding structures is presented. In each case the optical characterization of the structures is presented. Furthermore, a new synthesis method for plasmonic structured is proposed.

In Chapter 5:, freshly synthesized nanogranular NiFe films of thickness in the 15-90 nm range are characterized. The films are then applied as OER catalysts and the efficiency is discussed as a function of the thickness.

In Chapter 6:, the response and transformation of the NiFe electrodes under prolonged OER activity is discussed for the representative 38 nm thick film. A new strategy for achieving high stability is proposed and correlated to the morphological and chemical evolution of the material.

In Chapter 7:, the OER efficiency of the NiFe electrode is investigated as a function of the film morphology, resulting from a variable mass loading in the 10 ng/cm^2- 30 $\mu g/cm^2$ range. The stability is also explored for the different morphologies.

CHAPTER 2:

MATERIALS AND METHODS

2.1 Supersonic cluster beam deposition

The supersonic cluster beam deposition (SCBD) technique was employed to synthesize the NiFe electrodes.

The SCBD setup, is reported in Figure 2-1 (adapted from [90]). The first step of the process takes place in the ablation chamber, where a NiFe nanoalloyed metal rod (90 % /10 % weight fraction) undergoes an electrical discharge, while simultaneously an inert He gas at 45-50 bar pressure is injected. This induces the ablation of the metal rod and the sputtering of Ni and Fe metal atoms that condense in nanoparticles (NP) due to the surrounding He pressure. Afterwards, the pressure gradient directs the He beam, containing the solid NPs, through a series of focusing lenses into the expansion chamber, where the gas is pumped out by means of turbo pumps. At this stage, the expansion of the beam stops the condensation of the sputtered NiFe atoms and NPs are directed towards a skimmer that selects the central part of the beam. In the following vacuum sector, at a pressure of $10^{-5}\ mbar$, the NiFe cluster beam flows ballistically to reach the deposition chamber, where the NPs are deposited on the substrate surface (Indium Tin Oxide – ITO). The substrate lays on a mobile stage that can be controlled remotely in order to extend the NP

coating region with respect to the beam spot size (3-4 cm). A quartz microbalance is also mounted on the stage to measure in situ the NiFe deposited mass loading through the Sauerbrey equation (section 7.6.1). The quartz microbalance can resolve a minimum of 120-150 ng/cm^2, while for the lower nanoparticle density determination a different technique was employed by using AFM. Conversely, for mass loadings higher than 1 $\mu g/cm^2$, a one-to-one correspondence between the microbalance reading and the NiFe thickness was determined through a calibration (performed by measuring with AFM the NiFe thicknesses for a set of samples). More information on the mass loading and nanoparticle density determination can be found in section 7.6.1.

After the NPs deposition the electrode is extracted to air to perform the following analyses.

In this work, SCBD was chosen as it offers a number of advantages that not only were crucial in the synthesis of the electrodes under investigation but also could be applied in perspective applications:

1) The NP chemical composition can be tuned independently form the substrate, since the nanostructures are formed before being ballistically deposited
2) The individual NP structure is independent of the substrate
3) The mass loading of the deposited material can be achieved with high precision ($\sim 10\ ng/cm^2$)
4) The deposition can be achieved on wide classes of substrates (provided that these are compatible with the vacuum conditions in the synthesis)

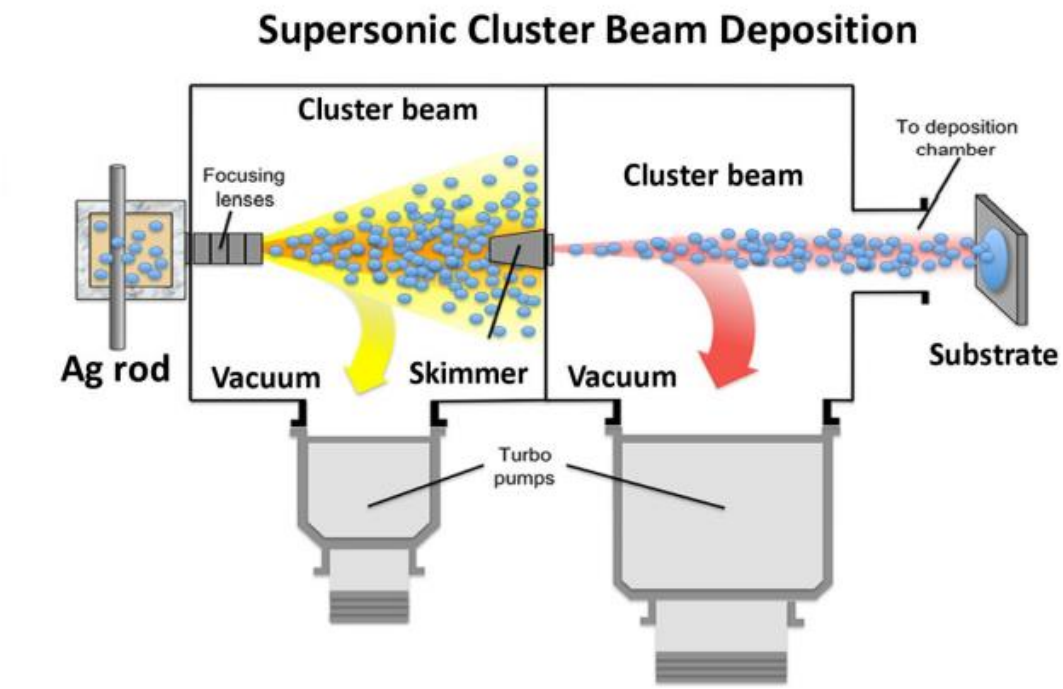

Figure 2-1. From [90]. Schematic representation of the SCBD synthesis system.

2.2 Atomic force microscopy

Atomic force microscopy (AFM) allows to image the nanomaterial surface by means of the interaction between the sample and a tip.

In the AFM setup, the tip, of typical 7-10 nm size, is mounted at the end of a cantilever and approaches the sample surface at a distance between 0.1 and 100 nm, depending on the operation mode [91]. The tip/surface interaction induces a bending of the cantilever, that is measured by focusing a laser beam on the cantilever backside and by detecting the reflected light spot through a spatially resolved photodetector [92]. (Figure 2-2). The elaboration of the photodetector output allows to reconstruct the tip z position and the sample topography in different ways, depending on the operation mode.

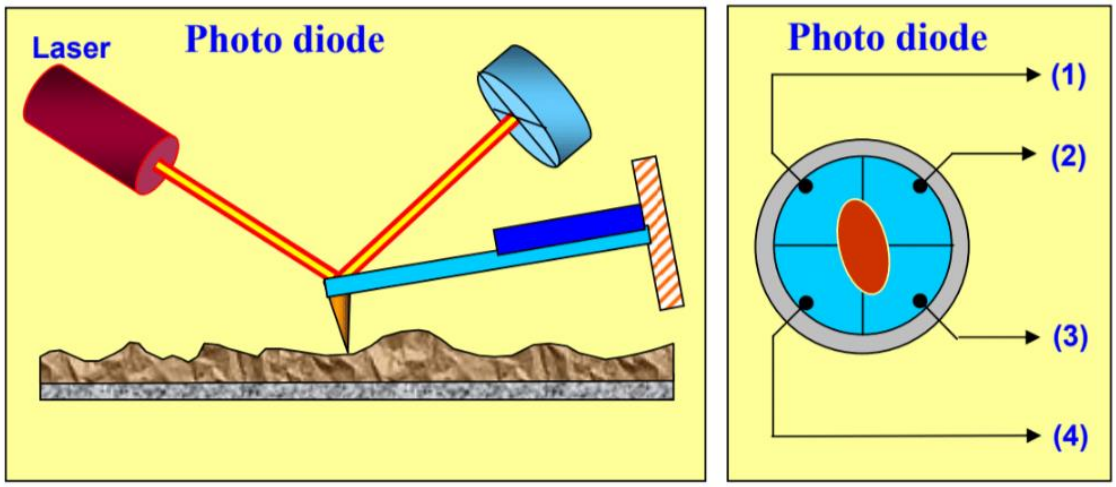

Figure 2-2. From [91]. The cantilever-tip setup, where the laser beam is focused, reflected, and detected by a photodiode to determine the tip position.

The tip/surface interaction is reproduced as a function of the distance (r) by a Lennard-Jones potential [91] (U_{LD}) in Figure 2-3. The equilibrium point at r_0 delimits two regions: for higher distances the tip undergoes an attractive force due to van der Waals molecular interactions, while for shorter distances the force becomes repulsive due to the electrical interactions between nuclei and electron clouds.

In the static operation mode, the force/distance curve can be measured at a given position on the sample surface by scanning the tip z position and measuring the cantilever deflection, with a typical resolution of 0.01 nm in the z value and 1 pN in the force. Through this technique it is not only possible to quantify the Lennard-Jones interaction with the sample surface, but also to probe the material mechanical properties such as elasticity. Conversely if the tip/surface interaction force is kept fixed through a feedback loop signal, while scanning the sample surface, the material topography is reconstructed.

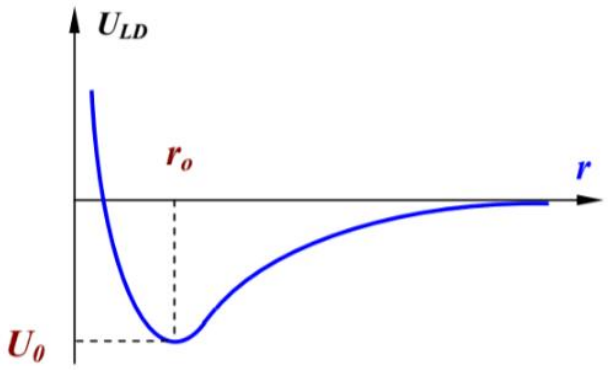

Figure 2-3. From [91]. The Lennard-Jones potential describing the tip/sample interaction.

In the dynamic AFM operation mode, an oscillation of the cantilever around its resonance frequency is forced while the measurement of the oscillation amplitude, that is affected by the intensity of the positive or negative Lennard-Jones force, allows to deduce the tip/surface distance. It is possible to distinguish between three operational modes: 1) the non-contact, in which the tip undergoes a purely attractive force, 2) the contact mode, when the force is attractive, and the 3) tapping mode in which the tip oscillates between the attractive and repulsive regions.

The map of the material topography is achieved by scanning the oscillating tip along the sample surface, while a feedback loop keeps the amplitude (i.e. the tip/surface distance) fixed by tuning the tip z position.

The resulting image, consisting of a z value for each x-y pixel on the sample surface, can be processed through a series of techniques described in each chapter depending on material under investigation.

2.3 X-ray photoelectron spectroscopy

The X-ray photoelectron spectroscopy allows to characterize the material chemical composition by means of the photoelectric effect under X-ray irradiation.

The X-ray generation process makes use of a filament (typically tungsten) from which, upon heating up through a constant current flow, electrons are extracted and accelerated towards a target material such as Mg or Al. In the target, the collision can determine the expulsion of a valence electron from the K level that is replaced by another electron from the L energy level, coupled with an X-ray emission ($K\alpha$). The typical photon energy, equal to the difference between the two energy levels, is 1253.6 and 1486.6 eV for Mg and Al. The X-ray is then focused on the sample under high or ultra-high vacuum conditions (typical pressure $10^{-10} - 10^{-13}\ mbar$).

The interaction between an impinging X-ray photons and an electron in the material, occupying a bound state of energy E_B, determines the emission of the electron with a measured kinetic energy E_K of [93], [94]:

$$E_K = h\nu - E_B - \phi \tag{2-1}$$

where $h\nu$ is the photon energy and ϕ is the detector work function. The electron kinetic energy is measured by an hemispherical spectrometer shown in Figure 2-4 (from [93]). The electrons enter the detector through a slit were an applied voltage V_i reduces the kinetic energy. Afterwards, a potential difference $V_{out} - V_{in}$ is applied between the external and internal hemispheres, to induce a circular motion of the electrons and select the ones with kinetic energy equal to E_0 (called pass energy, typically 10 or 20 eV), according to the equation:

$$e(V_{out} - V_{in}) = E_0 \left(\frac{R_{out}}{R_{in}} - \frac{R_{in}}{R_{out}} \right)$$

(2-2)

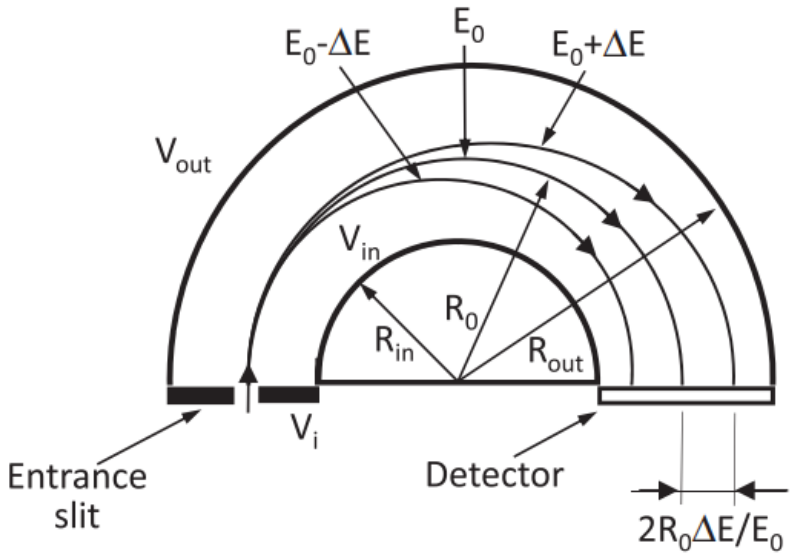

Figure 2-4. Working principle of a photoelectron detector (from [93]).

A multichannel detector is placed at the end of the hemisphere, where the number of electrons is counted. The kinetic energy $E_k = V_i + E_0$ is then found by knowing the V_i value at the hemisphere entrance and the binding energy of the electron is found through equation (2-1). By scanning the applied potential V_i it is possible to explore photoelectrons belonging to the different bounded energy levels in the material. This results in a typical plot of the electron counts as a function of the binding energy, where the position of the individual peaks associated with the bounded states in the material, allow to characterize the chemical composition and oxidation state.

In addition to electrons directly generated form the atom under X-ray irradiation (Figure 2-5a), the Auger process may also take place afterwards, determining a further electron emission (Figure 2-5b). If E_B^1 is the binding energy of the first photoemitted electron (discussed above), the vacancy left behind right after the photoelectric emission can be filled by another electron belonging from a state of energy E_B^2. A photon of energy $E_B^2 - E_B^1$ is generated by the latter process, which can in turns induce the photoemission of a third electron (Auger electron) in a bounded state of energy E_B^3. The final kinetic energy of the Auger electron is [95]:

$$E_K^{AU} = E_B^2 - E_B^1 - E_B^3 - \phi \tag{2-3}$$

where ϕ accounts again for the detector work function. The Auger kinetic energy is independent of the incident photon energy.

It should be noted that, despite the X-ray penetration depth in materials is of the order of micrometers, a much smaller mean free path of the electron in the material limits the detection of spectral lines to the photoelectrons generated within few nanometers from the sample surface. The electrons that are emitted from inner regions of the materials and are scattered before reaching the sample surface, are characterized by a randomly dispersed kinetic energy and contribute to the background of the XPS spectra.

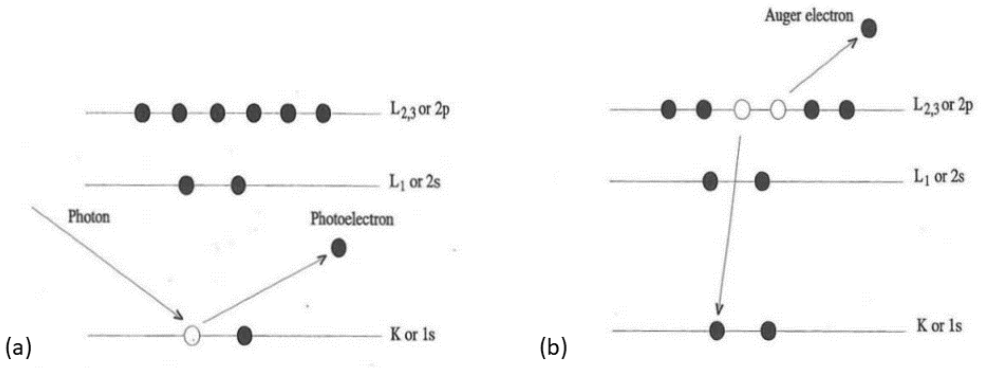

Figure 2-5. From [95]. (a) emission of a photoelectron upon X-ray irradiation and (b) Auger mechanism.

2.4 UV-VIS-NIR optical spectroscopy

Spectrophotometry consists in exposing the sample to a light beam and measuring the reflected and transmitted light percentage. A typical double beam spectrophotometer apparatus is reported in Figure 2-6 (from [96]).

In order to cover a broad wavelength range in the UV, visible and near infrared (200-2000 nm), multiple lamps are used as light sources. In the VIS-NIR range a tungsten filament is commonly used, while hydrogen or deuterium are required in the 200-400 nm region (UV) [97]. The light source is then directed towards a grating that, thanks to a micropatterned scattering surface of period d, can separate and reflect each wavelength λ at an angle $\sin^{-1}\left(\frac{\lambda}{d}\right)$ [98]. The rotation of the grating allows to scan the wavelength, with an accuracy depending on the rotation mechanism as well as the light selection by means of an entrance slit. After this monochromating system selects the desired light wavelength, the light beam is directed into a beam splitter that generates two rays of approximately

same intensity. One of these is considered as a reference signal, while the other one is used to probe the material under investigation in the sample cell. Finally, the light, passing through a system of mirrors, is collected by a detector. Before the measurements, the calibration of the instrument is performed by acquiring a spectrum by blocking the sample light beam (0% baseline) or by leaving the sample slot empty (100% baseline). Therefore, for each wavelength, the measurement takes place by firstly blanking the sample channel to detect the reference beam intensity, and secondly by recording just the sample cell signal after blocking the reference one. The comparison between the two signals allows to compensate for possible variations of the lamp source emission intensity.

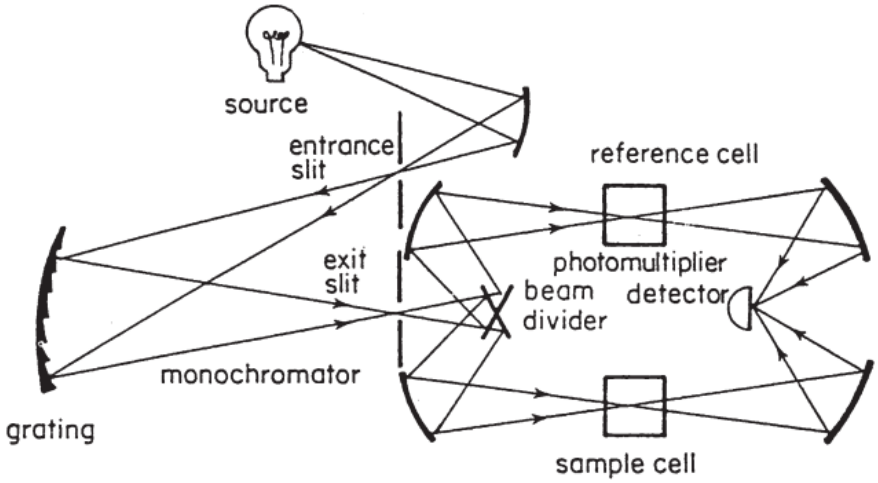

Figure 2-6. Setup and optical path in a typical spectrophotometer (from [96])

In case of the reflection measurements, the spectrophotometer includes an integrating sphere containing the photodetector, whose internal coating acts as an irregular light scattering surface (Figure 2-7). This setup allows the light to enter from a hole and impinge on the sample that is placed at the opposite edge of the sphere. The reflected light

is scattered uniformly in the sphere and is collected by the detector. As main advantage of this system, since the light beam is not directly focused on the detector, the measurement is not affected by small variations in the reflection angle from the sample surface, while also allows to acquire the scattered reflectivity [99].

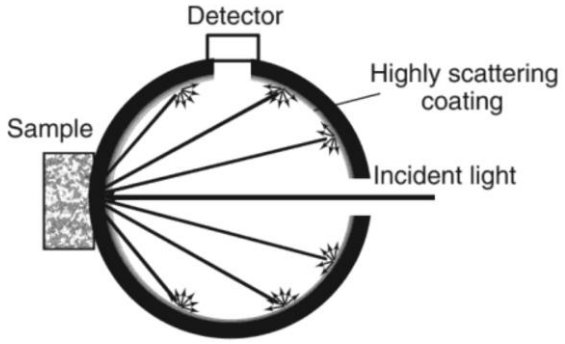

Figure 2-7. Integrating sphere used in the reflection measurement (from [99]).

In order to analyze the reflectivity and transmission optical spectra of nanogranular materials, a new home-made software is written in python, elaborated and presented in Chapter 3:. The software (DEMON- Determination of Multilayer Optical constants for Nanotechnology), allows to calculate and fit the R and T optical spectra as well as the ellipsometry parameters, as a function of the light wavelength, by employing a multiple-layer stack model. In each layer a Bruggeman effective medium approximation is employed, in which the depolarization factor accounts for the nanostructure shape and orientation and the filling fraction parameter accounts for the presence of void pores as well as mixture of metal/dielectric structures. Furthermore, the scattering rate parameter in the metal dielectric functions models the metal grain dimension. In the fit these parameters can be determined from the direct fitting of experimental optical spectra. A plasmonic

response is naturally reproduced within this model, while the employment of a multi-layer stack allows to reproduce the gradients of the chemical/morphological properties along the film depth. All the details of the software and the applications to Ag plasmonic films are presented Chapter 3:, while in Chapter 4: and Chapter 5: the optical spectroscopy analysis is used to investigate NiFe electrocatalysts and Au plasmonic materials.

2.5 X-ray diffraction

The X-ray diffraction (XRD) technique allows to determine the crystalline composition of a material by irradiating it with a light beam of wavelength comparable with the interatomic distance and by measuring the diffracted light, as a function of the deflection angle with respect to the incident direction. Typically, the wavelength ranges from 0.07 nm (Mo sources) to 0.22 nm (Cr).

In the instrument setup (Figure 2-8 from [100]), the X-ray beam is impinging the sample at an angle θ_0 with respect to its surface, while the detector is collecting the diffracted radiation at an angle θ_f. The deflection angle $2\vartheta = \theta_0 + \theta_f$ represents the variation in direction of the diffracted beam with respect to the incident one. The material characterization is carried out by measuring the diffracted light intensity as a function of these angles. Typically, in the $\theta - 2\theta$ mode, $\theta_0 = \theta_f$ and the X-ray source and detector are both scanned simultaneously. In thin films, due to the low material thickness (<100 nm) with respect to the X-ray penetration depth (microns), the grazing incidence measurement is usually performed by keeping θ_0 in a fixed position at an angle smaller than 0.5°, while the acquisition runs as a function of θ_f. The main advantage of this latter

operation mode stems from a signal intensification of a factor $1/\sin\theta_0$ with respect to the normal incidence, due to the extended penetration depth inside the film experienced by the radiation before reaching the substrate.

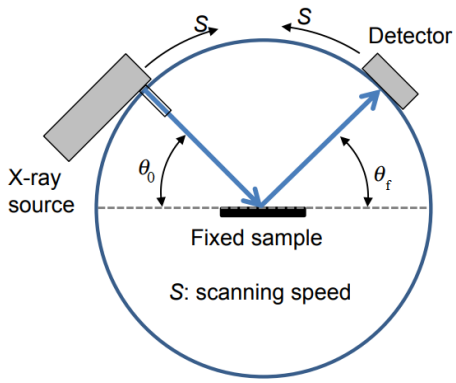

Figure 2-8. XRD setup with a radiation source, a detector and the sample laying at the center (from [100])

The diffraction process takes place when the impinging light, that can be considered ideally monochromatic on the length scale of few crystalline units, excite the atoms in the crystal, which in turn generate spherical waves. As shown in Figure 2-9, the interference between the waves generated at the different atomic sites are constructive when the incident and the reflected rays are specular with respect to a crystalline plane and the Bragg's law is verified [101]:

$$2d \cdot \sin\alpha = n\lambda \tag{2-4}$$

where α is the incidence/diffraction angle (Bragg angle) with respect to the crystalline plane and d is the crystal plane separation.

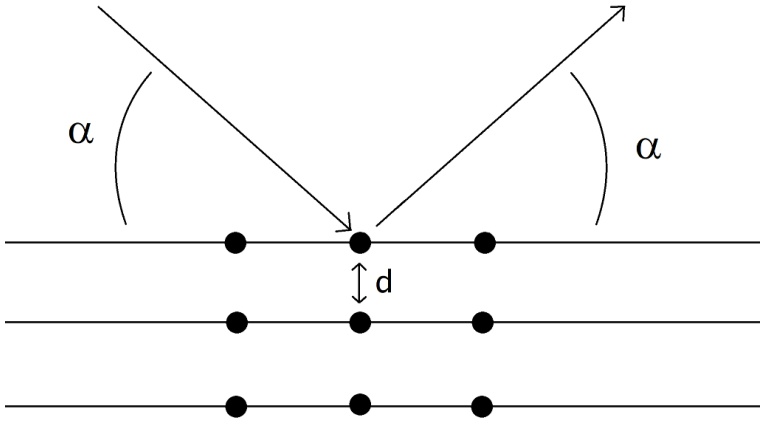

Figure 2-9. Schematic representation of an X-ray impinging on a crystalline structure and determining a diffracted light beam.

In single crystal samples, the incidence angle α relative to each crystalline facet can be related to the measurement angles $\theta_0, \theta_f, \vartheta$, while in the case of powders or nanogranular films, made of randomly oriented nanoparticles, this is not possible. In the latter case, for a given (θ_0, θ_f), the signal will be determined by the grains whose crystalline facet happens to be oriented at the Bragg angle with respect to the impinging light. As a consequence, the associated diffraction peak occurs at an angle $2\vartheta = \theta_0 + \theta_f = 2\alpha$ (where α is the Bragg angle defined in equation (2-4)), but cannot be associated to specific (θ_0, θ_f) angles. In this framework, the angle 2ϑ contains all the significant information to characterize the crystalline facets of the nanograins and therefore the diffracted intensity is usually represented in terms of this angle rather than θ_i and θ_f.

Furthermore, the finite size of the crystalline domains determines a broadening of the diffraction peak according to the Debye-Scherrer relation [101]:

$$L = \frac{K\lambda}{\beta \cos \vartheta}$$

(2-5)

where L is the crystalline domain size, ϑ is the Bragg angle at which the peak is centered, λ is the X-ray wavelength, K is a factor of order of 1 (typically 0.9) accounting for the crystal shape, and β is the peak full width half maximum.

The relation (2-5) allows to deduce the size of the crystalline domain in a nanogranular system by measuring the width of the detected peak.

2.6 Electrochemistry setup

In a typical electrochemical measurement, an electrochemical cell consists of a liquid electrolyte in which three electrodes are immersed as shown in Figure 2-10 (from [102]).

- The electrode is a water solution obtained by dissolving a salt, in which ions such as OH^- (for alkaline experiments) are contained. The ions serve as charge carriers to complete the electrical circuit composed by the electrodes. In this work a 1 M KOH electrolyte is employed.

- The reference electrode is a component in which there is no current flow, but its chemical composition determines a very stable equilibrium potential with respect to the electrolyte. Its potential serves as a reference for the other potentials measured in the electrochemical cell. In this work a saturated calomel electrode (SCE) is employed (Hg_2Cl_2). In this work, the potentials, measured with respect the SCE, are then referred to the reversible hydrogen electrode (RHE) according to: $V_{SCE} = 0.241\ V - pH \cdot 0.0591\ V$, where $pH = 14$.

- The working electrode is the component under examination, where OER takes place. The potential at this electrode is controlled by a potentiostat and referred with respect to the reference electrode, while the current flowing is measured simultaneously.

- The counter electrode has the role of completing the electrical circuits made of the previous components, by carrying out an opposite half reaction (HER in the present work). It is fundamental that its surface is considerably larger than that of the working electrode, in order to be able to sustain the desired amount of current without limitations for the experiment. In this work a Pt counter electrode is used.

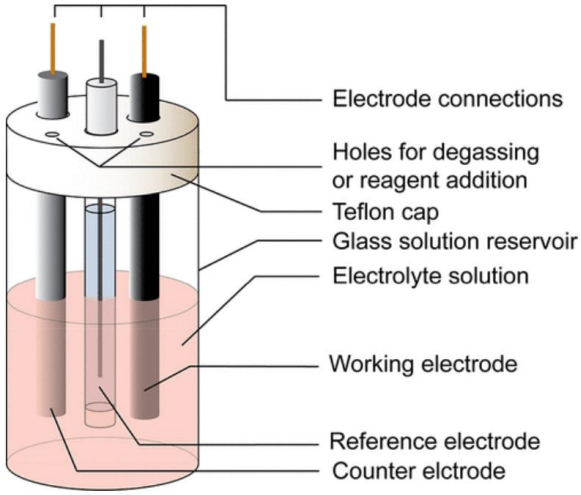

Figure 2-10. Typical electrochemical cell and its components (from [102])

The types of electrochemical tests include the electrochemical impedance spectroscopy (EIS), cyclic voltammetry (CV) and chronoamperometry (CA).

In the EIS measurement, the potential applied to the working electrode is oscillating around a fixed value with a small amplitude (few mV), while the variations in the current flowing in the cell are recorded. The impedance, given by the ratio of the potential and current amplitudes and dephasing, is measured as a function of the oscillation frequency. This allows to evaluate the capacitive effects of the electrode, as well as the resistance of the electrical contacts in the cell. The latter is obtained as the impedance value at high frequency (usually > 50 kHz) when capacitive effects vanish.

In the CV, a potential V is applied to the working electrode and scanned repeatedly forward and backwards within a predetermined range, while the current flowing through the electrochemical cell I is recorded. This results in a $I(V)$ curve that reveals the occurrence of redox processes as well as the OER under interest.

Conversely, in the chronoamperometry, a fixed potential is applied to the working electrode, while the current flowing is measured as a function of the elapsed time.

The measured currents are usually normalized by the electrode geometrical surface, in order to have an estimation of the intrinsic material behavior and efficiency as catalyst.

Furthermore, the electrical contacts in the cell are a random limiting factor in the current flow, that can mislead the electrochemical evaluations if not properly addressed. In this framework, after measuring the cell electrical contact resistance (R) through EIS, the applied potential is corrected according to:

$$V_{effective} = V_{applied} - RI \tag{2-6}$$

where $V_{effective}$ is the effective potential occurring applied to the working electrode.

A series of analysis of the $I(V)$ curves as well as the EIS and CA measuremets were performed in this work, as reported in each chapter. The two most common evaluation parameters in an electrochemical cell are the overpotential η and the turnover frequency (TOF).

The overpotential, usually calculated at 10 mA/cm^2, is defined as the $V_{effective}$ applied potential value exceeding the thermodynamical OER activation voltage (1.23 V vs RHE) in order to obtain such OER current density at the working electrode surface.

Conversely, the TOF value, usually at 350 mV overpotential, is calculated as the moles of O_2 molecules production rate at the working electrode surface, normalized by the moles of active sites in the catalyst.

2.7 Nanoimprinting lithography, dynamic templating and liquid/solid interface growth

The fabrication of array of Au crystalline plates is accomplished through three main steps [83]:

1. Nanoimprinting lithography (NIL), in which the substrate is coated with a polymer-based mask patterned with periodic features (Figure 2-11a)
2. Dynamic templating (DT), in which an array of Au crystalline nanoparticles is synthesized (Figure 2-11b)
3. Liquid/solid interface growth (LSG), in which the Au plates are grown off the Au nanoparticles (Figure 2-12a)

2.7.1 NIL

In the first step of the process, a crystalline sapphire substrate (c-plane, 0001-oriented) is spin coated with a bi-layer resist. The first layer (100 nm thick) consists of a PMGI lift-off polymer, while the second layer (400 nm thick) is a 7030R thermal polymer resist. Afterwards a silicon stamp is used to imprint a specific pattern on the top of polymer layer, consisting of a hexagonal array of holes with 600 nm lattice spacing, where the holes are 350 deep and 240 nm in diameter. This process is accomplished by pressing the stamp on the coated substrate while warming up at 140 °C to let the top layer resist adjust to the

desired morphology. Therefore, the patterned surface is exposed to an ion etching (RIE) in two cycles at 20 W – 4sscm (90 seconds) and 40 W-2sscm (50 seconds). In the RIE treatment, the surface is bombarded with Ar^+ ions with the aim of increasing the depth of the pattern and expose the sapphire substrate inside the holes.

2.7.2 DT

Then the DT part of the fabrication takes place, with an initial uniform deposition on the patterned surface of a layer of Sb and then a layer of Au by sputter coating. Subsequently, the bi-layer resist is removed by dissolving it in a dioxolane solvent EBR-PG, leaving an array of Sb+Au pillars. This Sb+Au system is then heated up to 1010 °C in a controlled N_2 atmosphere in a furnace, causing the sublimation of Sb (Sb dewetting process) and the aggregation and crystallization of Au to form an array of gold crystalline nanoparticles. In each pillar, the presence of Sb helps the Au material to aggregate properly without forming multiple smaller nanoparticles, as well as it enhances the Au/sapphire adhesion in order to induce a specific crystalline structure in the nanoparticles with stacking faults in the vertical direction and an (111) facet as a top surface. It was shown that this structure is needed in order to have the 2D formation of plates in the following LSG process, rather than an isotropic crystal configuration that determines 3D structures [83].

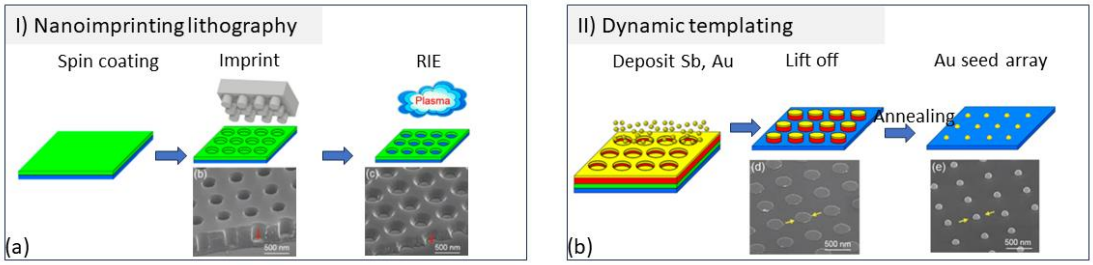

Figure 2-11. The NIL+ DT process to synthesize arrays Au crystalline nanoparticles (adapted from [83] and [103])

2.7.3 LSG growth

The array of nanoparticles is then immersed in a growth solution composed of 10.5 mL deionized water, 1 mL of 30 mM Brij-700 polymer (Polyoxyethilene(23)lauryl ether $(C_2H_4O)_{23}C_{12}H_{26}O$ – 1199 g/mol) and 1.2 mL of 10 mM Au salt ($HAuCl_2$). The Au planar growth is carried out in a glass beaker under magnetic stirring at 300 rpm (Figure 2-12a). At this stage the Brij-700 component plays a dual role: it caps the (111) top surface of the Au particles in order to prevent the growth in the vertical direction and it serves as a reducing agent in order to reduce the Au^{3+} ions in the solution at the moment they attach to the crystal surface. The growth then proceeds through the progressive reduction of the Au^{3+} ions at the solid/liquid interface, resulting in the nanostructures extending in the plane parallel to the substrate.

In some experiments the LSG process was carried out in a controlled light environment, in which the beaker was covered by a black box to prevent the external ambient light exposure. On 4 or 6 points at the top of the box, some holes were opened to insert LED light source. As shown in Figure 2-12b, two precautions were adopted in order to achieve a good uniformity of the light intensity inside the box. First of all, the light

sources were placed above the beaker and directed horizontally, in order to not shine directly the growth solution with the inhomogeneous LED light beam. Secondly, the box was internally coated with a crisp aluminum foil that, acting as a scattering surface, made the light irradiation uniform and more intense. In this setup, the light intensity was measured in different points inside the box, revealing uniformity within 5%.

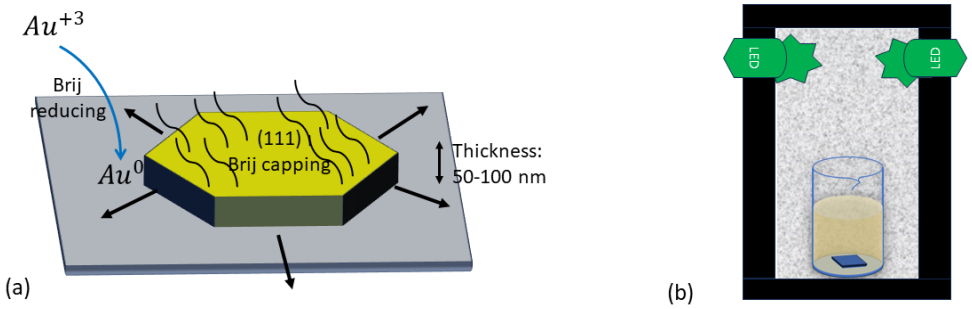

Figure 2-12. Reducing/capping process during the Au plate growth (a) and setup designed for the LSG growth under controlled light irradiation (b), where the grey background indicates the internal reflective scattering surface.

CHAPTER 3:

OPTICAL SPECTROSCOPY AND ANALYSIS TECHNIQUES

This chapter is based on:

L. Ciambriello, E. Cavaliere, L. Gavioli, "Influence of roughness, porosity and grain morphology on the optical properties of ultrathin Ag films", Applied Surface Science, Vol 576 B, Feb 2022, 151885, DOI: 10.1016/j.apsusc.2021.151885

3.1 Abstract

One of the most powerful tools to characterized nanomaterials is represented by the optical spectroscopy, due to its strict correlation with the material's morphology and chemical composition. In thin and ultrathin metal films, the optical behavior is determined by the dielectric function $\varepsilon(\omega)$, crucial for many research areas and devices. Surprisingly, even for the paradigmatic case of evaporated Ag films, a large scattering of $\varepsilon(\omega)$ exists, mainly because the film is modelled by neglecting grain structure and surface roughness. In this chapter, we quantitatively describe the optical – morphological relationships for Ag films in the 5.4 to 63 nm range thermally evaporated on fused silica. The experimental reflectance and transmission spectra are reproduced by a multilayer model employing an effective medium approximation for each layer. For the 9 nm thick film we describe how the film grain size and shape, porosity and surface roughness determine the reflectance and

transmission spectra, and the total film $\varepsilon(\omega)$. Moreover, we provide the thickness dependent trend of the morphology-optical response correlation thus obtaining a complete quantitative description of the Ag films behavior up to the transition to the bulk regime. These results represent a milestone in the morphology-optical understanding for ultrathin metal films and open new perspectives in the interpretation of thin film properties and in the design of the optical response of a tailored system.

3.2 Introduction

In thin and ultrathin systems, the interplay between the optical response and the morphological structure, e.g. grain size and shape, porosity and surface roughness, is greatly enhanced. Localized surface plasmon resonances (LSPR) are determined by the grain extension and crystallinity [104], [105], which confines free electron motion, and possible grain percolation [104], [106], [107], [108]. The surface roughness of film acts in a similar way as a scattering interface for electron propagation, also influencing the electromagnetic and chemical enhancement of Raman scattering [109]. Moreover, the Stransky-Krastanov or Volmer-Weber growth mode of such systems results in the presence of voids or pores inside the film and a surface roughness comparable to the film height. Hence the distribution and shape of the voids gives rise to a non-trivial behavior of light/film interaction, making the determination of the optical constants – film morphology relationship complicated. A recent review [104] indeed underlines the large differences in the dielectric function $\varepsilon(\omega)$ determined from experimental data obtained on nominally similar Ag thin and ultrathin films deposited by thermal evaporation. The calculated $\varepsilon(\omega)$ of such paradigmatic systems, obtained on oxide or glass substrates, turns out to be strongly affected by deposition conditions [110], [111] and by in-growth or subsequent substrate annealing treatments [112], [113], [114]. One of the basic and yet unresolved issues determining such reported data scattering [104], [115] is due to the assumption of modelling the system with a single homogeneous and uniform bulk layer. In this framework the $\varepsilon(\omega)$, obtained by the numerical inversion of reflectance € and transmission (T) data, or of ψ and Δ coefficients in spectroscopic ellipsometry [116], completely neglects the grain structure and the surface roughness influence on the optical response

[117], [118]. Moreover, normal incidence R and T data are not sufficient to determine unambiguously the dielectric function [119], since different solutions are compatible with experimental data. Hence, further R or T data at other incidence angles [120] have to be included in the numerical inversion [108]. In other cases, an analytical expression for the film dielectric function is built up ad hoc by adding oscillators to match the calculated R and T [121] or ψ and Δ [107], [122], [123] with the measured ones.

A further issue stems from the presence of pores or voids in the film structure, which strongly influence the physical properties [124], [125]. In such case, a mean field Bruggeman's effective medium approximation (BEMA) [126], [127] is adopted to calculate the dielectric function. If the characteristic film grain size, void size and surface roughness are limited to 1/10 of the impinging light wavelength [128], the BEMA model is able to account for the shape of the inclusions through the depolarization factor q [129]. Since q describes the charge redistribution occurring in the volume and surface of the voids or grains subjected to the propagating electric field, this model is notably able to account for localized surface plasmon resonances (LSPR) without forcibly introducing external oscillator terms in the dielectric function of the material. However, for nanostructured materials a single BEMA layer may not be enough to properly describe the surface roughness and the gradients along the film depth, either in porosity or in grain size and shape. These effects can be accounted for only by modelling the sample as a multi-layer stack in which each layer is described by a proper EMA with suitable depolarization and void factor, as applied in similar the cases of AgTiO2 thin films [130], [131] or nanoporous gold [132].

The third issue raises when morphology data of the film are present but no quantitative relation with the optical spectra is established. For instance, the LSPR shape and position are qualitatively ascribed to the presence of Ag domains [111], [133] with different densities and sizes [134], [135], [136]. For spheroidal inclusions each spectral resonance has been associated to a spheroid axis, while the redshift has been attributed to a grain deformation [133]. In [111] the LSPR frequency redshift is empirically related to the grain size increase measured by AFM.

Finally, if the extracted dielectric function is compared to the one calculated from an effective medium approximation (EMA) model [107], [122] and the film grain shape and film porosity is estimated [137], [138], [139], surface roughness, morphology gradient, dependence of porosity and domain shape along the film depth are not considered. A two layer model is employed in [106], with a top roughness layer and a core Ag region. However, in this configuration the roughness thickness is determined, while no morphological insight is provided for the inner region, being not described by an EMA. Only one recent work included the surface roughness in the BEMA model to describe a Ag ultrathin film deposited on an aluminum oxide crystal, the film being however obtained by direct deposition of Ag grains, thus giving rise to a very different system with respect to a thermally evaporated Ag film [130].

To summarize, a complete and quantitative characterization of ultrathin thin Ag films to establish a precise relationship between morphological parameters and optical properties including porosity, grain shape, percolation and roughness, is still missing. In this work, we present the results for the paradigmatic case of ultrathin Ag films obtained by thermal evaporation on fused silica. The experimentally measured morphology and

optical characteristics are quantitatively described by modelling reflectance and transmission spectra with a multi-layer BEMA configuration. The model, implemented through a new home-made code for ellipsometry, reflectance and transmission spectra computation and fitting (Determination of Effective Multilayer Optical constants for Nanotechnology – DEMON), provides fundamental physical insights on the morphology-optical correlation. In particular, the thickness and morphology dependence of the optical features is described in detail, highlighting the role of the film roughness and the presence of voids in the determination of the dielectric function of the films.

The novel methodology discussed in this chapter represents a powerful tool in many applications, such as plasmonic devices, photovoltaic cells, transparent conductive multi-layers, energy storage, sensors, optical and antimicrobial coatings.

3.3 The DEMON software

The Ag films have been deposited on 1 mm thick silica (SiO_2) substrates (MaTeck GmbH Germany) at room temperature in medium vacuum (base pressure = 1x10-6 mbar), employing 99.999% purity Ag in a home-made thermal evaporator placed at 20 cm from the substrate, with typical deposition rate of 3 nm/min. Films heights range from 5 nm to 63 nm, as measured from the film/substrate edge by atomic force microscopy (AFM) (Park NX10) in both non-contact and tapping mode using a PPP-NCHR tip (resonance frequency in the 250–280 kHz range, nominal tip radius 10 nm) by nanosensor. The 49oot mean square (RMS) roughness has been obtained from AFM data on different 1x1 μm2 images acquired with a 512x512 square pixels size using the Gwyddion software. Transmission

(T) and reflectance € spectra in the 250 nm – 1500 nm range have been measured in air at normal incidence and 7° incidence angle, respectively, by a Perkin-Elmer Lambda950 spectrophotometer equipped with an integrating sphere.

The new home-made fitting and computation software DEMON has been written in Python and implemented to analyze optical spectra. A detailed description of the code can be found in the supplementary information (section 3.6.1). Any experimental film is modelled by a stack of an arbitrary number of layers, assuming the light incident from the top at an incidence angle which can be chosen arbitrarily, as depicted in Figure 3-1a, and assuming a wavelength 10 times larger than the inclusion size [128].

Each layer is described by its own dielectric function $\varepsilon_L(\omega) = \varepsilon_{1L}(\omega) + i\varepsilon_{2L}(\omega)$ or, equivalently, by a refractive index $N_L(\omega) = n_L(\omega) + ik_L(\omega) = \sqrt{\varepsilon_L(\omega)}$. If a layer is not homogeneous in composition or morphology, ϵ becomes an effective dielectric function deriving from an appropriate EMA. In the present case we have adopted a BEMA model. If the material composing the layer consists of n elements, the effective dielectric function ε can be identified as the solution of the Bruggeman's equation:

$$\sum_{i=1}^{n} f_{(i)} \frac{\varepsilon_{(i)} - \varepsilon_L}{\varepsilon_L + q\left(\varepsilon_{(i)} - \varepsilon_L\right)} = 0 \tag{3-1}$$

where $\varepsilon_{(i)}$ are the dielectric functions of each of the composites, q is the depolarization factor describing the shape of the inclusions and f_i are the volume fractions of each composite. Clearly $\sum_i f_i = 1$. q, varying in the range $0 \leq q \leq 1$, depends on the shape and the orientation of the inclusions with respect to the incident electric field [140]. For $q = 0$

the inclusions assume the shape of a plane parallel to the incident electric fields (Figure 3-2a); for $q = 1/3$ the inclusions are modelled as spheres (Figure 3-2b); for $q = 1$ the inclusions are pillar-like structures with the longer side normal to the electric field (Figure 3-2c).

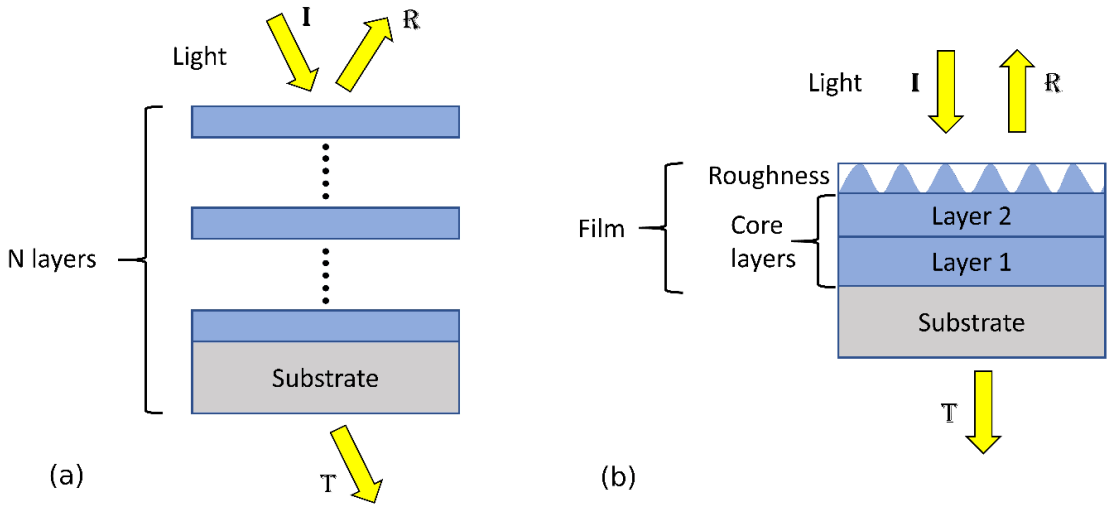

Figure 3-1: (a) General configuration of a stacked multilayer model that can be used in the home-made DEMON code. Each layer has its own dielectric function that can be modeled by a BEMA. Furthermore, the top layer may represent the film surface roughness if the void filling fraction is set to 50%. (b) The configuration adopted in this work to reproduce the Ag ultrathin films: on the 1 mm thick silica substrate, either one or two core layers are considered, and each layer is modelled with its own BEMA. In the top layer film, the porosity is fixed to 50% to reproduce the film roughness.

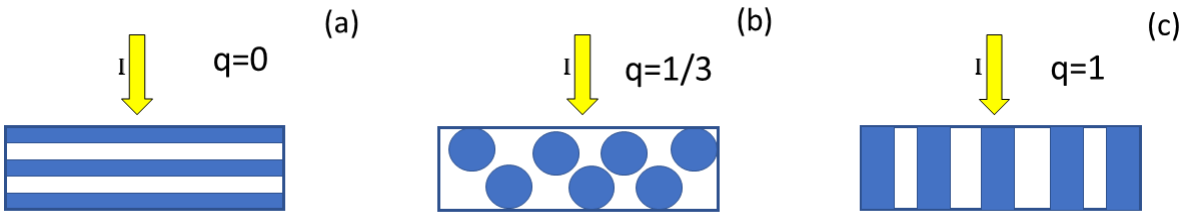

Figure 3-2 Geometry dependence of the Inclusion shapes associated to different depolarization factors q for the case of normal incidence light. (a) For q=0 the inclusions have a sheet shape and the plane is parallel to the incident electric field. (b) For q=1/3 the inclusions assume a spherical shape. (c) For q=1, the inclusions become pillar-like with the longer side normal to the incident electric field.

To reproduce the porosity of a layer it is sufficient to attribute one of the inclusions in eq. (3-1) to the pore's vacuum ($\varepsilon_{(i)} = \varepsilon_{(v)} = 1$), hence we refer to $f_{(i)} = f_{(v)}$ as the porosity. In this framework, the f and q EMA parameters describe the layer morphology, while the possibility of stacking multiple layers accounts for a morphology gradient, allowing to select for each layer the same bulk $\epsilon^{(i)}$ but different q and f values in each Bruggeman's EMA (eq. (3-1)). In particular, the film roughness is modelled by a top layer with a fixed 50% void factor in the EMA, i.e. $f_{(v)} = 0.5$. The DEMON software allows to fit the experimental R and T intensities (or as an option the ψ and Δ ellipsometry data), by means of the transfer matrix method, within any multi-layer and EMA configurations assumed for the model. An in-depth validation of the routine on previously published results obtained on gold films has been described in detailed in the supplementary information (S.2). In this work we have analyzed the R and T optical spectra acquired at normal incidence. The fitting routine minimizes the quantity:

$$\left(R_{exp} - R_{calc}\right)^2 + \left(T_{exp} - T_{calc}\right)^2 \qquad (3\text{-}2)$$

where, “exp” indicates measured quantities and “calc” the computation outputs. The fit has been considered to converge if the deviation of both calculated R and T from the experimental values do not exceed 2% in the entire spectrum, while the uncertainty on the fitting parameters corresponds to a 4% standard deviation. In the case of thermally evaporated Ag films the multi-layer configuration is schematically reported in Figure 3-1b: starting from the bottom, a 1 mm thick fused silica substrate is followed by one or two core Ag layers, ending the stack with a roughness layer. The pure Ag dielectric function is expressed as a function of the photon angular frequency ω:

$$\varepsilon_{Ag}(\omega) = \varepsilon_{\infty} + \varepsilon_{IB}(\omega) - \frac{\omega_{pl}^2}{\omega^2 + i\Gamma\omega} \tag{3-3}$$

Here, ε_{∞} is the constant dielectric background, which accounts for all the contribution from oscillators centered at energy scales far out of the investigation range. The second term ε_{IB} is the interband contribution, while the third term is the Drude oscillator, with a plasma frequency ω_{pl} and a scattering rate Γ. In the present work, the only fit parameter in the eq. (3-3) has been Γ, while all the other ones have been kept fixed and equal to the pure bulk Ag ones, reported in the supplementary information (S.3). The deviation of Γ from the bulk reference value may be included by considering the electron scattering with the inclusion boundaries, hence quantifying the size of metal inclusions through:

$$\Gamma = \Gamma_{bulk} + \frac{A}{r} v_f \tag{3-4}$$

where v_f is the Fermi velocity and r is the inclusion radius [130], [132], [141], [142]. A is a factor of the order of unity which depends on the inclusion shape [143]. Eq. (3-4), which

directly relates one of the film morphological characteristics with the optical response, has been discussed through several models, leading to values for A around unity, with a dispersion of the order of 20% for the same given inclusion shape [144], [145], [146]. In the following $A = 1$ will be assumed. The silver dielectric function of eq. (3-3) has then be combined with the $\varepsilon = 1$ vacuum dielectric function within the BEMA described by eq. (3-1) with n = 2, to obtain the effective dielectric function of each layer.

3.4 Validation: Ag thin films

The Ag films have been deposited on 1 mm thick silica (SiO_2) substrates (MaTeck GmbH Germany) at room temperature in medium vacuum (base pressure = 1x10-6 mbar), employing 99.999% purity Ag in a home-made thermal evaporator placed at 20 cm from the substrate, with typical deposition rate of 3 nm/min. Films heights range from 5 nm to 63 nm, as measured from the film/substrate edge by atomic force microscopy (AFM) (Park NX10) in both non-contact and tapping mode using a PPP-NCHR tip (resonance frequency in the 250–280 kHz range, nominal tip radius 10 nm) by nanosensor. The root mean square (RMS) roughness has been obtained from AFM data on different 1x1 μm2 images acquired with a 512x512 square pixels size using the Gwyddion software. Transmission (T) and reflectance (R) spectra in the 250 nm – 1500 nm range have been measured in air at normal incidence and 7° incidence angle, respectively, by a Perkin-Elmer Lambda950 spectrophotometer equipped with an integrating sphere.

The data have been acquired and analyzed for nine different Ag films, with thicknesses from 5 nm to 63 nm. However, for the sake of clarity we present here the AFM

images and the optical spectra for five films only to outline the trend of the physical and morphological features as a function of the film thickness. Figure 3-3 shows the morphology of the selected films obtained by AFM. For 5 and 9 nm thickness, the films are constituted by well separated grains. From 17.7 to 24.3 nm thickness, one observes the formation of much larger wormlike structures, still clearly separated, while at higher coverage a more compact distribution of the surface structures is observed.

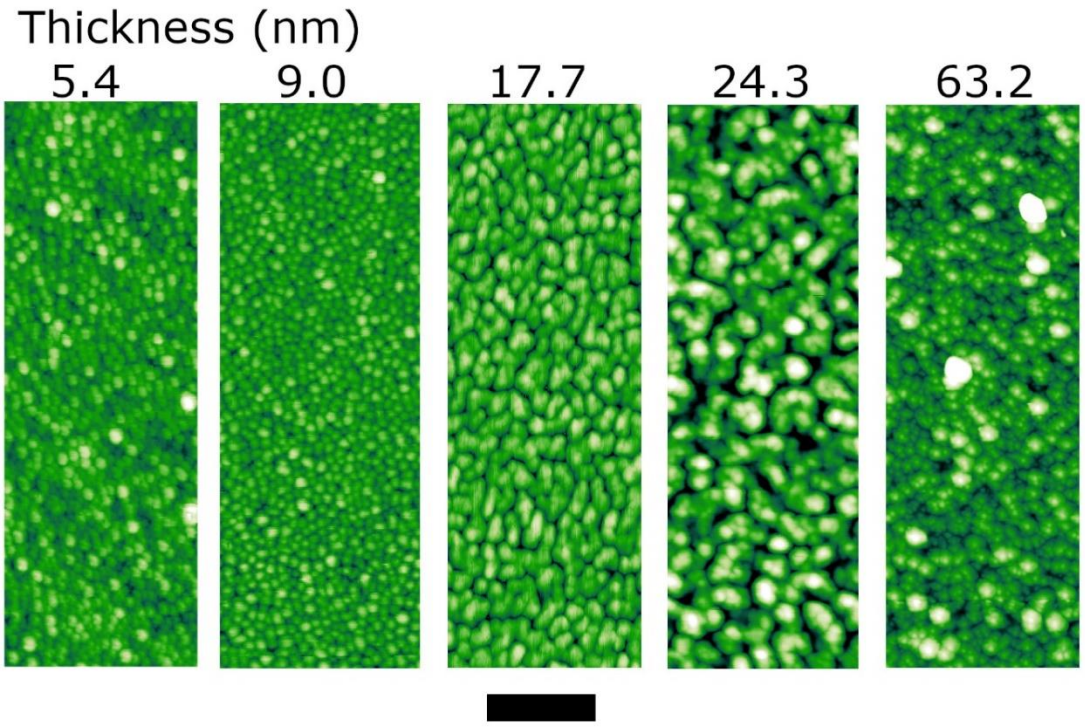

Figure 3-3. (0.25 x 1 μm^2) AFM data on selected films. Scale bar 200 nm.

The AFM data, quantified in Figure 3-9f by the measured roughness, clearly indicate that the morphology of such systems is far from being bulk-like and should be taken into account for a correct evaluation of the optical properties.

The insights on the optical-morphological properties relationships are obtained through the application of the multilayer model previously described (see Figure 3-1a) to fit the R and T data. The number of layers describing the different films, including the top roughness layer, is two up to 9.0 nm and three for all other films (see

Table 3-1). This choice allows to keep the number of layers as small as possible, supposing that the bottom layer in contact with the silica substrate is not affected by the growth of the Ag films on top of it. The free fitting parameters for each of the layer are: 1) the scattering rate Γ; 2) the individual layer thickness t; 3) the porosity f_v; and the depolarization factor q. The general criterion is to maintain the fitting parameters values as constant as possible to fit the data when moving from one film to the next.

3.4.1 Optical – morphology features correlation

To outline the important features of R and T data and the role of each fitting parameter with respect to the physical response of the film, we discuss first the results obtained on the 9 nm and 63.4 nm thick systems. Figure 3-4 reports the experimental R and T spectra (open dots) for the 9 nm film together with the best fitting curves obtained from the model. Below 330 nm, one can note a sharp minimum followed by a steep increase in the R spectrum and a sharp maximum in the T spectrum. Above 330 nm, the R data present a small shoulder in the 350-400 nm interval, followed by a broad peak centered at 500 nm and by a smooth intensity decrease in the infrared region. Conversely, the transmission data are characterized by a shoulder at 400 nm and a deep minimum at 500 nm, reaching a 90 % transmission above 800 nm.

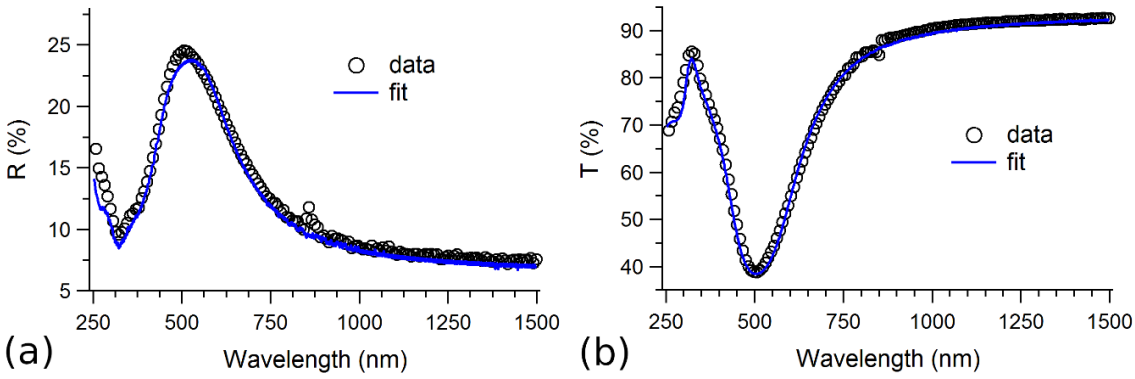

Figure 3-4 Experimental data (open circles) of reflectance (a) and transmission (b), respectively, taken on a 9 nm thick Ag film deposited on a silica substrate. The blue lines represent the best fit obtained with the model described in the text.

The optical model employed for this particular film height consists of two Ag layers (a core layer in contact with the substrate and a roughness layer, see the scheme reported in Figure 3-1b) on top of the 1 mm thick fused silica substrate. For the BEMA of each layer a dielectric function as described in equation (3-3) has been used as input, where ε_∞, ε_{IB} and ω_{pl} are the bulk values derived from the experimentally measured Ag metal refractive index in [118] (more details in section 3.6.4). The results from the R and T data fitting shown as blue lines in Figure 3-4 provides for the core layer a 4.5 nm height with porosity $f_{(v)} = 10.2\%$ and depolarization q=0.996, and for the top roughness layer a 4 nm height with $f_{(v)} = 50\%$ and q= 0.7. In the core layer the scattering rate is $\hbar\Gamma$ = 0.4 eV, while in the roughness layer the optical response is not significantly affected (<2% variation in the R and T data) by $\hbar\Gamma$ for values in the range $0\ eV \leq \hbar\Gamma < 1.5\ eV$. The two features below 330 nm are completely reproduced in the fitting model by the presence of ϵ_{IB}, which stems from the interband transitions of bulk Ag. The other spectra characteristics are reproduced

thanks to the film porosity, the depolarization factor and the scattering time included in the EMA model (see equation (3-4)). Q and Γ are related to the shape and size of grains inside the film, determining the morphology-dependent behavior of the LSPR resonance peaks. In our model, each resonance originates from an EMA as described in equation (3-1)) and therefore one expects that the peak shape and position will depend on $f_{(v)}$, q and Γ.

We indeed now discuss the influence of the fitting parameters on the spectral characteristics of the optical data for the representative case of the 9 nm thick film to clarify the physical feature of the model. Figure 3-5 presents the dependence of the calculated R and T spectra as a function of these three important parameters of the BEMA model, together with the experimental data. The influence of the layer porosity $f_{(v)}$ on the calculated optical response is shown in Figure 3-5a and Figure 3-5b. The main peak centered at 500 nm for both R and T is significantly blue-shifted by increasing $f_{(v)}$ from 10.2 % to 13% (blue curve), while it is red-shifted when $f_{(v)}$ is lowered to 7%, i.e. the overall trend is a blue shift of the LSPR peak related to an increasing layer void factor. The depolarization factor q has also a major impact on the LSPR peak since it affects the amplitude, the width and the wavelength position (see Figure 3-5c and Figure 3-5d). By increasing q from 0.996 to 1, i.e. to a pillar like film morphology (see the scheme in Figure 3-2c), the calculated R and T curves change from the black to the blue ones. The 510 nm peak shape becomes sharper, the amplitude increases and the wavelength is blue shifted. On the other hand, a decrease of q results in a R and T curves modification from the black to the red ones, in which we observe a larger peak width, an amplitude decrease and a red shift. Hence a small layer morphology modification from a complete the pillar like arrangement determines a red shift and a width increase of the LSPR.

Finally, the scattering rate Γ of the Drude oscillator affects mainly the peak amplitude as shown in Figure 3-5e and Figure 3-5f, while the impact on the peak width is limited. A 60% increase of Γ (from the black to the blue curve) corresponds to a 20% decrease of the peak intensity, as well as a decrease by 60% (from the black to the red curve) brings a 25% increase of the peak intensity. Since the scattering rate is inversely proportional to the inclusion radius as shown in equation (3-4)), the presented behavior indicates that LSPR amplitude is increasing when the grain size is decreasing.

The BEMA employed in top roughness layer is also very important since it allows to reproduce the shoulder located around 360 nm. For the 9 nm film the effect is barely evident, being overwhelmed by the main peak, but its effect becomes clear for thicker films as shown in Figure 3-6 for the 63.4 nm case. For wavelengths higher than 500 nm the R and T spectra are almost flat, while a shoulder in the 350 to 450 nm range is visible in the R spectrum. The black curve results from the data fitting for a film modelled by a three-layers stacking, as described in detailed below, in which the central core layer is bulk-like and homogeneous and the top layer describes the film roughness, with $f_v = 50\%$ and $q = 0.82$. The fit is well reproducing the experimental data throughout the entire wavelength range for both R and T.

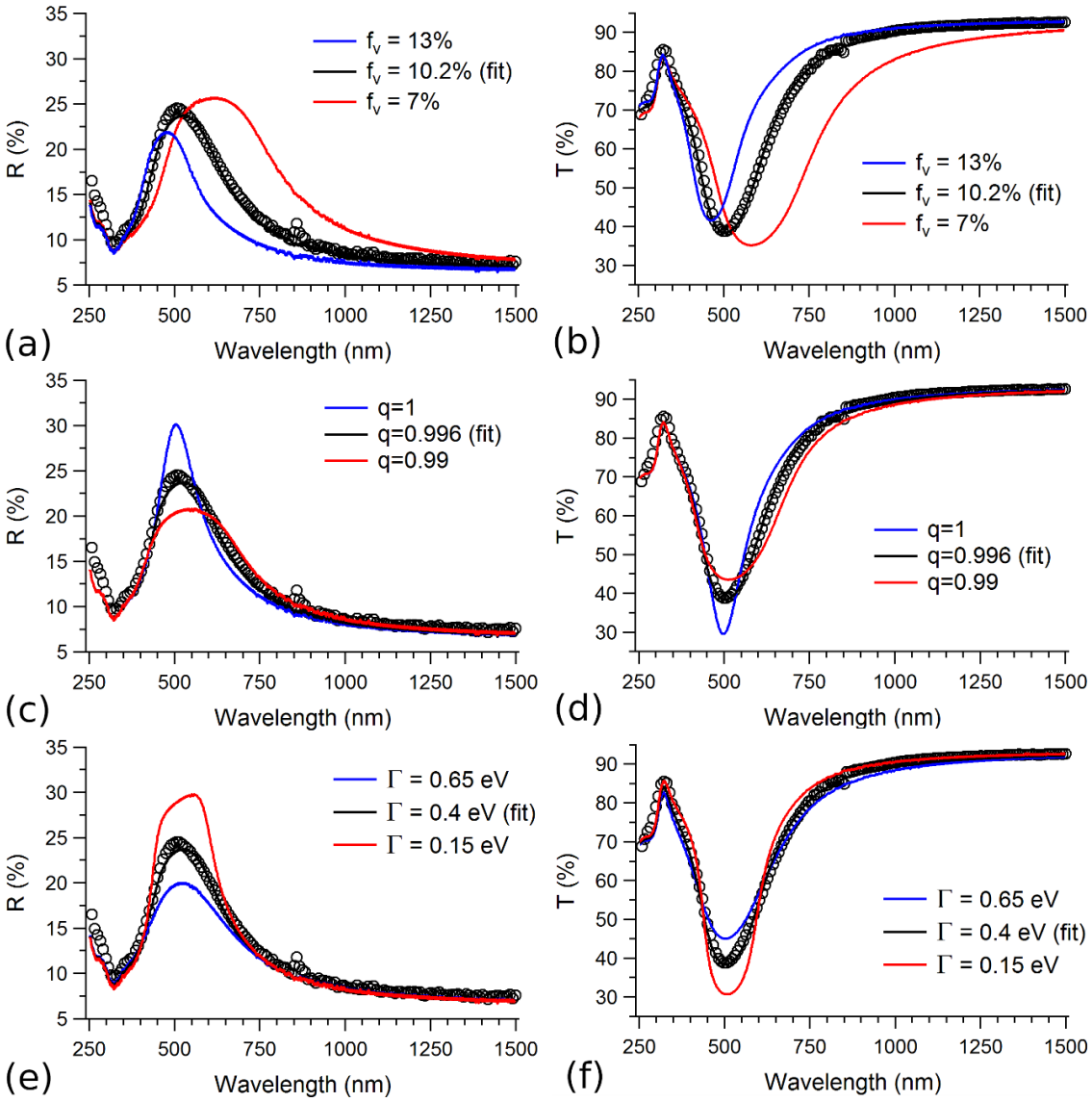

Figure 3-5. Influence of the porosity (panels (a) and (b)), depolarization factor (panels (c) and (d)) and scattering rate (panels (e) and (f)) on the R and T spectral features for the case of 9 nm thick film. The black lines represent the best fit.

In Figure 3-6 we also report the fitting results for a model configuration without the top roughness layer (blue curve). It is clear that such case cannot reproduce the experimental data, in particular the reflectance in the 280-450 nm range, while it does not significantly differ for the transmission. The discrepancy can be accounted for only when the roughness layer is included. This clearly indicates that even for a 63 nm thick Ag film a roughness layer of 4 nm must be considered to justify the experimental data up to 500 nm wavelength, also clearly indicating that the bulk layer determines the optical behavior above 500 nm.

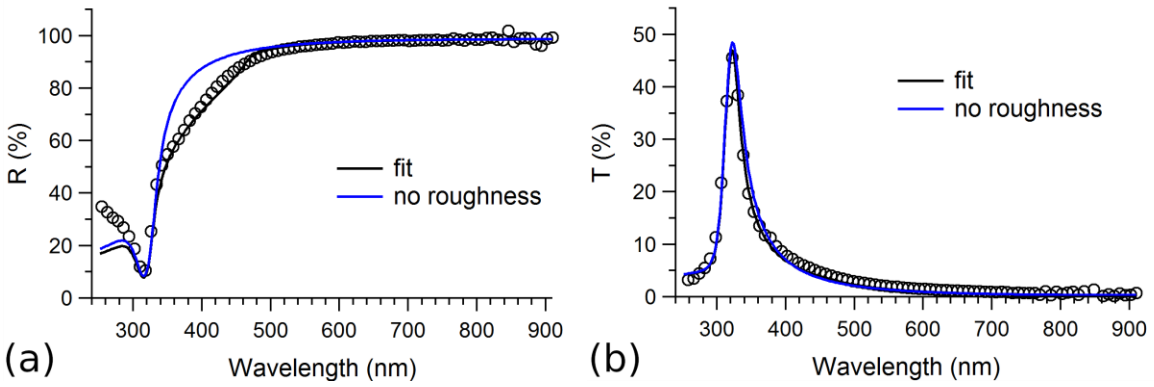

Figure 3-6. R and T experimental spectra (dots) and fit curves (black lines) of the 63.4 nm film in the 250 nm – 700 nm range. The blue lines are the simulation for a model of the same thickness but without a roughness top layer.

To underline the importance of appropriately considering the system morphology by modelling the film with a multilayer stack, we report in Figure 3-7 the real (ε_1) and imaginary (ε_2) parts of the effective dielectric functions of the top roughness layer (red line) and the core layer (blue line) for the 9 nm film case. The imaginary part ε_2 tends to zero for wavelengths above 1000 nm in both layers, indicating a vanishing infrared

absorption. In the same region of the spectrum, the real part ε_1 shows small variations, resulting in a limited excursion in R and T spectra. In the 350-800 nm range, the core layer is characterized by a marked peak in ε_2 at 500 nm accompanied by a zero of ε_1, implying an absorption structure and giving rise to the LSPR peaks found in the R and T spectra. We remark how the resonance centered at 500 nm wavelength is produced directly from the core layer BEMA without introducing other oscillators in the dielectric functions. The roughness layer is characterized by a much lower and broader ε_2 peak and a more limited ε_1 excursion with respect to the core layer. The fact that the is positive is related to the combination of the metal Ag dielectric function with the vacuum dielectric function inside the Bruggeman equation. The effective dielectric functions obtained for the two layers can also be combined to give the overall film ε (Figure 3-6, black lines). For this purpose, each individual layer ε is summed by using a BEMA with $q = 0$ (this value corresponds to the parallel layers configuration as in Figure 2a) to reproduce the stacking of the two layers. In this case the total dielectric function results as an average of the two layer's dielectric functions weighted by their thicknesses. As shown in Figure 3-7, the total ε shape is mainly determined by the core layer contribution, while the roughness layer act as a damper of the feature intensities. It is clear that the possibility to describe the overall film behavior through a multilayer model provides the physical insights on the optical-morphology correlation. Furthermore, this approach is also very flexible and could be easily adapted to other types of ultrathin films in which the composition and morphology may be more complicated.

To summarize, the presented results establish a direct quantitative connection between experimental R and T data and important morphological information such as

porosity, inclusion size and shape, and film roughness. For each layer the f_v, q and Γ BEMA parameters can be determined by the shape and position of the resonances occurring in spectra.

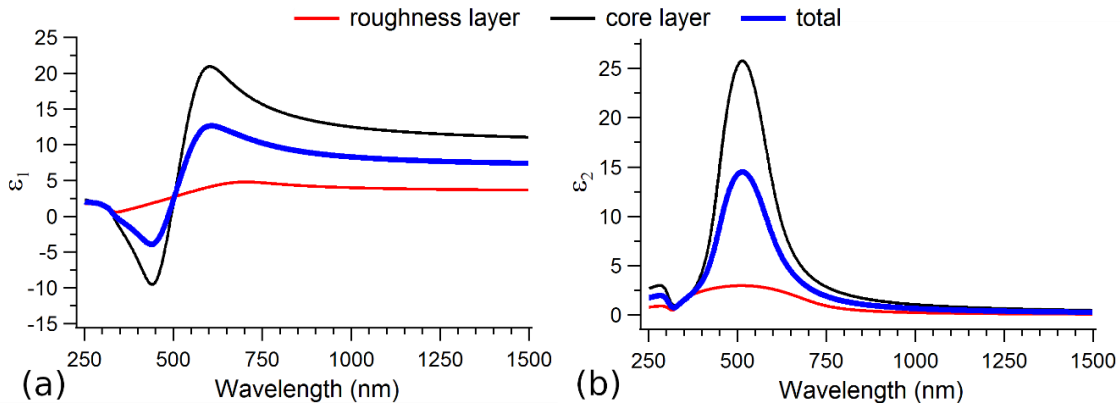

Figure 3-7 Real ε_1 (a) and imaginary ε_2 (b) part of the dielectric functions of the top roughness layer (red line) and the core layer (blue line) for the 9 nm film model. The black line is the total dielectric function of the film calculated by combining the top and core dielectric functions through a BEMA with q=0.

3.4.2 Thickness dependence of the morphology-optical properties correlations

We now discuss the relationships among the model parameters and the physical quantities as a function of the film thickness. Figure 3-8a and Figure 3-8b show the reflectance and transmission experimental data (open circles) and the fit results (lines) for selected film heights, as well as the absorption (A) in Figure 3-8c, obtained as A=100%-R-T. The reflectance behavior (Figure 3-8a) is characterized by a small peak centered around 460 nm for the 5.4 nm film, increasing in intensity and shifting to 500 nm for the 9.0 nm thick film. The R intensity is then increasing for thicker films, in particular in the infrared region, to reach an almost flat plateau above 500 nm for the 63.2 nm film. The

transmission is characterized by a marked dip centered at 470 nm for the thinnest film, shifting to 500 nm and broadening for the 9.0 nm thick film. The spectrum shape is then strongly modified above 550 nm for the 17.7 nm, becoming sharply peaked at 320 nm for the 63.2 nm film. The resulting absorption curves present a distinct peak centered at 460 nm, accompanied by a shoulder around 360 nm for the 5.4 nm film. By increasing the film thickness to 9.0 nm the absorption peak shifts to 500 nm increasing its intensity. A major spectrum modification is observed at 17.7 nm thick film, characterized by an intense absorption (up to 40%) above 500 nm. Such behavior is further modified for the 24.3 nm film, since the overall absorption intensity above 500 nm starts to decrease. Reaching a constant 2 % value for the 63.4 nm film, characterized by the absorption structure below 470 nm.

The fitting of the thickness-dependent R and T data through the application of the multilayer model (see Figure 3-1b) provides the insights on the optical-morphological properties relationships. The number of layers describing the different films, including the top roughness layer, has been limited to two up to 9.0 nm and to three for all other films (see Table 3-1), while the free fitting parameters for each of the layer are: 1) the scattering rate Γ; 2) the individual layer thickness t; 3) the porosity f_v; and the depolarization factor q. The general criterion is to maintain the fitting parameters values as constant as possible to fit the data when moving from one film to the next. The initial parameter values have been selected taking into account the film roughness and height measured by AFM.

The calculated R and T curves are shown for the selected films in Figure 3-8 as straight lines, while the corresponding values of the fitting parameters are reported in Table 1. The R and T data and the fitting results for all the investigated films are presented in the

supplementary information (Figure 3-13 and Table 3-4). The transmission, reflectance and absorption curves obtained from the fitting model are in very good agreement with the data.

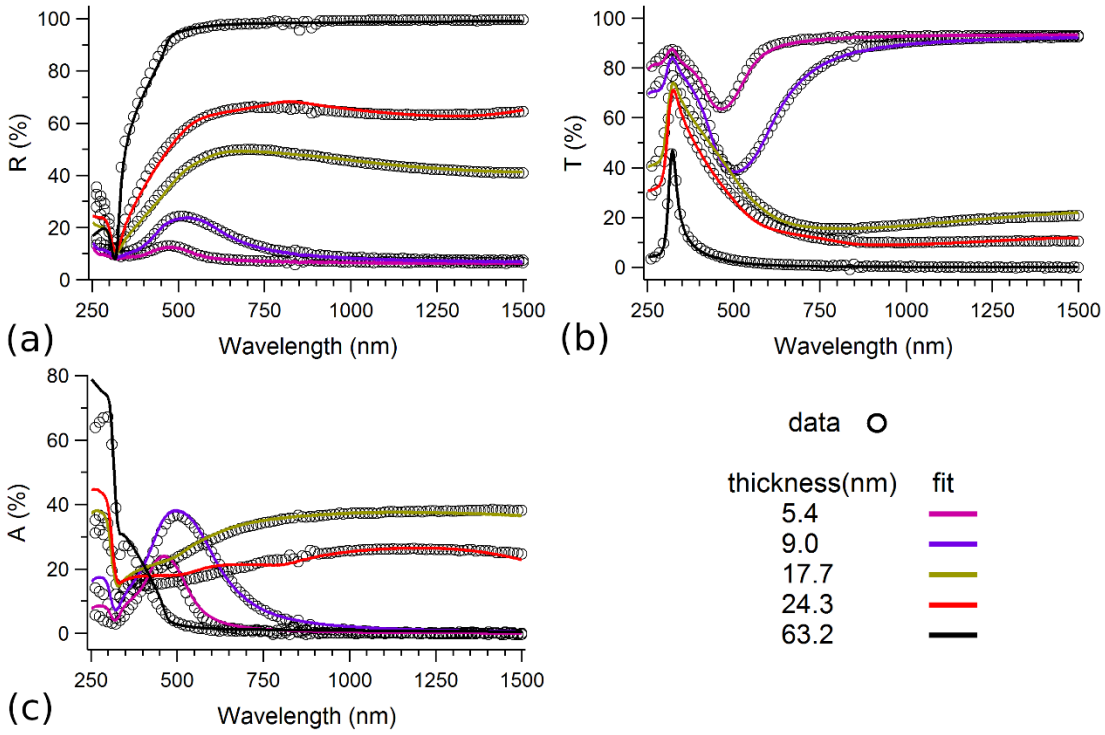

Figure 3-8. R (panel a) and T (panel b) of five thermally evaporated silver films: dots are the measured values, while solid lines are the fitting outputs. Panel c shows absorption spectra obtained as A=1-R-T. In panel c is also shown a simulated absorption (broken line) of a 9 nm bulk silver film.

The thickness dependent trends of the relevant physical parameters are summarized in Figure 3-9 and reported in detail in Table 3-1 and Table 3-4 of the supplementary information. The porosity $f_{v1}$of the bottom layer (Figure 3-9a), in contact with the substrate, is decreasing from 13% to 3 % at 24.7 nm, while the porosity f_{v2} of the core layer (appearing only from a film height of 13.5 nm) rapidly decrease from 5% to reach an almost bulk-like value at 24.3 nm. The depolarization factor (Figure 3-9b) q_1 is varying

only by 1% in the entire thickness range, indicating a pillar-like structure of the film/substrate interface layer, while the depolarization factor q_2 shows a dip at the intermediate coverages. Note that for the film/substrate interface layer, both $\hbar\Gamma_1$ (giving a grain size of 2.4 nm) and the thickness t_1 (Figure 3-9d and Figure 3-9e, respectively) are basically unmodified for all the thicknesses, suggesting that this is little affected by the film growth. On the other hand, $\hbar\Gamma_2$of the core layer (and the layer height t_2) is decreasing (increasing) as a function of the increasing film thickness. This corresponds to an increase of the grain size up to 5.2 nm (Figure 3-9d). The roughness layer height shown in Figure 3-9f is in rather good agreement with the experimentally measured RMS roughness.

The presented results establish a clear morphology – optical properties relation as a function of the film thickness and explain the origin of the optical features observed in the spectra. Below 330 nm wavelength the R and T spectra are dominated by the Ag interband transitions, whose intensity variation is explained simply by the increased film thickness. In the 330 – 900 nm region, the features are strongly thickness dependent. In the present model, describing each film up to 9 nm height by a single core layer plus a roughness layer, the main LSPR (the broad peak around 500 nm) emerges from the BEMA adopted in the core layer, that directly connects the peak shape and wavelength position to the layer porosity f_v and to the Ag inclusions structure. The core layer is organized in pillar-like structures (q_1 close to 1, Figure 3-9b) with a grain size of 2.4 nm (Figure 3-9d). The LSPR redshift is accounted for by the porosity decrease (f_{v1} in Figure 3-9a), the unchanged peak shape indicates a constant Ag inclusions structure, and the peak intensity variation is completely reproduced by an increase of the core layer thickness (t_1 from 1.8 nm to 4.5 nm, Figure 3-9e). The further although less evident LSPR around 360 is reproduced by the

BEMA of the top roughness layer (with porosity set to f_v =50%). Above 900 nm wavelength plasmonic oscillations do not affect the spectra behavior, typical of the underlying substrate. These results are in good agreement with the formation of grains in the growing film following the Volmer-Weber growth mode.

Above 9 nm, the much broader and asymmetric resonance extending in all the visible-infrared region (Figure 3-7) requires the introduction of a second core layer, as detailed in the supplementary information 3.6.6. The elbow around 650 nm is deriving from the first core layer keeping constant thickness, q_1 and Γ_1 and a decreasing porosity justifying the redshift. The featureless part of the spectra above 650 nm is then accounted for by a resonance appearing in the BEMA of the second core layer. The lower depolarization factor q_2 determines the large resonance width and the lower porosity f_{v2} with respect to the underlying first core layer explaining the position in the infrared region. In terms of film growth, the second core layer is schematized by grains growing on top of the first core layer, with a lower porosity, a grain size increasing up to 4.6 nm radius and shape converging to that of the first layer. At 24.3 nm film thickness, f_{v2} approaches the bulk value (0%) and Γ_2 decreases, suggesting a formation of connected Ag domains larger with respect to the first core layer. For the 63.4 nm film the presence of a core layer 1 is no more effective since the light penetration length is lower than t_2. Furthermore, the core layer 2 optical response is compatible with that of a bulk Ag metal. The only deviation from a perfectly homogeneous thin film is determined by the shoulder at 360 nm accounted for by the top roughness layer as discussed in paragraph 3.3.

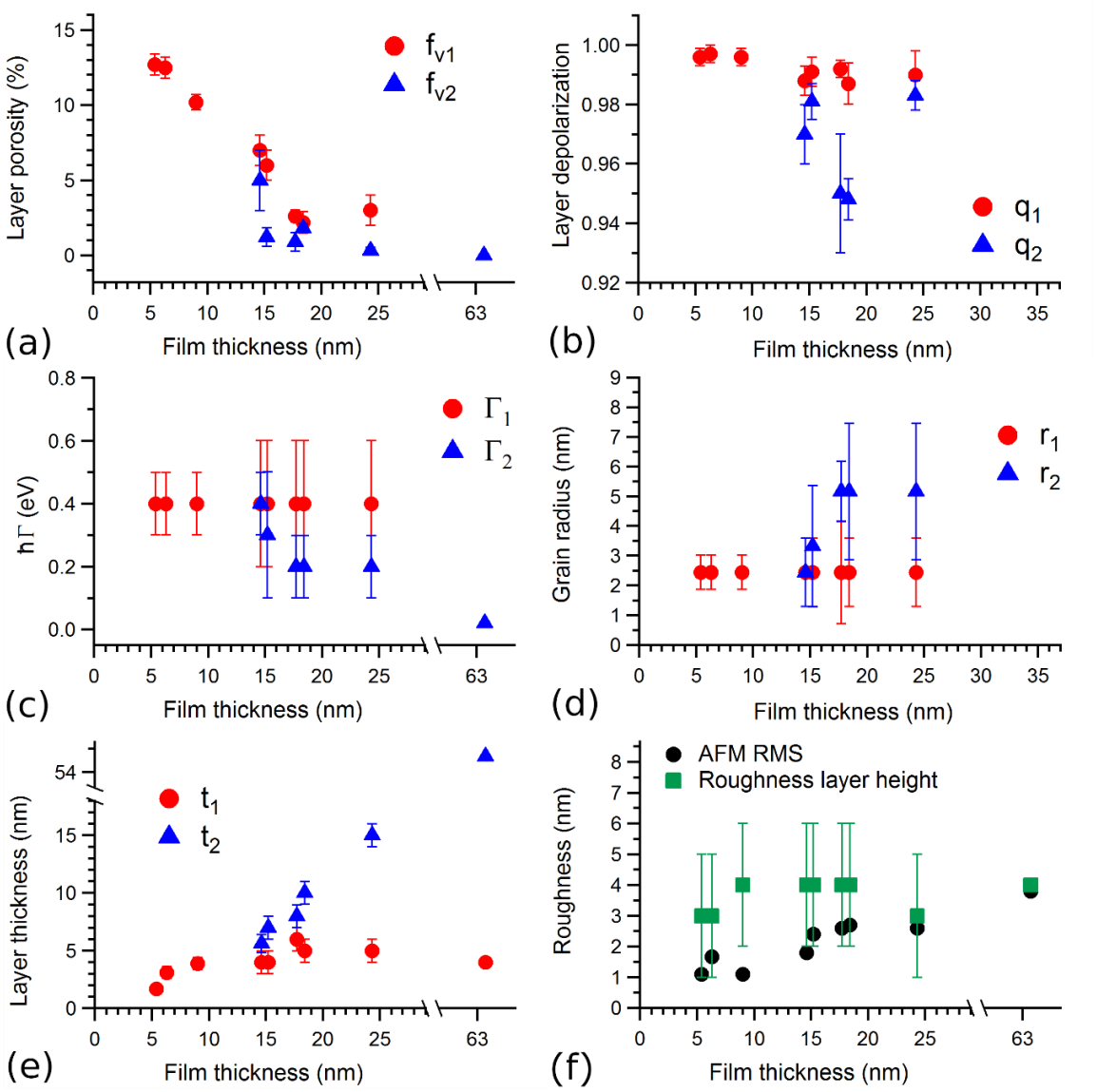

Figure 3-9. The panels (a) to (d) present the thickness dependence of the porosity (a), depolarization factor (b), scattering time (c) and radius (d), respectively, of the first bottom (red dots) and second (blue triangles) layers employed in the model. Panel (e) reports the height of the layers employed for the different film thicknesses and panel (f) compares the film roughness (black dots) with the top roughness layer height employed in the model.

TABLE 3-1:

SUMMARY OF THE FIT RESULTS FOR FIVE SELECTED AG FILMS

Film thickness (nm)	Parameter	Core layer 1	Core layer 2	Roughness layer
5.4	**t** (nm)	1.7±0.4	-	3±2
	f_v (%)	12.7±0.7	-	50
	q	0.996±0.03	-	0.8±0.1
	$\hbar\boldsymbol{\Gamma}$ (eV)	0.4±0.1	-	N.R.
9.0	**t** (nm)	3.9±0.5	-	4±2
	f_v (%)	10.2±0.5	-	50
	q	0.996±0.03	-	0.70±0.5
	$\hbar\boldsymbol{\Gamma}$ (eV)	0.4±0.1	-	N.R.
17.7	**t** (nm)	6±1	8±1	4±2
	f_v (%)	2.6±0.4	0.9±0.6	50
	q	0.992±0.03	0.95±0.02	0.6±0.1
	$\hbar\boldsymbol{\Gamma}$ (eV)	0.4±0.2	0.2±0.1	N.R.
24.3	**t** (nm)	5±1	15±1	3±2
	f_v (%)	3±1	0.3±0.2	50
	q	0.990±0.8	0.983±0.005	0.6±0.2
	$\hbar\boldsymbol{\Gamma}$ (eV)	0.4 ±0.2	0.2±0.1	N.R.
63.2	**t** (nm)	4*	55±5	4±2
	f_v (%)	<5*	0	50
	q	0.995*	-	0.82±0.04
	$\hbar\boldsymbol{\Gamma}$ (eV)	0.4*	0.02(≤ 0.08)	N.R.

Summary of the fit results for five selected Ag films, corresponding to the curves reported in Figure 3-8. t is the layer thickness, $\mathbf{f_v}$ the porosity and q the depolarization factor. For each film thickness data are organized in four columns, following the configuration sketched in Figure 3-1b. The first column identifies the parameter, the second column provides the values for the core layer in contact with the substrate, the third column contains the parameters of the second core layer while the fourth presents the results for the top roughness layer. For the thickest film, the core layer 1 is beyond the light penetration hence its parameters are assumed in analogy to the other samples and labelled with an *. N.R.: not relevant with respect to the fitting results. The complete results are reported in Table 3-4 in the supplementary information.

To summarize, the results provide fundamental insights on the influence of roughness, porosity and grain characteristics on R and T for thin Ag films.

The results presented may find a direct application in fields employing thin Ag films, e.g. plasmonic devices [123] or transparent conductive multilayers [147]. The correlation of the Ag ultrathin dielectric function with the grain size and roughness would allow to explain the data reported by e.g. ref. [123] and describe the plasmonic behavior in relation to the film morphology without arbitrary oscillators. The application of the present results to the data obtained for the Ag films presented in ref. [147] could explain the transmission and reflection response as a function of the aluminum zinc oxide (AZO) roughness, the possible presence of voids in the Ag film and the effect of the top coating AZO layers on the Ag film morphology. Such work would also allow to guide a further improvement of the transmission of the conductive layer by simulating the response of the sandwiched structure and determining the optimal roughness, grains size and thickness parameters required for the actual system growth. Finally, it is worth noting that the results presented in this work are easily transferable to any type of optical system that can be modelled with a stacked multilayer configuration. For example, multicomponent systems where two or more materials are present can be described through appropriate EMA, while gradients on the composition can be accounted for by employing multiple layers. Moreover, the DEMON code can be employed to physically explain data obtained from spectroscopic ellipsometry (as shown in section 3.8 of the supplementary information) in addition to UV-VIS spectrophotometry. The code may also be used to predict the R and T response and the dielectric function of a custom-devised system, thus providing a powerful

tool for devising an optical system with the desired features, avoiding a trial and error approach.

3.5 Conclusions

In this work we presented a quantitative optical and morphological characterization of ultrathin thin Ag films in the 5.4 – 63 nm range deposited by thermal evaporation on fused silica. By exploiting a new home-made code (DEMON), we reproduce the reflectance and transmission data by modelling each film with a stacked multilayer geometry. The code calculates the dielectric function of each layer through the BEMA and the model describes the overall film morphology. We showed the influence of roughness, porosity, grain radius and shape on the R and T spectra in the 250 – 1500 nm wavelength range, obtaining the effective dielectric function of a 9 nm thick film. Moreover, we show the thickness dependence of the relevant physical quantities providing a complete description of Ag films behavior up to the transition to the bulk regime. These results establish a milestone in the understanding of the Ag ultrathin films and open new perspectives in the interpretation of thin film properties and in the design of the optical response of a tailored system.

3.6 Supplementary information

3.6.1 An overview on the DEMON software

In this section the general features of the new computing code will be outlined. The simulations and fitting routines that will be described can be applied to any multi-layered physical system.

The new computing code named Determination of Effective Multilayer Optical constants for Nanotechnology (DEMON), has been implemented in Python for computation and/or fitting of optical spectra. A physical system is modeled trough a multi-layer stack as shown in Figure 3-1 of the main text. A thickness t_i and a dielectric function ε_L , or equivalently a refractive index $N_L = \sqrt{\varepsilon_L}$, are associated to each layer. ε_L can be a pure material dielectric function or an effective one deriving from an Effective Medium Approximation (EMA) by mixing dielectric functions of different composites in case of a non-homogeneous layer. Transmitted and reflected electric and magnetic fields are calculated for each layer by means of the Mueller matrices [148]

$$\begin{pmatrix} E^T \\ B^T \end{pmatrix} = M_{tot} \begin{pmatrix} E^I - E^R \\ B^I + B^R \end{pmatrix} \tag{3-5}$$

where I, T and R are the incident, transmitted and reflected fields and M_{tot} is the Muller matrix describing the optical response of the overall system. M_{tot} can be expressed in terms of the Mueller matrices M_i of each single layer as the matrix product:

$$M_{tot} = \prod_{layer\ i} M_i \tag{3-6}$$

where

$$M_i = \begin{pmatrix} cos(2\pi N_{iL} t_i/\lambda) & isin(2\pi N_{iL} t_i/\lambda)/N_{iL} \\ iN_{iL} sin(2\pi N_{iL} t_i/\lambda) & cos(2\pi N_{iL} t_i/\lambda) \end{pmatrix}$$

(3-7)

is characterized by a phase shift dependent on the wavelength λ, the refractive index N_{iL} and thickness t_i of the i-th layer.

The computation code applies formulas (3-5),(3-6) and (3-7) for the following simulations and fitting purposes:

- Simulation of reflection and transmission spectra for a multi-layer configuration of known composition and morphology. In this section of the code, no experimental data are required. Conversely, all the model parameters of the simulated system are needed as inputs: the layer thicknesses and dielectric functions ε_L. In case of non-homogeneous layers, all the parameters in EMA are required as inputs to determine the layer ε_L. The simulation code outputs the plots of R and T optical spectra and ψ and Δ ellipsometry parameters at any incidence angle as a function of the wavelength.

- Numerical inversion of R and T spectra to obtain an effective dielectric function of a layer. This routine allows to obtain the dielectric function ε_L of a given layer from the experimentally measured R and T spectra. The inputs needed for the extrapolation are the dielectric functions of all the other layers at each measured wavelength and all the layer thicknesses. The extrapolation of ε_L is carried out for each measured wavelength, without assuming any analytical form for the dielectric function. The output is the best ε_L such that the calculated R and T spectra (R_{calc}, T_{calc}) match the measured ones (R_{exp}, T_{exp}), corresponding to the minimization of the quantity:

$$\left(R_{exp} - R_{calc}(\varepsilon_L)\right)^2 + \left(T_{exp} - T_{calc}(\varepsilon_L)\right)^2$$

(3-8)

- This operation can be interpreted as a numerical inversion of $R_{calc}(\varepsilon_L)$ and $T_{calc}(\varepsilon_L)$ as functions of ε_L . As pointed out by [149], just two independent measurements (in this case R and T) for each wavelength are not generally sufficient to determine unambiguously the dielectric function. For this reason, the algorithm requires an initial guess for the

unknown dielectric function at the highest or lowest acquired wavelength and the extrapolated ε_L is the closest dielectric function minimizing equation (3-8). If available, the algorithm allows also to add another optical spectrum to the minimization of (3-8), such as R or T at a different incidence angle.

- Fitting R and T experimental spectra in order to determine layer thicknesses and layer composition and morphology. R and T optical spectra at any incidence angle are fitted to determine some parameters in the multi-layer and BEMA model. For each composite in each layer, a dielectric function is required in an analytical form or, alternatively, can be given numerically. Fitting parameters can be chosen among the layer thicknesses t_i, the parameters involved in the analytical expressions of the composites and, in case of non-homogenous composition, the EMA parameters. The minimized quantity in the fitting routine is:

$$\left(R_{exp} - R_{calc}(t_i, \varepsilon_{Li})\right)^2 + \left(T_{exp} - T_{calc}(t_i, \varepsilon_{Li})\right)^2 \quad (3\text{-}9)$$

and involves both R and T data. A similar procedure can be applied also to ellipsometry data.

3.6.2 Layer roughness

DEMON can include the roughness effect. From the morphological viewpoint, a layer roughness is an oscillation of the surface delimiting the layer. It is necessary to distinguish two regimes, depending on the length scale l of the surface oscillations. When $l < \lambda/10$ (short-scale roughness) the roughness is modelled by just adding a layer described by a Bruggemann's EMA with fixed 50% void fraction.

In the long-range regime ($l > \lambda/10$) the EMA approach is not valid [150]. The layer irregular surface results in as an oscillation of the layer thickness, that destroys the interference effects between electromagnetic fields after multiple internal reflection inside the layer.

In order to characterize the effect of long-range roughness, reflection and transmission of a dielectric non-absorbing single layer has been simulated, providing also an example of a typical substrate optical response. Figure 3-10 (blue line) shows the simulation of R in the range 1500 - 1502 nm wavelength range for a 1mm thick dielectric material with $N = 1.5$ and with no roughness. R oscillations as a function of the wavelength λ are due to the coherent interference effect between the electromagnetic fields after different numbers of internal reflections. Since the phase shift through a slab of thickness t is $e^{2\pi i N t/\lambda}$, the oscillation period is $T_\lambda = \lambda^2/(2Nt - \lambda)$.

However, in spectra obtained from real samples such oscillations are not detected. The sample faces are not perfectly plane and regular but are characterized by oscillations in thickness at a length scale higher than $\lambda/10$. This type of long-range roughness spoils the coherent interference between multiple internal reflections. This effect can be taken into account by two different methods. The first one consists in assuming a distribution of values for the layer thickness, whose width is identified as the long-range roughness. The resulting optical spectra are then calculated averaging over the thickness distribution. Figure 3-10 shows the results considering a 1 μm long range roughness, averaging over 5, 10 and 20 thicknesses uniformly distributed in the range between t and t+1μm. The higher is the number of thicknesses, the more the oscillations are reduced and R approaches a constant mean value. In the second approach, valid for R and T spectra, all the multiple internally reflected intensities are summed incoherently. As shown in Figure 3-10 (black line), the interference effect is completely destroyed, leading to a flat R spectrum corresponding to the average of the oscillations. This latter method is employed for all the

substrates in this work. In case of non-absorbing materials, these operations are independent of the layer thickness, which then will be fixed to 1 mm in this work.

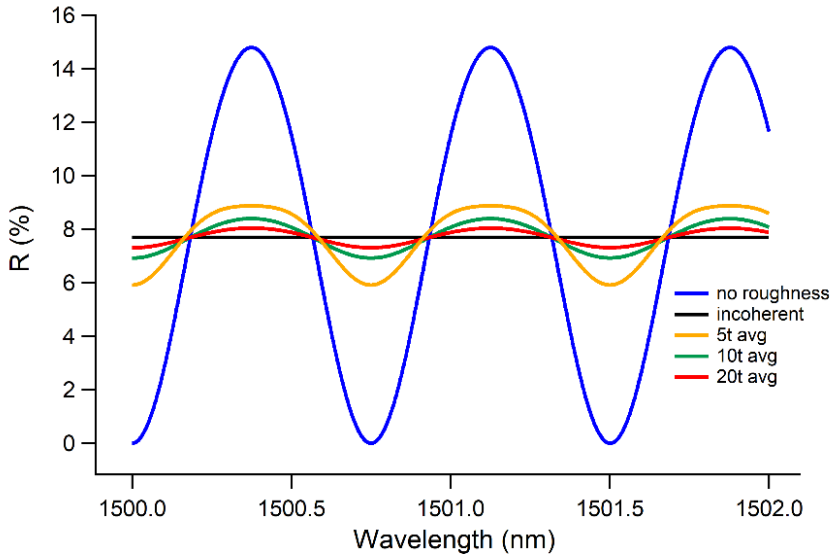

Figure 3-10. 1mm thick glass substrate simulations. Calculated reflection for a single layer with N=1.5 in which the faces are perfectly planes (blue line). Reflection resulting from the incoherent sum of multiple internally reflected intensities (black line). Average of reflected intensities over 5, 10 and 20 thicknesses uniformly distributed between 1 mm and 1 mm+1 µm

3.6.3 Numerical inversion

The numerical inversion algorithm allows to extrapolate a dielectric function of a layer from the experimentally measured R and T data. Nonetheless, more than one dielectric function resulting from the inversion can be compatible with the experimental data, leading to an ambiguity as pointed out by [149]. In this section, we discuss an example of two different possible inversion results deriving from the same R and T data. The experimental data employed are the R and T spectra of the 9 nm thick Ag film (Figure

3-11a), described in detail in section 2 of the main text. The multi-layer configuration that is modelling the film consists in a 1 mm thick SiO_2 fused silica substrate with a long-range roughness and a 9 nm thick top layer corresponding to the Ag film. The top layer refractive index $N = n + ik$ has been extrapolated after fixing the two layer thicknesses, assuming the substrate dielectric function of [151] and giving an initial guess for N at 1500 nm. Figure 3-11b shows two possible results for the Ag layer refractive index corresponding to two different initial guesses. The first solution is obtained for the initial guess N=2+0.01i, while the second one for N=0.01+2i.

Both solutions show a flat n and k behavior for wavelengths higher than 800 nm, corresponding to a constant trend of R and T spectra, while a peak in n and k is located around 500 nm due to the Ag film LSPR. At 320 nm, both solutions are characterized by a minimum in n and k, that for the second solution is a marked deep for k.

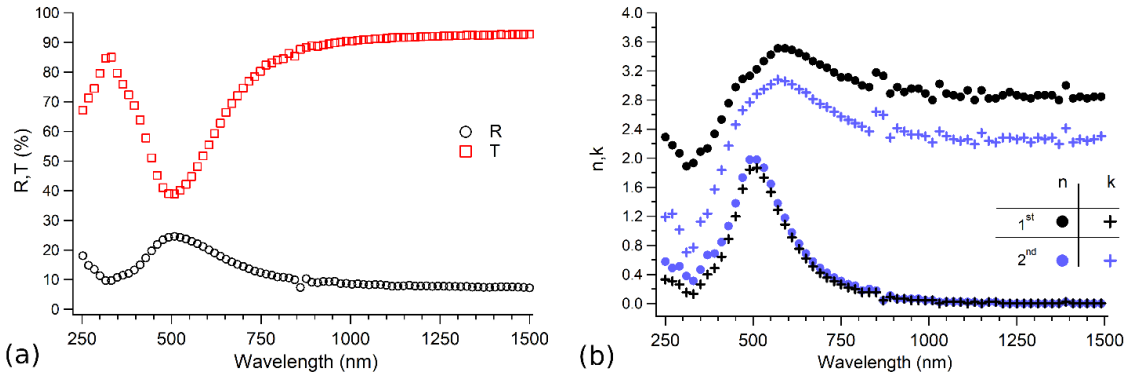

Figure 3-11. Measured reflection and transmission of 9nm Silver film thermally deposited (a) and two possible refractive indices N=n+ik inverted from R and T data (b) within the two-layer model

The existence of more refractive indices corresponding to the same spectra can be understood in terms of the interplay between n and k. Starting from the first solution, one can imagine to decrease n, increasing the transmission and reducing the reflection at metal/dielectric interfaces. At the same time, an increase of k can balance the variation of reflection and transmission at the interfaces with an increase of absorption along the film thickness.

The two results are not in agreement, confirming the ambiguity of the numerical inversion process obtained by considering two spectra only [149]. For this reason, this approach will not be applied to Ag films in this work, in favor of a direct experimental spectra fitting. Nonetheless, the numerical inversion will be adopted with optical spectra of non-absorbing substrates, whose refractive index determination result to be not affected by such ambiguities, as explained in section 3.7.1.

3.6.4 Gold and Silver bulk refractive index

Here we describe in detail how we obtained the Ag and Au bulk dielectric functions employed in this work, in particular to validate the code as explained in section S.3 and as input of the BEMAs employed in the main text. We started from the Ag and Au optical constants as taken from references [118] and [152], that are supposed to describe the response of ideally pure and homogeneous bulk metals. Each dielectric function is expressed by three terms:

$$\varepsilon_{Ag/Au}(\omega) = \varepsilon_{\infty} + \varepsilon_{IB}(\omega) - \frac{\omega_{\mathrm{pl}}^2}{\omega^2 + \mathrm{i}\Gamma\omega}$$

(3-10)

where the background constant ε_{∞} accounts for oscillators out of our investigation range, the contribution ε_{IB} stems from the interband transitions in the ultraviolet regime and the last term is the Drude oscillator. An analytical form for the bulk Au dielectric function of eq. (3-10) can be found in reference [152], where the interband term is expressed as:

$$\varepsilon_{IB} = \sum_{i=1,2} A_i \left[\frac{e^{i\phi_i}}{1 - \frac{\omega}{\omega_i} - i\gamma_i} + \frac{e^{i\phi_i}}{1 + \frac{\omega}{\omega_i} + i\gamma_i} \right]$$

(3-11)

A_i, ω_i, γ_i and ϕ_i are parameters describing amplitude, angular frequency, width and phase of the i-th Lorenz oscillator, respectively.

The values for the parameters employed in (3-10) and (3-11) for the bulk Au dielectric function are showed in Table 3-2.

TABLE 3-2:

PARAMETRIZATION OF BULK GOLD DIELECTRIC FUNCTION

ϵ_{∞}	$\hbar\omega_{pl}$	$\hbar\Gamma$	A_1	$\hbar\omega_1$	γ_1	ϕ_1	A_2	$\hbar\omega_2$	γ_2	ϕ_2
1.54	8.65 eV	0.085 eV	1.27	2.63 eV	0.25	$-\frac{\pi}{4}$	1.1	3.8 eV	0.31	$-\frac{\pi}{4}$

Parametrization of bulk gold dielectric function provided by reference [152]

In the Ag case, the Johnson and Christy reference [118] provides the bulk refractive index N_{JC} for a set of wavelengths in the range 188-1940 nm (red squares in Figure 3-12) as obtained from a direct numerical inversion of the data considering a single homogeneous bulk layer, rather than any analytical expression.

In the present work, we assumed the analytical function ε_{Ag} in equation (3-10) for the Ag dielectric function with an interband contribution of the form:

$$\varepsilon_{IB} = A_{lor}\frac{(\Gamma_{lor}^2)}{(\omega-\omega_{lor})^2+\Gamma_{lor}^2} + i\left[b + \frac{H}{1+e^{(\omega_c-\omega)/s}}\right] \tag{3-12}$$

where the real part is a Lorenz oscillator with amplitude A_{lor}, width Γ_{lor} and position ω_{lor}, and the imaginary part is a step function centred at ω_c with amplitude H, width τ and offset b. The analytical expression for the refractive index is hence $N_{Ag} = \sqrt{\varepsilon_{Ag}}$. We then determined a numerical value for each parameter in (3-10) and (3-12), by matching our analytical refractive index N_{Ag} to the Johnson and Christy dataset N_{JC}. Bulk values for ω_{pl}, Γ and ϵ_∞ have been found by matching the region 380-2000 nm where interband effects are absent, while the interband parameters in equation (3-12) are determined in the region 250-380 nm. Table 3-3 shows the results for the numerical values of each parameter, while Figure 3-12 shows a complete agreement of our analytical refractive index N_{Ag} and the one from reference [118].

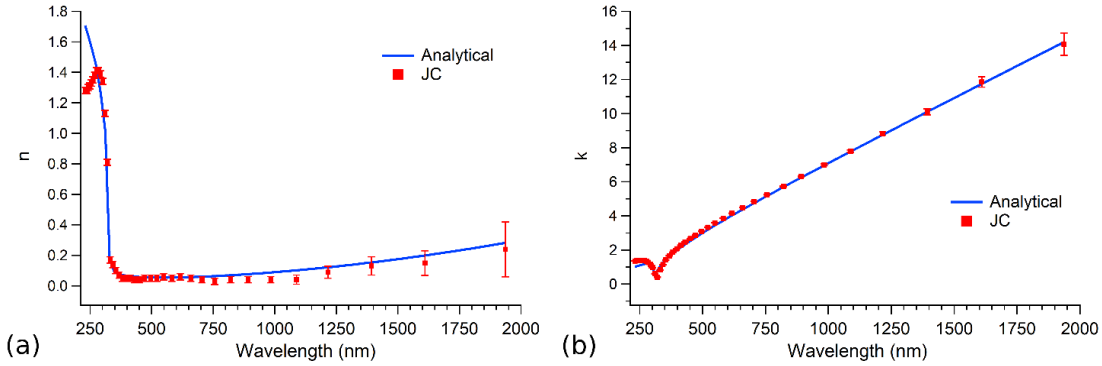

Figure 3-12. Jhonson and Christy data NJC in [118] (red squares) and our analytical expression N_{Ag} (solid lines) for the bulk silver refractive index n+ik.

TABLE 3-3:

PARAMETRIZATION OF BULK SILVER REFRACTIVE INDEX

ϵ_∞	$\hbar\omega_{pl}$	$\hbar\Gamma$	A_{lor}	$\hbar\omega_{lor}$	$\hbar\Gamma_{lor}$	H	b	$\hbar\omega_c$	$\hbar s$
4.8	9.2 eV	0.023 eV	1.70	3.94 eV	0.25 eV	3.26	0.19	4.06 eV	0.09 eV

Parameters for our analytical expression N_{Ag} of the bulk silver refractive index found by matching Johnosn and Christy data [118]

3.6.5 Complete fit results for silver films

Figure 3-13 shows measured R and T spectra (dots) for the complete set of thermally evaporated Ag films. Solid lines represent the fitting curves, showing excellent agreement with experimental data within 2%. The associated model parameters determined by the optical spectra fitting are reported in tab Table 3-4. The uncertainties are associated to a 4% displacement of the simulated R and T curves from the measured ones in any point of the wavelength spectrum. For thicknesses lower than 10 nm, the films are modelled as a two-layer Ag stack, with a roughness layer and just one core layer. For higher thicknesses, two core layers and a top roughness region have been considered. For the thickest sample,

an hypothetical core layer 1 with the same $f_{(v)}$, q and Γ parameters (labelled with a *) as all the other films does not affect the spectra. All the quantities labelled with N.R. (not relevant) do not affect R and T spectra for more than 2 %. Each two or three-layer stack, modelling the Ag film, is supposed to lay on a 1 mm thick fused silica substrate. A detailed description of data and models is elaborated in section 3.3.

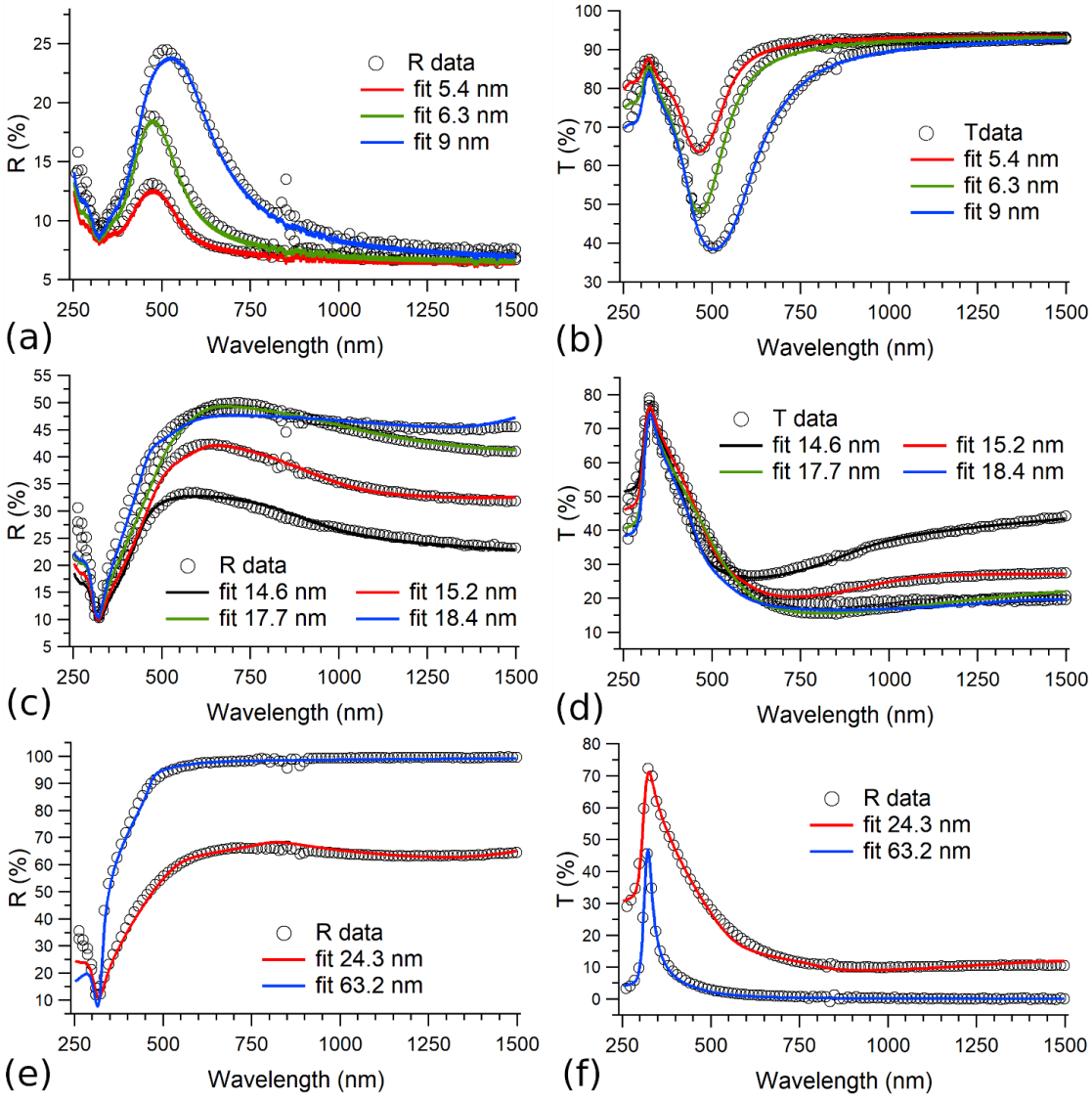

Figure 3-13. R and T measured data (dots) and best fit curves (solid lines) for thermally evaporated silver films. Thicknesses in the legends are measured at the film edges by AFM.

TABLE 3-4:

FIT RESULTS FOR THE COMPLETE SET OF AG FILMS

Film thickness (nm)	Parameter	Core layer 1	Core layer 2	Roughness
5.4	t (nm)	1.7±0.4	-	3±2
	$f_{(v)}$ (%)	12.7±0.7	-	50
	q	0.996±0.003	-	0.8±0.1
	$\hbar\Gamma$ (eV)	0.4±0.1	-	N.R.
6.3	t (nm)	3.1±0.5	-	3±2
	$f_{(v)}$ (%)	12.5±0.7	-	50
	q	0.997±0.003	-	0.8±0.1
	$\hbar\Gamma$ (eV)	0.4±0.1	-	N.R.
9.0	t (nm)	3.9±0.5	-	4±2
	$f_{(v)}$ (%)	10.2±0.5	-	50
	q	0.996±0.003	-	0.70±0.05
	$\hbar\Gamma$ (eV)	0.4±0.1	-	N.R.
14.6	t (nm)	4±1	5.6±0.8	4±2
	$f_{(v)}$ (%)	7±1	5±2	50
	q	0.988±0.005	0.97±0.01	0.7±0.2
	$\hbar\Gamma$ (eV)	0.4±0.2	0.4±0.1	N.R.
15.2	t (nm)	4±1	7±1	4±2
	$f_{(v)}$ (%)	6±1	1.2±0.6	50
	q	0.991±0.005	0.981±0.006	0.6±0.2
	$\hbar\Gamma$ (eV)	0.4±0.2	0.3±0.2	N.R.
17.7	t (nm)	6±1	8±1	4±2
	$f_{(v)}$ (%)	2.6±0.4	0.9±0.6	50
	q	0.992±0.003	0.95±0.02	0.6±0.1
	$\hbar\Gamma$ (eV)	0.4±0.2	0.2±0.1	N.R.
18.4	t (nm)	5±1	10±1	4±2
	$f_{(v)}$ (%)	2.2±0.7	1.8±0.3	50
	q	0.987±0.007	0.948±0.007	0.6±0.2
	$\hbar\Gamma$ (eV)	0.4±0.2	0.2±0.1	N.R.
24.3	t (nm)	5±1	15±1	3±2
	$f_{(v)}$ (%)	3±1	0.3±0.2	50
	q	0.990±0.008	0.983±0.005	0.6±0.2
	$\hbar\Gamma$ (eV)	0.4 ±0.2	0.2±0.1	N.R.
63.2	t (nm)	4*	55±5	4±2
	$f_{(v)}$ (%)	<5*	0	50
	q	0.995*	-	0.82±0.04
	$\hbar\Gamma$ (eV)	0.4*	0.02(≤ 0.08)	N.R.

Table 3-4: Fit results for the complete set of silver films modelled by a two or three layers stack. t is the layer thickness, $f_{(v)}$ the porosity, q the depolarization factor and Γ the scattering rate in the Drude

oscillator. For each sample, data are organized in four columns, following the configuration in figure 1b in the main text. The first column identifies the parameter, the second column provides the values for the core layer in contact with the substrate, the third column contains the parameters of the second core layer while the fourth presents the results for the top roughness layer. For the thickest film, a core layer 1 (whose parameters are assumed in analogy to the other samples and labelled with a *) is not visible from R and T spectra. The film thicknesses, labelling the different samples, have been measured by AFM at the film edge.

3.6.6 The role of two core layers in the 10-20 nm thick Ag films

This section will focus on Ag films with thicknesses between 10 nm and 20 nm. In section 3.3, these films were modelled as a three-layer stack to fit R and T data, with a top roughness layer and two core layers (Figure 3-1b). In this section we show that two core layers are necessary to reproduce experimental data, while the influence of the roughness has already been described in detail in section 3.4.1.

R and T measured spectra (dots in Figure 3-14) show a broad and asymmetric peak around 550 nm with a long infrared tail for all the films. As discussed in section 3.4.1, for wavelengths higher than 350 nm, the peaks appearing in R, T and A spectra are associated to Localized Surface Plasmon Resonances (LSPR). In our multi-layer model, each LSPR is reproduced by a BEMA, whose parameters can tune the peak width and frequency. In section 3.4, the peak at 550 nm was reproduced by two overlapping LSPRs, originating from two BEMAs with different $f_{(v)}$ and q, associated to the two core layers. The bottom core layer, with a q around 0.990 and a porosity ranging from 7% to 2.2%, accounted for the peak amplitude at 550 nm, by producing a narrow resonance such as in the 9 nm film (Figure 3-4 in the main text). The other core layer determined a wide peak, extending in the infrared region, and was characterized by lower depolarization factor (around 0.96) and

porosity (from 5 % to 0.9 %). R and T fitting curves (Figure 3-13) resulted then from the combined contributions of the two resonances.

In this section, a two-layer configuration with just one core layer and a top roughness is considered, leading to a best fit output in Figure 3-14 (solid lines). The model cannot reproduce the experimentally measured data for wavelengths higher than 500 nm, where the deviation between fitted and experimental curves reaches 5 %. The associated results for the fitting parameters are reported in Table 3-5, where the error bars correspond to a 10 % deviation. The roughness layer depolarization factor has been constrained in the range 0.7-0.8, in analogy with thinner films. For each film, the core layer depolarization factor and porosity are in line with the average of the core region values obtained within the three-layer configuration (Table 3-4). Nonetheless, the fitting R and T curves show a flat behavior in the 500-750 nm range instead of a maximum and minimum respectively, while do not agree with the convexity of the experimental spectra for higher wavelengths.

In conclusion, Figure 3-14 shows how a configuration with just one core layer is not able to reproduce R and T spectra for wavelengths higher than 500 nm, implying that two core layers must be necessary included in the model.

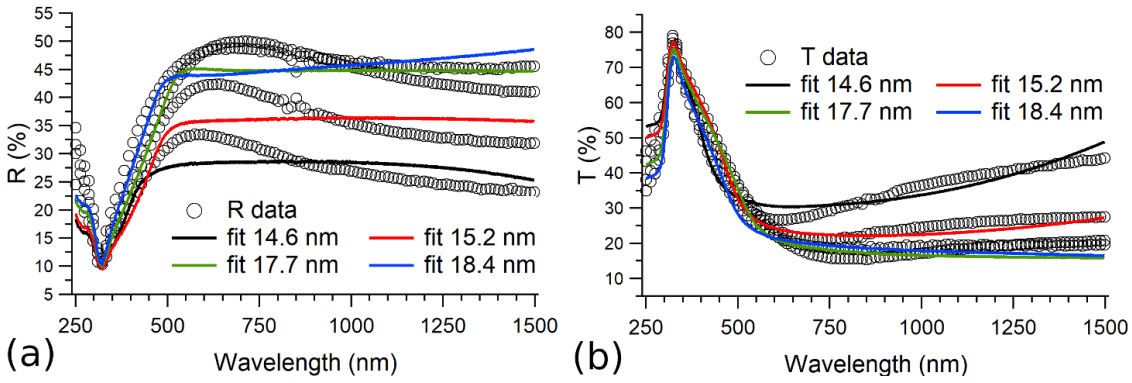

Figure 3-14. Measured R and T spectra (dots) of Ag thin films in the 10 -20 nm thickness range. Outputs (solid lines) of the fitting routine, considering just one core layer.

TABLE 3-5:

FIT RESULTS FOR AG FILMS WITH A SINGLE CORE LAYER MODEL

Film thickness (nm)	Parameter	Core layer	Roughness
14.6	t (nm)	9±2	5±4
	$f_{(v)}$ (%)	7±2	50
	q	0.966±0.004	0.7
	Γ (eV)	0.4±0.2	N.R.
15.2	t (nm)	10±2	5±5
	$f_{(v)}$ (%)	4±1	50
	q	0.98±0.01	0.7
	Γ (eV)	0.4±0.2	N.R.
17.7	t (nm)	13±3	3±3
	$f_{(v)}$ (%)	2±1	50
	q	0.97±0.01	0.7
	Γ (eV)	0.3 ±0.2	N.R.
18.4	t (nm)	15±2	3±3
	$f_{(v)}$ (%)	2±0.5	50
	q	0.96±0.02	0.7
	Γ (eV)	0.3±0.2	N.R.

Fit results for parameters involved in a model with just one core layer. Ag thin films in the 10 – 20 nm range are considered.

3.7 Software validation

In this section, the new software is tested against some physical system already studied in the literature. The comparison between the outputs from this code and other references provides a validation of DEMON.

In section 3.7.1, we applied the numerical inversion routine to obtain the fused silica (SiO_2) refractive index from experimental R and T optical spectra, obtaining a very good agreement with standard reference values.

In section 3.7.2, we calculated the R and T of ideally pure and homogeneous gold films, with thicknesses between 3 nm and 36 nm. The spectra are then compared to the transmission simulations taken from reference [153].

In section 3.7.3, the experimentally measured R and T of gold thin films taken from reference [154] have been fitted within a multi-layer configuration based on the Bruggeman's EMA. The film thicknesses provided by our fitting routine are in complete agreement with those obtained from the X ray interference technique [154], providing also a film porosity trend in line with the conductivity data from the same reference. In addition, the software is able to provide more detailed information about inclusion shape and size and the morphology gradient along the gold film depth, not studied in [154].

3.7.1 Fused silica substrate

Reflection and transmission of a 1 mm thick fused silica (SiO_2) layer have been measured at normal incidence (Figure 3-15a) in the range 250-1500 nm by a Perkin Elmer Lambda 950 spectrophotometer. The sample is modelled by a single dielectric layer with

a long-range roughness. The layer thickness is fixed to 1mm, though its exact value is not relevant for the model, being the material not absorbent, and the interference fringes absent due to the roughness. Experimental spectra shown in Figure S.4(a) have been numerically inverted leading to the result in Figure 3-15b.

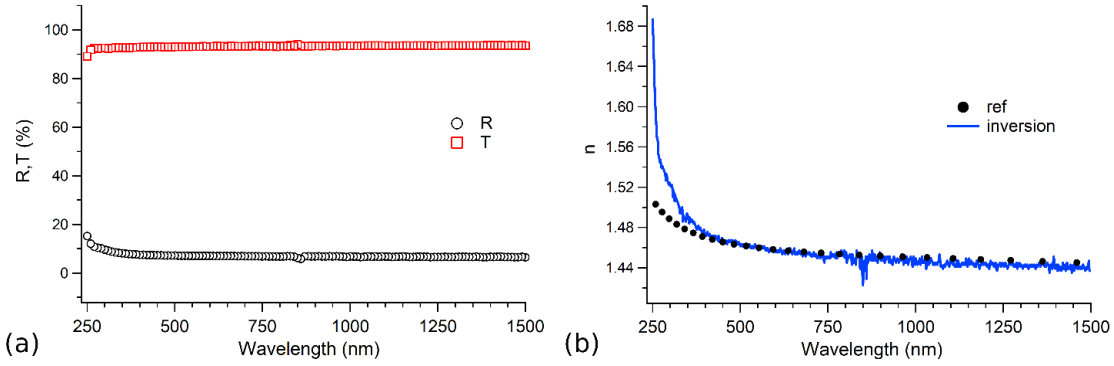

Figure 3-15 Measured reflection and transmission of a 1 mm fused silica substrate (a). In panel (b) the numerically inverted refractive index (solid lines) and the refractive index from reference [151] (dots). The imaginary part k is not given by the reference since the value k=0 is assumed by [151] in all the spectrum.

The refractive index resulting from the numerical inversion (solid line in Figure 3-15b) shows a decreasing behavior of n from 1.5 to 1.44 due to a 2% and 1% variation in R and T spectra respectively. In all the wavelength range, the value $k = 0$ is found, resulting from the vanishing absorption. The extracted refractive index $N = n + ik$ is completely in agreement with [151] (dots in Figure 3-15b), validating the numerical inversion in the case of an homogeneous dielectric material. It is important to note that the small deviation of the numerically inverted n from the reference value below 270 nm wavelength is due to small changes observed experimentally in this range, that are due to

an instrumental inaccuracy related to the material used in the integrating sphere of the spectrophotometer.

Differently from the section 3.6.3, the numerical inversion of SiO_2 spectra does not provide ambiguous solutions. Indeed, the fused silica layer is not absorbing and the interplay between n and k, giving rise to the ambiguity, is not possible in this case. *We conclude that, even considering two optical spectra such as R and T at normal incidence, the numerical inversion algorithm can determine unambiguously the refractive index of a dielectric non-absorbing material, such as single-layer substrates.*

The SiO_2 refractive index obtained in this way has been used to model the substrates supporting the Ag thin film.

3.7.2 Simulation of gold thin films in the bulk assumption

In this section the simulation routines in the new optical software are validated. R and T spectra of gold thin films of thicknesses between 3 nm and 36 nm are simulated. The metal film is assumed to be bulk and the results are then compared to the outputs of transmission simulations carried out by [153].

The model consists in a two-layers configuration where the top one represents a pure and homogeneous bulk gold film and the bottom one a glass substrate. In the top layer, the Au is described by the bulk dielectric function shown in equation (3-10) and (3-11) with the parameters of Table 3-2. A BK7 glass with refractive index taken from [155] has been considered as the bottom layer, with a long range roughness. A thickness of 1 mm has been fixed for the substrate, though not relevant for the optical response.

Figure 3-16 reports our simulated R and T spectra (solid lines) in the 400 nm – 900 nm wavelength range. While increasing the film thickness from 3 nm to 36 nm, the reflectance grows in intensity in all the spectrum and in particular for higher wavelengths, where from 10% reaches 90%. A minimum is located around 500 nm, narrowed and enhanced for higher thicknesses. Transmission decreases with film thickness in all the spectrum, with a peak around 550 nm sharpening for thicker samples.

Our simulation outputs were compared to transmittance outputs of [153] shown in Figure 3-16b as dashed lines. The transmittance values are in agreement within 3%. The slight difference between these two simulations may be ascribed to different input gold dielectric functions, since in ref. [153] those are not specified.

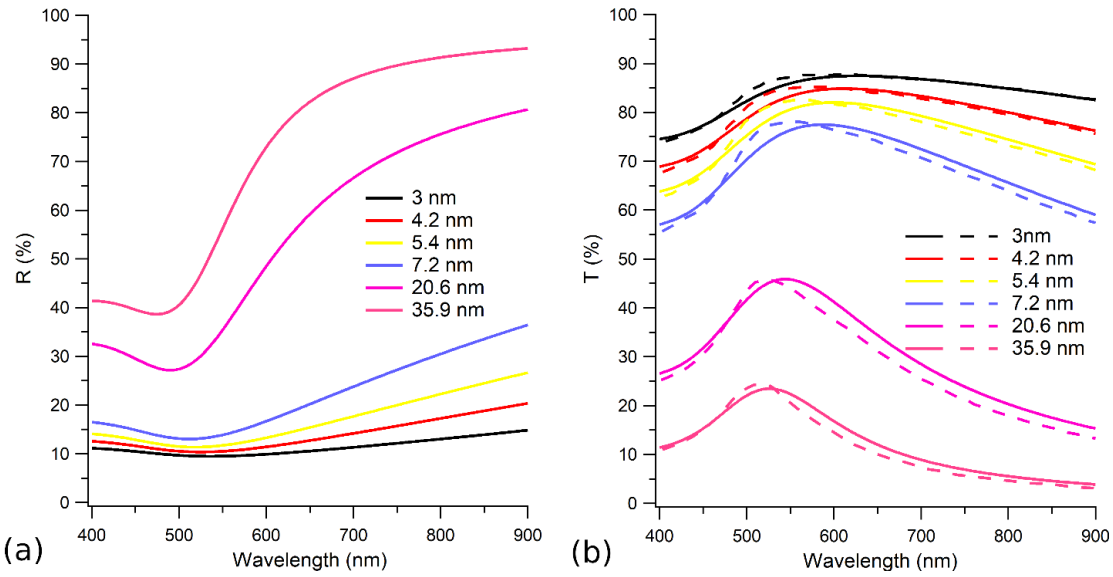

Figure 3-16. Simulated reflectance and transmission (solid lines) of bulk gold films deposited over a glass substrate, compared with the transmission calculated in [153] and reported as dashed lines.

The agreement between our simulation and the one of [153] validates the new algorithms for multi-layer reflection and transmission calculations.

As noticed in the same reference, these R and T spectra do not reproduce real measurements, since thin films have more complex structure and further morphological properties, such as roughness and porosity, which should be considered. As discussed in the next sections, more complex multi-layer configurations and EMAs will be able to reproduce real experimental data.

3.7.3 Fitting thin gold film spectra

Further elaboration in the modelling is required to reproduce the experimental optical response of non-homogeneous and porous films, where morphological properties may also be not uniform inside the film. The R and T data are hence fitted by the new software, employing a multi-layer model where Bruggeman's EMAs (BEMA) provide each layer dielectric function ε_{Li} (equation (3-1)). In order to validate this approach, R and T data of thin gold films have been taken from reference [154] and fitted with DEMON. Our fit outputs, in particular film thicknesses and porosity, are then compared to the results from [154].

We recall that the Au films with thicknesses between 5 nm and 28 nm were thermally evaporated onto a glass substrate as described in ref. [154]. Reflection and transmission spectra at normal incidence in the wavelength range 350 nm -2500 nm are taken from the same reference.

In our fitting model, a two or three-layer configuration is employed. The bottom layer consists in a 1 mm thick glass substrate with long range roughness, described by the refractive index of [155]. The Au film is described by the other layer or as the stack of the other two layers. The pure Au dielectric function is parametrized by Table 3-2. For each film, the scattering rate Γ can deviate from the reference value depending on the inclusions size (equation (3-4)), and its value is assumed to be common for all the Au layers in the film. The Au dielectric function is then combined with that of the vacuum ($\varepsilon = 1$) in a BEMA for each metal layer, to obtain the layer effective dielectric function ε_{Li}. Consequently, the porosity and the gold inclusions shape are quantified through the f and q parameters of the BEMA. Moreover, the gradient of such morphological properties in the entire film is accounted for by the presence of two Au layers with different BEMA parameters.

In Figure 3-17, measured spectra from [154] (dots) and our fit results (solid lines) are reported. For each layer the thickness and f and q BEMA parameters have been considered as fitting variables, while Γ is considered as a fitting parameter in common for all the Au layers in each film. Fit results are in excellent agreement with experimental data. The results for the fitting parameters are showed in Table 3-6, where each uncertainty is associated to a displacement of 4% of the simulated curves with respect to the measured ones in any point of the spectrum.

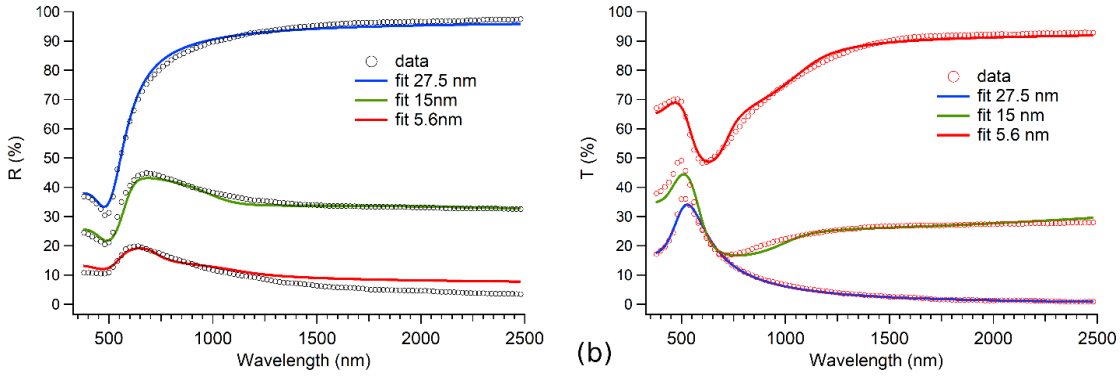

Figure 3-17. R and T experimental data (dots) from reference [154] and best fit curves (solid lines) for thermally evaporated gold films. Thicknesses in the legend are the ones from reference and have been obtained by X-ray interference technique.

R and T spectra are dominated by the interband transitions in the region below 550 nm, where the spectra show the same bulk-like trend as simulated in Figure 3-16 with a minimum in R and a maximum in T at 500 nm for all the films. For higher wavelengths the thicker film is characterized by a typical bulk-like optical response with an increasing reflectance, reaching 100%, and a decreasing transmission, approaching 0%. The film is modelled as a single 28 nm thick and completely bulk Au layer, with no modifications to the dielectric function parametrized in Table 3-2. The result is in agreement with [154], where the thickness obtained by the X-ray interference technique is 27.5 nm, while the order of magnitude of the resistivity ($4.7 \cdot 10^{-8} \Omega m$) is that of the bulk metal.

Decreasing the film thickness, a decrease of the reflectance and an increase of the transmission is found in all the wavelength spectrum. The optical responses show a completely different behavior with respect to the thicker sample. Indeed, a wide peak centered around 600 nm and with a long infrared tail appears for both 5.6 and 15 nm films, blue-shifting for the thinnest sample. Moreover, for higher wavelengths R and T have opposite trends with respect to the bulk one.

As shown in section 3.3, each resonance is identified as a Localized Surface Plasmon Resonance (LSPR) and it is reproduced by a BEMA, whose f and q parameters can tune the peak frequency and width. For the 5.6 nm and 15 nm samples in figure S.6, the Au film is modelled as a two-layer stack where the BEMA in the Au inner layer reproduces the central region of the peak (around 600 nm) while the long tail is determined by the top Au layer with a much broader resonance. Fit results reported in Table 3-6, show that in both films the inner Au layer is characterized by a depolarization factor q around 0.99, associated to a pillar like inclusion shape (as in Figure 3-2). This gives an insight on the Au morphology at the metal/dielectric interface: the amount of deposited metal influences the inner layer thickness and porosity but not the inclusion shape. In both films, the top Au layer shows a 3% lower porosity and a lower depolarization factor (around 0.975) with respect to the inner region, resulting in a broader and redshifted resonance (as in section 3.4.1).

The mean film porosity is 10% for the 5.6 nm film, while decreases to 4% and 0% for the 15 nm and 27 nm samples respectively. This trend is correlated to a resistivity behavior decreasing with thickness: the value of the thinnest sample is too high to be measured by [154], while a result 10^4 times higher than the bulk one is found for the 15 nm film and finally the thickest sample shows a resistivity twice the bulk value. This is consistent with the fact that the presence of voids reduces the film conductivity.

The scattering rate $\hbar\Gamma$ is 0.3 eV for the 5.6 nm and 15 nm films. The equation (3-4) in the main text allows to extrapolate an inclusion radius r= 4 nm, assuming for gold $v_F = 1.39 \cdot 10^6$ m/s. For the thicker sample the fit converges for $\hbar\Gamma$ <0.15 eV implying the

inclusion radius must be $r > 14$ nm, confirmed in [154] by the presence of crystals with size between 30 nm and 100 nm.

Finally, for each film, the total thickness is completely in agreement with the value provided by [154] obtained by X-ray interference technique (reported in Table 3-6).

In conclusion the gold films spectra analysis has provided a validation for the fitting routine since thicknesses and morphological properties deriving from the fit results are in agreement with [154]. Additionally, we also provided porosity, inclusion shape and dimension and morphological variations through the film depth.

TABLE 3-6:

FIT RESULTS OF GOLD FILMS

Film thickness (nm) (from ref [154])	Parameter	Inner Au layer	Top Au layer
5.6	t (nm)	3.3±0.7	1.9±0.5
	$f_{(v)}$ (%)	11.0±0.8	8±1
	q	0.990±0.004	0.979±0.005
	$\hbar\Gamma$ (eV)	0.3±0.1	
15	t (nm)	5±1	9.5±0.8
	$f_{(v)}$ (%)	6±1	3±1
	q	0.991±0.005	0.973±0.007
	$\hbar\Gamma$ (eV)	0.3±0.1	
27.5	t (nm)	28±2	-
	$f_{(v)}$ (%)	0	-
	q	-	-
	$\hbar\Gamma$ (eV)	0.085 (<0.15)	-

Fit results of gold layers shown in figure S.6. For the thickest sample, a single bulk and perfectly homogeneous layer can fit data. For the other two films a two-layer model is employed with two different EMA parameters and thicknesses. For each layer the thickness t, porosity $f_{(v)}$, depolarization factor q and scattering rate Γ deriving from the fitting routines are reported. The parameters uncertainties are associated to a 4% displacement of the simulated curves from the measured ones in any point of the spectrum. The first column reports the thickness values from [154].

3.8 Other applications

The new software can provide the refractive index $N_L = n + ik$ of each individual layer composing the multi-layer stack model (Figure 3-1). Each refractive index is obtained from the layer effective dielectric function ε_L through the relation:

$$N_L = \sqrt{\varepsilon_L} \tag{3-13}$$

where ε_L can result from an EMA in case of a non-homogeneous layer.

Figure 3-18 shows the case of the 9 nm thick Ag film, modelled as a stack of a core and a roughness layer (described in detail in section 3.3). The refractive indices associated to each of the two layers are reported. Each curve is obtained from equation (3-13), where the dielectric functions result from two BEMAs with parameters in

Table 3-4. The total refractive index (blue line in Figure 3-18), describing the overall film response, is calculated as the square root of the total dielectric function (defined in section 3.4.1 from the mixing of the individual dielectric functions of the two layers).

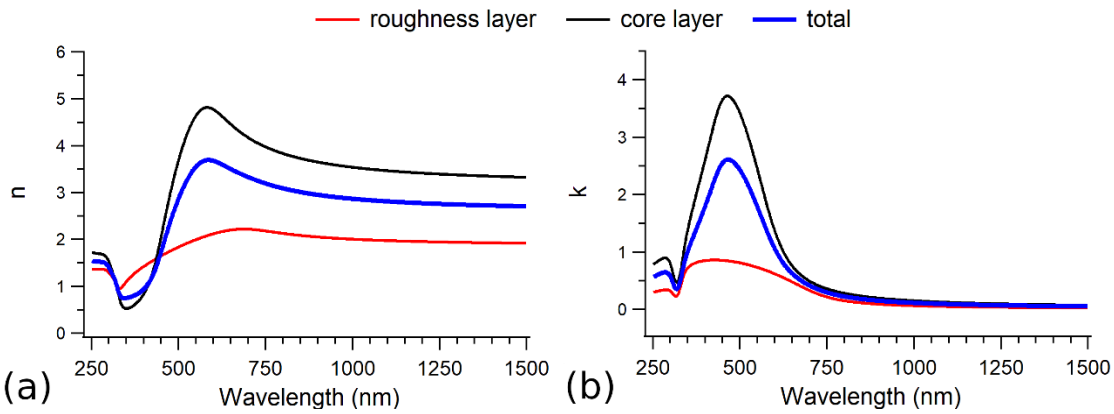

Figure 3-18. Refractive index N=n+ik of the core layer (black lines) and top roughness layer (red lines) for the 9 nm thick Ag film. The total refractive index (blue curve) describes the overall film optical response.

The new software can also simulate and fit ellipsometry data at any incidence angle. For instance, in figure S.10, the simulation of ψ and Δ variables at 70° incidence for the 9 nm thick Ag film is shown in the wavelength range 250- 1500 nm. The domains of both the two angular variables have been chosen between -90° and +270°. Therefore, the jump at 590 nm in figure S.10b is not a physical effect but is due to the variable definition.

The film is modelled as a two-layer stack with dielectric functions defined with parameters in

Table 3-4. An infinite silica half-plane is considered as substrate, in order to remove the oscillating contribution which would originate from the multiple internal reflections at silica/air interface in a substrate layer.

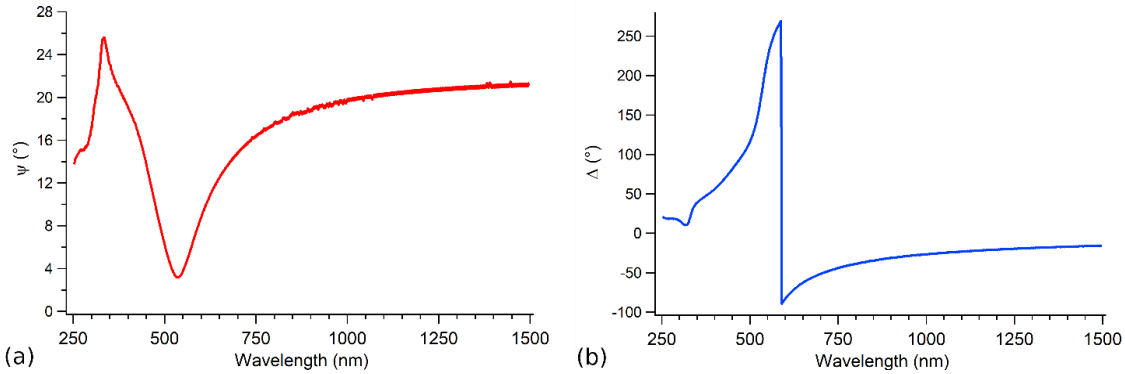

Figure S.10. Simulation of ψ and Δ ellipsometry angles at 70° incidence for the 9 nm thick Ag film. The film is modelled as a two layer stack with dielectric functions defined in Table 3-4, while an infinite silica half plane is considered as substrate.

CHAPTER 4:

SYNTHESIS AND CHARACTERIZATION OF PLASMONIC AU CRYSTAL ARRAYS

4.1 Abstract

As discussed for Silver nanomaterials in the previous chapter, the material's optical properties can be directly correlated to the nanostructure's morphology and chemical composition. This is the focus of Plasmonics, in which the optical response is discussed in terms of collective electron's oscillation at the metal/dielectric interfaces, with applications in sensing devices, catalysis and optical communications. In this chapter a novel system of Au nanoplate array with tunable morphological and plasmonic properties is presented. The system is synthesized through the combination of dynamic templating and liquid/solid phase growth. After describing the synthesis approach, two main research objectives will be presented. In the first one, the synthesis process itself is investigated, with a particular focus on how the liquid solution growth is affected by the presence of reducing agents and the light irradiation. In the second objective, the synthesis process is employed to create (i) large area conductive regions arising from merging Au nanoplates and (ii) asymmetric hexagonal plates with embedded nanogaps that are of interest to plasmonics, sensors and nanoelectronics. Furthermore, an alternative method is also proposed to synthesize Au nanoplates by utilizing colloidal solutions.

4.2 Introduction

The combination of dynamic templating (DT) and liquid/solid interface growth (LSG) has shown great potential in the fabrication of plasmonic nanostructures [84] and sensing devices [85], [156].

The DT process allows to place in a regular lattice configuration an array of noble metal nanocrystals, all of them sharing the same crystal orientation[83]. This is accomplished through the high temperature crystallization of nanoclusters obtained by depositing the metal through a nanopatterned polymer mask. In the second stage (LSG), the metal crystals are used as seeds for the epitaxial nucleation of bigger structures. This is performed in a liquid solution where the dissolved metal ions are transferred to the solid structures through a reduction process.

The main advantages of this technique are the possibility of designing the nanostructure's architecture by modifying the crystal seeds or the LSG solution, chemical composition, and the possibility of covering large areas ($\sim 1\ cm^2$) with high yield array. For instance, among the many structures designed in the last few years, array of nano-stars[85], chiral structures with spiral geometry[86] and asymmetric bimetallic Janus nanoparticles[87] were synthesized, that can find direct applications in plasmonics, surface enhanced Raman scattering (SERS), and catalysis[157].

Planar structures can be obtained when a capping agent in the LSG solution prevents a crystalline facet from growing, allowing the structure to extend in the other directions. This is the case of 30-50 nm thick Au nanoplates, characterized by an atomically

flat surface parallel to the substrate and a growth along the substrate to form triangular[84] or hexagonal[83] nanoplates.

In addition to enhanced plasmonic properties, due to their sharp corners, these structures represent a great potential as nano-electronic devices. When two adjacent plates, sharing the same crystallographic orientation, are growing sufficiently, their atomically flat edges could merge and potentially create a perfect electric contact. This would be impossible with nanogranular pads, where inhomogeneities and pores decrease the electric conductivity with respect to a bulk metal[158]. Furthermore, a very thin nanogap can be realized in case the two edges are separated by few nanometers instead of merging. These architectures are particularly relevant in the field of SERS[159], chemical and molecular sensing[160] due to the high concentration of electromagnetic fields in the gap under optical and electrical excitation. In this framework, the use of single crystal structures with atomically flat facets can overcome the limitations of state-of-the-art devices, where the nanogap narrowness is very limited by the rough edges of conventional polycrystalline pads[89].

In this section I will outline my results and perspectives in the DT combined with LSG synthesis process of Au nano-hexagons. In the first part of the result section, I will outline some developments in the improvement of the synthesis process through two pathways: tuning the capping/reducing agents and optimizing the light irradiation during the LSG. Afterwards I will discuss some applications of the Au hexagons fabrication to different contexts: the merging of adjacent plates to create large conductive pads, creation of composite morphologies by milling one side of the hexagon and inducing an

asymmetrical growth. Finally, an alternative way to nanoimprint lithography (NIL) process to produce Au seeds is presented.

4.3 Materials and methods

The nanoimprinting lithography followed by the dynamic templating (NIL + DT, also referred to as simply DT), described in detail in section 2.7, has been employed to synthesize arrays of Au crystalline nanoparticles on crystalline sapphire substrates. In the DT process a sapphire (0001 facet oriented, MTI corporation) is initially spin coated with a two-layered polymer resist (a 100 nm thick PMGI SF 3S lift-off resist and 400 nm thick 7030R thermal resist), where an array of holes is then imprinted through a silicon stamp (600 nm lattice spacing, 350 nm deep and 240 nm in diameter- Lightsmyth Technologies). After increasing the holes depth through radiative ion etching (RIE with Ar ions for two cycles at 20W - 4 sscm and 40 W – 2 sscm, Samco RIE-1C system), a layer of Sb and Au (1 mm thick foil of 99.9985% purity from Alfa Aesar as Au source) are sputter deposited uniformly on the patterned surface (with a model 681 Gatan coater), followed by the resist lift off using a dioxolane solvent EBR-PG, Kayaku Advanced Materials. The Au nanocrystals are then obtained by heating up to 1010 °C in N_2 gas flow (in a Lindberg Blue M furnace). These assembled nanoparticles of size in the 50-70 nm range, spatially arranged in a regular array configuration, share the same substrate induced crystalline orientation with the (111) plane as a top surface.

Furthermore, instead of the DT, an alternate technique of synthesizing Au nanocrystals is proposed, where no imprinted resists and sputter coating are employed but

the Au nanoparticles are obtained from an Au colloidal solution prepared through the Turkevich method[161]. In this technique a sapphire, coated with poly(4-vynilpyridine) (P4VP) sticking agent, is exposed to the Turkevich solution to allow the colloidal nanoparticles to attach to its surface. The substrate surface is then exposed to an UV light source (254 nm wavelength, 200 mW/cm^2) and annealed at 500 °C in air to clean from carbon-based contamination, followed by the Au seeds assembly at 1100°C in N_2 atmosphere.

The Au nanocrystals are then used as seeds to grow epitaxially larger structures through a liquid/solid interface growth (LSG). The LSG solution, in which the array is immersed in the growth solution composed of 10.5 mL deionized water, 1 mL Brij-700 polymer (30 mM concentration, average MV 4670, Spectrum Chemical) and 1.2 mL $HAuCl_2$ salt (10 mM, Beantown Chemical). The growth process is carried out at room temperature, under 300 rpm stirring. A series of LSG growth experiments under controlled light environment were performed, by using LEDs light sources of different wavelengths and intensities connected to an Arduino device. In order to protect the LSG process from uncontrolled external light, the growth experiments were carried out in a closed box, in which a home-made aluminum foil coating of the internal walls served as a scattering surface for the LED light and assured an homogenous irradiation distribution (see section 2.7 for further details). A light meter was measuring the LED intensity expressed in lux and converted to W/m^2, according to section 4.6.3. The light intensity was set to 1 W/m^2, while five different colors, i.e. wavelengths, were explored: UV light at 410 nm, blue at 456 nm, green at 520 nm, yellow at 585 nm, and red at 657 nm.

In section 4.4.4, a combination of atomic layer deposition (ALD, Savannah 100 instrument), milling (Gatan model 685 PECS II system), and etching processes have been employed to induce an asymmetric growth in the hexagons. The ALD was used to coat the arrays with a 5 nm thick TiO_2 (titania) film. In the milling process the titania-coated seeds were irradiated with an Ar ion beam at 9° incidence angle, 0.5 keV kinetic energy for 10 seconds. Afterwards, the titania coating was etched from the milled sides by immersing the array for 15 seconds in a solution of 2 mL deionized water, 1 mL H_2O_2 and 1 mL NH_4OH.

The optical characterization of the arrays is carried out in the 350-1100 nm wavelength range by a JASCO V-730 UV-VIS spectrophotometer, while the morphology is characterized by scanning electron microscopy (SEM, FEI Helios G4 UX Dual Beam SEM/FIB workstation). The conductivity of some of the Au structures has been measured with a two-point probe system by contacting the edges of the structure, applying a defined voltage, and measuring the current flowing.

4.4 Results

The results presented here can be classified in two types, involving respectively the improvement of the LSG growth mechanism and the synthesis of specific nanostructures.

The LSG growth improvement has been investigated as a function of the Brij capping agent concentration and type (section 4.4.1) and the light irradiation during the growth (section 4.4.2). On the other side, the specific fabricated nanostructures consisted of large conductive regions of merged hexagons (section 4.4.3) and asymmetric hexagon growth achieved after milling selectively one side of the hexagons (section 4.4.4). Finally,

the alternate method of synthesizing small Au seeds using a Turkevich colloid is proposed (section 4.4.5).

4.4.1 Tuning the capping/reducing agent

Brij solution plays the dual role of reducing and capping agent in the nanostructure growth. The reduction process allows the Au^{3+} ions to transfer from the solution to the solid crystals, determining the growth. Conversely, as capping agents, the Brij molecules bind to the (111) Au crystal top facet (parallel to the substrate) and prevent the plates from growing in the direction perpendicular to the substrate, thus promoting a planar growth. Figure 4-1 shows a 3.5-hour growth of an Au array performed with four different concentrations of capping agents: 2, 4.6, 9.2 and 13.8 mM of Brij L35 polymer (Polyoxyethilene(23)lauryl ether $(C_2H_4O)_{23}C_{12}H_{26}O$ - 1199 g/mol). It should be noticed that for 9.2 and 13.8 mM concentrations, an overcapping of the plates results in the deformation of the nanostructure edges, resulting in an irregular shape. For the intermediate concentration of 4.6 mM, the plates are showing very regular hexagonal geometry and flat edges. Good plate shapes are also reported for 2.0 mM, in which, however, the low concentration results in decreasing the Au ion reduction rate, implying a considerably slower growth rate.

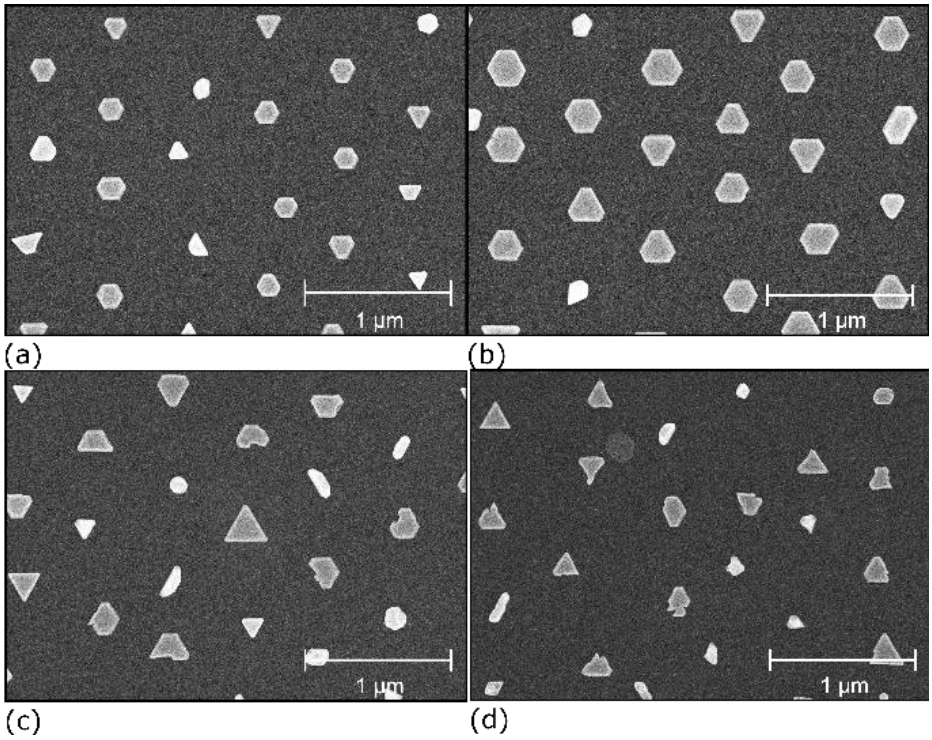

Figure 4-1. 3 hours growth of Au hexagons for four Brij L35 concentrations: 2 mM (a), 4.6 mM (b), 9.2 mM (c) and 13.8 mM (d).

Based on these results, an ideal concentration of 4.6 mM has been determined for the Brij-L35 capping agent. Similar investigation carried out for Brij 700 (Polyoxyethilene(100)stearyl ether $C_{18}H_{37}(OCH_2CH_2)_{100}OH$ - 4670 g/mol) allowed to identify an ideal concentration of 2.4 mM.

4.4.2 Growth under controlled light environment

In the LSG process, light might play a crucial role in the Au^{3+} ions reduction, affecting the nanocrystal growth rate as well as their morphology. In this section, we conduct a set of experiments in which, the Au crystalline seeds, obtained through DT, are

then immersed in a LSG solution (10.5 mL Di water + 1 mL of 30 mM Brij-700 + 1.2 mL 10 mM Au salt) and the growth is carried out in a controlled light irradiation. As outlined in section 2.7, a closed box was used to avoid any uncontrolled light irradiation from the external ambient luminosity, while the LED sources were placed on top of the stirring plate. A home-made aluminum foil coating the box internal walls served as a scattering surface for the LED source, assuring a spatially homogenous irradiation of the LSG solution. In this set up, less than 5% fluctuations in the light intensity were observed between different points inside the box.

The first experiment (shown in Figure 4-2) was performed by continuously exposing Au seeds arrays to 1 W/m^2 LED lights during the LSG growth and comparing the results to a growth performed in the dark. Five different LED colors were considered: UV at 410 nm wavelength, blue at 456 nm, green at 520 nm, yellow at 585 nm, and red at 657 nm. The Au crystal growth was monitored by acquiring each 30 minutes an UV-VIS optical extinction spectrum, that is characterized by a LSPR peak whose redshift is proportional to the plate size increase. The complete optical spectra dataset is reported in section 4.6.1. Figure 4-2 shows the LSPR peak measured after 30 minutes growth in darkness and under the five different LED colors, compared to a representative spectrum of an initial Au seeds array. In all the cases a redshift never exceeding 30 nm occurs with respect to the initial LSPR peak position ($550 \pm 20\, nm$). It should be noted that the differences between the LSPR peaks in Figure 4-2a after 30 minutes growth could be determined not only by the exposure to different LED light colors but also by a different initial peak position for each array.

In order to discriminate between the two different effects, in Figure 4-2b we report for each array the LSPR peak redshift with respect to its initial position, that can be considered representative of the plate edge growth rate. The array grown in the dark reports the slowest growth rate, with less than 10 nm shift in 30 minutes, while a maximum in the growth rate is registered for the green and the yellow light experiments (30 nm shift in the LSPR). Furthermore, the LSPR peak position of the initial Au seeds spectrum (solid vertical line at $550 \pm 20\,nm$ in Figure 4-2b) matches the LED light wavelength range corresponding to the fastest growth, suggesting a plasmon mediated growth mechanism at this stage. This is also supported by some previous works, in which the role of the LSPR excitations as mediators of the growth mechanism emerged [83]. After the first 30 minutes, the growth rate remains constant in the red, yellow and dark environments, while a much higher growth is reported for the UV and blue light. As shown in extinction spectra in Figure 4-2c, after 1.5 hours the LSPR reaches just 610 nm in the dark experiment and 660 nm in the red and yellow lights, while the peak is centered at 710 and 900 nm for the UV and blue growths. This is also confirmed by Figure 4-2d, displaying the redshift occurring between 1 hour and 1.5 hour of growth. The arrays exposed to blue light (220 nm shift in 30 minutes) are growing 6 times faster than for higher wavelength colors. Moreover a 50% higher redshift occurring in the green light with respect to yellow and red suggests that the light effects on the growth rate are not limited to just blue and UV light. The lower shift value reported for the UV experiment could arise from an underestimation of the measured UV light intensity. As discussed in section 4.6.3, this uncertainty, affecting in a greater extend the UV region, is determined by the convolution of the light sensor spectral response and the LED spectrum width.

In Figure 4-2e, the LSPR peak shift with respect to the Au seeds spectrum along the entire duration of the experiment is reported for each array, revealing three behaviors.

1) The growth in the darkness is characterized by a constant rate ($15 - 20\ nm/h$), that persists for at least 6 hours.

2) In case of exposure to red and yellow light, the growth rate in the first 1.5h is linear and faster with respect to the dark (with $60\ nm/h$ shift) and then decreases between 2 and 4 hours, slowing down to 0 after 5 hours. In this case, the plates plasmonic excitations might be responsible for the growth enhancement, while this effect might disappear when the plates become sufficiently large so that the associated LSPR resonance does not overlay with the LED light frequency, as showed in the complete set of optical spectra in section 4.6.1 (supplementary).

3) In the UV and blue light, the growth rate increases in time, starting form $50 - 60\ nm/h$ in the first 30 minutes and reaching $400\ nm/h$ after 1.5 hour.
In this case no LSPR excitation is expected to occur, while the much faster growth rate could be ascribed to the formation of intermediate colloidal Au aggregates in the LSG solution that then are transferred to the Au plates through the reduction process. The progressive formation of such intermediates during the experiment would also explain the progressively increasing plate growth rate. The formation of such structures is also supported by the optical extinction of the LSG growth solution acquired at the end of the tests, reported in Figure 4-13. In such spectra an increase in absorption in the 500-700 nm range with respect to a freshly prepared solution could be ascribed to the formation of plasmonic colloidal nanoparticles.

The green light growth shows an intermediate behavior between 2) and 3) with an increase in shift rate in the first 1 hour and a decrease thereafter.

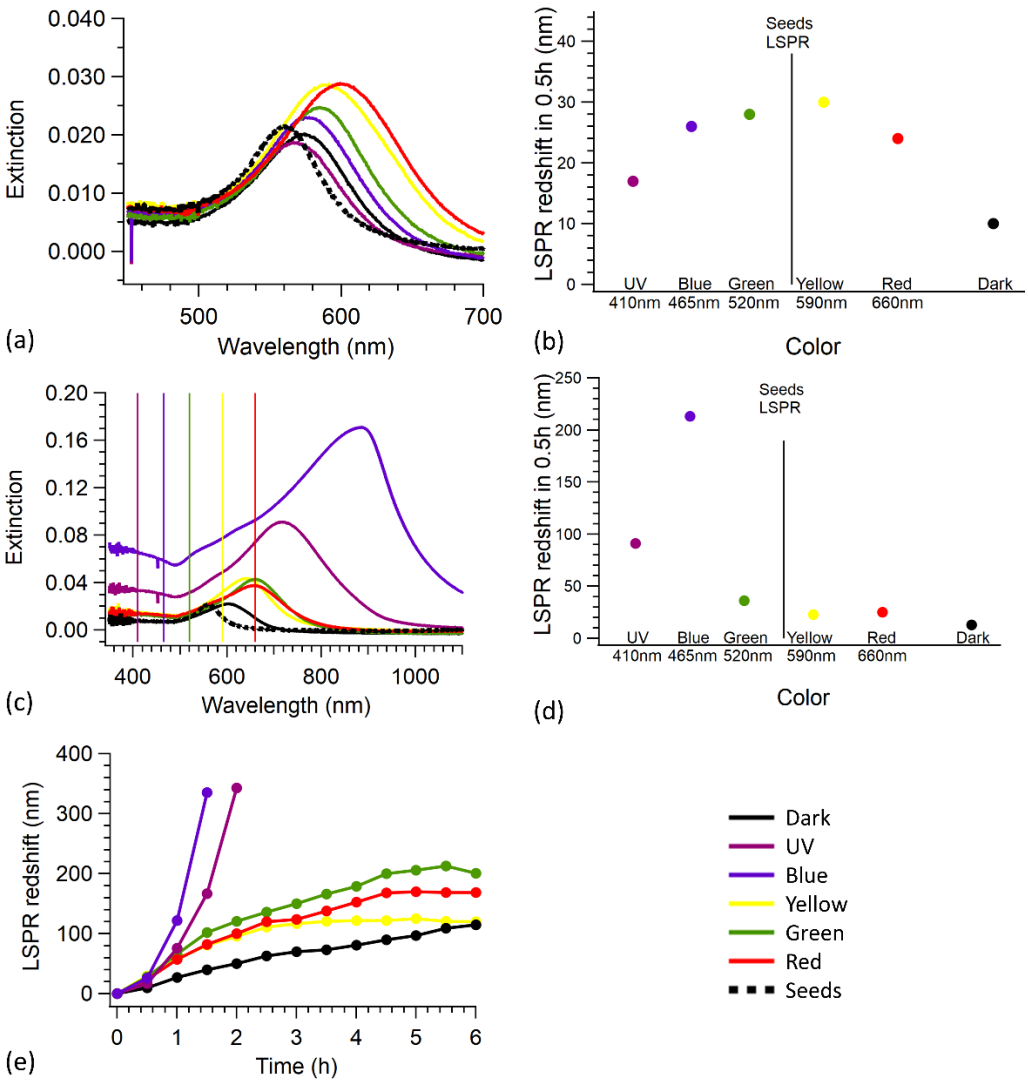

Figure 4-2. Extinction spectra of Au arrays grown in different light environment for 0.5 (a) and 1.5 hours (c), compared to the initial seeds plasmon peak (dashed line). In (c) the individual wavelength of each LED is also indicated as a vertical line. LSPR peak maximum redshift between 0 and 0.5 hours (b) and between 1 and 1.5 hours growth (d) are reported for the different colors. In (e), the time evolution of the LSPR peak maximum along the overall experiment duration for the different colors.

After the optical characterization (Figure 4-2) of the Au plate arrays grown for 2h (UV), 1.5h (blue) and 6h (green, yellow, red lights and in darkness), SEM images were acquired to provide a morphological insight on the structures (Figure 4-3a-f). In all the arrays, the hexagonal structures that are normally expected in presence Brij capping agents, coexist with triangular shapes. In case of UV and blue light, the hexagon yield is higher than 80%, while this percentage decreases to 50 % in the other cases (Figure 4-3g, where non hexagonal shapes were identified as the plates with at least one edge smaller than 1/3 of the structure diameter). Two possible arguments to explain these discrepancies can be made, observing that the arrays were grown for a different total duration and the interruption of the growth process each 30 minutes to measure the optical spectra could also affect the growth.

In order to explore these hypotheses, a further experiment (described in section 4.6.1) has been carried out, in which three arrays were grown in UV, green and red light environments for the same total duration of 6h and with no interruption (the optical spectra reported in Figure 4-14 in section 4.6.1 were acquired only before and after the growth and not each 30 minutes). The LSPR peak position at the end of the experiment shows an increase of the growth rate for the UV and red lights with respect to the interrupted experiments, while a decrease in the growth is reported for the green LED instead. This opens new questions on how the repeated interruption of the growth process (and the temporary removal of the capping agents from the plate surface) affects the LSG mechanism. Furthermore the SEM images of these arrays (in Figure 4-15) show that, similarly to the interrupted experiments, a 20-30% lower hexagon yield is always reported

for the green and red light growths compared to the UV one, confirming the correlation between the plate morphology and the impinging light wavelength.

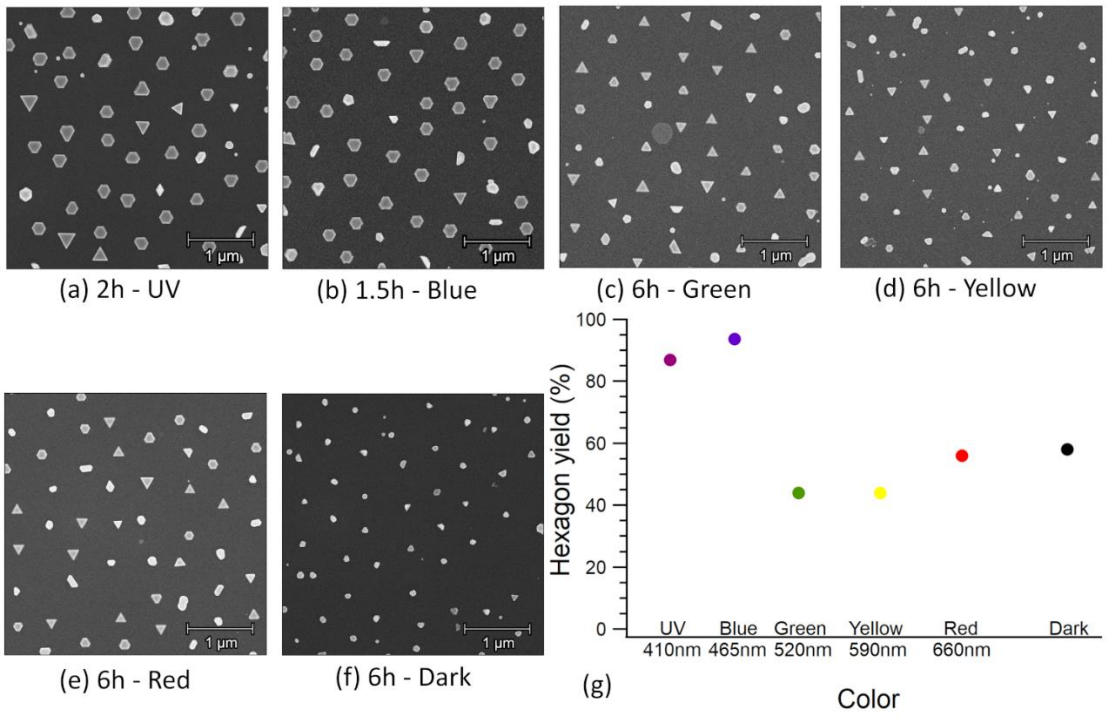

Figure 4-3. SEM images of Au plate arrays grown under LED light illumination of different colors (a-f) with associated growth duration. In (g) the hexagon yield calculated from the SEM images.

In order to demonstrate the formation of intermediate structures and investigate their role in the growth, a further set of experiments were carried out with a different lighting protocol. The solution was initially exposed to LED light for 1.5h before starting the plate growth and thereafter, immediately after switching off the LED sources, the same solution was used to grow an array of Au seeds in the dark. Figure 4-4a-b show the LSPR spectra and associated shifts in the first 30 minutes of the Au seeds growth. A three times higher shift is reported for the UV and blue pretreatments (150 nm redshift in 30 min) with

respect to the green and red ones (50 nm shift). This supports that the UV and blue light exposure is inducing the formation of intermediates, that persist in the growth solution even after the irradiation, affecting the growth in the dark. These growth rates are also retained between 30 minutes and 1 hours for the UV, green and red light experiments, while a 50% increase occurs for the blue one (Figure 4-4c-d). These values are comparable to the rates reported after 1.5 hours growth carried out under constant light irradiation (Figure 4-2). Furthermore, the approximately linear trend in the shift along the first hour (Figure 4-4e) instead of a rapidly increasing behavior suggests that in the darkness no significant formation or depletion of intermediates takes place.

After 1 hour, in the UV and red pretreated solutions, a decrease of the LSPR shift suggests that the depletion of such colloidal structures might start.
In order to better understand the formation of intermediates, two additional experiments were performed, in which the just Au salt or just Brij solution were irradiated with blue light for 1.5 h before starting the growth. Thereafter, after switching off the LED light, the pretreated Au salt and Brij were used to prepare separately two LSG growth solution, where two arrays were grown. As shown in Figure 4-4e, in both cases the LSPR shift rate does not exceed 30 nm/h and is constant along the experiment duration. This proves that the intermediate formation can only occur when the light is impinging on a solution containing both the Au salt and Brij components.

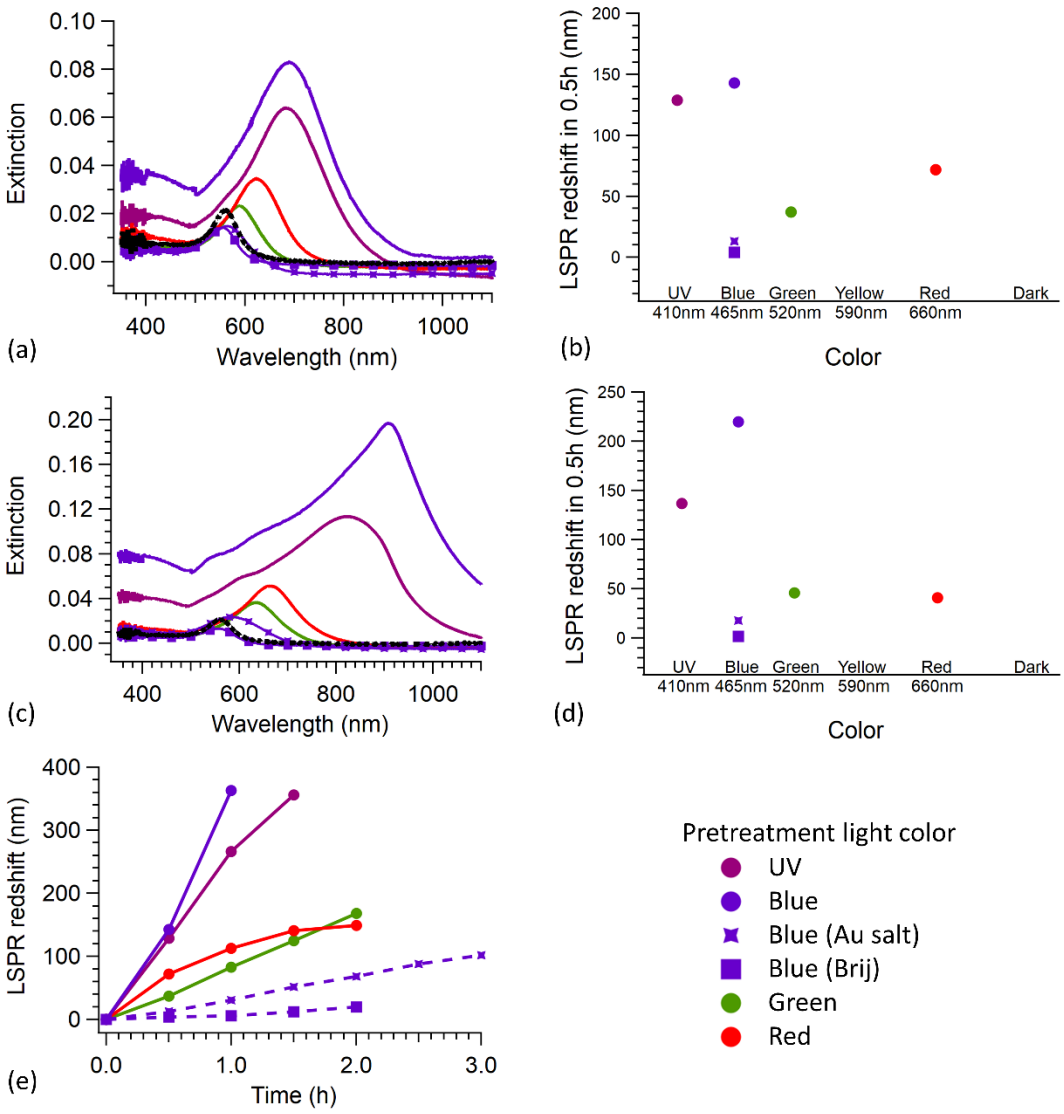

Figure 4-4. Au plate arrays grown for 0.5 (a) and 1 hour (c) grown in the dark with an LSG solution previously exposed to different LED lights for 1.5 hours. In case of blue light, two more experiments were performed by exposing just the Au salt or Brij components separately before starting the growth. Associated LSPR peak maximum shift between 0 and 0.5 h (b) and between 0.5 and 1 h (d). In € the LSPR peak maximum time evolution is reported along the entire duration of the growths.

The SEM images of the Au seeds grown in the dark in the various pretreated solutions are shown in Figure 4-5. Similarly to the growths under constant light irradiation, a hexagon yield as high as 80% is reached for the UV with a maximum of 95% for the blue pretreatment, while just a 40% is reported in the green, red and dark cases (where non hexagonal shapes were identified as the plates with at least one edge smaller than 1/3 of the structure diameter). This suggests that the intermediates might affect significantly not only the growth rate but also the resulting shapes.

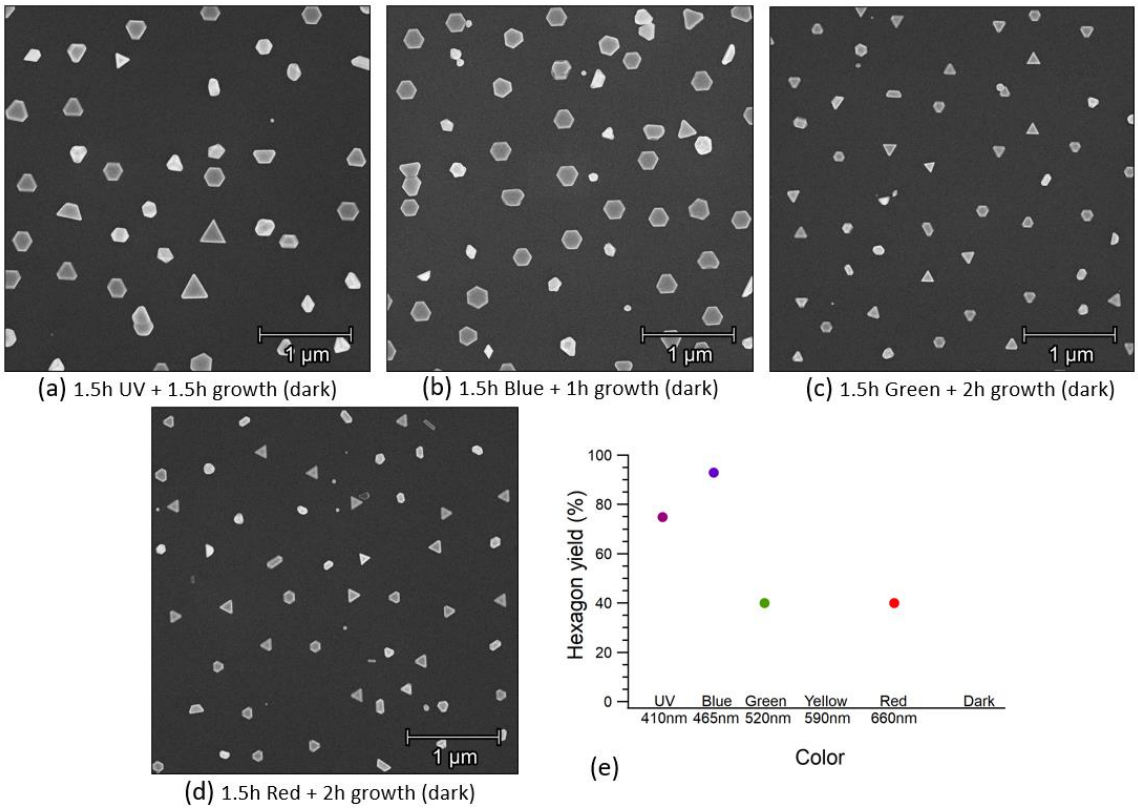

Figure 4-5. SEM images of Au plates grown in the dark with a LSG solution previously exposed to LED lights (a-d). The duration of the growth is also reported. In (e), the hexagon yield calculated from the SEM images.

4.4.3 Conductive merging hexagons

The nano-hexagon growth described in section 4.4.1 was extended in time in order to increase the nanoplate size and merge of the edges of adjacent plates. As a result, connected Au regions are expected to form from the merging of neighboring hexagons, whose size depends on the degree of percolation of the array. The synthesis of such connected structures can be crucial in the development of innovative electronic components at the micro and nano- scale, since the uniform substrate induced crystallinity of the percolated regions is expected to develop an enhanced electrical conductivity.

An array of Au seeds, SEM image in Figure 4-6a, was grown in ambient light environment (impinging light spectrum in Figure 4-18 in supplementary) in a LSG solution with optimized Brij concentration according to section 4.4.1 (2.36 mM).

During the growth process, 80% of the Au structures is evolving in 2D plates forming along the substrate, while a 20% of them are showing a 3D growth that can compromise the formation of a uniform Au film. Such a difference between the 2D and 3D morphology is arising from a different crystal structure of the initial seeds[83]. The planar growth is indeed occurring when the seeds are characterized by substrate induced stacking faults along the 111-axis. This configuration forms in the dewetting stage of the Au seeds synthesis process (described in section 2.7) and, in the LSG process, allows for the reduction of Au ions at the seed edges [83]. Conversely, in case of isotropic crystalline seeds, the lack of an in-plane preferential orientation results in a 3D growth.

The presence of 3D particles can be directly shown in SEM images, as in displayed Figure 4-6b for a 4.5 h growth. Furthermore, from the optical viewpoint, such 3D structures are associated to a LSPR peak centered around 600 nm, persisting and increasing in

intensity during the LSG growth [162]. This peak is clearly distinguishable from the Au plate resonance contribution, that is instead redshifting during the growth and reaches 700 nm after 4.5 h. At this stage of the growth, it was proven that a few seconds treatment of the array in a ultrasonic bath can selectively remove the 3D structures, without altering the planar shapes [162]. In this work, such treatment was optimized by identifying two parameters: 1) the ideal time elapsed from the beginning of the growth, at which the ultrasound exposure is best effective, 2) the ideal duration of the ultrasound exposure. For the identification of the first parameter, several attempts of sonication were performed from 1 to 7 hours after the beginning of the growth. For less than 4 hours, the structures were not sufficiently large to be affected by the ultrasound waves, while after 5 hours large 2D regions of connected merging hexagons were forming and were lifted off by the ultrasonic pulses together with 3D structures. As a consequence, 4.5 hours was identified as the best time elapsed between the start of the growth and the sonication treatment. Similarly, in order to tune the second parameter, different durations of the ultrasound treatment were investigated in the 0-2 minutes range, while monitoring the plate yield through SEM images and optical spectra. Below 1 minute, the mechanical removal of the 3D structure was still not complete, while for longer timing the array was not affected by the ultrasound anymore, suggesting a complete planar structure for the Au crystals. Consequently, 1 minute was identified as the best duration of the ultrasound.

In Figure 4-6, the SEM image of an Au plates array right after the ultrasound treatment performed after 4.5 h growth for 1 minute, shows how the 2D plate density was not modified, while the 3D structures were completely removed.

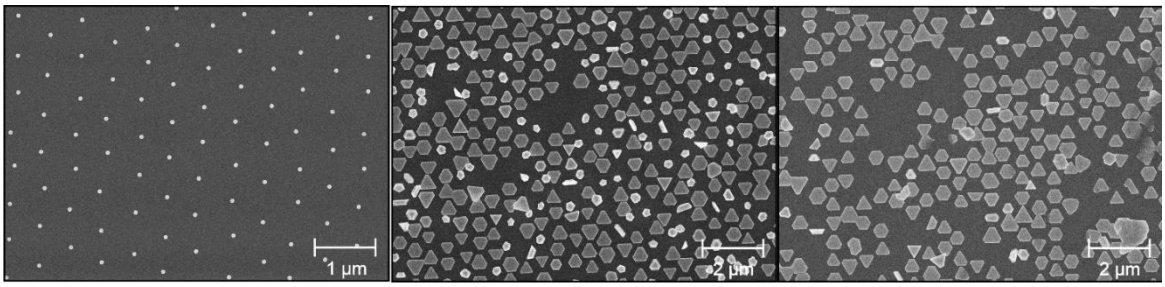

Figure 4-6. Au seed array (a), grown for 4.5 hours (b) and then exposed to an ultrasonic treatment for 1 minute to remove 3D structures (c)

In this work, a set of arrays (Figure 4-7) was grown for 9, 10.5, 11 and 12.5 hours. In all the cases, the growth was interrupted after 4.5 h, an ultrasound treatment was performed to remove the non-planar structures and the growth was restarted. The SEM images (Figure 4-7a-c) show a progressive degree of percolation between 9 and 12.5 hours of growth. For 9 h growth the array is characterized by few micrometer-size islands, while 10 μm wide connected regions appear in the last one. These differences are supported by the conductivity measurements (Figure 4-7d), where two probes were contacting the Au coating at a distance of 50 ± 20 μm, a potential ramp in the 0-0.5 V range was applied, the associated current was measured, and the resistance was calculated. For each array, a set of 15-20 measurements with fixed probe separation but in different points of the sample were carried out, showing significant (50%) fluctuations. This variability can be explained as a consequence of the percolation length ($\sim$10-20 μm) being comparable to the relative distance between the probes ($\sim 50\mu$m). In Figure 4-7e an average of the resistance was calculated for each array and reported as a function of the growth time, with an error bar given by the standard deviation of the values. For just 9 h growth no conduction was detected, corresponding to an infinite resistance, while after 10.5 hours the resistance

decreased from 13 Ω to 6 Ω after 12.5 hours. This trend qualitatively agrees with the increase of the percolation length shown in the SEM images. From the lowest resistance value, it is possible to estimate the material's resistivity using the formula:

$$\rho = R_{meas} \cdot \frac{d \cdot t}{L} \tag{4-1}$$

where $R_{meas} = 6 \pm 2\ \Omega$, $d = 20$ μm is the nominal probe's tip diameter, $t = 50 \pm 20\ nm$ is the hexagon thickness and $L = 50 \pm 20\ \mu m$ is the distance between the two tips. A value of $\rho = 1.2 \pm 0.7 \cdot 10^{-7}\ \Omega\, m$ is found from equation (4-1), that is comparable to the pure Au bulk reference resistivity ($2.4 \cdot 10^{-8}\ \Omega\, m$) and confirms the excellent conductivity of the connected regions.

A more precise evaluation of the electrical conductivity would require not only a better knowledge of the parameters involved in the measurements, including also the contact resistance between the Au crystal and the probes, but also a 2D modelling of the current flow between the two tips in an inhomogeneous thin film. Furthermore, as shown in the SEM images (Figure 4-7f), the surface of the plates exhibits an increase in roughness when they merge, by forming a thicker ring at their edges. This effect might arise from the inhomogeneous rearrangement of the Brij capping molecules moving along the (111) facets of the plates when they are merging. A possible mitigation of this roughness effect could be provided by growing and merging thinner hexagon plates.

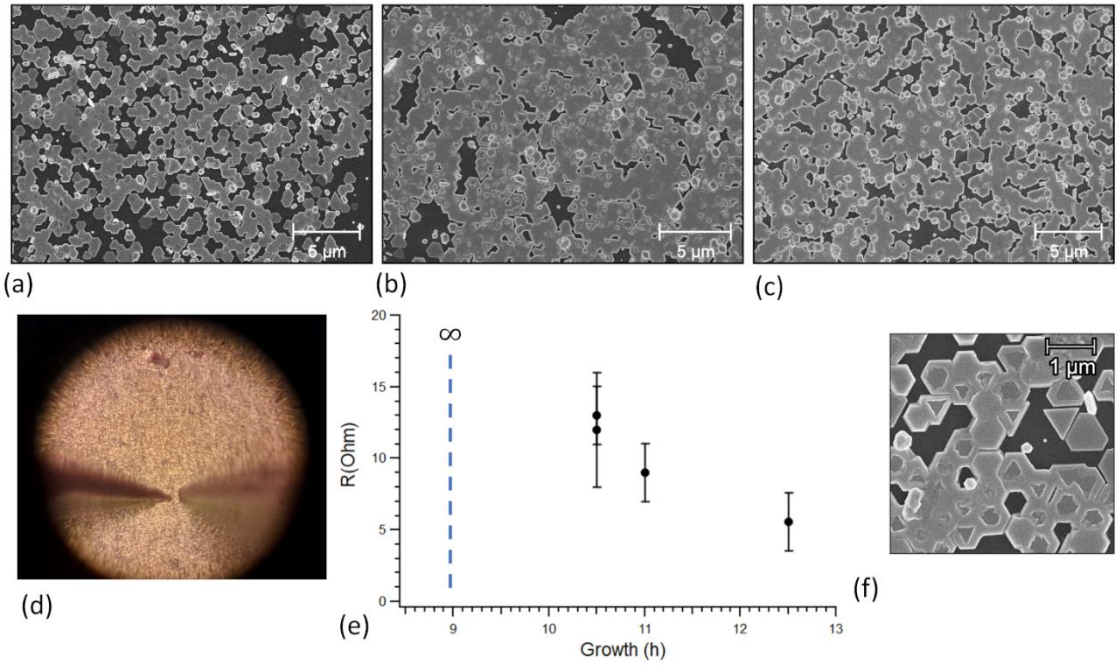

Figure 4-7. Au hexagon arrays grown for 9 (a), 10.5 (b) and 12.5 (c) hours. Picture (d) of a two-point probe conductivity measurement and associated results for the resistance (e). Formation of thicker edges in merging hexagons (f).

The advancement in the realization of conductive coatings presented above, if combined with the possibility of spatially arranging them in specific geometrical configurations, represents a great potential in the realization of nanoelectronics devices. The motivation stems not only from the excellent conductivity of the coating, but also on its crystallinity that implies the formation of atomically flat edges of the conductive patterns. For instance, an application as nano-gapped circuit can be achieved when two flat edges are separated by few nanometers distance.

4.4.4 Nanogaps in asymmetric structures

The growth of hexagon arrays described in section 4.4.1 was modified in order to obtain a specific architecture that can develop a nanogap. The nanofabrication process is outlined in Figure 4-8a. The Au hexagon array was grown for 2.5 hours and then it was uniformly coated using ALD with a 5 nm thick titania layer. Then, a glancing angle milling was performed, whose parameters (in materials and method section 4.3 above) have been tuned in order to thin the titania coating just on one edge of the hexagons (Figure 4-8a). Afterwards, the titania coating was uniformly exposed to a chemical etching agent for a limited time duration, in order to expose the underlying Au crystal just at the previously milled edge of the hexagons. Finally, when the LSG process was restarted, the Au crystalline expansion takes place just from the exposed side, leading to an asymmetric structure. The SEM image in Figure 4-8b-c shows how in the second stage of the growth, the hexagons are expanding from the exposed edges, while the growth is blocked by the titania coating at the other sides. Interestingly, the asymmetric structures are expanding two-dimensionally around the hexagon, reaching the titania coated sides, where a nanogap is therefore formed. The nanostructure is also schematically presented in Figure 4-8a. This architecture represents a great potential advancement in the nanogap manufacturing, since the crystallinity and the flat edges of the Au interfaces allow to gain a sub-nanometer control of the gap.

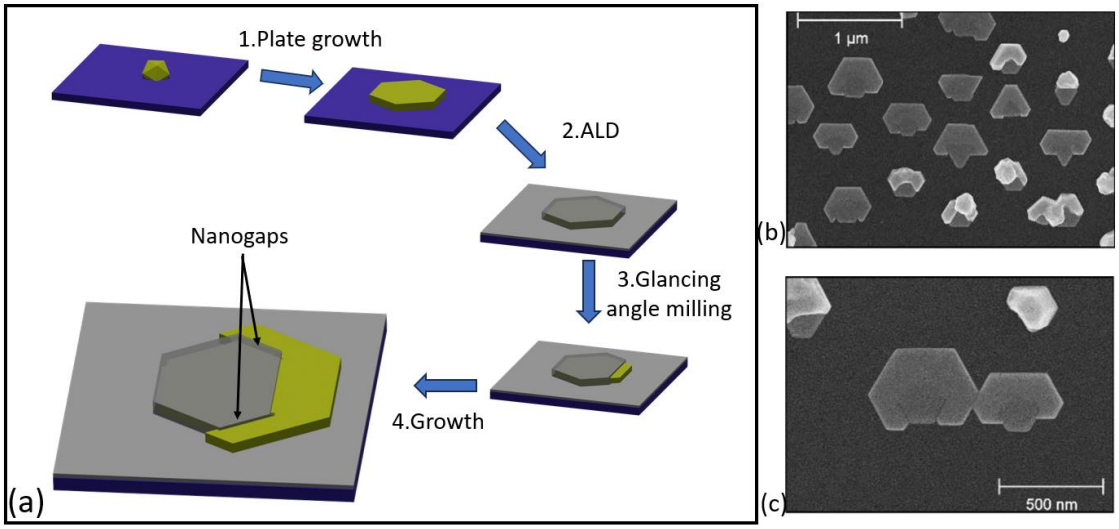

Figure 4-8. Au hexagon grown for 2.5 hours, coated with titania, milled at glancing angle, and regrown for 2.5 hours.

4.4.5 Au colloidal nanoparticles as seeds

In this section an alternate technique to grow hexagons of uniform thickness and crystalline orientation is proposed.

Figure 4-9 reports the steps of the synthesis process. In this case the bare sapphire is initially immersed in poly(4-vynilpyridine) (P4VP), a polymer acting as a sticking agent on the substrate surface. Afterwards, the P4VP coated substrate is exposed to the Turkevich colloid, where the already formed nanoparticles attach to the surface. The substrate is then irradiated with 254 nm UV light for 20 minutes and subsequently annealed at 500 °C in ambient air environment, to clean carbon-based contamination. The nanoparticles are then crystallized by annealing at 1100 °C in N_2 environment. Even though the seed position on the substrate is random, these are expected to be characterized by the same crystal

orientation as induced by the substrate during the annealing and by a very narrow size distribution as determined by the nanoparticle dimension in the Turkevich colloid.

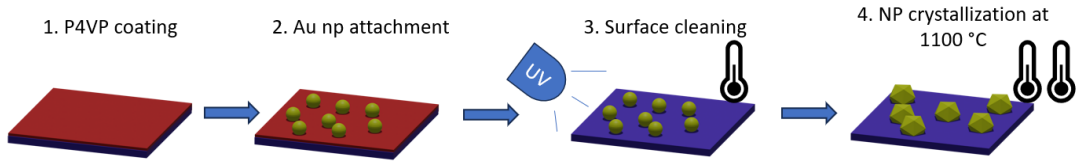

Figure 4-9. Schematic representation of the proposed synthesis of Au crystal seeds.

Figure 4-10 shows the result of the nanoparticle attachment (a), crystallization (b), and growth for 3 hours (d). The initial Turkevich nanoparticle radius distribution (Figure 4-10c) is centered at 32 nm with a full width half maximum (FWHM) of 10 nm. After the crystallization, the distribution is shifting to 28 nm and broadening (FWHM ~15 nm)), while new smaller particles are appearing with a 5 nm radius. This might be ascribed to the partial evaporation of the nanoparticles during the crystallization at 1100°C and redeposition to form smaller clusters.

After the seeds were grown for 3 hours, just 20 % of them was showing a two-dimensional growth, while 3D structures were forming in the other cases (Figure 4-10d). This low yield for the 2D structures could be due to either a carbon contamination affecting the seeds crystallinity or to the lack of stacking faults in the seeds [83], as discussed in section 4.4.3.

In order to increase the plate yield in the growth two improvements were devised: 1) before the nanoparticle attachment the substrate was coated with a thin (~ 6 nm) Sb layer and 2) after the attachment the sapphire was annealed at 500°C in air.

Similarly to the NIL fabrication process, Sb is acting as a sacrificial layer, in that it sublimates during the 1100 °C annealing process. Its presence is expected to affect the Au/substrate adhesion during the annealing and induce the stacking faults in the crystal structure, that are necessary to grow 2D plates.

Conversely the annealing at 500 °C in air environment is expected to remove the C-based contaminations on the substrate, resulting from P4VP residuals.

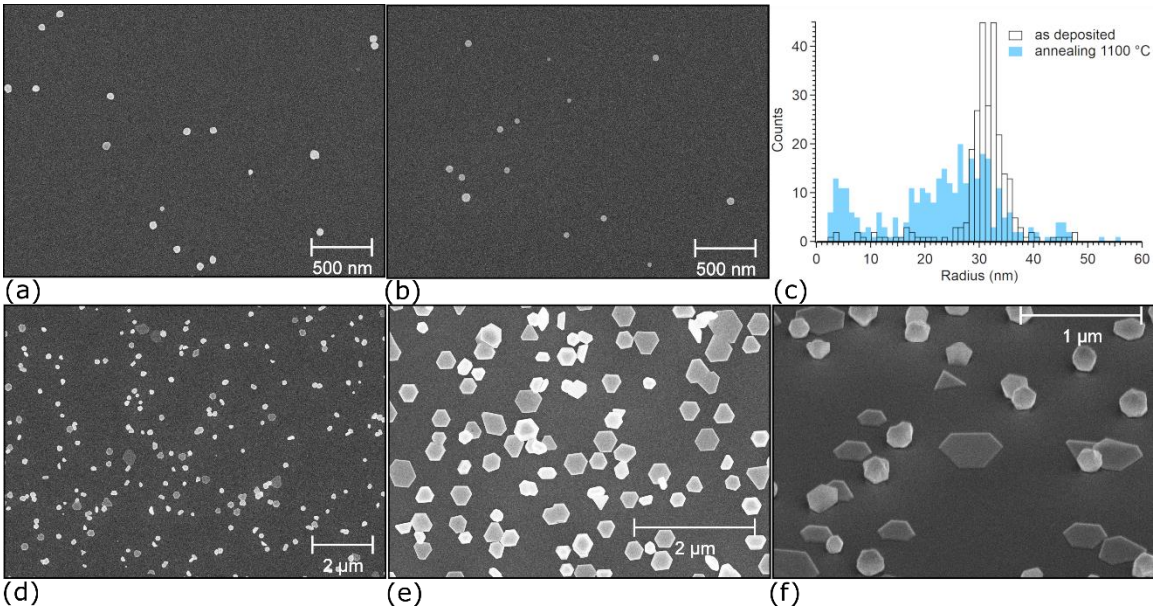

Figure 4-10. Au Turkevich nanoparticles attached to the sapphire surface (a) and annealed at 1100 °C (b). In (c) the associated nanoparticle radius histogram calculated from the SEM images before and after annealing at 1100 °C. Results of the 3.5 h growth (d-e-f). In (e-f), in addition to the standard synthesis procedure, a Sb sacrificial layer was used before the attachment and the nanoparticle were heated up at 500°C in air before crystallization.

Figure 4-10e (and Figure 4-10f tilted view) show how the yield is increased considerably to 50 % after these improvements and how it is possible to grow large (~1 μm) and thin (30 nm thick) hexagons.

This technique can represent a very powerful tool to develop crystalline coatings, provided that a better yield and control on the plate thickness size will be achieved. The yield can be improved by tuning the sacrificial Sb layer thickness or increasing the UV exposure and annealing duration at 400 °C, while a better control on the nanoparticle thickness can be obtained by using a colloidal solution of narrower nanoparticle size distribution.

4.5 Conclusions

In this research project, the combination of dynamic templating and liquid/solid interface growth to synthesize crystalline Au nanostructures was explored. A two-fold approach was adopted, where on one side the investigation of the growth mechanism was carried out and, on the other hand, the synthesis method was applied to obtain specific nanostructure geometries. The growth mechanism revealed high sensitivity upon light irradiation and capping agent concentration, opening new perspectives in the optimization of the process and in the synthesis of new type of nanostructures. Two specific nanostructure architectures were then proposed, where (i) neighboring hexagons were grown sufficiently to merge forming larger area conductive pads and (ii) asymmetric hexagonal structures embedded nanogaps, with promising applications in nanoelectronics and sensors. Furthermore, an alternate technique to grow thin crystalline plates by using colloidal nanoparticles as seeds were proposed and discussed.

4.6 Supplementary information.

4.6.1 Au plates grown under constant irradiation

Figure 4-11 reports the complete optical spectra of the Au seed array grown under constant light irradiation for 2h (UV light), 1.5h (UV light), and 6h (dark, green, yellow, and red). Spectra were acquired each 30 minutes, after interrupting the growth process and before restarting it in the same conditions.

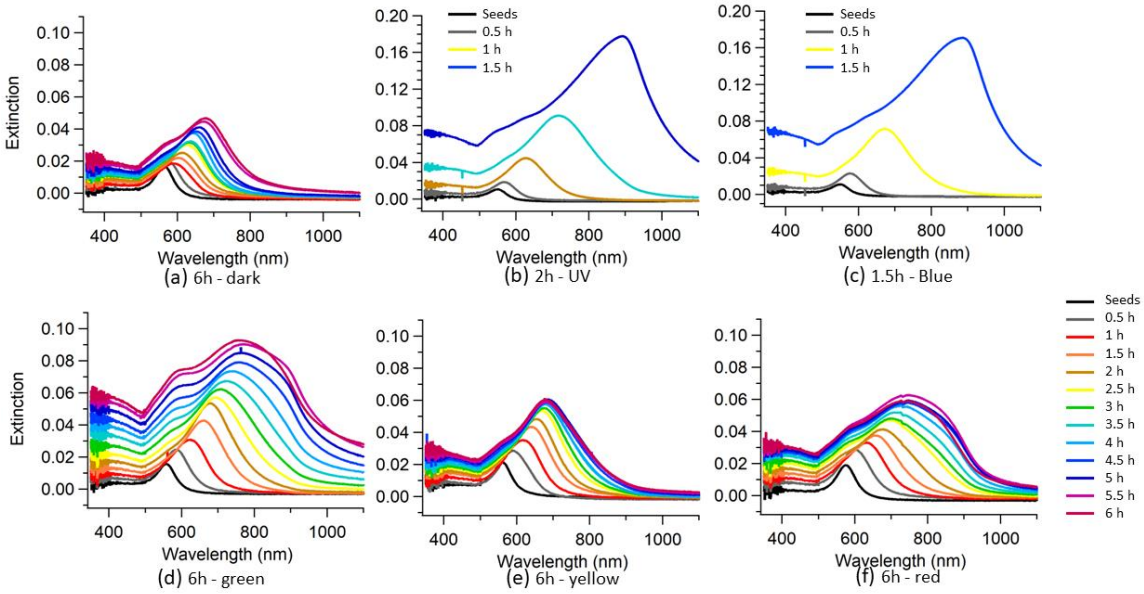

Figure 4-11. Complete optical extinction spectra acquired each 30 minutes for Au plates grown under different light irradiation. The duration of the growth is specified.

Figure 4-12 shows the LSPR shift occurring each 30 minutes of growth under constant light irradiation. These values, obtained from Figure 4-11, show a progressive

growth increase in the blue and UV lights, while a decrease is registered for the other colors, as discussed in section 4.4.2.

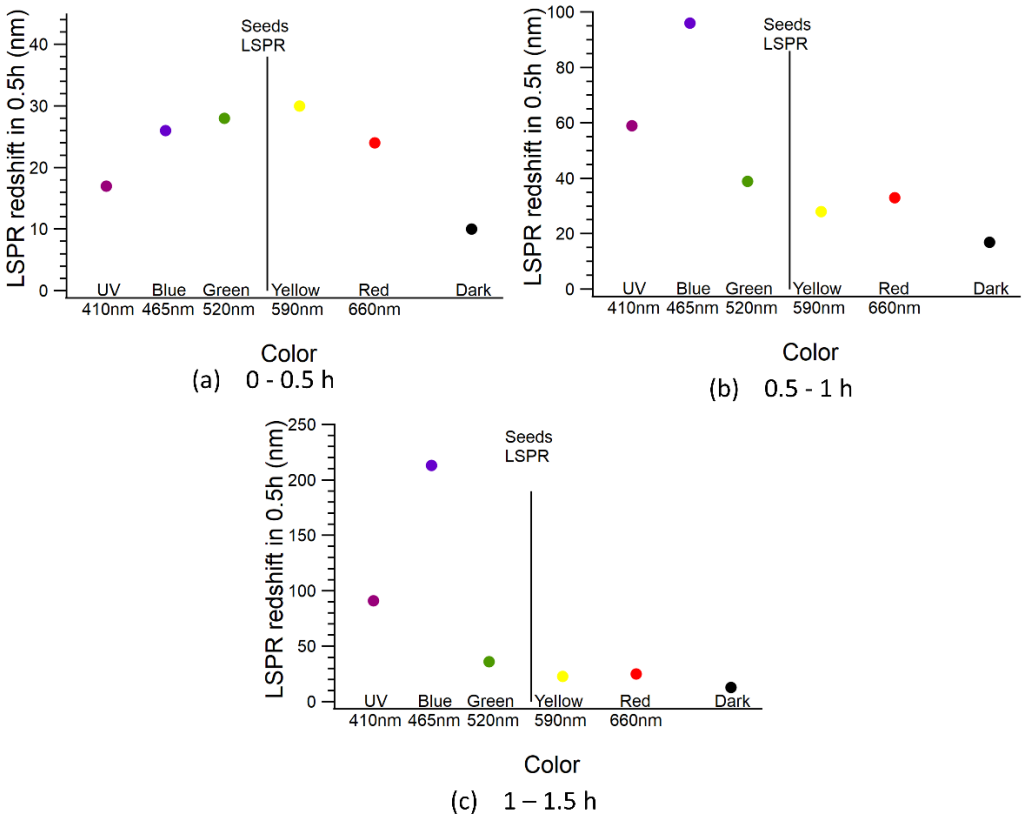

Figure 4-12. LSPR shift registered each 0.5 hours growth for Au arrays grown under different light irradiation.

The optical extinction of a freshly prepared LSG growth solution and its individual components (Brij and Au salt) are reported in Figure 4-13a. All the spectra are characterized by an absorption peak around 1000 nm associated to a water excitation mode and aby a plateau in the 500-900 nm range. Below 500 nm, a rapid increase in absorption is determined by the Au salt component of the solution. After the Au seeds growth under constant light irradiation, the LSG growth solution extinction spectra (Figure 4-11b) show

an increase in the 500-700 nm range, suggesting the formation of intermediates with a plasmonic optical response. The variability of the extinction shapes in this region could be ascribed to different experiment durations as well as the exposure to different light colors.

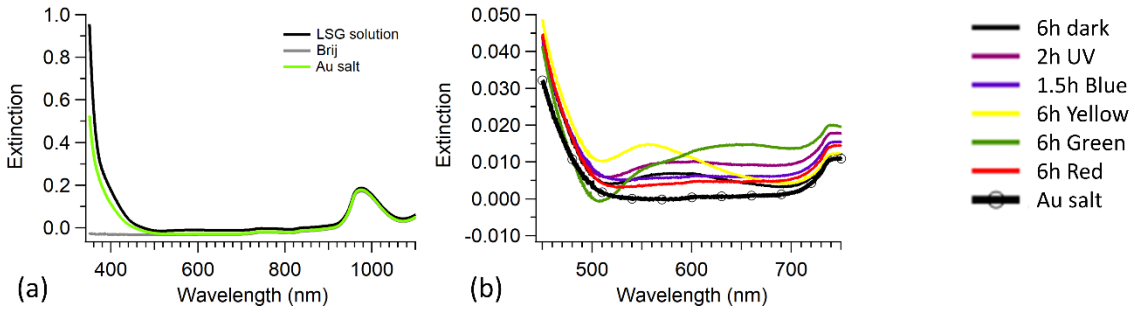

Figure 4-13. Extinction spectrum of a freshly prepared growth solution and its components (a). Modification of the extinction spectrum in the 500-700 nm range after using the solution in a growth experiment for the indicated duration.

Figure 4-14 reports a comparison between the optical extinction spectra of different arrays grown under constant UV, green and red light irradiation. The solid lines correspond to arrays grown without interrupting the LSG process, while for the dashed curves the Au array was cleaned from the solution each 30 minutes after interrupting the LSG growth process and before restarting it in the same conditions. It is possible to notice that for the UV and red lights the interruption corresponds to an increase of the LSPR redshift, i.e. growth rate (visible from the comparisons after 2h and 6h respectively). Conversely, in the green light experiments, the interrupted growth is slower (comparison after 6 hours).

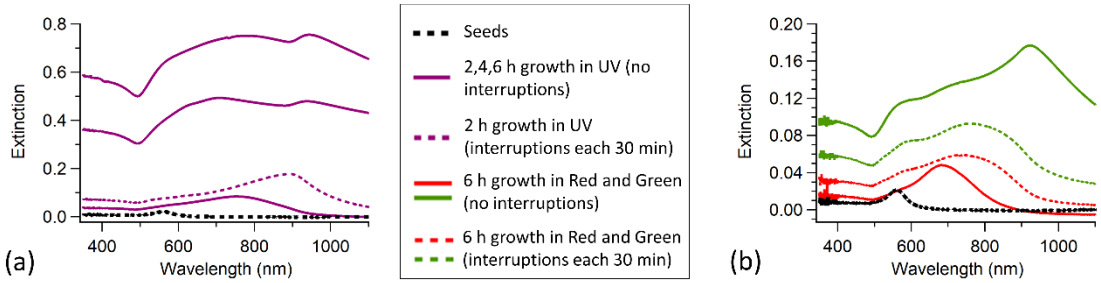

Figure 4-14. Different growth experiments performed under UV (a), green and yellow lights (b) irradiation. Growth interrupted each 30 minutes (dashed lines) are compared to uninterrupted growths (solid lines).

The SEM images of the growths carried out under constant illumination without interruptions are reported in Figure 4-15. After 4 h and 6 h growth in UV light the hexagons start to merge, while the optical extinction (in Figure 4-14a) is characterized by a broad structure with an oscillation around 900 nm rather than a sharp plasmonic peak, whose intensity increases with the growth time. In the UV case a high hexagon yield exceeding 90% is reached, while just a value around 50% is reported for the green and red one.

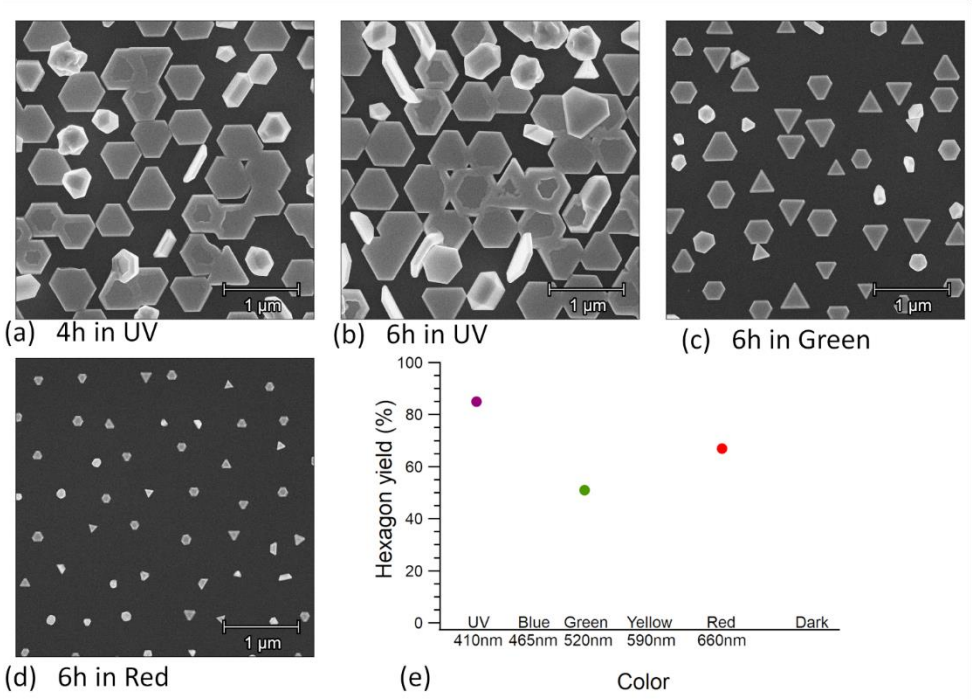

Figure 4-15. SEM images of Au plates grown without interruption under UV, Green and Red light irradiation (a-d). Associated hexagon yield calculated from the SEM images (e).

4.6.2 Growth in pretreated solution

In Figure 4-16, the extinction optical spectra were recorded each 30 minutes during the growth in the dark in a LSG solution previously exposed to LED light of different colors for 1.5 h.

As discussed in section 4.4.2, the solutions exposed to UV and blue lights develop the highest growth rate, suggesting the formation of the intermediates.

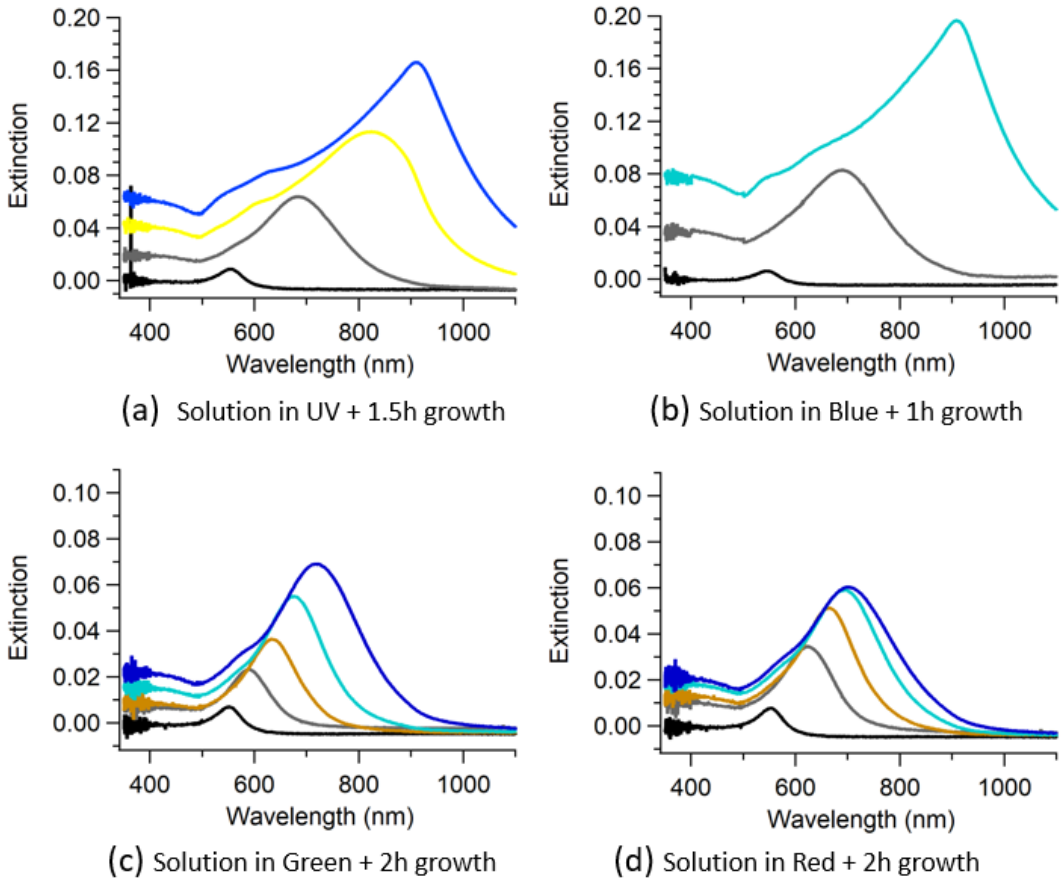

Figure 4-16. Extinction spectra of Au plates grown in the dark in a solution previously exposed to UV (a), Blue (b), Green (c) and Red (d) light for 1.5 hours.

In the experiments reported in Figure 4-17 three arrays were grown in the dark in a LSG growth solution whose components were separately exposed to UV light for 1.5h before the growth. In Figure 4-17a and Figure 4-17b just the Au salt and just Brij components respectively were exposed to the UV light, while in panel c the entire solution was irradiated. In the third case the growth rate is significantly higher.

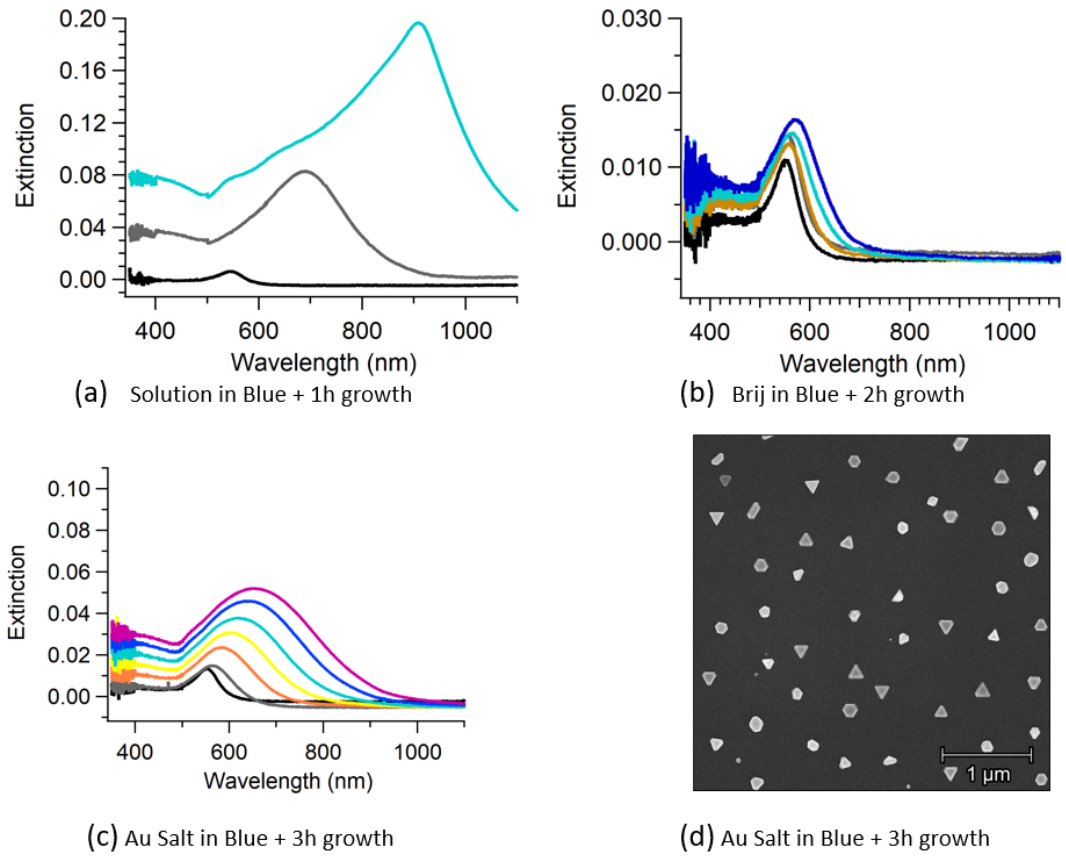

Figure 4-17. Extinction spectra of Au plates grown in the dark after previously exposing the whole solution (a), just the Brij (b) or just the Au salt components (c) to Blue light. SEM image (d) of Au plates grown according to (c).

4.6.3 Light intensity measurements

The measurement of the LED light intensity relies on the distinction between $I_{lux}(\lambda)$ and $I_{W/m^2}(\lambda)$ for a monochromatic light component of wavelength λ. $I_{W/m^2}(\lambda)$ is the luminous power intensity, i.e. the irradiated power (in Watts) per unit of meter square. Conversely $I_{lux}(\lambda)$ is the vale measured by the light sensor and consists in the light intensity as perceived by the human eye, in $lux = lm/m^2$. There exists an universally

accepted conversion factor between $I_{lux}(\lambda)$ and $I_{W/m^2}(\lambda)$ based on the human eye light response, according to the relation:

$$I_{lux}(\lambda) = R(\lambda) \cdot I_{W/m^2}(\lambda) \tag{4-2}$$

The conversion factor $R(\lambda)$, also called photopic response, is reported in Figure 4-18a as a function of the light wavelength, showing a bell shape with a maximum of 680 $\frac{lux}{W \cdot m^{-2}}$ at 550 nm (green light) and a FWHM of 120 nm.

In real light sources the spectrum is not monochromatic, as shown in Figure 4-18a, where the spectrum of the ambient environment where experiments in sections 4.4.1, 4.4.3, 4.4.4 were performed is reported together with the spectra of each LED used in section 4.4.2. These spectra were acquired, in arbitrary unit of intensity, by an Ocean optics spectrophotometer device.

It is possible to express the total lux intensity

$$I_{lux}^{tot} = \sum_{\lambda} I_{lux}(\lambda) \tag{4-3}$$

and the total W/m^2 intensity

$$I_{W/m^2}^{tot} = \sum_{\lambda} I_{W/m^2}(\lambda) \tag{4-4}$$

as the sum of each individual monochromatic components of the light spectrum.

By plugging (4-3) and (4-4) in (4-2) we obtain:

$$I_{lux}^{tot} = R^W \cdot I_{W/m^2}^{tot}$$

(4-5)

where

$$R^W = \sum_{\lambda} \left[R(\lambda) \cdot I_{W/m^2}(\lambda) \right] \Big/ \sum_{\lambda} I_{W/m^2}(\lambda)$$

(4-6)

is the weighted conversion factor, depending on the convolution of the photopic response $R(\lambda)$ with the light spectrum shape. Furthermore, the wavelength dependent W/m^2 intensity can be expressed as $I_{W/m^2}(\lambda) = I_{W/m^2}^0 \cdot s(\lambda)$, where $s(\lambda)$ is the light intensity shape (provided by the Ocean optic sensor) and I_{W/m^2}^0 is the wavelength independent intensity. By rewriting equation (4-5) in this notation, we obtain

$$R^W = \sum_{\lambda} [R(\lambda) \cdot s(\lambda)] \Big/ \sum_{\lambda} s(\lambda)$$

(4-7)

One may notice that R^W just depends on the light intensity shape (as provided by the Ocean optics sensor) and not on its absolute intensity. As a consequence, for each LED color, the direct measurement of the I_{lux}^{tot} value (through the light meter) and of the spectrum shape (Ocean optics curves in Figure 4-18b) allows to compute the total W/m^2 intensity I_{W/m^2} by means of equation (4-5).

For each LED color, Table 4-1 reports the conversion factor $R(\lambda)$ calculated for the wavelength at the peak maximum, compared to the weighted R^W conversion factor. It should be noted that a good agreement within 10% occurs for green and yellow colors,

where the photopic response is maximum, while the discrepancies increase to 20% for red and blue light. Conversely, for the UV light, the $R(\lambda)$ value is three time lower than R^W, revealing a high dependence of the lux intensity measurement on the spectrum shape.

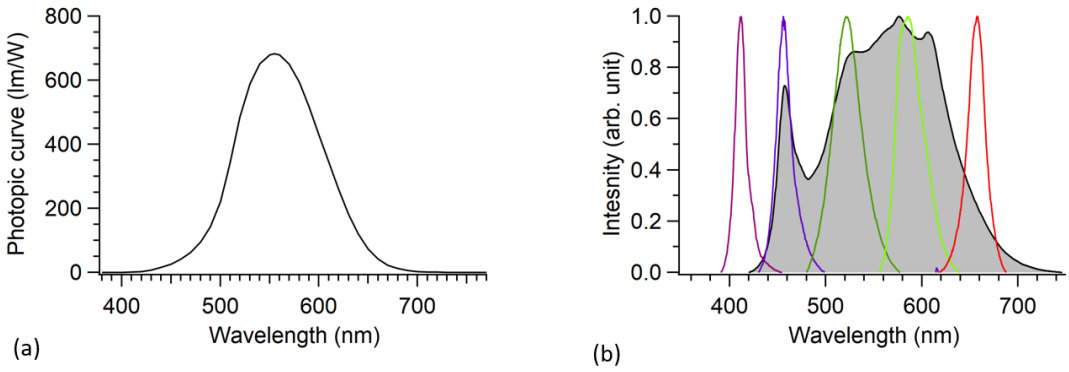

Figure 4-18. Photopic conversion curve(a). (b) LED emitted light intensity (colored peaks) and laboratory ambient light spectrum during a standard LSG growth (grey background).

TABLE 4-1:

LED WAVELENGTHS AND ASSOCIATED LUX/W CONVERSION FACTOR

LED color		Conversion factor (lm/W)		
	λ at peak maximum (nm)	Tabulated value $R(\lambda)$ (at peak maximum)	Weighted R^W	Weighting range (nm)
UV	410	0.826	2.17	389-450
Blue	456	35	42.85	430-499
Green	520	484.93	486.2	480-576
Yellow	585	556	509	556-638
Red	657	51	60.3	620-687

For each color, the wavelength of the emission spectrum maximum is reported in the second column. In the third column the tabulated conversion factor value at the peak maximum is compared to the weighted conversion factor (fourth column). The last column reports the wavelength range in which the convolution of the LED spectra and the photopic curve is performed to calculate R^W.

CHAPTER 5:

OER ACTIVITY OF NIFE NANOALLOYS AT VARIABLE FILM THICKNESS

This chapter is based on:

L. Ciambriello, E. Cavaliere, I. Vassalini, I. Alessandri, M. Ferroni, L. Leoncino, R. Brescia, and L. Gavioli, "Role of Electrode Thickness in NiFe Nanogranular Films for Oxygen Evolution Reaction", Journal of Physical Chemistry C, 2022, 126, 51, 21759-21770, DOI: 10.1021/acs.jpcc.2c06669

5.1 Abstract

Nanostructured materials may provide a route to overcome the current electrode-limiting performance step in water-splitting reactions, the oxygen evolution reaction (OER). Although alloyed NiFe nanostructures show promising efficiencies, many issues are still open. In particular, the relationship among the OER efficiency and the electrode charateristics (morphology, porosity, size, thickness or mass loading) is largely unknown, despite the topic relevance in the framework of low-cost catalysis search. Here we investigate such dependence by obtaining alloyed NiFe(90/10 % at) nanogranular electrodes for OER obtained by supersonic cluster beam deposition (SCBD), which provides control over the film morphological and stoichiometric properties. Alloyed nanoparticles (NPs) of NiFe with 0.3-3.8 nm size assemble from the gas phase to form ultrathin films with thickness in the 15-88 nm range, corresponding to 5-30 $\mu g/cm^2$ mass

loading. The films are characterized by a high porosity and a thickness dependent surface roughness up to 6nm. Optical spectroscopy suggest a complete hydroxidation of the films independently on the thickness. The resulting catalytic efficiency is independent on the film thickness, whilst the turn over frequency decreases with increasing electrode loading. This suggests an excess of deposited mass with respect to the OER active sites in the thicker electrodes and sets the 15 nm film as an upper thickness limit, representing a crucial step towards the thickness optimization for low-cost OER catalysts.

5.2 Introduction

The application potential of nanoalloyed materials in energy,[163] electrocatalysis,[18] sensors,[164] antibacterial coatings[165] and medical diagnosis[166] stems from the opportunity of tuning both the chemical composition and the morphological structure, aiming at reducing mass loading at similar efficiency. Nanoalloyed catalysts are a key point in the electrochemical water splitting (WS), a crucial green method for the production of hydrogen fuels.[5] To produce O_2 and H_2, the two WS half reactions under an external power source[8] are the hydrogen evolution reaction and the oxygen evolution reaction (OER),[10] both requiring a catalyst. The most energy-demanding part and current bottle-neck of the WS[12] is the OER, requiring high potential drops in the electrochemical cell. Nanoalloyed catalysts may overcome this limitation by tailoring the catalyst stoichiometry to reduce the potential drop and the morphology to increase the electrochemically active surface area. Alloying of first row transition metals[30] increases the OER activity[24], [167] depending on the relative stoichiometry,[23], [168] thanks to their numerous possible oxidation states.[9], [18] One of the most promising alloys is NiFe,[169] where a Fe incorporation in the 10%-70% weight fraction range determines a 10 and 100 -folds activity enhancement with respect to pure Ni or Fe compositions, respectively.[26], [28] On these systems, the metal oxides and hydroxides forming at the alloy surface are expected to serve as active sites for the OER catalysis.[12], [170] However the role of these phases as OER mediators and their identification among all the oxy/hydroxide species[171] at the electrode surface is still under debate.[29], [39], [170]

The cell activity is also influenced by the film surface roughness, porosity[172] and electrode thickness/mass loading.[171] In particular, the high electrode surface/volume

ratio and/or porosity[172] have been claimed to justify the catalytic efficiency improvement through an increase of the electrochemical surface area (ECSA, the electrode surface available as OER active site) for many micro/nano structures.[27] However, the effort to improve the ECSA through the synthesis of nanosheets, nanocubes, micro-boxes and microspheres is not extended to a thickness/mass loading dependence of these geometries.

Furthermore, the use of the current density normalized by the ECSA (J_{ECSA}) and the turnover frequency (TOF, the O_2 molar production rate normalized by the moles of active sites in the electrode[27]) were very recently suggested as intrinsic activity parameters that better quantify the electrode performance.[173] This is even more important in view of identifying cheap electrodes for large-scale industrial synthesis[6] to minimize the electrode mass loading.

The ECSA and the TOF were so far obtained for few noble/noble[51], [52] or noble/non-noble[19], [22], [53] metal compounds, and the OER catalysis is solely discussed in term of one of the two metal loadings, as for Ir[19], [22], [51], [52] or Ni.[174], [175] This analysis is conversely very limited for noble-metal-free electrodes. For MnO/Si[176] and LaSrMnO films[177] a thickness analysis in the 1-27 nm range revealed the best OER efficiency for 4 nm thick films, while for NiFe hexacyanoferrate (0.5-10mg/cm^2 range) a 5 mg/cm^2 has been identified as ideal concentration.[54] For electrodeposited transition metal oxides[55] the TOFs reported in the 0.1-100 $\mu g/cm^2$ density range show a high dependence on the oxide type, going from 10 s^{-1} for CoFeO to 0.001 s^{-1} for MnO. Moreover, NiFe oxyhydroxides (1.5-20 $\mu g/cm^2$ loading range)[57] and NiFeO (0.3-3.8 $nmol/cm^2$)[56] present a substrate dependent TOF/loading behavior,

since the substrate is affecting the catalytic particle dispersion in the electrode. This highlights the lack of studies providing the dependence of the OER efficiency on the electrode morphology, porosity and loading.

This may be obtained with an electrode synthesis method able to grow nanostructured materials with controlled stoichiometry, morphology and thickness, independently on the supporting substrate. Very recently cluster assembled films deposition[72] emerged as a green and high throughput route to obtain porous, nanostructured and nanogranular films of different materials[90], [178], [179] in alloy form,[165] with a very good control on the stoichiometry and nanoscale morphology of the films. However, this technique has never been used so far neither to synthesize any NiFe electrode nor to investigate the electrode morphology and thickness influence on OER reaction. Here, we employ supersonic cluster deposition (SCBD) to synthesize novel OER electrodes, composed by porous nanoalloyed NiFe thin films, to unveil the morphological, chemical and catalytic features as a function of electrode thickness/mass loading. The electrodes, consisting of films of thicknesses in the 15- 88 nm range and characterized by a nanogranular morphology with a porous structure, correspond to a catalyst loading range of 5-30 $\mu g/cm^2$, with a fixed 90%/10% NiFe alloying fraction. We present a detailed chemical and physical characterization of the as-deposited films and then investigate the OER catalysis efficiency and electrochemical behavior as a function of the film thickness/mass loading at fixed chemical composition.

5.3 Materials and methods

The NiFe alloy NPs were synthesized by SCBD and deposited onto a glass substrate coated by an Indium-Tin oxides (ITO) conductive layer or onto plain Si(100) surface for the other characterizations. In SCBD,[90], [178], [179] an arc discharge synchronized with a pulsed injection of He generates a plasma ablating the bulk metal rod. The material condenses in NPs that are then directed towards the substrate by a system of lenses and deposited ballistically onto the target.[90] The deposition process was carried out at a base pressure of 10^{-6} mbar. In this work a Ni/Fe alloy rod with a nominal 90%/10% weight fraction has been employed.

The NP size and shape distributions produced by SCBD were obtained from atomic force microscopy (AFM) and transmission electron microscopy (TEM), analyzing sparse NPs deposited both on a Si substrate (0.1 nm RMS roughness) and on a 12 nm thick holey carbon film on Au TEM grid, with a density of 350 ± 50 particles/μm^2. The set of AFM (Park NX10) images were acquired in tapping mode with a PPP-NCSTR tip (Nanosensor, resonance frequency 120-250 Hz, nominal tip radius 10nm), with 0.25 pixels/nm. The distribution of the NP heights (more than 7000 data) were elaborated by Gwyddion software[180] (more details in 5.6.1). The TEM analyses have been carried out using an image-C_s-corrected JEOL JEM-2200FS microscope operated at 200 kV, equipped with a Schottky emitter and with a Bruker XFlash-5060 SDD based energy-dispersive X-ray spectrometer (EDS). The images have been obtained by employing the high-resolution TEM (HR-TEM) and high angle annular dark field scanning TEM (HAADF-STEM) modes. The elemental maps included in the manuscript were obtained by integration of the Kα peaks of Ni and Fe in the EDS spectrum. The Scanning Electron Microscopy (SEM)

measurements have been performed with a LEO 1525 high-resolution (1.5 nm beam diameter at 20 keV) microscope, operating in secondary-electrons imaging mode.

The NP distribution is representative of the supersonic beam composition employed to grow the NiFe electrode films (thicknesses in the 15-90 nm range) on a commercial ITO/glass conductive layer (ITO: 80-120 nm nominal thickness, Sigma-Aldrich). The NiFe deposition was monitored in situ during the synthesis by means of a quartz microbalance, providing the NiFe mass loading in the electrodes. Just after the film depositions, the height with respect to the ITO substrate region was estimated by acquiring a 20x20 μm^2 AFM image at the film boundary. The nano-granular film surface analysis was performed on 2x2 μm^2 AFM images by using the Gwyddion watershed algorithm for the NP identification. The root mean square (RMS) of the film height profile was taken as the film roughness (more details 5.6.1).

The film composition was evaluated by X-ray photoelectron spectroscopy (XPS) using a Mg X-Ray source (incident photon energy was 1253.6 eV) and a Phoibos 100 SPECS analyzer at 20 eV pass energy. Data were acquired for a 150 nm thick NiFe deposited onto a Si substrate. The corresponding photoelectron sampling depth for the elements composing the film is up to 5 nm. The data were analyzed using CasaXPS software,[181] by employing a Shirley background and modelling each metal components by a LA(1.2,2.2,10) asymmetric curve and GL(30) peaks for all the other components. The relative distances between the peaks were kept fixed, allowing just a possible global shift due to the sample charging. For each element oxidation state, the ratios between the areas and widths of the different components were kept fixed, according to literature, while the total sum of all the components was a fitting parameter indicating the stoichiometry.

Crystallinity was checked by a Bruker XRD diffractometer. The diameter d of the crystalline domains has been retrieved from the Debye-Scherrer equation:

$$d = \frac{K\lambda}{\beta cos\theta} \tag{5-1}$$

where K is a shape factor set to 0.9 for spherical particles, $\lambda = 1.54$ Å is the wavelength of the incident X-ray light, β is the peak FWHM.

The μ-Raman measurements were performed by LabRam HR-800 with a 632.8 nm wavelength laser. All the measurements have been obtained in the same operational conditions: a 40 seconds exposure to the laser focalized by a 100x microscope objective (0.9 N.A.) and attenuated to 10% of the original power.

Reflection (R) and transmission (T) spectra have been acquired at normal incidence by a Perkin-Elmer Lambda 950 Spectrometer in the 200-2000nm range. The optical spectra have been modelled and fitted through the home made DEMON software,(chapter 3.3 and [182]) by employing a multi-layer model with each layer dielectric function being described by a Bruggeman's Effective Medium Approximation (BEMA). The quantity:

$$(R_{exp} - R_{model})^2 + (T_{exp} - T_{model})^2$$

was minimized in order to refine the parameters in the multilayer model.

The electrochemical cell consisted in a saturated calomel electrode (SCE) as reference and a Pt counter electrode, with the NiFe/ITO/glass system as working electrode in a 1M KOH electrolyte solution. Measurements were performed by a Frequency analyzer

equipped PGZ402 Potentiostat from Voltalab (Radiometer Analytical). The open circuit potential was acquired for 4 minutes, followed by an impedance measurement at 63.3 kHz, that provides R=12.5 Ω as the electrical resistance of the overall cell. Cyclic voltammetry was performed in the range -500 mV - +800 mV vs SCE at 10mV/s scan rate. All the potentials measured have been converted to the reversible hydrogen electrode (RHE) reference by opportunely shifting the values found with respect to SCE. The cyclic voltammetry curves have been rescaled according to:

$$V = V_{measured} - iR \tag{5-2}$$

where i and R are the measured current and resistance at 63.3 kHz. The iR term in equation (5-2) stems from the resistivity effects associated to the limited charge transportation in the solution, the electrodes resistivities and the electrical connections. Equation (5-2) aims to cancel such contributions, evidencing the electrode catalytic behavior. The measured currents were normalized to the working electrode geometrical area. Turn over frequency (TOF) was calculated as the O_2 moles production rate normalized by the deposited NiFe moles in the electrode, when an overpotential of $\eta = 350\ mV$ is applied. The reaction considered for the calculation is the four-electron process of eq. (5-3), including a ¼ factor from the stoichiometry (more details in supplementary section 5.6.4).

5.4 Results and discussions

5.4.1 Nanoparticle characterization

The size and composition of the individual NPs composing the supersonic beam may have a major impact on the electrochemical properties of the electrodes and is therefore fundamental to characterize the NP properties. The NP size distribution, obtained extracting each NP height from the AFM images of sparse NPs (Figure 5-1a), is shown in Figure 5-1c. The three maxima at 0.36 nm, 0.6 nm and 2.8 nm, respectively, correspond to the center of three log-normal distributions reported as solid lines in Figure 5-1c, as expected for ballistic deposition. Furthermore, the NPs with the 2.8 nm mode present an ellipsoidal shape characterized by an elongation in the substrate plane (more details in the supplementary section 5.6.1), likely related to some clustering of the NPs. The result agrees with the HAADF-STEM imaging results of Figure 5-1b, showing NPs organized in composite structures extending along the substrate surface with a size up to a few tens on nanometers. This composite shape may form as an assembly of 2.8 nm NPs as a consequence of a diffusion of the single NPs during the landing onto the substrate or due to an in-flight clustering during the SCBD process. The HR- TEM image (Figure 5-1d) shows that the elongated structures consist of smaller crystalline domains with a lateral size ranging from 1 to 3 nm, compatible with the NPs height provided by AFM. The interatomic distances extracted from HR-TEM imaging match with fcc Ni (ICSD 8688), as the expected lattice contraction due to Fe incorporation is less than 1%, well below the inherent accuracy of magnification calibration in HRTEM, not easily better than 5%.[183] Furthermore, the STEM-EDS Ni/Fe elemental mapping (Figure 5-1e) shows uniform

distributions of both Ni and Fe species inside the composite NPs without evidence of element segregation, compatible with an alloying of the two species at the atomic level. The data hence show that the beam employed to grow the electrodes is composed by alloyed NPs of NiFe with a trimodal size distribution.

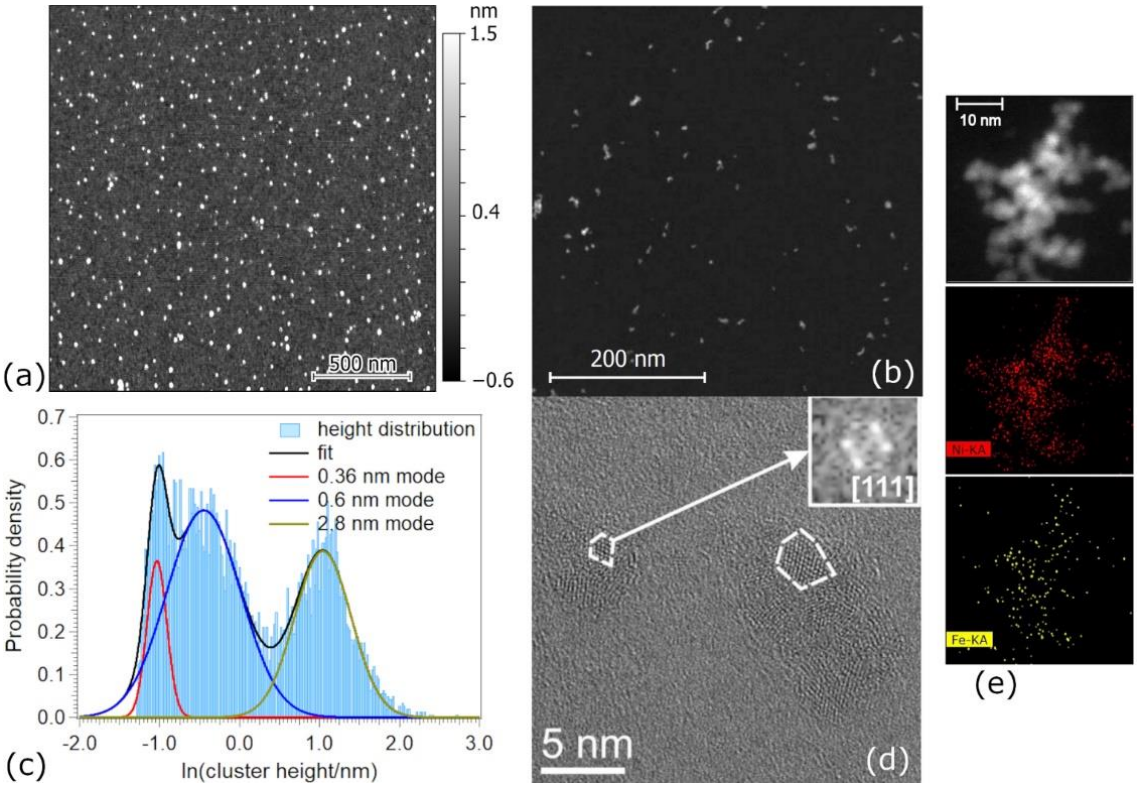

Figure 5-1. (a) 2x2 μm^2 AFM image of a sparse NiFe NP distribution deposited onto Si substrate, with the associated NP height distribution (c). (b) 0.5x0.5 μm^2 HAADF-STEM image of sparse NiFe NPs. (d) HR-TEM image of two NPs, each composed of 1-2 nm-size single-crystal domains; the panel shows the FFT of the indicated grain, matching with [111] zone axis of Ni (ICSD 8688). (e) HAADF-STEM image of aggregated NPs and corresponding STEM-EDS maps, showing Ni and Fe spatial distribution.

5.4.2 Electrode characterization

The electrodes designed for the OER application are obtained by SCBD deposition onto ITO layers covering a 1 mm thick glass substrate. The electrodes consist of thin NiFe alloy films in the 15 nm to 88 nm range, composed by the previously described NPs. By measuring *in situ* the deposited mass by a quartz microbalance, the electrode loading was determined to range from 5 to 30 $\mu g/cm^2$. Independently of the NiFe loading, the comparison between deposited mass and the AFM thickness reveals that the film volume is always higher than what expected for an ideally uniform and homogeneous (*i.e.* bulk) NiFe layer. This implies that oxide/hydroxide phases and void pores must coexist together with the NiFe metal phase inside the films. Furthermore, the film volume turns out to be always 140% higher than an ideal bulk NiFe layer, independently of the electrode loading. This corresponds to a constant NiFe density in the film, i.e. deposited NiFe moles/film volume ratio, for all film thicknesses (more information in the supplementary section 5.6.1, Figure 5-7a-b). A hierarchical film surface structure is evident from the AFM, SEM and optical data, deriving from the clustering of the individual nanometer-sized NPs. At the nanometer scale, the AFM data of four films with thicknesses in the 15-88nm range are shown in Figure 5-2a. The NPs are assembled in the typical configuration observed for SCBD deposited films,[90], [178], [179] with the RMS roughness increasing as a function of the film thickness, ranging from 4.5 nm to 6 nm (Figure 5-2b). These values agree with the convolution of a constant 3 nm ITO roughness and a power law contribution with exponent $\beta = 0.3$ [184] due to the NiFe film, typical of ballistically deposited clusters (more details in supplementary section 5.6.1).[72], [184] A detailed NP size analysis with a watershed algorithm (described in supplementary section 5.6.1) suggests a NP size

distribution peaked at 5 nm, with a tail reaching 20 nm (Figure 5-10b), and consistent with the size obtained for the sparse NPs.

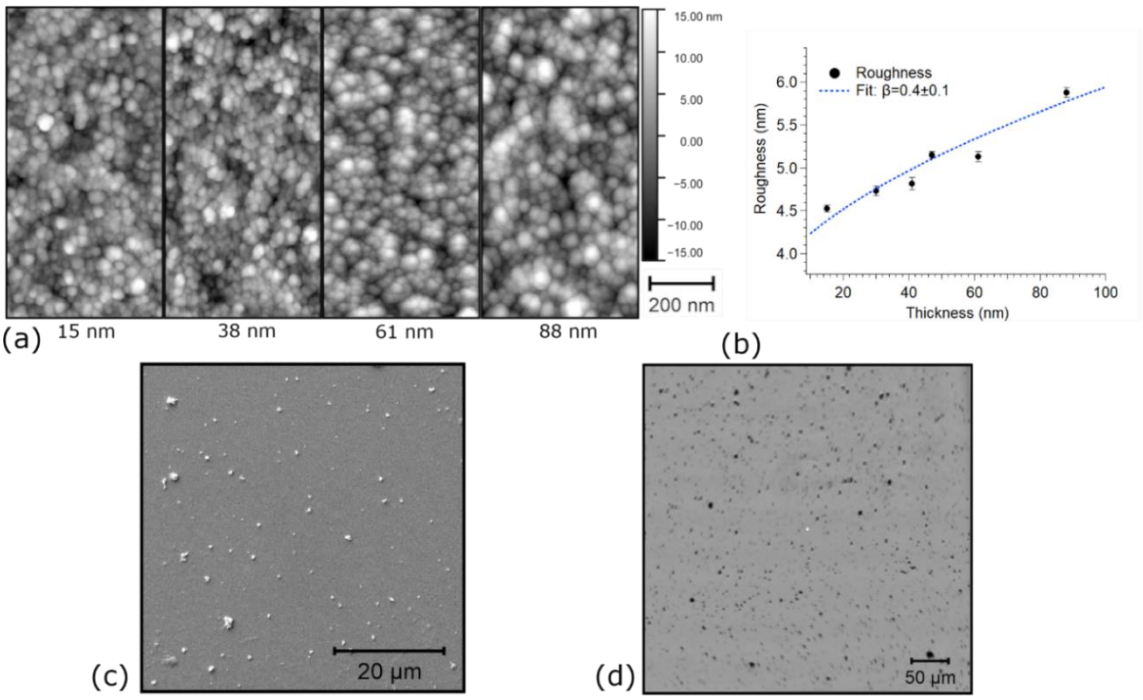

Figure 5-2. (a) 0.5x1 µm^2 AFM images of selected NiFe electrodes with thicknesses between 15 and 88 nm and (b) associated surface roughness calculated from the AFM images. (c) SEM images of a 38 nm thick film revealing the presence of micro-clusters. (d) Micro-clusters distribution at the optical microscope

At the micron length scale, a sparse distribution of micrometer-sized clusters is evidenced both in SEM and optical microscopy data, reported in Figure 5-2c-d for the representative case of the 38 nm thick NiFe film. The 500 x 500 μm^2 optical image was used to determine the micro-cluster density on the film surface for sizes higher than 1 μm (Figure 5-10d in supplementary section 5.6.1). The micro-clusters show a density decreasing with the size, with about 3000 grains/mm^2 in the 1-3μm range and less than 60 cluster per mm^2 for values higher than 7 μm. From the same image, such micro-clusters

have been estimated to cover 15% of the total film surface (more information in supplementary section 5.6.1).

In the XRD spectrum taken at grazing incidence angle and shown in Figure 5-3a for the 38 nm thick NiFe film, a broad peak centered at 2θ =44.5° appears, due to the metal Ni(111) crystalline plane.[185] The corresponding crystalline domain size from eq. (5-1), is 3.6 $\pm$ 0.5 nm. This value agrees with the AFM distribution in Figure 5-1c, considering that the third mode has a predominant mass contribution due to a much larger NP volume with respect to the smaller modes. The presence of a Fe alloying percentage would result in a 0.3° shift of the (111) peak,[185] which however is not detectable in Figure 5-3a, due to the peak width. However, XRD reveals the crystallinity of the nanometer-sized building blocks, while the aggregated structures and the bigger clusters may be interpreted as the assembly of the smaller crystalline NPs, as directly visualized by HRTEM imaging.

The ITO substrate Raman measurements (Figure 5-3b) show a background with a monotonously increasing trend and a broad peak around 600 cm^{-1}. In the NPs region, a three times lower signal is registered without any relevant resonance. Conversely, the micro-cluster region presents richer features, with two peaks at 489 cm^{-1} and 567 cm^{-1} and a shoulder at 685 cm^{-1}. These excitations can be associated to the presence of Ni oxides contributing near 570 cm^{-1}[186] and hydroxides with two distinct features around 480 cm^{-1} and 560 cm^{-1}.[187] The detection of oxide and hydroxide species is in agreement with XPS results. The large intensity difference between NPs and microcluster regions agrees with a corresponding difference in the volumes probed by the laser, as a consequence of the two order of magnitude higher thickness of the micro-clusters.

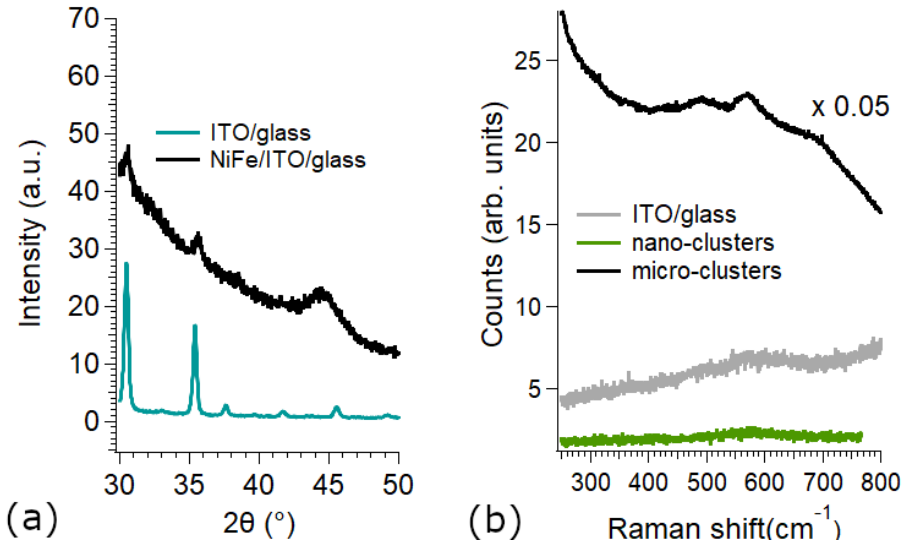

Figure 5-3. (a) XRD pattern of bare ITO and NiFe electrode. (b) Raman spectrum of a bare ITO, NP and microcluster regions.

Figure 5-4 summarizes the chemical characterization of the electrode films obtained by XPS. The O1s, Ni2p and Fe2p photoemission lines were fitted including Ni and Fe metal phases as well as NiO, $Ni(OH)_2$ and a combined Ni-Fe-O component, the latter being ascribed to the oxidation of alloyed Ni and Fe atoms. In this analysis, the $NiFe_2O_4$ spinel peak series from Biesinger *et al.*[188] was employed to model the Ni-Fe-O states. The XPS spectra fitting were carried out simultaneously for all the regions of Figure 5-4, by constraining the relative oxidation weights to be consistent among all the spectra (more information in supplementary section 5.6.2).

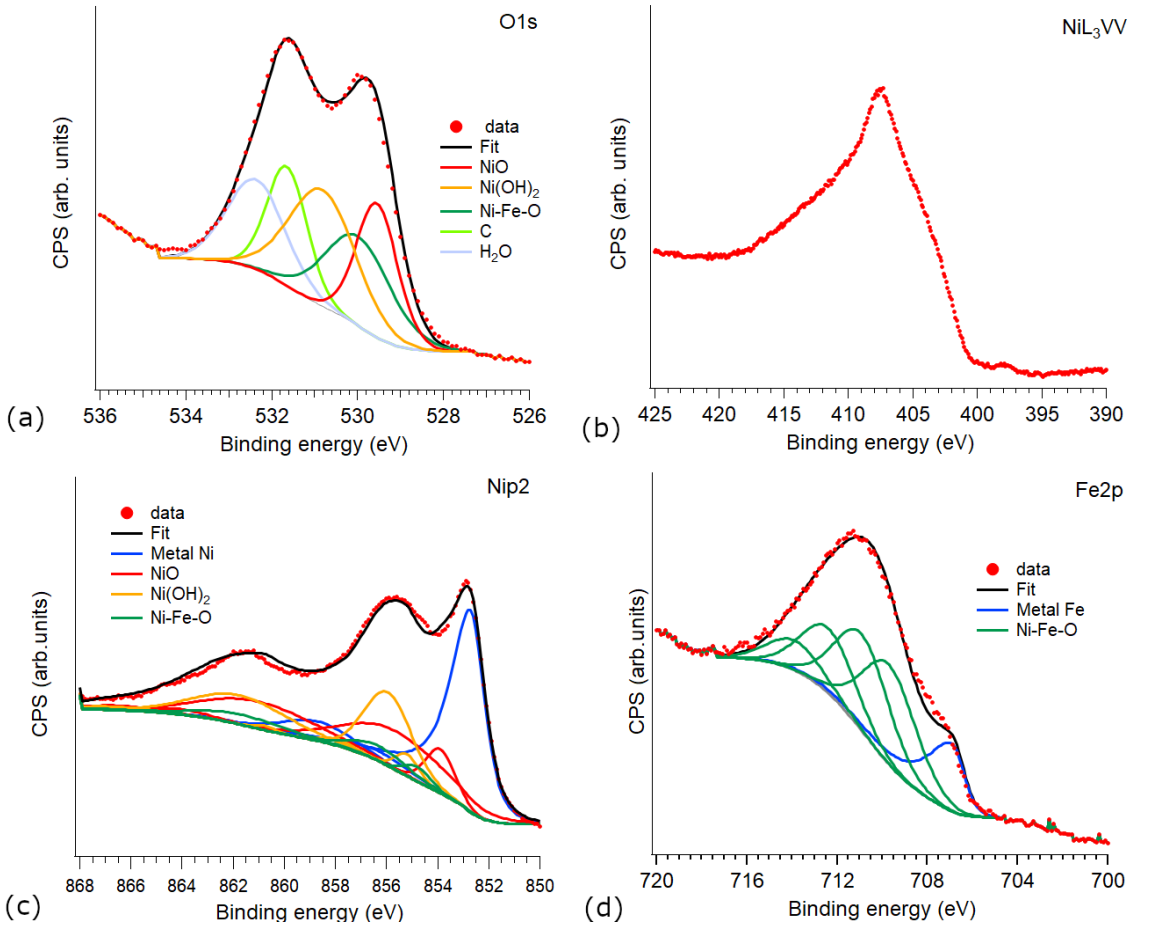

Figure 5-4. XPS spectra: (a) O1s, (b) Ni Auger LVV, (c) Ni2p and (d) Fe2p regions. Spectra have been fitted simultaneously including metal Ni and Fe and NiO, $Ni(OH)_2$ and Ni-Fe-O oxidized species.

In the O1s spectrum (Figure 5-4a), the 531.5-534 eV region is mainly affected by water species and carbon oxide contaminations, accounted for by two peaks at 532.4 eV and 531.6 eV. The lower binding energy region is reproduced by a combination of NiO, $Ni(OH)_2$ and Ni-Fe-O[189], [190] in a 36:47:17 relative weights. The Ni LMM Auger peak (Figure 5-4b) corresponds to a 1699 Auger parameter, typical of metal Ni. In the Ni2p region (Figure 5-4c) the metal phase, appearing with a main peak at 852.7 eV,[191] represent the 37% of total Ni species, while the peaks at 855.5 eV and 681.7 eV results

from the superposition of NiO (33%), $Ni(OH)_2$ (25%) and Ni-Fe-O (5%) phases.[188] The oxide relative weights are consistent with those from O1s spectrum. The Fe2p region is characterized by a 17% metal Fe component at 706.9 eV, while a Ni-Fe-O phase (83%) is sufficient to fit the wide peak centered at 711.3 eV, with no further Fe oxides. A Ni/Fe ratio of 92/8 is found by comparing Ni2p and Fe2p total counts, in agreement with the nominal chemical composition of the SCBD source. XPS results are compatible with a complete alloying of Fe atoms inside the NP, being Fe oxides reproduced totally by Ni-Fe-O peaks.

The optical properties of four representative NiFe electrodes and of the ITO/glass substrate are reported in Figure 5-5. In the reflection and transmission spectra acquired in the 280-1900 nm wavelength range (Figure 5-5a and Figure 5-5b, respectively), the ITO/glass substrate show an oscillating behavior due to interference fringes arising from multiple internal reflections inside the ITO coating. By modelling the substrate as a two-layer system with a 1 mm thick BK7 glass (with fixed refractive index from Rosete-Aguilar[192]) and a 130 ± 5 nm thick ITO coating layer, the ITO dielectric function was obtained by fitting the experimental data through the DEMON code (more information in chapter 3.3 and [182]). The set of oscillators identifying the ITO dielectric function and reported in section 5.6.3, were obtained by fitting the ITO/glass experimental R and T data. These parameters were employed to calculate the ITO dielectric function, leading to the ε_1 and ε_2 reported in Figure 5-5e and Figure 5-5f, respectively. In the 500-1900 wavelength range $\varepsilon_1(\varepsilon_2)$ is characterized by a decreasing (increasing) typical trend of the Drude oscillator. For lower wavelengths ε_1 shows a peak centered at 280 nm while ε_2 an edge at 320 nm. The ITO dielectric function was considered as fixed input to model the NiFe/ITO/glass overall optical response.

The R and T spectra of the NiFe electrodes (Figure 5-5a-b) retain the same ITO/glass substrate interference fringes, while for R the infrared minimum at 1000 nm redshifts to 1200 nm and for T the maxima undergo a 200 nm blueshift. As the NiFe film thickness increases, a global increase in R and decrease in T is shown, accompanied by a reduction of the oscillation amplitude.

The NiFe film was modelled through the DEMON software as one layer (Figure 5-5c) with an effective dielectric function ε_L (Figure 5-11 in supplementary section 5.6.3). The ε_L was obtained by starting from the metallic Ni dielectric function in ref. [193] and modifying it to fit the experimental data through the BEMA. In the model, a size effect correction, due to the finite metal cluster results in a proper modification of the Drude oscillator, while the metal grain shape is included through the depolarization factor q. A grain dimension of 10 nm was considered in the size corrections, since the film optical response is expected to be influenced by NP aggregates of tens nanometer size rather than single NPs. Furthermore, the mean field model combines the dielectric functions of metal Ni, NiO, $Ni(OH)_2$ and void to account for the partial oxidation/hydroxidation and the presence of vacuum pores in the film (more details in section 5.6.3).

For all the electrodes the optical spectra fitting was achieved for a NiFe metal filling fraction $f_{metal} = 48\%$, an oxide/hydroxide phase of $(30 \pm 10)\%$ and a porosity (i.e. void fraction) of $(20 \pm 10)\%$. The errors in parenthesis represent the range of values providing a fitting result deviating less than 5% from the data. For each film the thickness resulting from the fit agrees with the value from the AFM with a deviation never exceeding 1 nm. In the fit, the oxide/hydroxide volume ratio was kept fixed according to the relative stoichiometry from XPS, leading to $f_{ox} = (13 \pm 4)\%$ and $f_{hydr} = (17 \pm 6)\%$ oxides and

hydroxides fractions. The depolarization factor, as shown in Figure 5-5f, shows a decreasing trend from 0.45 to 0.35 for increasing film thickness, corresponding to a variation of NP assembly shape from slightly elongated in the vertical direction to nearly spherical (q=0.33). The complete set of fitting parameters is reported supplementary section 5.6.3. The fitting curves (Figure 5-5a and Figure 5-5b) correctly reproduce the R and T spectra, while the variations between the different films are accomplished just by refining the depolarization factor q and setting the thickness.

For each electrode, the NiFe layer real and imaginary part of the dielectric function $\varepsilon_L = \varepsilon_1 + i\varepsilon_2$, calculated from the experimental data fitting with the model schematized in Figure 5-5e, are reported in Figure 5-5c and Figure 5-5d, respectively. Both ε_1 and ε_2 show considerable differences between the different film thicknesses, determined mainly by the different values for q (Figure 5-5f) in the BEMA. For the 15 nm film ε_1 shows positive values and an increasing trend in all the wavelength range, while for the 61-88nm thick films a decreasing behavior reaching negative values is found. Furthermore, an increasing trend for ε_2 is shown in the entire range for all the electrodes, in particular for the thicker electrodes above 700 nm wavelength.

It is important to note that these results are describing the entire electrode thickness at difference with respect to the XPS, and correspond to an effective description of the chemical/morphological properties along the film depth. The metal (48%), oxides (13%), hydroxides (17%) and void (20%) filling fractions result to be independent of the film thickness, as confirmed by the constant NiFe density provided by AFM and quartz microbalance. Conversely, the depolarization factor trend suggest that the NP agglomeration is changing with thickness. Furthermore, the comparison between the

optical results and XPS allows to quantify the chemical composition gradient along the film depth. As showed in the section 5.6.3, the XPS results constrain the metal filling fraction to be lower than 20% at the surface, implying at least a 28% excursion with respect to the film core region.

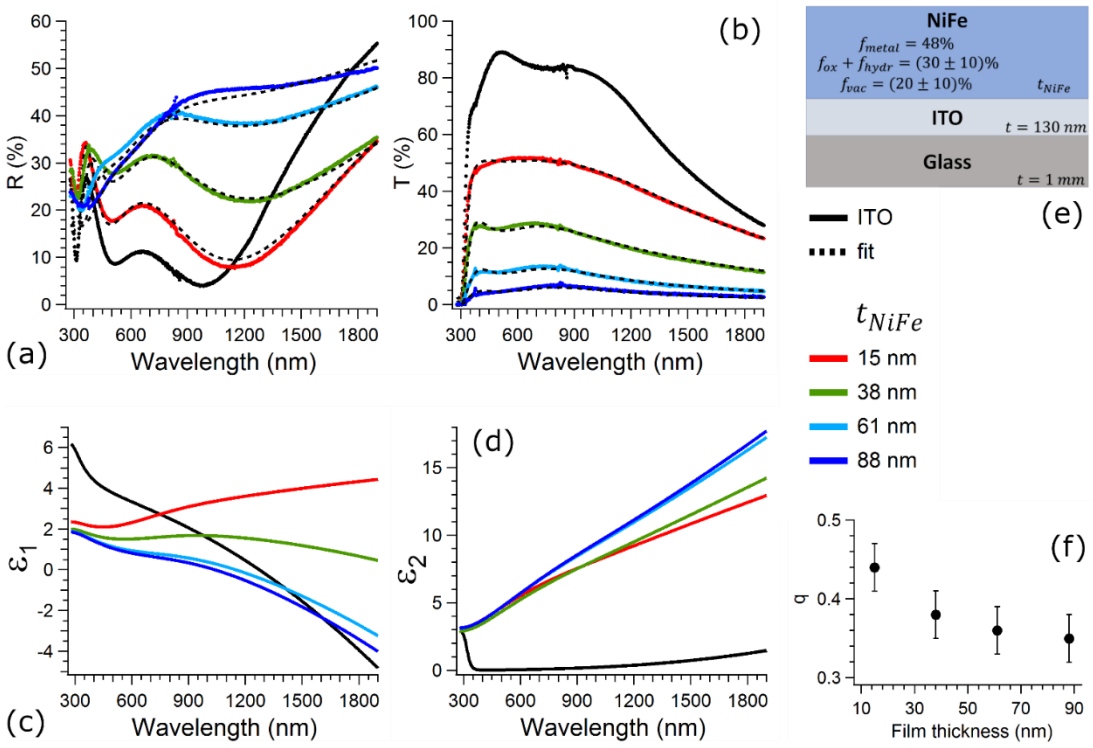

Figure 5-5. (a) Reflection and (b) transmission optical spectra and associated fit curves. (c) real and (d) imaginary part of the dielectric functions obtained from the fitting procedure of the spectra shown in panels (a) and (b). (e) Model employed to fit experimental data. (f) Depolarization factor q from fit.

5.4.3 Electrochemical behavior

Each NiFe film deposited on ITO/glass substrate has been employed as electrode for the OER evolution reaction, performing 5 voltammetry cycles in the range 570 mV-1870 mV vs RHE at 10 mV/s scan rate. Figure 5-6a reports, for selected NiFe thicknesses,

the electrode current density J_{geo} normalized to the geometrical area for the second j/V cycle, after subtracting the iR contribution due to the ohmic voltage drop (as in equation (5-2)). For potentials higher than 1.5 V, the OER

$$4OH^- \rightarrow 2H_2O + O_2 + 4e^- \quad (5\text{-}3)$$

takes place, determining the exponential increase of the current. In the OER region the curves are almost identical and no significant difference as a function of the electrode thickness can be detected in terms of current densities. The resulting thickness-dependent overpotential (Figure 5-6c) does not vary more than 3%, it is hence independent on the NiFe film thickness, i.e. on the catalyst loading.

This result is in contrast with a recent work [173], where the electrochemical behavior depends on the loading. Although in [173] the lack of an in-depth characterization of the electrode composition and physical structure does not allow a direct comparison with our electrodes, such difference in the catalytic response could be determined by a difference in the catalyst morphology and number of catalytic sites exposed to the electrolyte. As remarked in the same reference, this suggests that an effective quantification of the catalytic efficiency and comparison between different electrodes require the evaluation of the ECSA and the TOF, in which the direct electrochemical measurement is combined with a morphological parametrization of the electrode.

To this aim, we consider the area of the redox peaks (Figure 5-6b) associated to Ni hydroxide transformations:[194]

$$Ni(OH)_2 + OH^- \leftrightarrow NiOOH + H_2O + e^-$$

(5-4)

directly proportional to the number of $Ni(OH)_2$ sites involved in (5-4). Assuming the Ni hydroxides being spread in a surface monolayer (as in ref [195] and ref [196], more details in supplementary section 5.6.4) the ECSA can be calculated according to:

$$ECSA = S \cdot \frac{A_{peak}}{v\sigma}$$

(5-5)

where S is the electrode geometrical surface, A_{peak} is the oxidation peak area, $v = 10\ mV/s$ is the scan rate and $\sigma = 514 \mu C/cm^2$ is the $Ni(OH)_2$ surface charge density.[195]

The number of active sites independent on the electrode extension is then obtained by normalizing the ECSA to the geometrical electrode surface S (Figure 5-6d). This number is increasing by a factor of two as a function of the NiFe film thickness. The behavior, together with the film roughness increase observed by AFM (Figure 5-2b), suggests an increase of the active material surface exposed to the electrolyte solution as a function of the electrode thickness. In ref.[30] the $Ni(OH)_2$ is believed to play the role of active site in eq. (5-3), suggesting that an oxidation peak increase should correspond to an OER improvement. However, here we find that the oxidation peak growth does not correspond to any OER increase, with no direct correlation between the two reactions. We hypothesize that not all the generated active sites during the oxidation of the electrode are reached by the electrolyte solution, although the films are porous and granular.

The TOF at 350 mV plot (Figure 5-6e) presents a decreasing trend determined by the absence of significant changes in OER current while increasing the NiFe loading, indicating an excess of deposited mass with respect to the number of active sites participating to the OER catalysis. The maximum TOF of 0.09 s^{-1} is registered for the thinnest film, while highest values might be reached for small mass loading and a plateau in the TOF behavior could be obtained well below 15 nm, as suggested for catalysts loading below single layer coverage[173].

It is important to remark that such OER efficiency /mass loading correlation in Figure 5-6a-e can be established only at fixed nanostructure size and chemical composition, as for SCBD films. In case of incomplete control of such properties as a function of mass loading, the TOF behavior can be also affected implicitly by the nanograin[56]/crystalline domain[176] size or stoichiometry.[34] It is the case of NiFeO synthesized by laser assisted evaporation of ref [56], where the catalyst granular size has been shown to depend on the mass loading as well as on the substrate type.

In ref [55] electrodeposited NiFeO catalysts have been studied and, despite no insight on the nanostructure size is provided, a 1 s^{-1} TOF value has been computed, by considering only the Fe species as active sites.. This value is similar to the one found for the 15 nm film in this work, (0.9 s^{-1} if just the Fe fraction is considered).

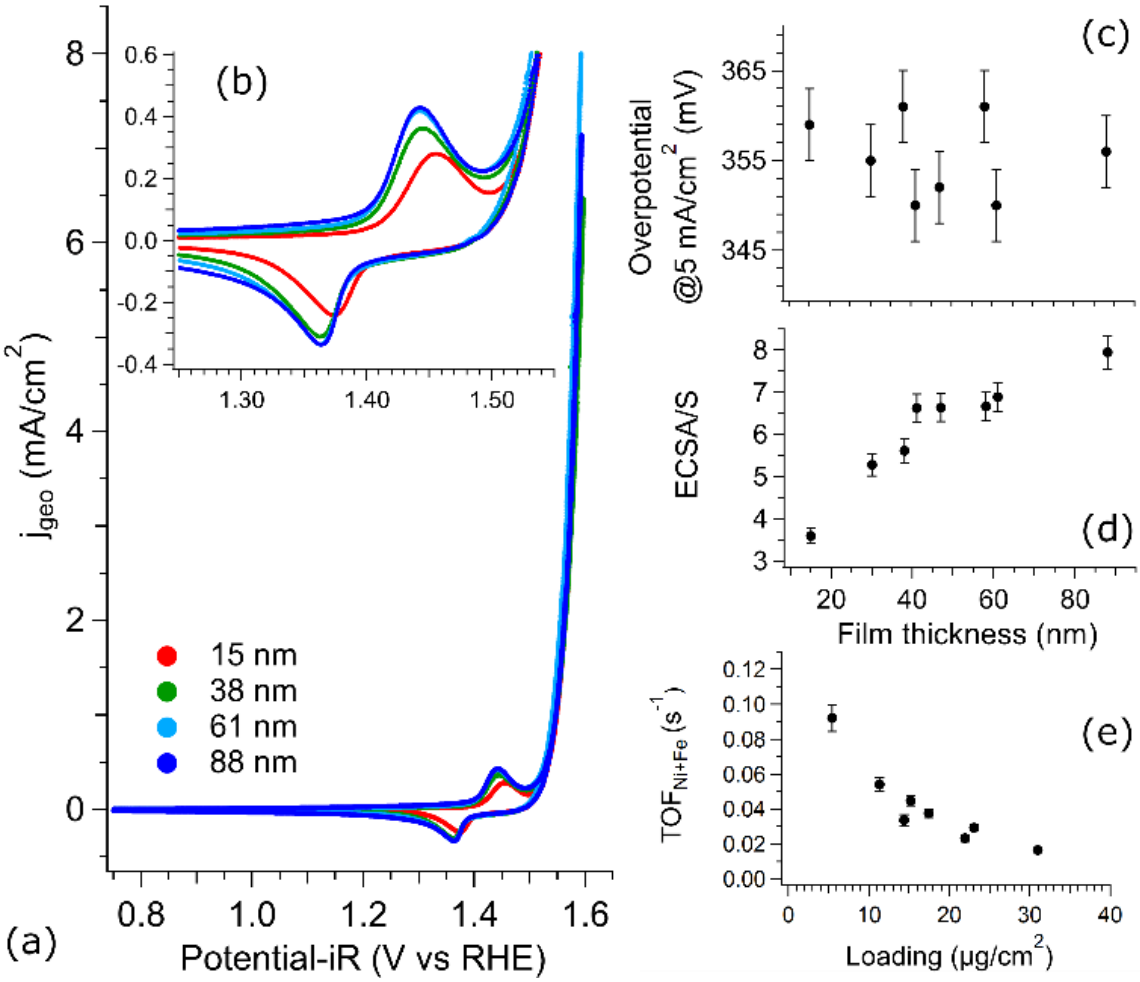

Figure 5-6. (a) The second voltammetry cycle of NiFe electrodes between 15 and 88 nm (for clarity, only selected curves are plotted). (b) Close up of the reduction and oxidation region. (c) Electrode thickness dependence of the overpotential at 5 mA/cm^2. (d) ECSA/S as a function of the NiFe film thickness. (e) Turn Over Frequency (TOF) for NiFe films as a function of the electrode loading at η=350 mV overpotential.

Our results on one side open new questions on how the redox-active species can participate to the OER catalysis and the relation between the efficiency and the film surface morphology, while on the other side are offering a well characterized and easy to tune model system. The role of film thickness and/or structure affects the redox activation potential could be unveiled in perspective works. Furthermore, the data indicate an effective strategy to reduce the electrode overall cost by exploiting films thinner than 15

nm to obtain the same OER catalysis efficiency at lower loading (higher TOF). The reduction of synthesis costs would be not only due to the limitation of metal species loaded on the electrode but also to the decrease of the energy demand in the manufacturing process, that is directly proportional to the film thickness for ballistic depositions.

5.5 Conclusions

NiFe nanogranular electrodes for the OER catalysis were synthesized by SCBD in a wide thickness range (15-88 nm, corresponding to 6-35 $\mu g/cm^2$ mass loading). The control over the film properties provided by SCBD allowed us to correlate the electrode morphological, chemical and electrochemical properties. The films were composed of aggregated alloyed NiFe (90%/10%) NPs, with a 20% porous fraction and a thickness dependent surface roughness. The oxidation/hydroxidation layer of the films were not dependent on the electrode thickness. The promising OER activity is independent of the film thickness, while the TOF is decreasing for increasing NiFe loading, questioning the role of the $Ni(OH)_2/NiOOH$ redox reactions in correlation to the catalytic efficiency. The thickness-dependent characterization suggested an excess of deposited NiFe mass with respect to the catalytic sites density indicating the low thickness films (15nm in this case) as the upper limit for most promising efficient and low-cost catalysts.

5.6 Supplementary information

5.6.1 Film morphology from AFM

5.6.1.1 Film loading/density

In situ during the SCBD synthesis, a quartz microbalance provided the NiFe mass loading μ_{NiFe}, i.e. the deposited NiFe mass (m_{NiFe}) per unity of electrode geometrical surface (S): $\mu_{NiFe} = m_{NiFe}/S$

In case of an ideal completely homogeneous and uniform NiFe metal, the film thickness can be calculated as:

$$t_{bulk} = \mu_{NiFe}/\rho_{NiFe} \tag{5-6}$$

where $\rho_{NiFe} = 0.9\rho_{Ni} + 0.1\rho_{Fe} = 8.8\ g/cm^3$ is the NiFe alloy mass density obtained as the weighted average of Ni and Fe (90%/10%).

Furthermore, for each electrode a direct AFM measurement provided the actual film thickness (t_{NiFe}), by analyzing the surface profile at the film edge with respect to the ITO substrate.

t_{NiFe} results generally higher than t_{bulk}, since a film volume increase may be determined by the presence of void's pores as well as of NiFe oxides/hydroxides (O/OH incorporation). The film excess thickness is defined as

$$\delta t/t = (t_{NiFe} - t_{bulk})/t_{bulk} \tag{5-7}$$

Figure 5-7a reports the film mass loading (equation (5-6)) and the excess thickness (equation (5-7)) as a function of the AFM thickness. Furthermore, the NiFe molar density MD_{NiFe} can be computed for each film as:

$$MD_{NiFe} = \frac{\mu_{NiFe}}{M_{NiFe} t_{NiFe}} \tag{5-8}$$

where $M_{NiFe} = 0.9M_{Ni} + 0.1M_{Fe} = 58.4\ g/mol$ is the NiFe average molar mass. MD_{NiFe}, shown in Figure 5-7b, indicates the average volume density of NiFe moles inside the film.

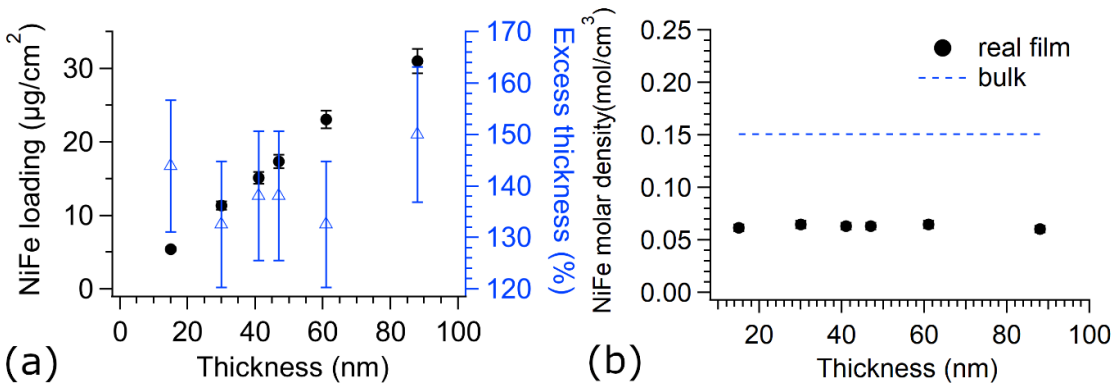

Figure 5-7. NiFe mass loading from the quartz microbalance and excess thickness according to equation (5-7) (a). NiFe molar density according to equation (5-8) (b). The values are reported as a function of the film thickness from AFM.

The mass loading shows a linear trend in terms of the film thickness (Figure 5-7a), whose slope is given by $MD_{NiFe} \cdot M_{NiFe}$. This linear trend reflects a constant $MD_{NiFe} = 0.06\ mol/cm^3$ in Figure 5-7b, corresponding to a molar density reduced by a factor 1/3 with respect to a bulk metal film. This low MD value may be originated by the presence of void/oxide/hydroxides inside the film. Furthermore, the constant MD trend also

corresponds to a constant 140% excess thickness with respect to a hypothetical bulk-like film.

5.6.1.2 Film roughness

For each NiFe electrode, a set of AFM images with a resolution of 0.26 pixel/nm^2 were considered. The output of the AFM acquisitions consists in the film height h_i for each pixel. The electrode RMS roughness σ_{EL}, computed directly from the image through the Gwyddion software [180], is obtained as:

$$\sigma_{EL} = \sqrt{\frac{1}{N-1}\sum_{pixel\ i}^{N}(h_i - \bar{h})^2} \tag{5-9}$$

where $\bar{h}$ is the mean film height $h = \frac{1}{N}\sum_{pixel\ i}^{N} h_i$.

The roughness σ_{EL} results from the convolution of two effects:

- The ITO substrate roughness σ_{ITO}.
  A value of σ_{ITO}=3.6$\pm$0.4 nm was obtained by applying the equation (5-9) to AFM images of bare ITO substrate, showed in Figure 5-8.

- The NiFe film contribution σ_{NiFe}, defined as the RMS roughness that would be measured for a NiFe film deposited on a perfectly flat substrate. From the ballistic deposition theory, σ_{NiFe} is related to the film thickness through:

$$\sigma_{NiFe} = \left(\frac{t_{NiFe}}{t_0}\right)^{\beta} \tag{5-10}$$

  where t_0 is a dimensional constant and β = 1/3 for ballistically deposited grains [184].

The overall electrode roughness can be written as the convolution of the film and ITO substrate effects as:

$$\sigma_{EL} = \sqrt{\sigma_{ITO}^2 + \sigma_{NiFe}^2}$$

(5-11)

Figure 5-2b in the main text shows the electrode RMS roughness (dots) obtained directly from the AFM images trough equation (5-9). The points have been fitted according to model in equation (5-11) (dashed line), assuming σ_{ITO}=3.6±0.4. A value of $\beta = 0.4 \pm 0.1$ results from the fit, in agreement with the predicted 1/3 for the ballistic deposition.

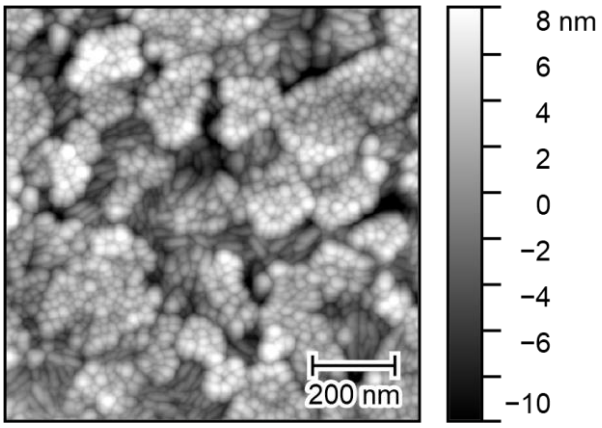

Figure 5-8. AFM image of the ITO substrate

5.6.1.3 Sparse NP analysis

A sparse NP distribution has been deposited onto a Si substrate, with a surface roughness lower than 0.1 nm. A set of $2\mu m$ x $2\mu m$ images have been acquired by AFM, as reported in Figure 5-1 in the main text for one representative case. The images have been processed by using a level mask within the Gwyddion software [180]. The method consists

in a multistep analysis of both the substrate and the NP profile. Firstly, the substrate region is flattened, accounting for possible sample inclination on the AFM plate, then the Si RMS roughness is calculated (<0.1nm). Finally, the NPs are identified as the regions whose height deviates from the Si substrate baseline for more than 3 times the Si RMS roughness. The NP height distribution results in the histogram in Figure 5-1c (main text), where 14% of NPs are distributed in the first (0.36nm) mode, 49% in the second (0.6nm) and 37% in the third one (2.8nm).

Furthermore, from the same AFM images, the NP area projected onto the x-y plane has been computed and the associated x-y projected radius (r_{xy}) has been extracted. The r_{xy} distribution is characterized by three lognormal peaks at 2.0±0.2 nm, 3.3±0.3 nm and 11.3±0.3 nm (Figure 5-9b). These values result from the convolution between the AFM tip dimension and the actual NP radius, as showed in Figure 5-9a in case of a spherical particle.

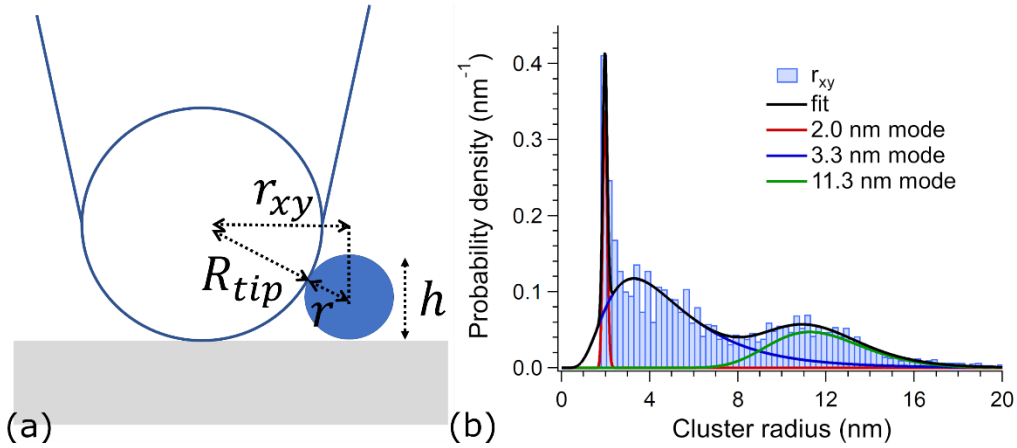

Figure 5-9. AFM tip/NP size convolution effect in a sparse NP image. R_{tip} is the AFM tip radius, r is the actual NP radius and h is the NP height measured as the maximum of the height profile (a).

In case of spherical NP, the measured projected radius (r_{xy}) can be predicted from the actual NP radius (r) through

$$r_{xy} = 2\sqrt{rR_{tip}} \tag{5-12}$$

where R_{tip} is the tip radius, set to $8 \pm 3\ nm$ in this work, while r can be obtained as the NP half height from the distribution in Figure 5-1c (main text). From the three measured height modes (0.36, 0.6, and 2.8 nm), equation (5-12) predicts three modes for r_{xy} at $2.4 \pm 0.9\ nm$, $3 \pm 1\ nm$ and $6.7 \pm 2.5\ nm$. By comparing these predicted values with the r_{xy} resulting from the projected areas, we conclude that the first two modes are consistent with a spherical geometry. In the third case, equation (5-12) predicts a smaller value for r_{xy}, suggesting that the NP are characterized by an elongated geometry along the xy plane.

5.6.1.4 Granular surface analysis

In order to evaluate the surface nanogranular composition of NiFe electrodes, a set of AFM images with 0.26 pixel/nm^2 resolution has been considered. As showed in Figure 5-10a for a representative image, the nanograins have been labelled through a watershed mask within the Gwyddion software [180] . The mask consists in reversing the image height profile, placing virtual water drops uniformly on the surface, let the drops evolve towards local minima leading to connected domains (grain location) and finally grow each separate domain to fill the grains (segmentation). The parameters involved in the process are listed in Table 5-1, according to the Gwyddion [180] definitions.

TABLE 5-1:

PARAMETERS EMPLOYED IN THE WATERSHED ALGORITHM IN GWYDDION.

Grain location			Segmentation		Threshold
N° steps	Drop size (%)	Threshold (px^2)	N° steps	Drop size (%)	(px^2)
60	0.1-0.5	0-1	20	25	7-9

Parameters employed in the watershed algorithm in Gwyddion. In case a range is reported instead of a precise value, the parameter has been tuned to best identify the grains depending on the image analyzed.

After applying the watershed mask each connected domain is identified as a single NiFe grain, as showed in Figure 5-10a. The domain lateral size is highly affected by the AFM tip size and would overestimate the actual grain dimension (as shown in Figure 5-9a). To overcome this issue, the grain radius has been evaluated in the vertical direction by computing the difference between the domain maximum and the minimum on its boundary. The resulting size (diameter) histogram is plotted in Figure 5-10b for the case of 38 nm thick film, resulting in a very broad distribution peaked at 5-10 nm and with a long tail reaching 20 nm. The solid fitting line corresponds to a lognormal curve with 5 nm mode and a 15 nm standard deviation. The results in the histogram Figure 5-10b generally underestimate the actual grain dimensions on the film surface, due to the particle overlapping: in case of a grain is partially covered, its dimensions appear lower and affect mainly the left tail in the histogram. Therefore 5 nm can be interpreted as a lower bound to the grain size rather than the actual dimensions.

The same watershed algorithm has been applied to identify the micro-clusters in an optical microscope image (Figure 5-10c). For each micro-cluster, the dimension was

determined as the grain x-y size (in the plane parallel to the substrate) appearing in the image. The micro-cluster density per unit of geometrical surface is reported in Figure 5-10d. The optical resolution and magnification allowed to identify only particles larger than 1μm. For sizes lower than 3μm the micro-grain density shows an oscillating trend with 3000 grains/mm^2 in the 1-3μm size range, decreasing for larger dimensions and approaching 0 after 7 μm. From the same histogram, the total micro-cluster surface area A_μ can be calculated as the sum of each cluster's surface, given for spherical geometry by:

$$A_\mu = \sum_{\mu\ clusters} 4\pi r_\mu^2 \tag{5-13}$$

where r_μ is the radius of each micro-cluster. From equation S.6, the micro-cluster result to cover 15% of the total electrode surface.

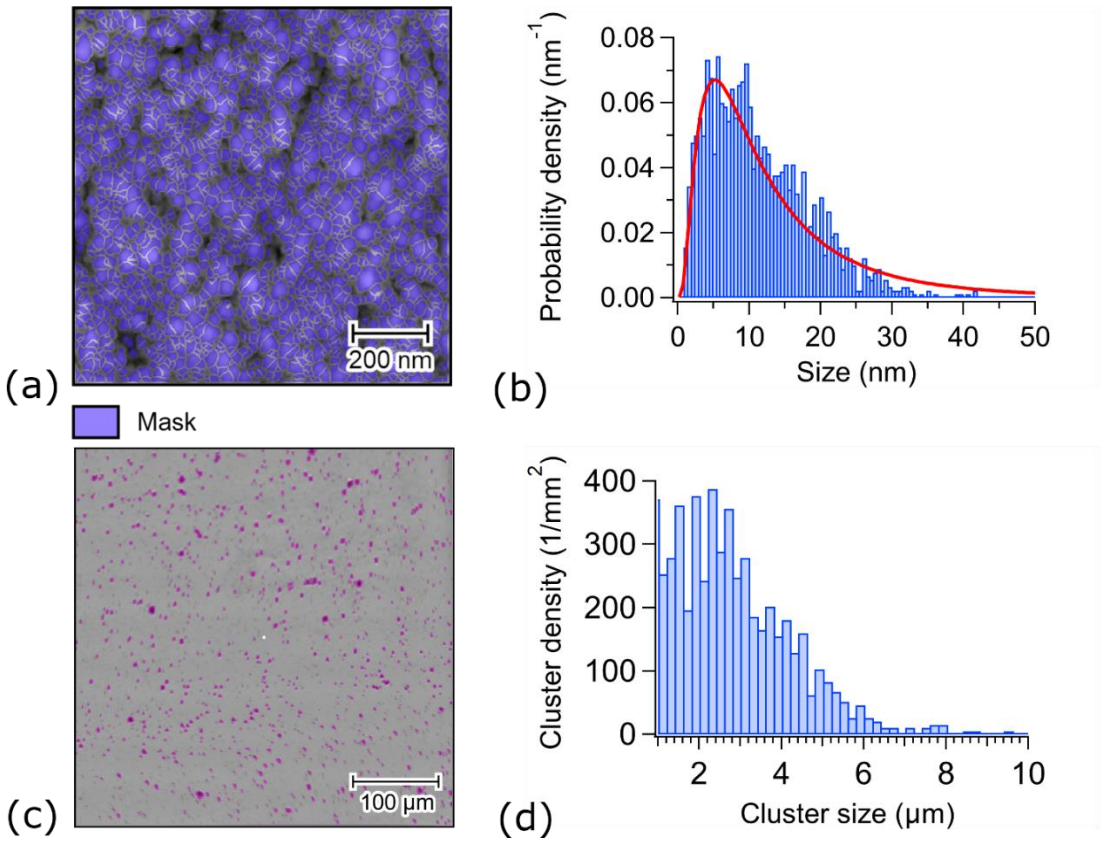

Figure 5-10. Watershed mask (a) applied to 1µm x 1µm AFM image to determine the cluster size distribution (b) at the film surface. Level mask (c) applied to an optical microscope image to determine the micro-cluster size density per unit of geometrical surface (d).

5.6.2 XPS

The XPS spectra analysis has been performed simultaneously for O1s, Ni2p and Fe2p spectra according to the following steps, where $N_{x:y}$ indicates the molar density of the atom x bound in the molecule y (in case of no y is specified the total x species are considered).

1) Comparing the total Ni and Fe counts a 92/8 NiFe ratio has been determined:

$$N_{Ni}/N_{Fe} = 92/8 \tag{5-14}$$

2) In the Fe2p spectrum, data can be reproduced by a combination of Fe metal component with a peak at 706.9 eV (17%) and a Ni-Fe-O alloyed oxide (83%), modelled by the $NiFe_2O_4$ spinel peak series from [188] (Figure 5-4d, main text):

$$N_{Fe:metal}/N_{Fe:NiFeO} = 17/83 \tag{5-15}$$

3) From Ni2p spectrum a 37% metal phase can be deduced from the main peak position at 852.7 eV, while 63% is associated to a mix of oxide/hydroxides whose ratio will be determined later:

$$N_{Ni:metal}/(N_{Ni:NiO} + N_{Ni:Ni(OH)_2} + N_{Ni:NiFeO}) = 37/63 \tag{5-16}$$

4) From $N_{Ni} = N_{Ni:NiO} + N_{Ni:Ni(OH)_2} + N_{Ni:NiFeO} + N_{Ni:metal}$ (i.e. definition of total Ni species) and equation (5-16), we find:

$$(N_{Ni:NiO} + N_{Ni:Ni(OH)_2} + N_{Ni:NiFeO}) = 0.63N_{Ni} \tag{5-17}$$

while from $N_{Fe} = N_{Fe:metal} + N_{Fe:NiFeO}$ (i.e. definition of total Fe species) and equation (5-15), we find:

$$N_{Fe:NiFeO} = 0.83N_{Fe} \tag{5-18}$$

By considering the (5-17)/(5-18) equation ratio and plugging equation (5-14), we than obtain:

$$(N_{Ni:NiO} + N_{Ni:Ni(OH)_2} + N_{Ni:NiFeO})/N_{Fe:NiFeO} = 90/10 \tag{5-19}$$

5) The relative stoichiometries in the oxide/hydroxide molecules can be written as: $N_{O:NiO} = N_{Ni:NiO}$; $N_{O:Ni(OH)_2} = 2N_{Ni:Ni(OH)_2}$ and $N_{O:NiFeO} = 4N_{Ni:NiFeO} = 2N_{Fe:NiFeO}$. By using these relations, equation (5-19) can be rewritten as $(N_{O:NiO} + 0.5N_{O:Ni(OH)_2} + 0.25N_{O:NiFeO})/0.5N_{O:NiFeO}$ =90/10 and, solving for $N_{O:NiFeO}$, we obtain:

$$N_{O:NiFeO} = 0.24 \cdot N_{O:NiO} + 0.12 \cdot N_{O:Ni(OH)_2} \tag{5-20}$$

6) With the constraints from equation (5-20), the O1s spectrum has been deconvoluted (Figure 5-4a main text), determining:

$$N_{O:NiO}/N_{O:Ni(OH)_2}/N_{O:NiFeO} = 36/47/17 \quad (5\text{-}21)$$

7) By using the stoichiometry relations in point 5) the result in equation (5-21) has been converted in terms of Ni species: $N_{Ni:NiO}/N_{Ni:Ni(OH)_2}/N_{Ni:NiFeO}$=56/37/7. This constraint has been employed in the Ni2p spectrum deconvolution (Figure 4c) obtaining:

$$N_{Ni:metal}/N_{Ni:NiO}/N_{Ni:Ni(OH)_2}/N_{Ni:NiFeO} = 37/33/25/5 \quad (5\text{-}22)$$

5.6.3 Optics

5.6.3.1 Substrate

The glass layer in Figure 5-5c (main text) has been modelled as an uniform and homogeneous material with refractive index from [192] and a 1 mm thickness.

The ITO substrate dielectric function has been parametrized as:

$$\varepsilon_{ITO} = \varepsilon_\infty + \varepsilon_{IB}(\omega) + \varepsilon_{\mathrm{Drude}} \quad (5\text{-}23)$$

with

$$\varepsilon_{\mathrm{Drude}} = -\frac{\omega_{\mathrm{pl}}^2}{\omega^2 + i\Gamma_{\mathrm{ITO}}\omega}$$

$$\varepsilon_{IB} = A_{lor}\frac{(\Gamma_{lor}^2)}{(\omega-\omega_{lor})^2+\Gamma_{lor}^2} + i\left[\frac{H}{1+e^{(\omega_c-\omega)/s}}\right]$$

where ϵ_∞ is a constant term, ε_{Drude} is the Drude oscillator, and ε_{IB} is the interband contribution. The parameters in (5-23) were tuned by fitting the bare ITO/glass R and T

spectra (Figure 5-5a-b in the main text) and are listed in Table 5-2, while the resulting dielectric function is reported in Figure 5-11a-b.

TABLE 5-2:

PARAMETERS IN THE ITO DIELECTRIC FUNCTION

ϵ_∞	$\hbar\omega_{pl}$	$\hbar\Gamma_{\mathrm{ITO}}$	A_{lor}	$\hbar\omega_{lor}$	$\hbar\Gamma_{lor}$	H	$\hbar\omega_c$	$\hbar s$
3.78	1.96 eV	0.11 eV	2.6	4.5 eV	1.13 eV	3.0	3.9 eV	0.13 eV

Parameters in the ITO dielectric function S.16 resulting from the ITO/glass optical spectra fitting.

5.6.3.2 NiFe film

The NiFe film has been modelled by adding a top layer to the ITO/glass stack. Considering the Ni/Fe relative composition, Ni is expected to mainly affect the optical response, while no Fe contribution is included in the model. The NiFe layer dielectric function ε_L results from a proper modification of the bulk Ni dielectric function ε_{Ni} to include grain size effects and the mixing of metal with void/oxide/hydroxide phases. The starting bulk Ni dielectric function ε_{Ni} is defined as

$$\varepsilon_{Ni} = \varepsilon_\infty - \frac{f_0\omega_{pl}^2}{\omega(\omega + i\Gamma_0)} + \frac{f_1\omega_{pl}^2}{\omega_1^2 - \omega^2 - i\omega\Gamma_1} + \frac{f_2\omega_{pl}^2}{\omega_2^2 - \omega^2 - i\omega\Gamma_2} + \frac{f_3\omega_{pl}^2}{\omega_3^2 - \omega^2 - i\omega\Gamma_3} + \frac{f_4\omega_{pl}^2}{\omega_4^2 - \omega^2 - i\omega\Gamma_4} \quad (5\text{-}24)$$

with a Drude oscillator as the first term and three Lorentz oscillators, where the values from reference [193] have been considered for each parameter (listed in Table 5-3).

TABLE 5-3:

PARAMETERS IN THE BULK NI DIELECTRIC FUNCTION

	Oscillator	f_i	$\hbar\Gamma_i\ (eV)$	$\hbar\omega_i(eV)$
$\hbar\omega_{pl} = 15.92\ eV$ $\varepsilon_\infty = 1$	0	0.096	0.048	-
	1	0.1	4.511	0.174
	2	0.135	1.334	0.582
	3	0.106	2.178	1.597
	4	0.729	6.292	6.089

Values for the parameters in the bulk Ni dielectric function (eq. (5-24)) from reference [193].

The finite size of the metal inclusions inside the nanogranular film results in an increase of the conduction electron scattering rate Γ_0 according to (chapter 3.3 and [182]):

$$\Gamma_0 \to \Gamma = \Gamma_0 + \frac{Av_f}{r} \tag{5-25}$$

where A is a factor of order of unity (set to 1 in this work), $v_f \cong 1 \cdot 10^6 m/s$ ([197]) and r is the average grain radius. According to Figure 5-10b, a grain radius of 5 nm has been considered, leading to $\hbar\Gamma = 0.2\ eV$ from equation (5-25). The size effect modified dielectric function $\bar{\varepsilon}_{Ni}$ is then obtained from ε_{Ni} by just replacing Γ_0 with Γ.

The presence of void pores and oxide/hydroxide phases is then accounted for by plugging $\bar{\varepsilon}_{Ni}$ in a BEMA model, where the NiFe film effective dielectric function ε_L is determined as the solution of:

$$f_{metal}\frac{(\bar{\varepsilon}_{Ni}-\varepsilon_L)}{\varepsilon_L+q(\bar{\varepsilon}_{Ni}-\varepsilon_L)}+f_h\frac{(\varepsilon_h-\varepsilon_L)}{\varepsilon_L+q(\varepsilon_h-\varepsilon_L)}=0$$

(5-26)

In Equation (5-26), q is the depolarization factor, accounting for the grain shape (more information in chapter 3.3 and [182]), f_{metal} is the Ni metal volume filling fraction, while f_h and ε_h are filling fraction and dielectric function of an host medium obtained by mixing vacuum, oxide and hydroxides. In particular:

$$f_{metal}+f_h=1$$

(5-27)

and

$$f_h=f_{vac}+f_{ox}+f_{hydr}$$

(5-28)

is the sum of void, oxide and hydroxide volume contributions, while

$$\varepsilon_h=f_{vac}\cdot 1+f_{ox}\varepsilon_{ox}+f_{hydr}\varepsilon_{hydr}$$

(5-29)

is the weighted average of vacuum/oxide/hydroxide phases, with $\varepsilon_{ox}=3.96+0.8i$ ([198]) and $\varepsilon_{hydr}=2.21+0.6i$ ([199]).

Being the NiFe film modelled by a single layer, each parameter can be interpreted as an average property over the entire film volume, even if metal/void/oxide/hydroxide fractions may not actually be uniform. Therefore, the XPS technique, consisting in just a surface region characterization, cannot provide direct constraints on the average film parameters. Nonetheless, one can expect that the ratio $\frac{f_{hydr}}{f_{ox}}$ could be constant along the film depth,

being just determined by the metal reactivity to air exposure and not by the morphology. The $\frac{f_{hydr}}{f_{ox}}$ can be determined from XPS as:

$$\frac{f_{hydr}}{f_{ox}} = \frac{\rho_{NiO/NiFeO}}{\rho_{Ni(OH)_2}} \cdot \frac{M_{Ni(OH)_2}}{M_{NiO}} \cdot \frac{N_{Ni:Ni(OH)_2}}{N_{Ni:NiO} + N_{Ni:NiFeO}} = 1.37 \tag{5-30}$$

where $\frac{N_{Ni:Ni(OH)_2}}{N_{Ni:NiO}+N_{Ni:NiFeO}} = 0.66$ is the hydroxide/oxide molar density fraction from XPS (Equation (5-22)), $M_{Ni(OH)_2} = 93\ g/mol$ and $M_{NiO} = 75\ g/mol$ are the hydroxide/oxide molar masses and $\rho_{NiO/NiFeO} = 6.5\ g/cm^3$ (obtained as weighted average of NiO and $NiFe_2O_4$ densities according to equation (5-22)) and $\rho_{Ni(OH)_2} = 4.1\ g/cm^3$ are the densities.

R and T data (in Figure 5-5a-b in the main text) have been fitted by employing the three layer model in Figure 5-5c where the layer dielectric function ε_L defined in equation S.19 has been considered in the NiFe layer, with the constraints from equation (5-27)-(5-30). The complete parameters resulting from the fits are reported in Table 5-4, where the layer thickness, f_{metal} , $f_{ox} + f_{hydr}$ and q were the independent variables refined in the fitting process (reported with a blue background), while the other parameters are either constant ($\hbar\Gamma$) or depend on the formers through the (5-27)-(5-30)constraints. The uncertainties correspond to the range of values corresponding to fitting curves deviating less than 5% from experimental data.

TABLE 5-4:

FIT RESULTS OF NIFE FILMS OPTICAL SPECTRA

AFM thickness (nm)	Layer thickness (nm)	f_{metal} (%) (± 3)	$f_{ox} + f_{hydr}$ (%) (± 10)		f_{vac} (%)	q (± 0.03)	$\hbar\Gamma$ (eV)
			f_{ox} (%)	f_{hydr} (%)			
15	**14.5±2**	**48**	**30**		14	**0.45**	0.2
			13	17			
38	**37±4**	**48**	**30**		24	**0.395**	0.2
			13	17			
61	**62±9**	**49**	**30**		21	**0.36**	0.2
			13	17			
88	**88 ±12**	**49**	**30**		21	**0.35**	0.2
			13	17			

R and T spectra (Figure 5-5 in the main text) fitting results according to the model in Figure 5-5c (main text). The bold numerical values are the refined independent variables in the model, while the other values are either constant (Γ) or depend completely on the former through the constraints in equations (5-27)-(5-30).

Figure 5-11c-d reports the bulk Ni (equation (5-24)) dielectric function as well as the ε_L effective dielectric functions employed for each electrode in the optical spectra fitting. The BEMA model highly affects the dielectric functions with respect to a bulk material, while a q decrease determines a decrease (increase) in the real (imaginary) part of ε_L.

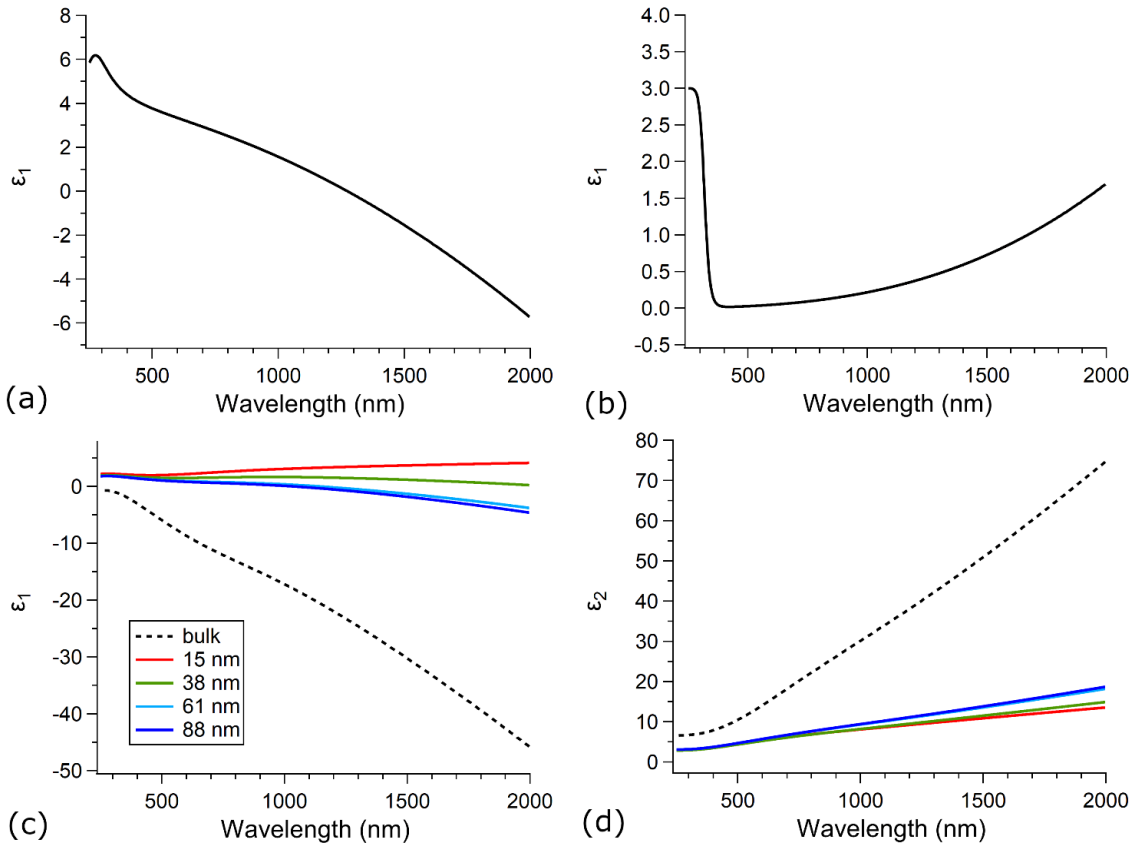

Figure 5-11. Real (a) and imaginary (b) part of the ITO effective dielectric function. Real (c) and imaginary (d) part of bulk Ni dielectric function (from equation (5-24)) and of the effective NiFe film dielectric functions employed to model the electrodes in the 15-88nm thickness range.

5.6.3.3 Chemical composition gradient inside the film

The parameters resulting from the optical analysis represent average properties over the film volume, while a comparison with the XPS results can provide an insight on the chemical composition gradient in the film depth.

A constraint similar to Equation (5-30) can be determined for f_{metal}/f_{ox}:

$$\frac{f_{metal}}{f_{ox}} = \frac{\rho_{NiO/NiFeO}}{\rho_{Ni}} \cdot \frac{M_{Ni}}{M_{NiO}} \cdot \frac{N_{Ni:metal}}{N_{Ni:NiO} + N_{Ni:NiFeO}} = 0.56$$

(5-31)

where $\frac{N_{Ni:metal}}{N_{Ni:NiO}} = 0.97$ is the metal/oxide molar density fraction from XPS (Equation S.15), $M_{Ni} = 59\ g/mol$ and $M_{NiO} = 75\ g/mol$ are the hydroxide/oxide molar masses and $\rho_{NiO/NiFeO} = 6.5\ g/cm^3$ and $\rho_{Ni} = 8.9\ g/cm^3$ are the densities.

By plugging Equations (5-31) and (5-30) in (5-27), we obtain:

$$f_{vac} + 5.2 \cdot f_{metal} = 1$$

(5-32)

where a maximum value of $f_{metal} = 19\%$ is obtained if $f_{vac} = 0$.

According to equation (5-32), the XPS results limit the metal volume filling fraction to be lower than 20% in the film surface region. Therefore, considering the deviation from the average value in the film provided from the optical spectra fitting, an excursion of at least 28% in f_{metal} must occur between the film surface and core regions.

5.6.4 Electrochemistry

5.6.4.1 ECSA and RF

Electrochemical surface area (ECSA) has been calculated from the reduction peak in the current/potential curves (Figure 5-6a, main text) corresponding to the reaction: $NiOOH + H_2O + e^- \rightarrow Ni(OH)_2 + OH^-$.

The reduction current peak area A_{peak} has fbeen calculated by integrating the current density/voltage curve in the 1.1-1.45 V (vs RHE) potential range for all the NiFe films,

when no iR ohmic drop corrections are considered. The quantity $S \cdot A_{peak}/v$ represents the total charge flowed through the electrode produced by the redox reaction, where S is the film catalyst geometrical surface and v=10 mV/s is the scan rate.

Assuming $Ni(OH)_2$ to be distributed in a rough surface monolayer, one can define the ECSA as the monolayer surface area: $ECSA = S \cdot \frac{A_{peak}}{v\sigma}$. The roughness factor is then defined as the ECSA/geometrical surface ratio:

$$RF = \frac{A_{peak}}{v\sigma} \tag{5-33}$$

5.6.4.2 TOF

Turnover frequency (TOF) consists in the O_2 molar rate production divided by NiFe moles in the electrode. The reaction $4OH^- \rightarrow 2H_2O + O_2 + 4e^-$ is considered here, while 100% of deposited Ni and Fe mass has been considered for the computation of the active sites moles.

If j is the current density (mA/cm^2) directly measured at $\eta = 350\,mV$ overpotential, the O_2 molar rate production (per unity of geometrical surface) is:

$$O_2\ molar\ rate = \frac{j}{4eN_A} \tag{5-34}$$

where e is the electron charge and N_A is the Avogadro number. The deposited NiFe moles (per unity of geometrical surface) can be obtained from the electrode NiFe mass loading μ_{NiFe} as:

$$NiFe\ moles = \mu_{NiFe}/M_{NiFe} \tag{5-35}$$

where M_{NiFe} is the average NiFe molar mass (also defined for equation (5-8)).

The TOF is then defined as:

$$TOF = \frac{jM_{NiFe}}{4eN_A\mu_{NiFe}}$$

CHAPTER 6:

NIFE NANOALLOY STABILITY UNDER PROLONGED OER CONDITIONS

This chapter is based on:

L. Ciambriello, I. Alessandri, M. Ferroni, L. Gavioli, and I. Vassalini, "Instability-Driven Resilience of NiFe Catalysts for Alkaline Oxygen Evolution Reaction", Submitted to ACS Applied Energy Materials

6.1 Abstract

Despite NiFe materials remain among the best low-cost alternatives to Ir- or Ru-based anodes for water splitting, instability and fast de-activation are major limitations to their implementation in commercial alkaline electrolyzer which must be quickly fixed. In this paper NiFe (90/10 % at) thin film (~35 nm) electrodes were synthesized through Supersonic Cluster Beam Deposition (SCBD) and they were successfully employed as electrocatalysts for the Oxygen Evolution Reaction (OER) in alkaline media for prolonged times (up to 96 hours under the application of a constant voltage, and up to 10 hours under intermittent cyclic conditions). At the basis of their long-term activity, we believe that there is an equilibrium between dissolution and re-adsorption of catalyst nanoparticles (NPs) from/to the electrode surface. During prolonged electrochemical activity an exfoliation process occurs, making most of the catalyst NPs (~99%) to detach from the electrode

surface and dissolve in the electrolyte. This process has a double positive effect: on one hand it enables the continuous creation of sparse catalytic centers for the adsorption and oxidation of OH^- ions from the electrolyte, on the other it leads to an electrolyte rich in catalysts which can be subsequently re-adsorbed on the electrode surface, hindering is complete consumption.

6.2 Introduction

Hydrogen represents one of the best alternatives to fossil fuels, however its production through electrochemical water splitting [10] is hindered by the slow kinetics of the oxygen evolution reaction (OER) [12]. This limitation can be overcome by designing efficient and stable OER catalysts. In this framework, the possible utilization of earth-abundant materials for alkaline electrolyzers is intensively investigated in view of bypassing conventional noble metal-based catalysts [11], [18]. In this context, NiFe nanoalloyed materials are the most promising, revealing a high OER catalytic efficiency, earth abundance of their constituents and limited cost of manufacturing [30]. Nonetheless, the NiFe electrode stability during prolonged OER working conditions, crucial for a large-scale diffusion of the catalysts, is still unsatisfactory [58], [59]. In NiFe based materials, the problem of electrode stability has been addressed mainly for (oxy)hydroxidized compounds [58], [200], such as layered double hydroxides [201], [202]. However, the state of the art Ni-Fe alloyed electrodes are not sufficiently stable for a practical industrial application, and the working mechanisms at the basis of their activity, the real chemical nature of the active sites [28], [29], [38] and their transformation [61] and the correlation with their stability for long time are still debated.

The major source of poor stability in this cases is the electrode corrosion [27], that can be mitigated if stable Ni/Fe oxides or (oxy)hydroxides phases form spontaneously during operation [70], especially during anodization, but this event is highly affected by the initial electrode crystallinity. Despite a relatively stable film can be formed directly in the electrochemical cells under operation, more frequently material stability is increased during the electrode preparation step, through the deposition of a C coating onto the NiFe

nanostructures, preventing metal/electrolyte direct contact [31]. However, C coatings also increase electrode resistivity, leading to a limitation in the OER current flow [71]. Corrosion due to the high applied potential is not the only problem, but another limiting factor arises from the O_2 bubble formation in presence of a persistent OER current. It has been proved that, in case of slow detachment from the electrode surface, they can cap up to 90% of the surface sites, leading to a considerable efficiency decrease [64]. Furthermore, in porous materials the process of bubble formation can increase O_2 pressure inside the pores, causing material delamination at the bubble detachment site [61], [64]. Recently, different studies reveal that in the case of NiFe nanoalloys the OER activity is not proportional to the Ni content and the number of $Ni(OH)_2$ redox active sites, but to the system capability to incorporate and release Fe atoms during the recovery/degradation stages [39]. Therefore, in order to maximize the OER activity and stability, during electrochemical operation it is necessary that the electrode is able to dynamically release and/or incorporate Fe atoms from the electrolyte by means of interaction with its Ni (oxy)hydroxide constitutive phases. [67]. Even though the presence of Fe doping in Ni catalysts is commonly believed to be beneficial in the OER catalysis, the effects of its leaching and redeposition are still controversial in literature. For instance Zhou et al [69] revealed that an improved stability is not associated with Fe absorption on the electrode surface from the electrolyte, but rather on an enhanced Fe leaching from the electrode, that allows the Ni oxy-hydroxide phases to reconstruct and form a protective coating. A similar mechanism has been proposed also for various perovskite electrocatalysts. Their high activity is linked to the fact that they easy dissolve in water and oxyhydroxide species with a high number of undercoordinated sites form on the electrode surface and can effectively

interact with the electrolyte. [203] It is evident that the determination of the mechanism at the basis of the high OER activity of NiFe alloys and their stability deserves further investigation.

Here we investigate the electric response of NiFe catalysts deposited by supersonic cluster beam deposition (SCBD) (more information in chapter 5.4 and [204]) upon the extensive application of electrochemical OER cycles. Although severely damaged, the electrodes exhibited unexpected resilience in promoting OER.

This study revealed new insights into the OER mechanism, highlighting the importance of dissolution/redeposition of the metal oxide phases generated upon electrochemical cycling.

6.3 Materials and methods

6.3.1 Synthesis of NiFe thin films

The electrode consists of a NiFe film deposited by Supersonic Cluster Beam Deposition (SCBD) onto an Indium-Tin oxide (ITO) coated glass substrate, similarly to what reported in chapter 5.4 and [204]. In the SCBD technique, carried out at 10^{-6} mbar base pressure, a He gas injection synchronized with a discharge generates a plasma ablating plume, which ablates some atomic clusters from a metal rod, which then condensate into nanoparticles that are ballistically deposited on the substrate. The nanoparticle aggregation results in the formation of a nanogranular film, whose mass loading is monitored *in-situ* by

a quartz microbalance. SCBD has been previously employed to synthesize nanogranular films with a large variety of elements [205], [206], [207].

In this work, electrodes composed by an ITO substrate covered by a 35±3 nm thick film of NiFe alloy (90%/10% weight fraction) have been considered, corresponding to 12±1 μg/cm^2 mass loading. The morphological and chemical characterization of freshly deposited NiFe films is reported in chapter 5.4 and [204].

6.3.2 Characterization

6.3.2.1 Atomic Force Microscopy (AFM)

The film thickness was estimated by acquiring an AFM image at the film boundary and evaluating the height with respect to the ITO substrate, as reported in chapter 5.4 and [204]. The image was obtained by a Park NX10 instrument with a PPP-NCSTR tip (Nanosensor, resonance frequency 120-250 Hz, nominal tip radius 10nm) in tapping mode and a resolution of 0.25 pixels/nm.

6.3.2.2 Electrochemical tests

The NiFe film has been employed as electrode for the oxygen evolution reaction (OER) catalysis inside a three-electrode cell using a 1 M KOH solution as electrolyte, with a platinum counter electrode and a saturated calomel reference electrode (SCE). The electrochemical measurements were performed by a Frequency analyzer equipped PGZ402

Potentiostat from Voltalab (Radiometer Analytical). Before the OER activity tests, the stability of the electrochemical setup was checked by measuring the open circuit potential for 4 minutes and impedance was measured in the 600 Hz - 80 kHz frequency range.

To evaluate the film catalytic efficiency, different types of various cyclovoltammetry (CV) cycles were performed, where the current was measured as a function of the applied potential ($V_{measured}$) and normalized by the electrode's geometrical surface (current density= j mA/cm^2). The resulting current density/potential (j/V) curves were referred to the reversible hydrogen electrode (RHE) and IR compensated according to:

$$V = V_{measured} - IR \tag{6-1}$$

where R is the electrochemical cell resistance measured at 80 kHz, typically in the range 10-20 Ω, and I is the current flowing in the cell.

First, a 2 CV cycle were recorded in the 0.57 – 2.27 V (vs RHE) potential range with a scan rate of 10 mV/s to determine the initial OER catalytic efficiency. The overpotential η at 10 mA/cm^2 or 5 mA/cm^2 was calculated directly from the j/V curves as the voltage necessary to obtain that current exceeding the thermodynamic value of 1.23 V (vs RHE). Where specified in the text, in case the measured current did not reach the reference current of 5 or 10 mA/cm^2, the overpotential was extrapolated from experimental data through an exponential fit, as showed in section 6.6.1.
The electrochemical surface area normalized by the electrode geometrical surface (ECSA/S), also referred to as roughness factor, was computed by integrating the area A_{red+ox} enclosed between the forward and backward j/V curves in the 0.5-1.8 V (RHE)

range, in correspondence of the $Ni(OH)_2$ redox peaks, and normalizing the result according to:

$$ECSA/S = \frac{A_{red+ox}}{2v\sigma} \tag{6-2}$$

where v is the scan rate and $\sigma = 514\ \mu C/cm^2$ is the $Ni(OH)_2$ charge surface density [195]. The factor ½ was included since each active site contributes to A_{red+ox} both in the reduction and oxidation peaks (further details in section 6.6.1).

A linear sweep voltammetry (LSV) was also performed by scanning the potential from -0.59 to 2.4 V (vs RHE) at 1 mV/s. The LSV curve was reported in a η - log(j) plot (Tafel plot), whose slope was identified as the Tafel slope (reported in section 6.6.1).

The efficiency of the electrode for oxygen evolution was evaluated by measuring *in situ* the oxygen produced and dissolved in the electrolyte during the application of a fixed potential of 1.86 V vs RHE for 50 min. This measurement was performed spectroscopically, by a Fox-Ocean Optics device. More information on the calibration of the device is available in supplementary section 6.6.1**.**

A 96h chronoamperometry (CA) test was performed on the electrode by measuring the current density while applying a constant potential of 1.6 V (vs RHE). Before, after 24h and at the end of this test, an impedance measurement followed by a CV cycle in the 0.57-2.4 V range were acquired to evaluate the variations of the value of overpotential η at 10 mA/cm^2 or 5 mA/cm^2, because of electrochemical work. In the CV acquisitions carried out after 24h, the CA test was interrupted without altering the electrochemical cell setup and it was restarted thereafter with the same settings as before.

Further sets of 2000 CV cycles were conducted using the same NiFe electrode considering the same potential range described before, increasing the potential scan rate up to 100 mV/s, to evaluate the electrode stability under continuous operation. In order to acquire more insights about the working mechanism of the electrode for prolonged times, comparisons were performed in relation to only ITO electrodes, or NiFe electrode, suspended in new fresh KOH electrolyte or electrolyte which has been previously in contact with other NiFe electrodes, under electrochemical work. For each set of CV acquisitions, the overpotential and the roughness factor, extrapolated from the j/V curves as discussed above and in section 6.6.1, were calculated as a function of the cycle number. Further electrochemical parameters, such as TOF and overpotentials at different current values, are reported in supplementary section 6.6.1 to provide a direct comparison to other references.

6.3.2.3 XPS

The electrodes were characterized by X-ray photoelectron spectroscopy using an Al X-ray source (1253.6 eV incident photon energy) and a Phoibos 100 Specs analyzer at 20 eV pass energy. Measurements were performed before and after the stability tests (2000 CV cysles).

6.3.2.4 MicroRaman Spectroscopy

Raman μ-spectroscopy was carried out using a LabRam HR-800 (HORIBA-JY) spectrometer equipped with a 632.8 nm laser. All the spectra were obtained with a 30 s laser exposure focalized by a 50X microscope objective.

6.3.2.5 Electron Microscopy

Scanning Electron Microscopy was carried out on the NiFe electrodes before and after the electrochemical stability tests.

Transmission Electron Microscopy was carried on solid residues recovered from the electrolyte after the electrochemical stability tests.

6.4 Results and discussions

In this work we investigated NiFe nanoalloys (90%/10% alloy fraction) deposited by Supersonic Cluster Beam Deposition (SCBD) in form of nanogranular films onto indium tin oxide (ITO) conductive substrates (Figure 6-1a-b), using the same protocol utilized for analogous samples of our previous work (chapter 5.4 and [204]). The resulting electrode consisted in a porous film, with 35 ± 3 nm thickness and $12 \pm 1\ \mu g/cm^2$ mass loading, characterized by a 20% porosity, composed of very small nanoparticles (0.3-2.8 nm), which agglomerated in 5-20 nm clusters as shown in the SEM image in Figure 6-1c, determining a 4.8 ± 0.1 nm roughness [204]. A minor fraction of the film surface (15%)

was covered by 1-3 μm clusters. As a result of the exposure to ambient air, only 37% and 17% of Ni and Fe surface sites were metallic, with a predominant oxide abundancy (38% for Ni and 83% for Fe) coexisting with a 25% of Ni hydroxide phases (see chapter 5.4, [204] and 6.6.1).

Figure 6-1d-e shows the initial electrochemical characterization of the as deposited NiFe electrode working as OER catalyst. The CV curves recorded with a scan rate of 10 mV/s, whose second cycle is shown in Figure 6-1d**,** were in accordance with the data previously reported in ref [204] and were characterized by a flat region below 1.3 V, followed by oxidation/reduction peaks centered at 1.45 and 1.36 V vs RHE in the forward and backward scan, associated to the Ni oxyhydroxidation process [194]:

$$Ni(OH)_2 + OH^- \leftrightarrow NiOOH + H_2O + e^- \tag{6-3}$$

For potentials higher than 1.5 V vs RHE the j/V curve increased exponentially, reaching a value of 19 mA/cm^2. This region corresponds to the oxygen evolution reaction (OER):

$$4OH^- \rightarrow 2H_2O + O_2 + 4e^- \tag{6-4}$$

The NiFe film catalytic efficiency can be quantified by the overpotential at 10 mA/cm^2 or at 5 mA/cm^2, resulting in $\eta_{10\ mA/cm^2} = 380 \pm 10\ mV$ and $\eta_{5\ mA/cm^2} = 365 \pm 10\ mV$, also in accordance to what reported in our previous work related to the general characterization NiFe SCBD films of various thickness in [204]. Furthermore, a Tafel slope of $50 \pm 10\ mV/dec$ was determined from the LSV acquisition as reported in section 6.6.1.

The occurrence of the reaction was confirmed through an in-situ spectroscopical measurement of the O_2 dissolved in solution, as reported in Figure 6-1e. A constant potential of 1.59 V vs RHE was applied to the NiFe electrode for 50 minutes while monitoring the current flowing in the cell and measuring the O_2 dissolved in the solution through a specific optical sensor. From an electrochemical point of view, the electrode demonstrated a good stability during OER operation at constant applied potential: a 10% drop in the current density occured in the first 5 minutes passing from 10 to 9 mA/cm^2, followed by a more stable behavior with just a further 5% decrease in the following 45 minutes. In the electrolyte solution, initially depleted of oxygen, the O_2 content showed a rapid increase in the first 20 minutes, confirming that hydroxyl ions of the electrolyte were effectively oxidized at a potential higher than 1.5 V vs RHE. The oxygen concentration was characterized by a nonlinear growth, that could be ascribed to the oxygen exchange with the surrounding atmosphere. At the end of the test, the concentration of O_2 dissolved in solution tended to stabilize around 19 mg/L, with a constant OER current of 8 mA/cm^2 flowing in the cell. We associate this stabilization to the balance between the O_2 generation at the electrode surface and the O_2 release in the surrounding environment. An OER faradaic yield $FY = 80 \pm 20\ \%$ was calculated by considering the measured oxygen concentration and the charge flowing through the cell in the first 1 minute of the test (as described in equation (6-11)). Such large uncertainty on the calculation is associated with the oscillation of the dissolved O_2 concentration in the first minutes of experiment, that might be due to the formation of bubbles at the electrode surface and can also imply an underestimation of the FY.

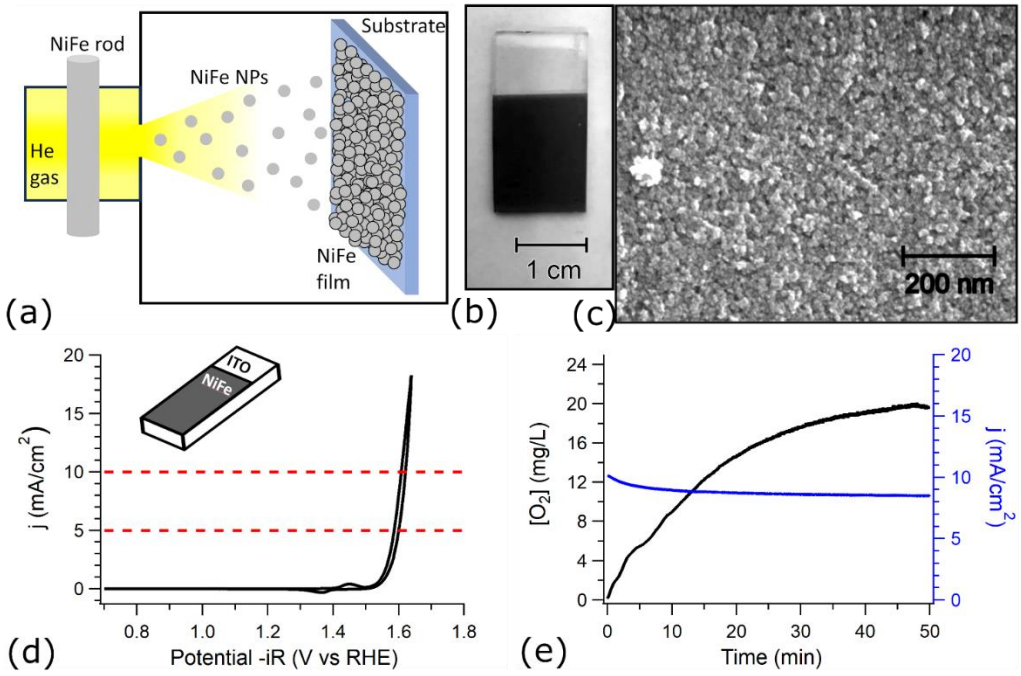

Figure 6-1. (a) The SCBD synthesis of nanogranular NiFe films. (b) Picture of an electrode in which the ITO transparent conductive substrate (visible in the top region) was coated by a 38 nm thick NiFe film. (c) SEM image of the NiFe film nanogranular surface. (d) representative CV curve of the fresh NiFe electrode recorded at 10 mV/s, used to compute the overpotential at 10 mA/cm^2 and 5 mA/cm^2 (e). In situ measurement of $\boldsymbol{O_2}$ content in the electrolyte while applying a constant potential of 1.59 V vs RHE and monitoring the current flowing through the electrode.

The behavior of the prepared NiFe under electrochemical work for prolonged time was investigated by evaluating the stability of its performances and the variation of its structural and chemical properties. Initially, the stability of the sustained current density under constant applied potential was studied for a fresh NiFe electrode through a 96 hours chronoamperometry (CA) test at the fixed potential value of 1.6 V vs RHE. This electrochemical characterization was combined with cyclic voltammetry, recording 2 CV cycles before the CA test, after 24 hours of CA and at the end of the 96 hours (scheme in Figure 6-2a). During the CA test the current density decreases of ~48% during the considered period, passing from 13.5 mA/cm^2 to 7 mA/cm^2 after 96 h, as reported in

Figure 6-2b. The trend can be approximately considered linear, with a decrease rate of 0.06 $mA\ cm^{-2}h^{-1}$.

Figure 6-2c shows the 2nd CV cycle at each time interval. These results enable to evaluate the variation of the overpotential at 10 mA/cm^2 because of the prolonged electrochemical activity and stay at high potential. The initial value of 380±10 mV increased to 390±10 mV after the electrode was biased at 1.6 V vs RHE for 24 hours and a further increase up to 490±20 mV was recorded after 96 hours of potential bias. Generally, a catalyst with an overpotential at 10 mA/cm^2 in the range of 300–400 mV is considered an excellent catalyst for OER process, and the fact that the overpotential of this type of NiFe electrode maintained in this range after 24 hours of operation is very promising. The overpotential increases at low rate not only in the first 24 hours (0.4 mV/h), but also in the following period, reaching a value of only 1.1 mV/h over 96 hours. Using the classification proposed in ref [32], even after 96h of activity the NiFe electrode can be considered a good catalyst for OER. [18]. The electrode efficiency, quantified as the overpotential and its evolution under continuous working conditions, is in line with typical transition metal based electrodes, as shown in Figure 1-2 (from [16]). From Figure 6-2b it is possible to notice that after the CV measurements performed on the same electrode after 24 hours of bias at 1.6 V vs RHE, there was an apparent increase of the current density, suggesting an improvement of the electrochemical activity of the electrode in the following 2 hours. Even if this effect, resulting in a spike of 10% in the current density was only temporary and did not affect the overall linearly decreasing trend of the current density, it suggested the possibility that under intermittent and cyclic electrochemical work a recovery process could take place.

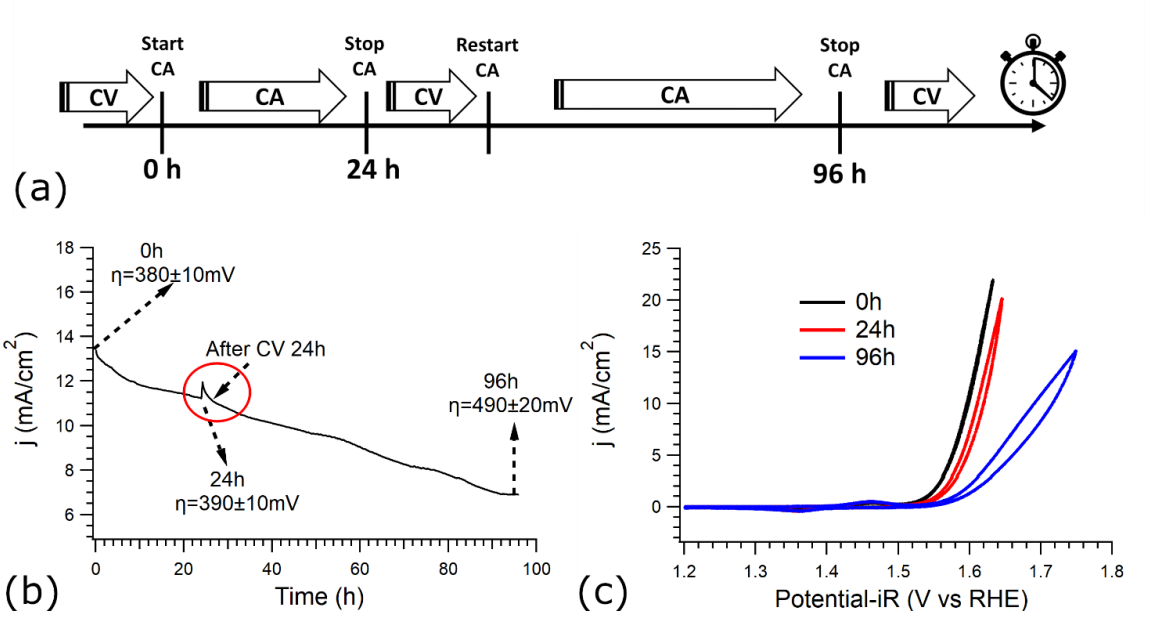

Figure 6-2. Scheme of the chronoamperometry-cyclovoltammetry (CA/CV) combined tests (a); 96 h chronoamperometry test at 1.6 V (vs RHE) applied voltage (b). The three values for the overpotential at 10 mA/cm^2 are obtained from CV curves reported in (c), performed at the beginning, after 24 h and at the end of the CA test. The CA restarting point after 24 h is highlighted by a red circle. See the main text for details.

In order to verify this possibility, NiFe electrodes were subjected to prolonged CV tests, as illustrated in Figure 6-3. A freshly deposited electrode underwent 2000 cycles (performed with a fast potential scan rate of 100 mV/s) for a total duration of 22 hours. In Figure 6-3a, some selected CV cycles are reported to illustrate the variation of the electrochemical properties during operation.

The most evident variation concerns the maximum OER current density measured at 2.0 V vs RHE, which decreased from 16 to 6 mA/cm^2 within the first 1000 cycles, when it set on a stable value. The decrease occurred very quickly in the first 400 cycles, getting slower in the next 600 cycles, and reaching the equilibrium value of 6 mA/cm^2 after ~ 10

hours of operation (~1000 cycles). In the next 1000 CV cycles no significant variations were measured.

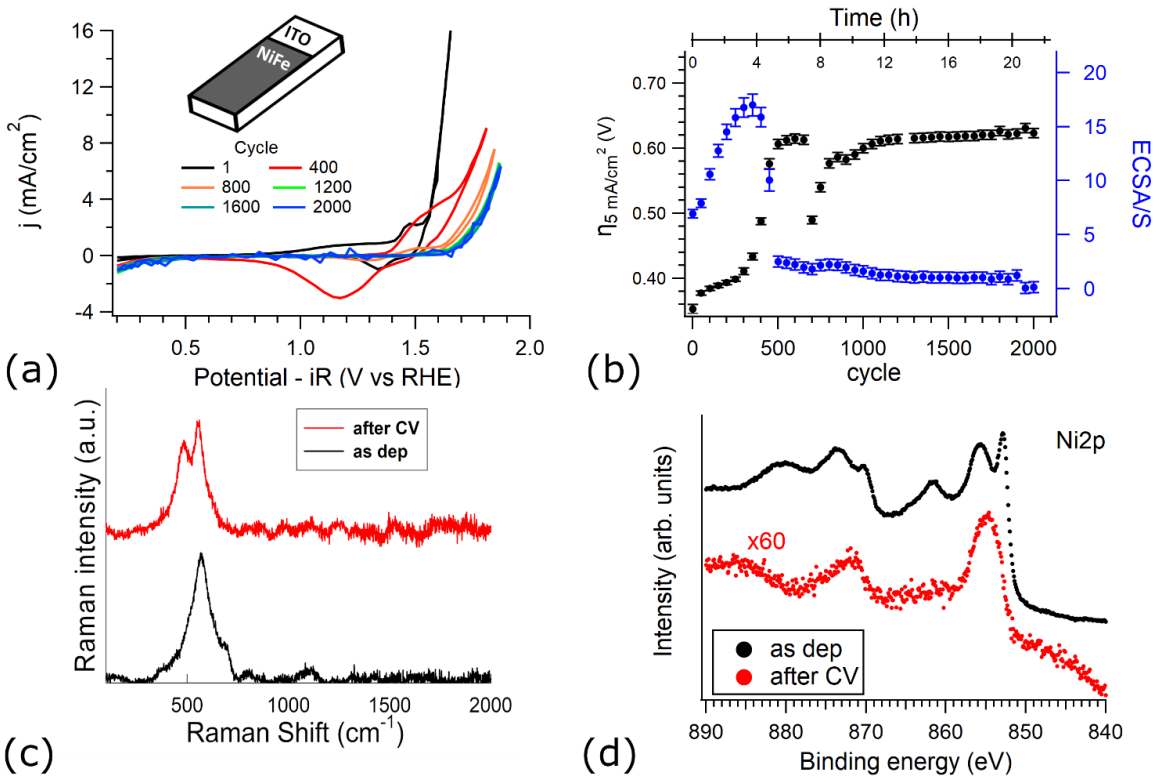

Figure 6-3. Stability assessment of the freshly deposited NiFe electrode. Selected CV curves (extrapolated from a 2000 cycles test) (a) and corresponding values of overpotential at 5 mA/cm^2 and roughness factor (ECSA/S) (b); Raman spectra of NiFe before and after 2000 CV cycles (c); XPS analysis of the NiFe electrode before and after 2000 CV cycles (d).

Other evident modifications concern the $Ni(OH)_2$ redox peaks. At the beginning, in presence of a fresh electrode, only small Ni redox features were visible, indicating that only a small portion of the film was oxidized and reduced. Over cycling, the size of the redox features increased suggesting that more metallic Ni was oxidized to Ni^{2+} or Ni^{3+}. Furthermore, during the first 400 CV cycles the oxidation peak became progressively

broader and shifted to higher potential, while the reduction peak became broader and moved towards lower potential. These data suggest that the kinetic of the reactions became more sluggish over cycling: there was a progressive conversion of the Ni species into oxy-hydroxides whose redox processes occurred with more difficulty. Interestingly, further increase of the number of cycles did not lead to the retention of the same trend and behavior, but, at the opposite, there was a gradual disappearance of the $Ni(OH)_2$ redox peaks. This behavior could be correlated to a gradual dissolution of the electrode into the electrolyte or a significant modification of its electrochemical properties. In particular, the simultaneous observation of a decrease of the maximum OER current density could indicate a lowering of the number of catalytic centers remaining on the electrode surface after ~ 400 CV cycles. Surprisingly, the OER current density did not go to zero over full cycling, but settled on an equilibrium value after 1000 CV cycles. Even after the complete disappearance of the redox peaks proper of $Ni(OH)_2$, the system was still able to preserve an OER activity, with a limited lowering of the OER current density.

The data recorded during CV measurements were furtherly elaborated to calculate the overpotential needed to achieve a current density of 5 mA/cm^2 and the roughness factor (ECSA/S). Their variation over cycling is reported in Figure 6-3b.

The overpotential at 5 mA/cm^2 showed an increase from 365 to 600 mV during the first 500 cycles, followed by an oscillation in the 500-600 mV range between 500 and 1000 cycles. A very high stability was then reached after 10 hours (1000 cycles), with a constant overpotential of 610 mV. This trend is in line with that reported for the maximum OER current density.

As regards the roughness factor (ECSA/S) a different trend was observed, meanly because it was calculated following equation (6-2), by integrating the redox peaks associated to the $Ni(OH)_2$ oxidation process (6-3). As a consequence, the evolution trend of its value was less regular over time and the number of cycles: it increased at the beginning of the test, reaching its maximum after 300 cycles, and subsequently it underwent to a remarkable fast decrease down to a constant value, reached around the 500th cycle and maintained for the next 1500 cycles. In the first 300 cycles, the roughness factor gradually increased, passing from 7 to 17, suggesting that not only the surface Ni species were involved in the redox process but also the internal layers. This bulk reactivity was also observed in our previous work related to freshly deposited NiFe electrodes, where the air exposure resulted in a partial oxidation/hydroxidation across the film depth (see chapter 5.4 and [204]). Interestingly, this progressive increase of the amount of NiOOH resulted in a slow decrease in OER efficiency, with the overpotential at 5 mA/cm^2 increasing from 365 to only 410 mV, suggesting that Ni sites (or, at least, not all of them) were not directly involved in catalyzing OER [39]. Afterwards, between 300 and 500 cycles, the ECSA/S showed a rapid drop from 17 to 1, which we ascribed to a mechanical exfoliation of the film from the ITO substrate corresponding to a material transfer from the electrode to the electrolyte. This is also supported by a very fast overpotential increase and by a considerable increase of the electrode transparency. Then, after some oscillations between 600 and 1000 cycles, the roughness factor stabilizes to 1. This value could be overestimated since a part of the area enclosed by the j/V curve can be determined by the charge/discharge of the double layer at the electrode surface. However, the ratio between this constant final value and its maximum at 300 cycles suggest that no more than 6% of the initial mass

loading remained over the electrode after the exfoliation, corresponding to 700 ng/cm^2 and 2 nm equivalent film thickness. The exfoliation process, together with the evolution of the nanogranular morphology and chemical composition of the film was characterized in detail in the first stages of the CV test in supplementary 6.6.7.

To verify the permanence of a small portion of the original NiFe NPs on the electrode surface, we investigated it through Scanning Electron Microscopy (SEM), X-ray Photoelectron Spectroscopy (XPS) and Raman Spectroscopy. Unfortunately, SEM analysis (data not shown) did not enable a satisfactory morphological analysis: the detection of residual NPs at the end of 2000 CV cycles was complicated by the elevated roughness of the ITO substrate, and its granular morphology, which could mask the presence of rare small NPs. Additional EDX (Energy dispersive X-ray) analysis did not allow the detection of Fe and Ni signals, suggesting that their concentration was below the detection limit of the technique.

At the opposite, the presence of residual NiFe NPs was demonstrated through Raman Spectroscopy and XPS, whose results are summarized in Figure 6-3c-d. Similarly to what reported in chapter 5.4 and [204], the most representative Raman feature of the as deposited NiFe electrode was a peak centered in the 560-570 cm^{-1} region, that can be associated to Ni-O or Ni-OOH stretching modes (Figure 6-3c). Additionally, in some regions of the electrode, a peak centered at 680 cm^{-1} (compatible with alpha phase of FeOOH) was visible. The detection of this peak was more sporadic since it is intrinsically characterized by a lower intensity and because of the lower concentration of Fe in comparison to Ni. It is notable that after 2000 cycles, the peak at 560 cm^{-1} was still present in the Raman spectra recorded in different areas of the electrode, confirming the presence

of Ni material on its surface. Generally, in the absence of deposited Fe atoms, the modes associated to Ni-O bond are settled to slightly lower value of Raman Shift (~530 cm^{-1} for pure $Ni(OH)_2$ and 550 for for pure NiOOH), while the codeposition of Fe leads to a small shift to higher value [26], [59], [208]. This observation can indirectly confirm the presence of Fe atoms on the electrode surface, suggesting a uniform but not complete, leaching of both Ni and Fe. Finally, in the case of worked electrode a new mode at 480 cm^{-1} appeared, corresponding to the NiOOH bending mode, suggesting a higher oxidation state of the electrode.

The XPS analysis enabled to confirm the retention of a fraction of NiFe NPs on the electrode surface. The spectra (Figure 6-3d and Figure 6-11 in supplementary 6.6.2) acquired after the 2000 CV cycles can be compared to the ones obtained for a freshly deposited electrode and a bare ITO substrate.
As shown in chapter 5.4 and [204], the freshly deposited electrode presented peaks due to mostly oxidized and hydroxidized Ni and Fe species, with just 37% and 17% metal phases, respectively. No signal deriving from the underlying ITO substrate were detected. Interestingly, after the prolonged CV stability test, even if the peaks were characterized by a lower intensity, as a result of the exfoliation process, they were still visible, confirming the presence of active material on the electrode surface.

The most significant spectrum is that of Ni2p, shown in Figure 6-3d, with a comparison between the before- and after-CV conditions. The initial peak corresponded to a mix of metal (centered at 853 eV), oxide and hydroxide phases (in the 854- 863 eV range) [204]. After the prolonged activity, the spectrum showed a broad peak centered at 855 eV,

whose area is 60 times reduced with respect to the fresh electrode and whose shape was completely compatible with a +2 oxidation state corresponding to oxide/hydroxide phases.

As discussed in 6.6.2, instead, the Fe 2p and O1s spectra were not relevant for the characterization of electrode after cycling, since Ni and Fe oxy-hydroxides contribute for less than 2% to the O1s spectrum and the Fe2p contribution was overwhelmed by a much more intense Sn3p signal. During the characterization of this worked electrode, in fact, the In and Sn peaks were also detected, proving that the NiFe material loss significantly reduced the film thickness with a possible exposure of the substrate to the electrolyte. Both In and Sn detected signals perfectly matched the spectra of a bare substrate (Figure 6-11c-d), confirming that ITO was not altered by the electrochemical treatment.

The amount of NiFe remaining on the electrode surface after the CV cycles was estimated through the Ni2p peak area and the equations (6-14)-(6-16) proposed in chapter 6.6.2. The calculated mass loading of the Ni + Fe atomic species was $80 \pm 10\ ng/cm^2$, compatible with the upper bound of 700 ng/cm^2 estimated from the ECSA data reported in Figure 6-3b. This mass loading value, in the assumption of a completely hydroxidized state after CV, results in a $126 \pm 16\ ng/cm^2$ mass loading of NiFe hydroxide molecules. The implication of these results on the electrode final morphology after the CV test can be discussed in two representative cases: 1) assuming the nanogranular morphology is retained after the test or 2) assuming the NiFe material is rearranging in a hydroxide uniform coating of the electrode (see chapter 6.6.3 for details). In the former case, a concentration of $1.3 \cdot 10^4$ nanoparticles/μm^2 on the electrode surface was calculated from the mass loading (equation (6-19)). Considering 2.8 nm as the average nanoparticle size as reported in chapter 5.4 [204], this implies that only the 11% of the surface would be covered

by NiFe nanostructures after CV (equation (6-21)). Conversely, in the assumption of a uniform hydroxide coating, the hydroxide mass loading value calculated from the XPS spectra ($126 \pm 16\, ng/cm^2$), matches the theoretical value calculated for an ideal single hydroxide monolayer coating of the electrode ($139\, ng/cm^2$, computed in equation (6-26)). This suggests that the CV operation not only determines the NiFe dissolution in the electrolyte, but might also induce the rearrangement of the active species morphology at the electrode surface, with crucial implications on the OER behavior.

As discussed in [39] for electrodeposited NiFe electrodes, the evolution of their electrochemical behavior under prolonged OER test can be affected by the Ni and Fe concentrations in the electrolyte. In particular, it was revealed that the electrochemical activity of the NiFe electrode can be controlled through the instauration of an equilibrium between material leaching-when the electrode was biased at high potential and the OER occurred-and incorporation of active species from the electrolyte at the catalyst/solution interface-when the electrode was biased at low potential, below the reduction peak. In [39] an intermittent stability test, in which the OER activity was alternated with a recovery period at low potential (anodization step), was performed on electrodeposited NiFe electrodes in purified (16.43 and 0.45 $\mu mol\ L^{-1}$ Ni and Fe concentrations) and unpurified (0.3 and 1.38 $\mu mol\ L^{-1}$) electrolytes. A high stability and even a slight increase of the OER efficiency was achieved in the unpurified solution, suggesting that the application of low potential in these conditions enables a Fe progressive incorporation at the electrode surface from the electrolyte.

During our experiments we decided to use as electrolyte a solution of KOH 1 M that was not previously purified from Fe and Ni to better reproduce the working conditions

of conventional electrolyzers. Assuming that nearly all the NiFe mass was transferred from the electrode to the solution after 500 cycles, it is possible to estimate the Ni and Fe concentrations in the electrolyte. It should be ~7 ± 3 and 0.8 ± 0.3 $\mu mol\ L^{-1}$, respectively (equations (6-28)). Even if these concentrations are comparable to those previously reported in literature for both purified and unpurified KOH electrolyte, thanks to the TEM analysis performed on the electrolyte collected at the end of 2000 CV cycles, we have the confirmation of the presence of some nanoparticles (Figure 6-4a-b and supplementary Figure 6-13). Their morphology was highly irregular, and it was possible to recognize both nanometric amorphous structures (Figure 6-4a) and amorphous micrometric aggregates (Figure 6-4b).

To further investigate the electrochemical behavior of the NiFe electrodes for prolonged time and the possible establishment of a dynamic equilibrium between dissolution and exfoliation of NiFe NPs from the electrode surface and their re-adsorption, we performed analogous CV stability tests on bare ITO substrates using different electrolytes. In one case we used as electrolyte a freshly prepared KOH 1M solution, in the other case we used as electrolyte a KOH 1 M solution, where the Ni and Fe leaching process had previously taken place during 2000 CV cycles using as working electrode a NiFe film (re-used electrolyte). As shown in Figure 6-4c and Figure 6-4d (and Figure 6-10–supplementary) when the ITO substrate was submerged into a fresh KOH solution, its electrochemical response was poor and constant along the duration of the test, with a current density never exceeding 0.5 mA/cm^2, which is ~1/30 of the maximum current density measured in the first CV cycle for a NiFe electrode and ~ 1/12 of the maximum current density measured in the 2000th CV cycle for the same NiFe electrode. These data

are a confirmation of the fact that bare ITO electrodes were not good electrocatalysts for OER, but they also demonstrate that NiFe electrode after electrochemical cycling was significantly different from a bare ITO substrate, suggesting that even after 2000 CV cycles some NiFe NPs still covered the electrode surface. The performance of bare ITO electrode was worst also in terms of overpotential, since it was higher than 1.1 V at 5 mA/cm^2 (extrapolated from raw data as described in 6.6.1 below and shown Figure 6-10). Conversely, when a re-used electrolyte was employed, we observed a lowering of the overpotential to 0.9 V in the first CV cycle, and a significant increase of the OER current density (it was 4 times higher). These data suggest the presence of a fraction of Ni/Fe species in the electrolyte, available for interaction and adsorption on the electrode (ITO) surface. Furthermore, in the first 300 cycles an increase in the electrochemical efficiency was observed: the current density significantly and constantly increased (for a factor of ~4) and the overpotential @ 5 mA/cm^2 decreased to reach a value of 0.720 V vs RHE. Interestingly, after 300 CV cycles a constant behavior was obtained, with no variations of the electrochemical performances within the following 1700 CV cycles.

These results show that we are in presence of dynamic systems whose functioning is based on the instauration of an equilibrium between the electrode surface and chemical species dissolved and/or suspended inside the electrolyte, trough adsorption processes.

Even though the Ni and Fe content in the re-used electrolyte was very small, these contaminants can affect significantly the OER efficiency of a NiFe free electrode, such a bare ITO substrate.

In this framework, a further evaluation is needed to determine whether the high stability of our NiFe electrode achieved in the 2000 CV test (Figure 6-3a-d) was caused by

a phenomenon of re-adsorption of NiFe NPs from the electrolyte. Therefore, after the 2000 CV test the used NiFe electrode was transferred into a new freshly prepared 1M KOH electrolyte, and a new set of 2000 cycles was acquired (Figure 6-4e-f). The j/V curves were initially characterized by a 50% lower value of current density with respect to the end of the previous 2000 cycles CV experiment. However, after a rapid increase of the efficiency, the electrode stabilized, recovering completely the overpotential and current values found at the end of the previous stability test. Interestingly the measured values were significantly higher (+180%) than the data obtained in the case of bare ITO substrate, indicating the important role of NiFe residues on the used electrode. The variation of the value of overpotential (Figure 6-4f) at 5 mA/cm^2 during the 2000 CV cycles shows a similar trend: initially the substitution of the electrolyte with a new fresh solution led to an increase of the overpotential up to 710 mV vs RHE, but it lowered in the following cycles. The behavior was not perfectly regular, since in first 400 cycles a lowering of the overpotential @5 mA/cm^2 down to 570 mV was observed, followed by a slow increase to recover the value of 610 mV after 1500 cycles, in perfect agreement to the steady value measured in the last 1000 CV cycles of the previous test. The trend of the ECSA/S shows a very similar behavior: a maximum value of 3 was measured in correspondence with the minimum of the overpotential, suggesting an electrode activation process, followed by a stabilization around 1, in agreement with the low mass loading left over the electrode occurred during the previous tests.

These results suggest that the efficiency of our electrodes and their capability to catalyze the OER for very long period were the result of a dynamic equilibrium between the electrode surface and the chemical species inside the electrolyte. Under electrochemical

work the NiFe electrode underwent a significant variation of its chemical composition, mainly through oxidation and dissolution, and morphology. An exfoliation process occurred, a significant portion of the electrode detached from its surface, leading to an electrolyte rich of NPs that could be re-adsorbed on the electrode surface during further use. In this way, a very stable configuration and system was achieved. Furthermore, the exfoliation process could lead to a catalyst that continuously expose pristine surface, with free active sites, available for the interaction and adsorption of OH^- ions from the electrolyte.

Furthermore, the set of experiments presented here suggest that the OER stability, achieved through the electrode/electrolyte dynamic exchange, depends on the initial catalyst composition. In particular, as shown by comparing Figure 6-3b and Figure 6-4d, the efficiency of an electrode preloaded with SCBD NPs is higher than a bare ITO substrate exposed to the same NiFe rich electrolyte. Moreover, after the electrode stabilization is achieved, the OER efficiency of the steady state electrode becomes independent of the electrolyte, as suggested by the constant catalytic properties upon CV cycling in a refreshed electrolyte (Figure 6-3f).

Even if the exact mechanism at the basis of NiFe electrocatalysis for OER is under debate, one of the most probable is the surface lattice-OER (LOER) mechanism, based on the evolution of O_2 through the combination of O atoms deriving from the electrolyte with O atoms deriving from the catalyst lattice. [209] Usually, only the 3% of O atoms of the catalyst can be effectively employed in this process, but the dissolution process we observed could help in the exposition of a higher number of oxidized sites from the catalyst.

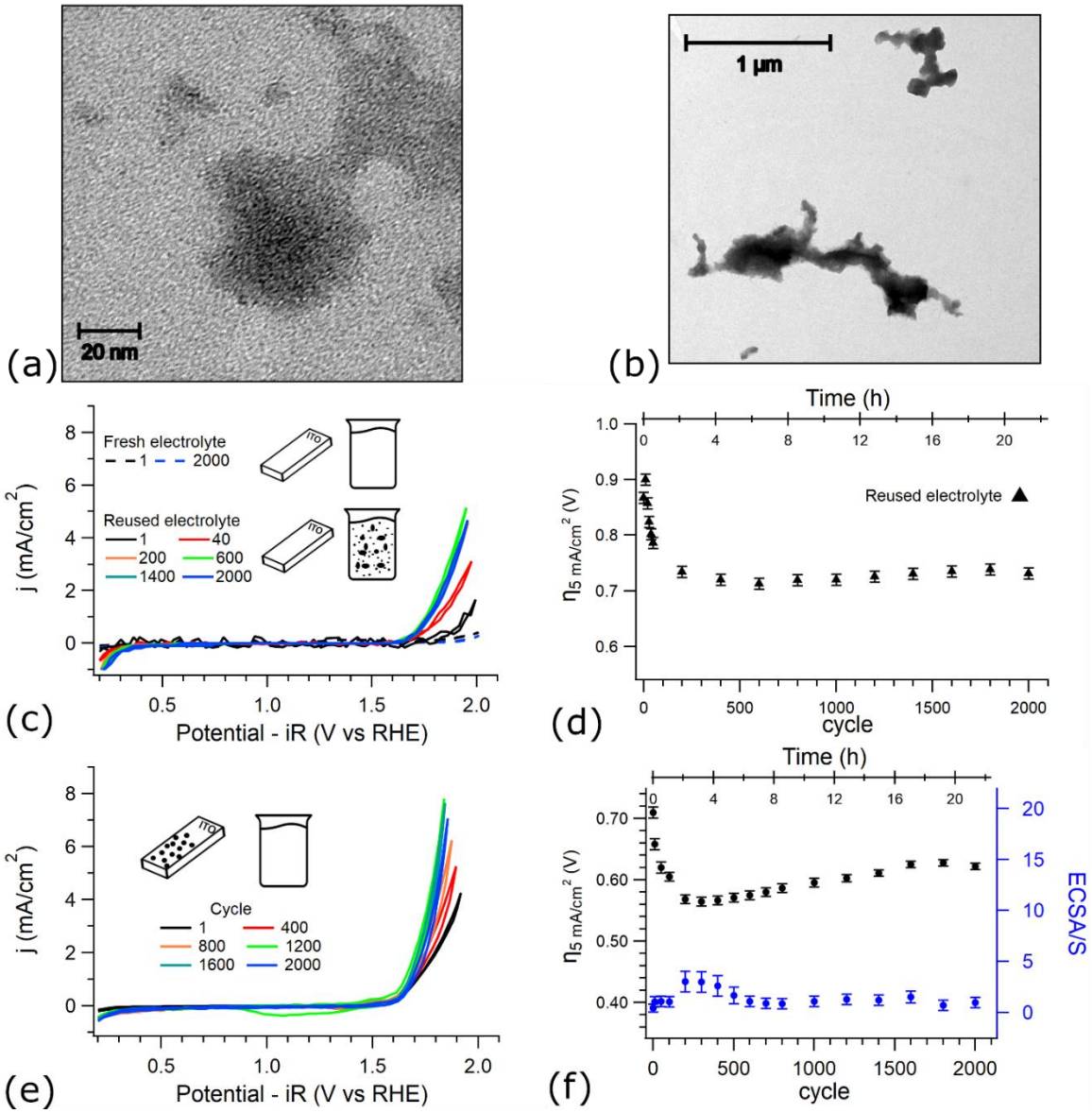

Figure 6-4. TEM images of NiFe nanostructures dissolved in KOH electrolyte after the 2000 cycles stability test performed with a freshly deposited NiFe film as working electrode (experiment in figure 3a-b). Various structures at the nanometer (a) and micrometer (b) scale are shown. Stability tests (2000 cycles) (c) and associated overpotential (d) for bare ITO substrates in a fresh electrolyte or in a reused electrolyte (electrolyte obtained from the NiFe stability test containing the NiFe exfoliated structures). Stability test (2000 cycles) (e) and associated overpotential and ECSA/S (f) carried out in a fresh electrolyte on a reused NiFe electrode after exfoliation.

6.5 Conclusions

In conclusion, the overall electrochemical characterization demonstrated that, even if a consistent NiFe leaching and chemical transformation of the nanostructures occurred in the first 6 hours of activity, the electrode we presented reached a remarkable OER efficiency and stability under prolonged activity. Despite only a small fraction of the original NiFe NPs remained on the electrode surface, leading to a very low NiFe mass loading on the electrode surface, the electrode was characterized by good electrocatalytic activity towards the OER. After the initial stabilization period, a turnover frequency (calculated from the CV curves, considering a NiFe residual mass loading of $80 \pm 10\ ng/cm^2$ as reported in (6-15)) of $0.3 \pm 0.1\ s^{-1}$was achieved at 350 mV overpotential, paving the way to the development of ultrathin electrode based on the same NiFe nanostructures. In fact, considering the final low NiFe coverage on the electrode surface, this value can be considered representative of an individual nanoparticle efficiency.

6.6 Supplementary information

6.6.1 Electrochemical analysis

6.6.1.1 Overpotential calculation

The overpotential η at 5 or 10 mA/cm^2 was calculated directly from the experimental CV curves, according to the following formula:

$$\eta = V - V_0 \tag{6-5}$$

where V is the IR compensated potential (vs RHE) measured experimentally required to reach a value of current density equal to 5 or 10 mA/cm^2 and $V_0 = 1.228\ V$.

In the cases specified explicitly in the main text, when such a reference value for the current density was not reached during the CV test, the j/V curve was fitted through the following formula:

$$j = a \cdot e^{\frac{V}{t}} + y_0 \tag{6-6}$$

where V is the iR corrected potential (vs RHE), a and t are parameters that account for the OER threshold and the current magnitude and y_0 accounts for any possible offset in the instrument. After determining the a, t and y_0 parameters by fitting experimental data, the overpotential can be obtained as:

$$\eta = t \cdot \ln\left(\frac{j - y_0}{a}\right) - 1.228\ V \tag{6-7}$$

where j is either 5 or 10 mA/cm^2.

Figure 6-5 shows an example of such method, in the case of experimental current density lower than 7 mA/cm^2. The exponential fit was used to extrapolate the value of the overpotential at 10 mA/cm^2.

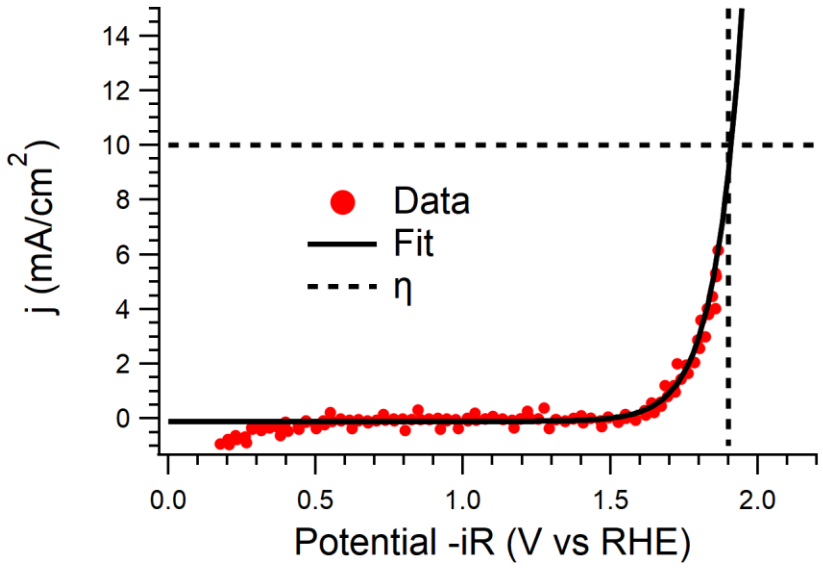

Figure 6-5. CV experimental data and exponential fit to determine the overpotential at 10 mA/cm^2.

6.6.1.2 ECSA calculation

The electrochemical surface area was calculated directly from the experimental CV curves, by integrating the $Ni(OH)_2/NiOOH$ redox peaks. If $j(V)$ is the current density (in mA/cm^2) measured as a function of the applied potential (V), the reduction + oxidation peak area A_{red+ox} in the j/V plot can be obtained as:

$$A_{red+ox} = \int_{V_{min}}^{V_{max}} j^F(V) \cdot dV + \int_{V_{max}}^{V_{min}} j^B(V) \cdot dV \quad (6\text{-}8)$$

where the two integrals, running in the range V_{min} - V_{max}, account separately for the forward and backward part of the CV curve. In this equation no IR correction was considered in order to retain the applied potential/ elapsed time proportionality, allowing to obtain the redox charge (integral of the current in the time domain) as the peak area (integral of the current in the voltage domain). It should be noticed that calculating the sum of the two integrals, rather than each individual part, automatically subtracts the contribution of the OER current. Figure 6-6 shows such calculation for a representative curve, where the colored red background indicates the area calculated through equation (6-8).

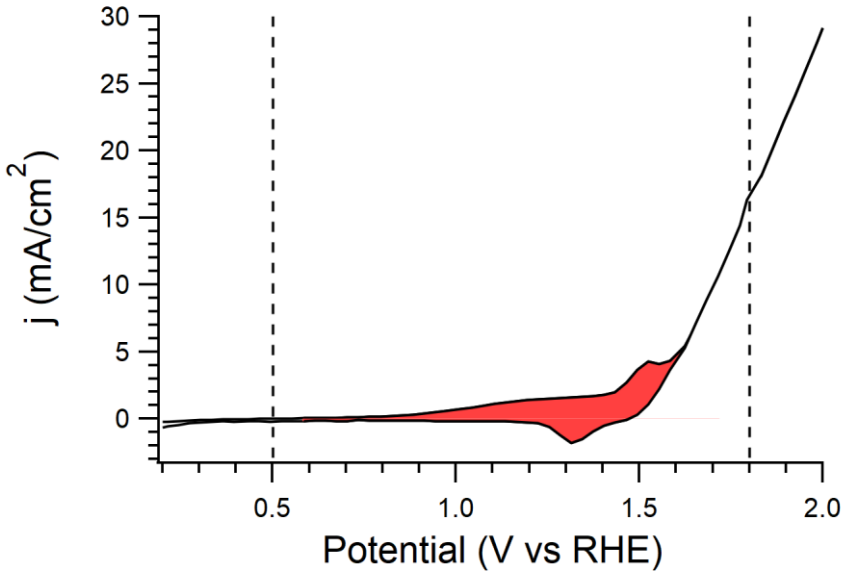

Figure 6-6. Calculation of the reduction + oxidation peak charge used for the ECSA computation in eq. (6-8). The red background indicates the area considered in (6-8) and the vertical dashed lines indicate the range in which the calculation runs.

The total reduction + oxidation charge per unit of area was obtained from the result in equation (6-8) as A_{red+ox}/v, where $v = 100\ mV/s$ is the scan rate. Then, the ECSA per unit of electrode surface (ECSA/S, also known as roughness factor) was calculated as:

$$ECSA/S = \frac{A_{red+ox}}{2v\sigma} \tag{6-9}$$

where $\sigma = 514\ \mu C/cm^2$ is the $Ni(OH)_2$ molecule surface charge density [195]. The factor ½ is necessary since each Ni specie appears both in the reduction and oxidation peaks.

6.6.1.3 Tafel plot

The Tafel plot reported in Figure 6-7a was acquired through LSV measurements recorded at a 1 mV/s scan rate. A Tafel slope of $50 \pm 10\ mV/dec$ was determined in the OER region between 200 and 350 mV overpotential. Conversely, the region for $j > 10\ mA/cm^2$ was highly affected by the value of resistance used in the iR correction. In Figure 6-7b, the Tafel plots for three values of the resistance from 11 to 13 Ω are reported, where 11 Ω is the value obtained from the impedance experimental measurement, while the blue dashed line indicates the Tafel slope extrapolated in the 200-350 mV range.

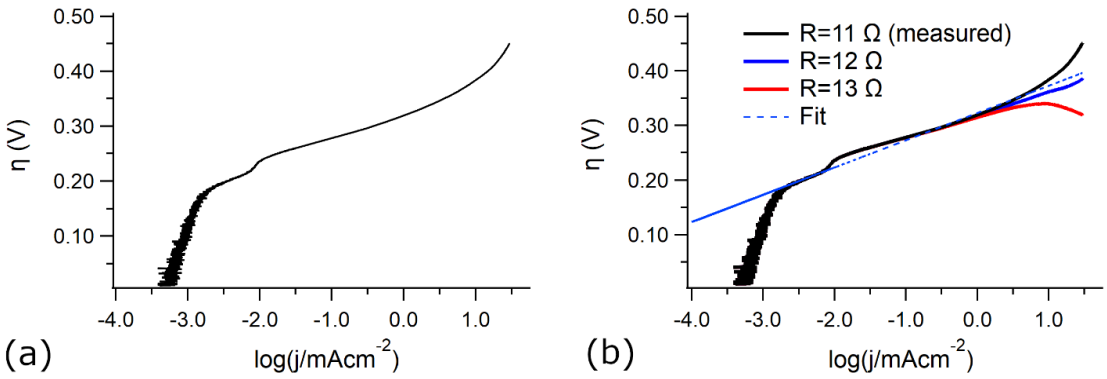

Figure 6-7. (a) Tafel plot obtained from an LSV acquisition at 1 mV/s scan rate (iR correction included using the measured ohmic drop). (b) Tafel plot for three values of the resistance used in the iR correction. 11 Ω is the measured ohmic drop.

6.6.1.4 Determination of oxygen concentration in solution

A Fox-Ocean optics device for oxygen sensing was used to determine the concentration of dissolved oxygen in the electrolyte, produced during the application of a constant potential of 1.59 V for 50 min (chronoamperometry curve shown in Figure 6-1e of the main text). The sensing device was previously calibrated by acquiring two reference values in: 1) an electrolyte solution in equilibrium with the ambient air and 2) the same electrolyte after being depleted from oxygen by bubbling N_2 gas. These two values were associated to oxygen concentrations of 8.7 mg/L and 0 mg/L respectively. The first value was obtained through the Henry law, stating that the oxygen mass concentration $[O_2]$ in the solution is directly proportional to the oxygen partial pressure $p_{O_2} = 0.21\ atm$ in the air surrounding the electrolyte:

$$[O_2] = m_m \cdot H \cdot p_{O_2} \tag{6-10}$$

where $H = 1.3 \cdot 10^{-3} \frac{mol}{L \cdot atm}$ is the Henry constant [210] and $m_m = 32\ g/mol$ is the O_2 molar mass.

Before the experimental determination of the O_2 produced at the considered voltage, the electrolyte was depleted from dissolved O_2, by flowing gaseous N_2.

The Faradaic efficiency was calculated from the oxygen concentration and current measured in the first 1 minute of the chronoamperometry test shown in Figure 6-1e (main text) through the formula:

$$FY(\%) = 100 \cdot nF \cdot \frac{[O_2]V}{m_m j S \Delta t} \tag{6-11}$$

were $n = 4$ is the number of electrons involved in the OER reaction, V is the electrolyte volume (50 ± 20 mL), j the current density, S the electrode geometrical surface, $m_m = 32\ g/mol$ is the oxygen molar mass and $\Delta t = 1\ min$ is the time elapsed from the start of the experiment.

A value of $FY = 80 \pm 20$ % was obtained for the chronoamperometry test shown in Figure 6-1e, main text.

6.6.1.5 Supplementary electrochemical plots

Turn Over Frequency (TOF) values at 350 mV, overpotentials at 1 and 5 mA/cm^2 and roughness factors ECSA/S were calculated from the j/V curves recorded with a scan rate of 100 mV/s, a representative selection of which is reported in Figure 6-3a and Figure 6-4c-d of the main text. Figure 6-8 displays the electrochemical results extracted from 2000

CV cycles performed on a freshly deposited NiFe electrode in a fresh electrolyte. Figure 6-9 shows the overpotential and TOF parameters related to further 2000 cycles performed on the same electrode (after the first set of 2000 cycles) submerged in a refreshed electrolyte. Figure 6-10 reports the overpotential values (at 1 mA/cm^2 and at 5 mA/cm^2) and roughness factors extracted from 2000 CV tests conducted on bare ITO substrates in a fresh and reused electrolyte. TOF values were obtained by normalizing the current at 350 mV overpotential by the initial NiFe mass loading in the as deposited electrode (12 $\mu g/cm^2$), without considering the Ni and Fe dissolution in the electrolyte, as done in the following section 6.6.6 (eq. (6-29)).

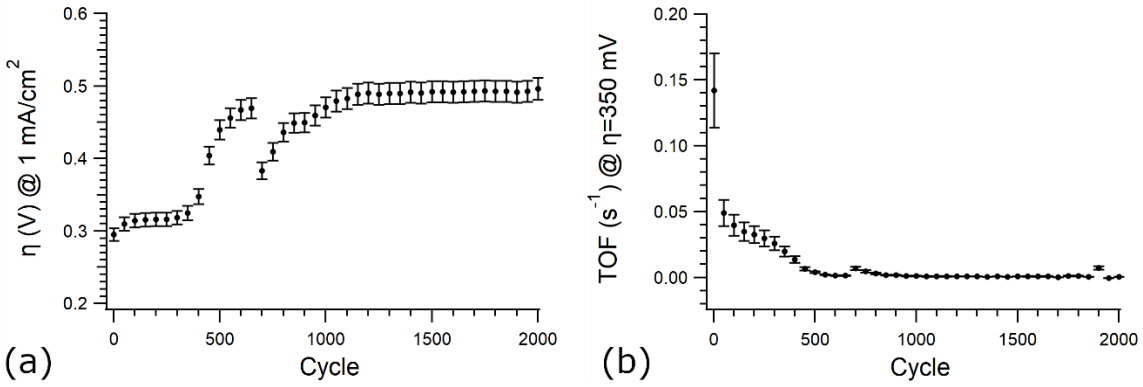

Figure 6-8. Overpotential at 1 mA/cm^2 (a) and TOF (b) values extracted from the 2000 CV cycles recorded on a freshly deposited NiFe electrode using a fresh KOH 1M electrolyte.

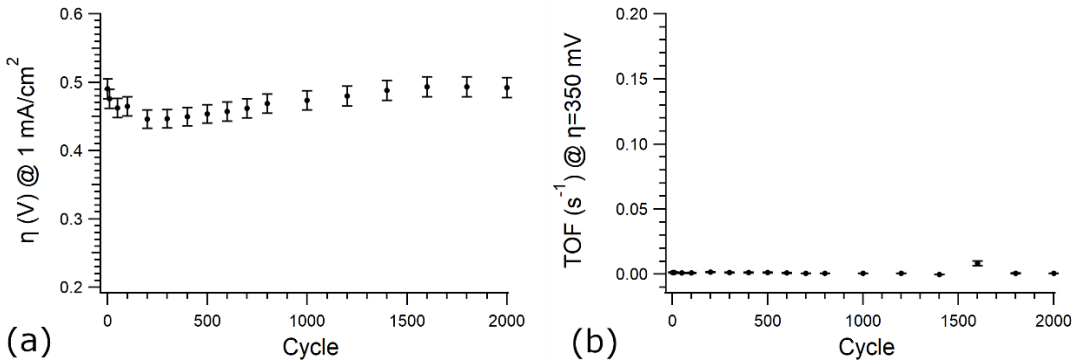

Figure 6-9. Overpotential at 1 mA/cm^2 (a) and TOF (b) values extracted from the 2000 CV cycles recorded on a reused (i.e. that had experienced 2000 CV cycles previously) NiFe electrode using a fresh KOH 1M electrolyte.

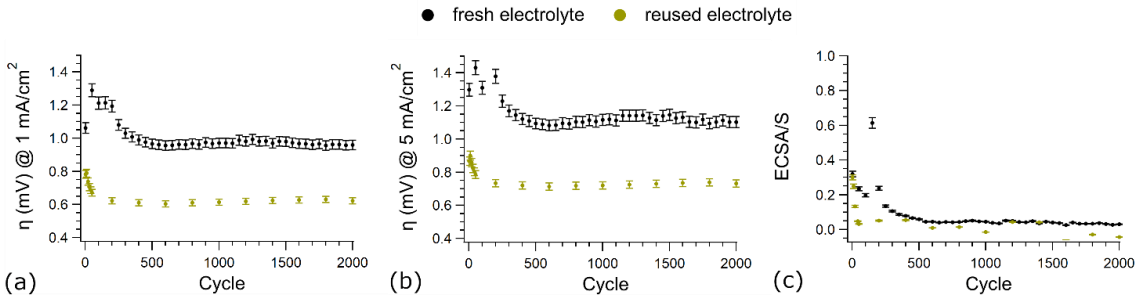

Figure 6-10. Overpotential at 1 mA/cm^2 (a), overpotential at 5 mA/cm^2 (b) and roughness factor ECSA/S (c) values extracted from the 2000 CV cycles recorded on a bare ITO substrate submerged in a freshly prepared electrolyte (black points) and in a reused electrolyte (green points)

6.6.2 XPS analysis

6.6.2.1 XPS spectra (O1s, K, In, Sn, Fe)

This section shows the XPS spectra of the NiFe electrode after the CV stability tests, compared to those of a freshly deposited NiFe film and an ITO substrate.

The O1s spectrum (Figure 6-11a) of the used electrode was characterized by a main peak at 530.7 eV with a shoulder around 532 eV. This structure was not expected to be affected by any Ni or Fe oxide/hydroxide species, whose limited mass loading would result in less than 2% contribution. Conversely, the peak structure was assigned mainly to the In and Sn oxides in the exposed ITO substrate, whose contribution was centered at 530.7 eV as shown for a bare substrate spectrum. A discrepancy between the substrate and the electrode spectra however was observed around 532 eV, where a more intense shoulder was reported for the used electrode. This difference can be associated to the contribution of hydroxide ions coming from the electrolyte solution, such as KOH [211], also affecting the 290-300 eV range with the K2p peak (Figure 6-11e). Figure 6-11b shows the XPS features in the energy range between 708-730 eV: the Fe2p peaks were not visible anymore in the electrode spectrum after the CV test, but the spectrum was dominated by the Sn3p contribution, deriving from the underlying ITO substrate.

The substrate contributions to the electrode spectrum after the CV test are also visible in Figure 6-11c-d, where the In3d and Sn3d peaks were visible, and in Figure 6-12a-b, showing In MNN Auger and Sn3p peaks. Remarkably, these peaks matched well with the spectra acquired for a bare substrate, proving that ITO was not altered by the prolonged electrochemical treatment.

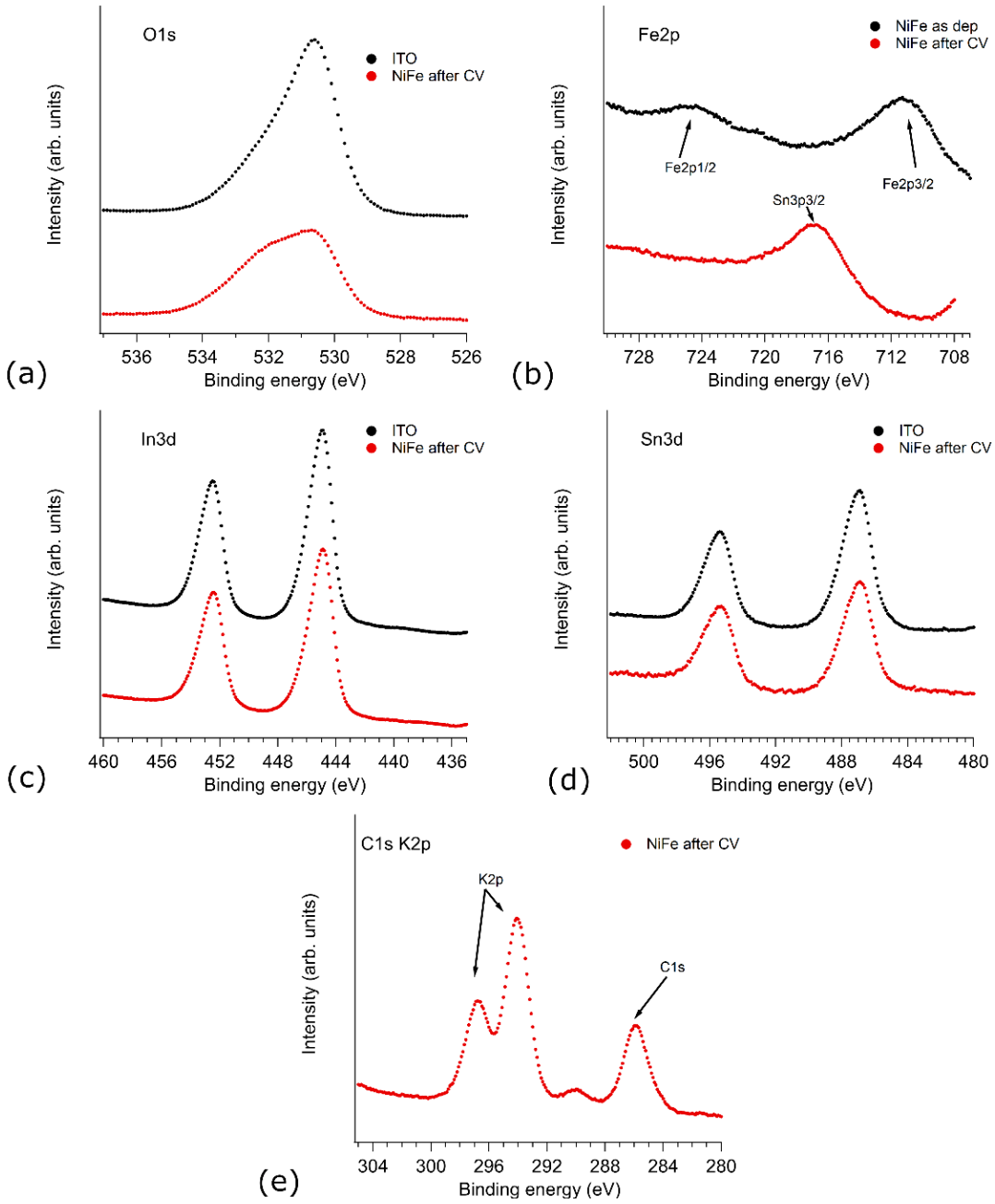

Figure 6-11. Supplementary XPS spectra acquired for a bare ITO substrate, an as deposited NiFe film and a NiFe electrode after CV stability test (4000 cycles). (a) O1s of a bare ITO and NiFe electrode after CV, (b) Fe2p spectrum of an as deposited NiFe electrode and after CV, (c-d) In3d and Sn3d of a bare ITO substrate and a NiFe electrode post CV (signal from the exposed substrate), and C1s and K2p spectra of a NiFe electrode after CV.

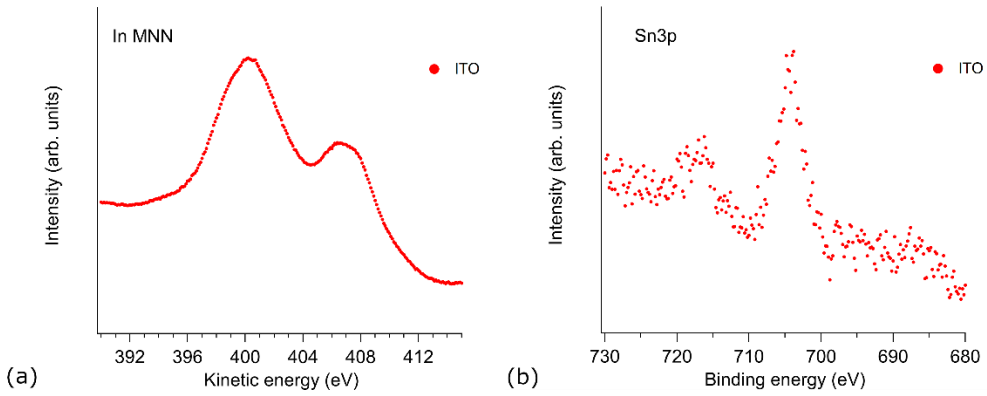

Figure 6-12. In MNN Auger (a) and Sn3p (b) spectrum of a bare ITO substrate.

6.6.2.2 Calculation of NiFe Mass loading from XPS analysis

The NiFe mass loading of the electrode was calculated from the Ni2p XPS spectra in Figure 6-3d (main text). The total peak areas I_0 and I_{CV} were calculated before and after the CV stability test and a ratio $\frac{I_{CV}}{I_0} = \frac{1}{60}$ was found. In the freshly deposited electrode, where no substrate was exposed to X-rays, the XPS signal was originated from a thin NiFe surface layer of the film, whose thickness was assumed to be determined by the electron mean free path in the material. In an ideal pure Ni metal the thickness of this layer (i.e. the electron mean free path) is $\lambda_{Ni} = 5.87\ nm$ [212]. The mass of the layer, per unit of surface, is:

$$\mu_0 = \rho_{Ni}\lambda_{Ni} = 5.2\ \mu g/cm^2 \tag{6-12}$$

where $\rho_{Ni} = 8.9\ g/cm^3$ is the metal Ni density.

When Ni oxide and hydroxides formed in the film, we assumed that the XPS signal was

originated from the same mass per unit of surface (μ_0), where oxygen and hydroxyl ions were included together with Ni atoms in μ_0 . Therefore, the Ni mass per unit of surface (in which just the Ni atom weight is considered) that produces the signal I_0 in the Ni2p spectrum is:

$$\mu_0 \chi_{\mathrm{Ni}} \tag{6-13}$$

where $\chi_{Ni} = 37\% + 33\% \cdot \left(\frac{59}{59+16}\right) + 25\% \cdot \left(\frac{59}{59+2\cdot(16+1)}\right) + 5\% \cdot \left(\frac{59}{59+56+16}\right) = 0.81$ is the Ni mass fraction in the as deposited film. χ_{Ni} was obtained by computing the fraction of Ni weight in each Ni metal, NiO, $Ni(OH)_2$ and NiFeO molecules and averaging the results according to the oxidation states abundances found in chapter 5.4 and [204] (37%, 33%, 25% and 5% respectively).

Considering that the XPS peak intensity was 60 times reduced after the stability test, we can calculate the residual Ni atom species mass loading on the electrode after CV as:

$$\mu_{CV}^{Ni} = \frac{I_{CV}}{I_0} \mu_0 \chi_{Ni} = 70 \pm 10 \ ng/cm^2 \tag{6-14}$$

and the NiFe atom species mass loading (including also Fe according to the Ni/Fe=90/10 relative composition):

$$\mu_{CV}^{NiFe} = 80 \pm 10 \, ng/cm^2 \tag{6-15}$$

where the error bar is based on the uncertainty on the Ni2p signal intensity.

It is important to note that equation (6-15) only accounts the Ni+Fe atom mass loadings but does not include the (OH) ion mass in the hydroxides. Assuming a completely hydroxidized oxidation state for the Ni and Fe species, the Ni + Fe hydroxide mass loading can be obtained as:

$$\mu_{CV}^{NiFe(OH)_2} = \mu_{CV}^{NiFe} \cdot \frac{59 + 2 \cdot (16 + 1)}{59} = 126 \pm 16\, ng/cm^2 \tag{6-16}$$

where the factor $\frac{59+2\cdot(16+1)}{59}$ is the ratio between the $Ni(OH)_2$ and the Ni metal molecular weights, that also holds for FeOOH/Fe (just a 3% difference in the ratio).

6.6.3 Morphology evolution over CV

In this section, two possibilities for the final NiFe morphology after the prolonged CV test are discussed, assuming both Ni and Fe species were converted completely into hydroxide species: 1) the NiFe mass retained the same nanoparticle morphology as in the fresh electrode and 2) the NiFe hydroxides formed a continuous coating of the substrate.

6.6.3.1 Nanogranular morphology

In this section we hypothesize that the NiFe mass surviving the leaching process retained the same nanostructure as in the freshly deposited electrodes, i.e. the same nanoparticle size and shape, up to a possible change in their volume due to the hydroxidation. Though as deposited nanoparticles were characterized by a trimodal

distribution in size (0.4, 0.6, and 2.8 nm) [204], we consider here only the $h = 2.8\,nm$ mode. Furthermore, the following calculations will be performed by considering just the Ni content of the nanostructures and neglecting Fe. The single nanoparticle mass is given by:

$$m_{NP} = \frac{4}{3}\pi\left(\frac{h}{2}\right)^3 \rho_{NP} \tag{6-17}$$

where $\rho_{NP} = 37\% \cdot \rho_{Ni} + 38\% \cdot \rho_{NiO} + 25\% \cdot \rho_{Ni(OH)_2} = 6.9\ g/cm^3$ is the nanoparticle density obtained as the weighted average of each Ni oxide and hydroxide abundancies. The Ni atomic mass enclosed in each individual nanoparticle is:

$$m_{NP}^{Ni} = m_{NP}\chi_{Ni} = 6.4 \cdot 10^{-20} g \tag{6-18}$$

with χ_{Ni} defined in equation (6-13)**.**

The nanoparticle density per unit of surface can be calculated from eq. (6-18) and (6-14) as:

$$\frac{\mu_{CV}^{Ni}}{m_{NP}^{Ni}} = 1.3 \cdot 10^4 \ \ nanoparticles/\mu m^2 \tag{6-19}$$

After the CV test, assuming Ni was completely converted into $Ni(OH)_2$, the nanoparticle mass was

$$m_{NP}^{CV} = \frac{m_{NP}^{Ni}}{\chi_{Ni}^{CV}} \tag{6-20}$$

where $\chi_{Ni}^{CV} = \frac{59}{59+2\cdot(16+1)}$ is the Ni atom weight fraction in a hydroxide molecule. Therefore, the nanoparticle radius (r_{CV}) after the CV test was obtained by solving the equation $m_{NP}^{CV} = \frac{4}{3}\cdot\pi\cdot(r_{CV})^3\rho_{Ni(OH)_2}$ and the electrode coverage was obtained by multiplying each individual particle surface ($\pi\cdot r_{CV}^2$) by the number of nanoparticle per unit of surface:

$$Coverage = \pi\left(\frac{3}{4\pi\chi_{Ni}^{CV}}\right)^{\frac{2}{3}}\frac{\mu_{CV}^{Ni}}{\left(\rho_{Ni(OH)_2}\right)^{\frac{2}{3}}\left(m_{NP}^{Ni}\right)^{\frac{1}{3}}} = 11\%$$

(6-21)

The value in equation (6-21) was obtained assuming no overlapping between nanoparticles and can be considered as an upper bound for the actual coverage, since thicker and agglomerated structures (in addition the micro-granular structures already present in the fresh film) can lay on the substrate after the CV test.

6.6.3.2 Hydroxide coating of the substrate

Assuming the electrode surface S is completely covered by a $Ni(OH)_2$ monolayer, the Ni hydroxide mass loading is:

$$\mu^{Ni(OH)_2} = \rho_{Ni(OH)_2}t$$

(6-22)

where $\rho_{Ni(OH)_2} = 4.1\ g/cm^3$ is the Ni hydroxide density and t is the monolayer thickness. t can be calculated by considering that the number of Ni hydroxide molecules contained in a volume V is

$$\frac{\rho_{Ni(OH)_2} V N_A}{m_m}$$

(6-23)

where N_A is the Avogadro number, and $m_m = 93\ g/mol$ is the Ni hydroxide molar mass. As a consequence, the volume of a single $Ni(OH)_2$ molecule can be calculated by dividing V by the number of molecules in equation (6-23):

$$\frac{m_m}{\rho_{Ni(OH)_2} N_A}$$

(6-24)

The average molecular diameter, i.e. a monolayer thickness, is then:

$$t = \left(\frac{m_m}{\rho_{Ni(OH)_2} N_A}\right)^{1/3} = 0.34\ nm$$

(6-25)

The mass loading, i.e. the mass per unit of surface, of a single $Ni(OH)_2$ monolayer is then obtained from equation (6-22) as follows:

$$\mu^{Ni(OH)_2} = \rho_{Ni(OH)_2} t = 139 \frac{ng}{cm^2}$$

(6-26)

This value is compatible with the mass loading estimation from XPS (equation (6-16)), supporting the hypothesis of a monolayer coating of the electrode as final morphology after the CV prolonged activity.

6.6.4 Calculation of the Ni and Fe concentration in the electrolyte after 2000 CV cycles

An estimation of the maximum values for the Ni and Fe concentrations in the electrolyte after the 2000 cycle CV test can be provided by assuming the NiFe material on the electrode was completely dissolved.

Considering the NiFe mass loading ($\mu_0 = 12 \pm 1\ \mu g/cm^2$) and an electrode surface area $S = 2\ cm^2$, the total Ni and Fe masses are:

$$M_{Ni} = 0.9 \cdot \mu_0 \cdot S = 22 \pm 2\ \mu g$$

$$M_{Fe} = 0.1 \cdot \mu_0 \cdot S = 2.4 \pm 0.2\ \mu g$$

(6-27)

The Ni and Fe molar concentration in the solution was obtained by dividing the masses in equation (6-27) by the electrolyte volume ($V = 50 \pm 20\ mL$) and the Ni and Fe molar masses ($m_{Ni} = 59\ g/mol$ and $m_{Fe} = 56\ g/mol$):

$$[Ni] = \frac{M_{Ni}}{V \cdot m_{Ni}} = 7 \pm 3\ \mu mol \cdot L^{-1}$$

$$[Fe] = \frac{M_{Ni}}{V \cdot m_{Ni}} = 0.8 \pm 0.3\ \mu mol \cdot L^{-1}$$

(6-28)

6.6.5 TEM analysis

Figure 6-13 shows the TEM images of a sample of electrolyte collected after a 2000 cycles CV test was carried out on a freshly deposited NiFe film used as working electrode. Structures of variable size were visible, ranging from few nanometers to microns, while no crystalline structure was detected, as displayed by the HAADF image (Figure 6-13e)**.** The

structures were also surrounded by a more transparent environment, that could be associated to electrolyte residuals.

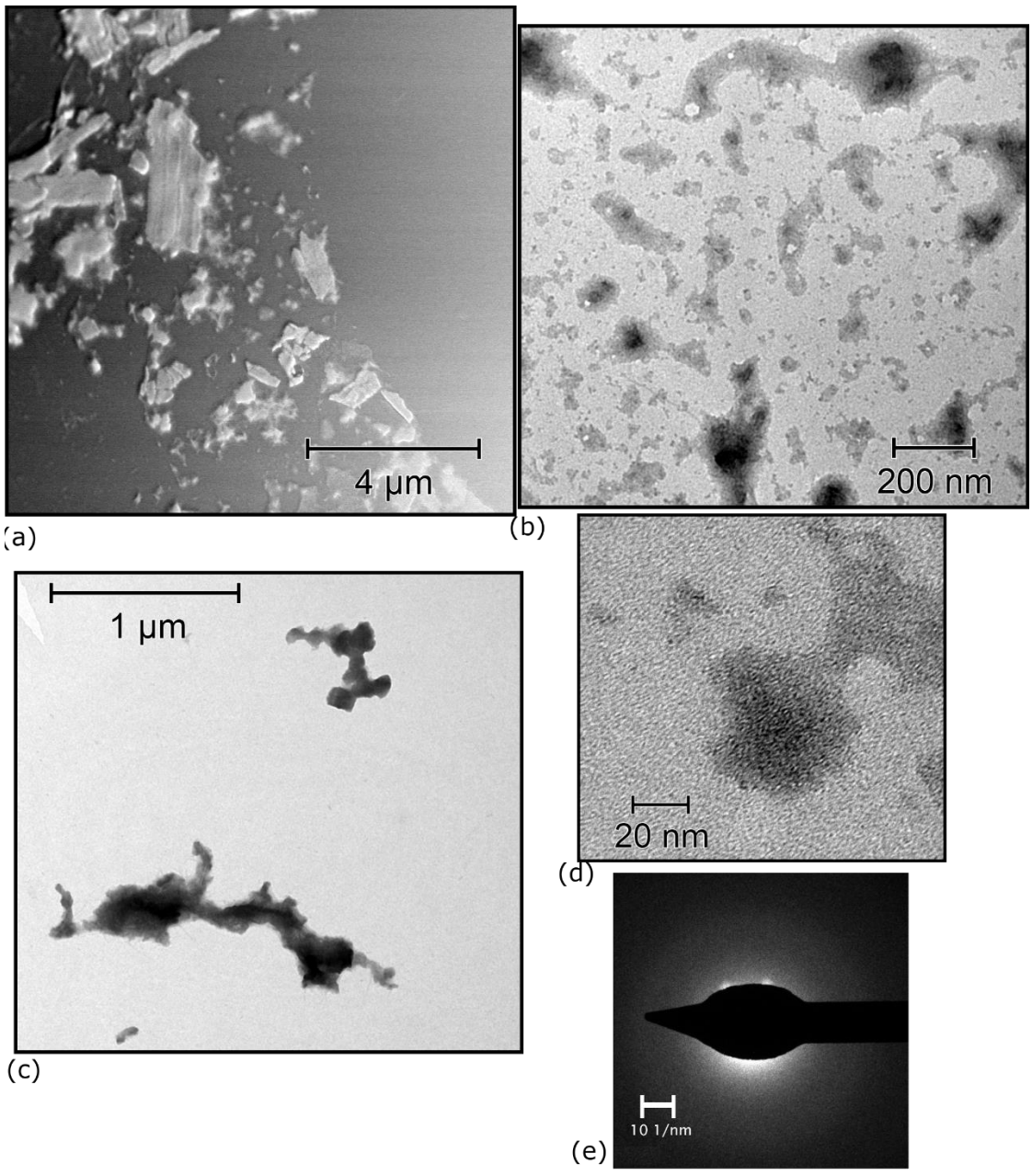

Figure 6-13. TEM analysis of a sample of electrolyte solution after being used in the 2000 cycles CV test with a freshly deposited NiFe film as working electrode. Variable structure sizes are displayed, from micrometers (a,b,c) to nanometers (d), while the HAADF image does not show any crystalline structure.

6.6.6 TOF calculation

From the Ni+Fe mass loading in equation (6-15) the turn over frequency (TOF), can be calculated at 350 mV overpotential according to chapter 5.4 ([204]):

$$TOF = \frac{jM_{NiFe}}{4eN_A\mu_{CV}^{NiFe}} = 0.3 \pm 0.1\ s^{-1} \tag{6-29}$$

where $M_{NiFe} = 58.4\ g/mol$ is the average NiFe molar mass and $j = 0.15 \pm 0.05\ mA/cm^2$ is the current measured at $\eta = 350\ mV$.

6.6.7 Electrode evolution over 25 CV

In order to have an insight on the film transformation process at the early stage, the NiFe chemical and morphological characterization has been carried out after performing a 25 cycles CV test at 10 mV/s scan rate.

6.6.7.1 Experimental results

The j/V curves, in Figure 6-14a, show an increase of the $NiOOH$ redox peaks (reaction (6-3)) during the electrochemical cycles, suggesting a growing film hydroxidation process. Furthermore, a shift of 10 mV towards lower potentials is registered for both reduction and oxidation peaks. This might result from a rearrangement of the $Ni(OH)_2$ sites inside the nanostructures, such as in the transition from β to α phases [174]. Despite a progressive growth of Ni oxy/hydroxide, no variations in the OER currents are

reported along the 25 cycles, implying that not all the $NiOOH$ species formed in the redox region can participate as active sites for the OER catalysis.
An XPS analysis of the Ni2p, Fe2p, O1s and Ni auger regions, carried out after the 25 cycles CV, is reported in Figure 6-14 and compared to the freshly deposited electrode. In each panel, the curves acquired after 25 cycles (Mg filament as source) were fitted through the CasaXPS software [181], by employing the peak series in [188], [213] for each Ni, Fe and O specie. For each oxidation state, the relative distances, widths, and amplitudes of the components were kept fixed according to the tabulated values, while the overall intensity was used as fitting parameter to quantify the abundancy in the film and a global shift lower than 1 eV was allowed due to a possible film charging. Furthermore, in each spectrum, the contributions from the underlying In and Sn components are visible, as a consequence of a partial exfoliation of the film and substrate exposure during the electrochemical tests, also confirmed by SEM images below. In the fitting process, these components are reproduced by using the In and Sn peaks reported in section 6.6.2 with the same widths and positions as measured for a bare ITO substrate. The maximum of the Ni LMM Auger spectrum (Figure 6-14b) undergoes a 5 eV shift towards lower kinetic energies after 25 CV cycles. Considering also the Ni2p maximum (Figure 6-14c), an auger parameter of 1698.5 ± 0.6 eV is calculated. This value is compatible with $Ni(OH)_2$ (1698.38 eV [213]) and excludes the presence of a significant amount of $NiOOH$ and NiO species in the film (auger parameter 1700 eV and 1697.7 [213]). The absence of predominant $NiOOH$ confirms the Ni oxyhydroxides formation as a reversible process, in agreement with equation (6-3). The Ni2p spectrum (Figure 6-14c) for a freshly deposited NiFe film shows a metal peak at 852.6 eV together with two other maxima at 855.6 and 861.5 eV, reproduced by a

combination of metal (36%), oxide (47%) and hydroxide (17%) components (according to chapter 5.4. The metal contribution completely disappears after 25 cycles, while the two peaks appearing at 856.4 eV and at 862 eV can be completely resolved in terms of the $Ni(OH)_2$ phase, in agreement with the auger parameter. Conversely, the 840-855 eV range is associated to the In MNN auger profile (also reported in section 6.6.2 for a bare substrate). The Fe2p spectrum (Figure 6-14d) after 25 cycles, overlapping two Sn 3p peaks at 704 and 717 eV (reported in section 6.6.2), is completely reproduced by a set of peaks of the Fe(III) oxidation state as in [188], with an overall 1 eV shift due to possible surface charge effects. This oxidation state may correspond either to a Fe_2O_3 oxide or to a $FeOOH$ hydroxide. Instead, the metal peak at 706.7 eV detected in the freshly synthesized electrode, is completely disappearing after 25 cycles.

In the O1s region (Figure 6-14e), the peak centered at 529.5 eV in the freshly deposited electrode, associated mainly to Ni oxide species, considerably decreases after 25 cycles and is completely reproduced by the underlying ITO contributions (see chapter 6.6.2). This suggests the disappearance of the Ni oxide component after the electrochemical test, in favor of the increase of the $Ni(OH)_2$, consisting in the main contribution to the 25 CV cycles spectrum with a peak centered at 532 eV (with charging effect shift similar to the other Ni components). A smaller component around 533 eV, representing the 20% of the film signal, reproduces the tail of the O1s spectrum, compatible with C oxy-hydroxide contributions, other hydroxylated components and H_2O [214], that could be absorbed in the film during the exposure to the electrolyte.

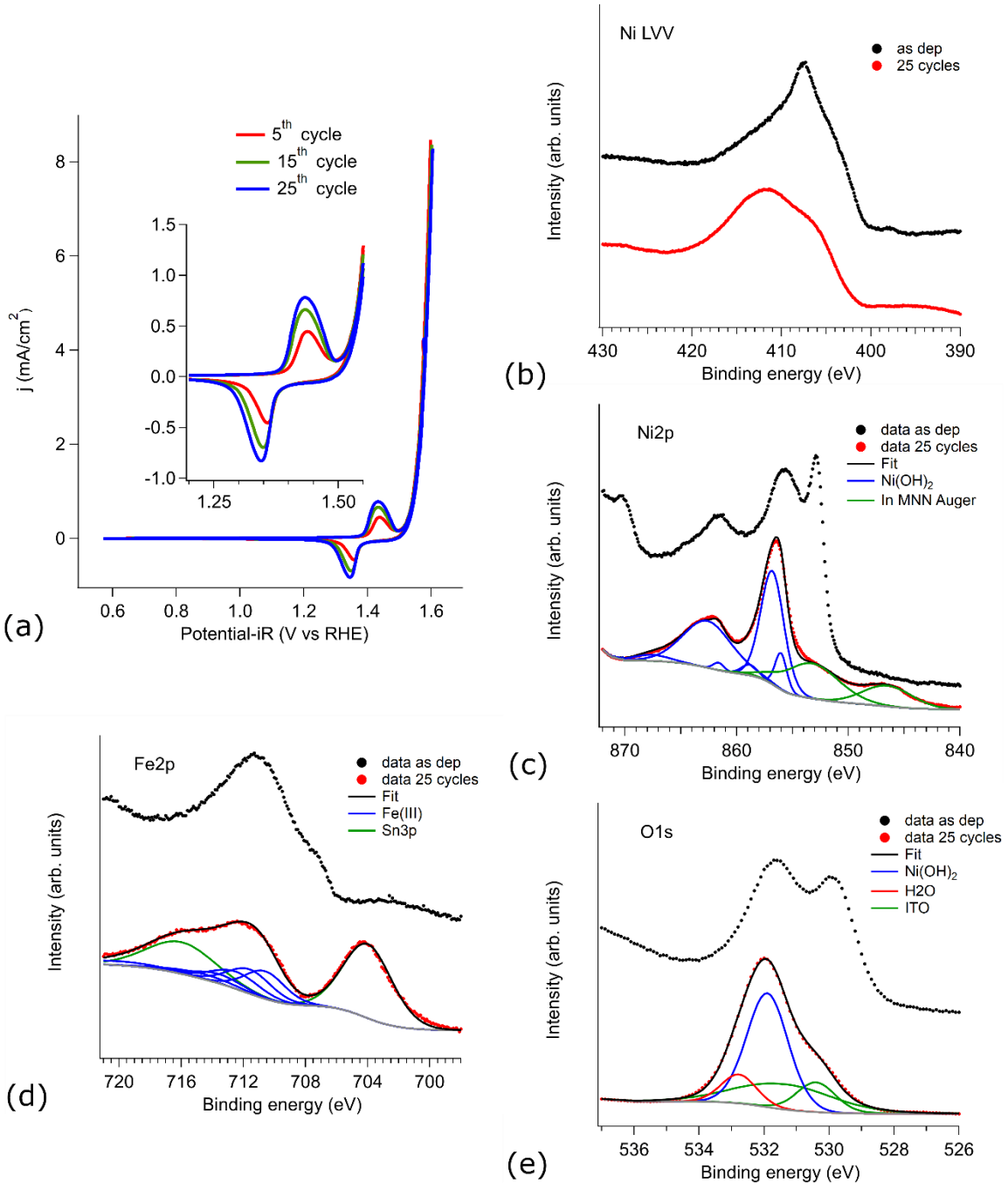

Figure 6-14. j/V curves recorded in a 25 cycles CV experiments (a). XPS spectra acquired after the 25 cycles CV: Ni LVV Auger (b), Ni2p (c), Fe2p (d) and O1s (e).

The combined analysis of the four XPS spectra suggests that the NiFe material is completely hydroxylated after the electrochemical treatment, with a possible incorporation of other components, such as H_2O, from the electrolyte. Furthermore, the possible presence of H_2O components suggests that $Ni(OH)_2$ may form in the α phase during the CV test [199]. This would also be compatible with the shift of the redox peaks in the j/V curves (Figure 6-14a), as a consequence of an enhanced ion transport and intercalation in the film bulk for the α phase with respect to a pure hydroxide [199].

The Raman spectra (Figure 6-15) were acquired for a bare ITO substrate, in a 38 nm thick nanogranular region of the NiFe electrode and for a micron-size NiFe particle. The ITO substrate as well as the freshly deposited nanogranular film surface are characterized by a nearly flat trend with no particular features. After 25 cycles the spectrum acquired at the film surface still does not show any evident resonance, while its general increase in intensity may be determined by the higher film mass resulting from the hydroxide formation. Before the electrochemical test, the micro-grain region shows three mild peaks at 489, 567 and 685 cm^{-1}, with the first two associated to (oxy)hydroxide phases [39]. After the CV, the signal shows a general decrease in intensity, while a single peak centered at 560 cm^{-1} is formed. This agrees with an increased presence of hydroxides species in the film [208]. In particular, as outlined by [39], the Ni(OH)2 phase results in the couple of peaks around 460 and 560 cm^{-1} , whose amplitude ratio is proportional to the Fe/Ni amount ratio. The disappearance of the peak at 460 cm^{-1} in favour of an increase of the 560 cm^{-1} resonance in the CV tested electrode is compatible with the growth of the the Ni hydroxide volume, overwhelming the starting Fe content that cannot generate a significant Raman response.

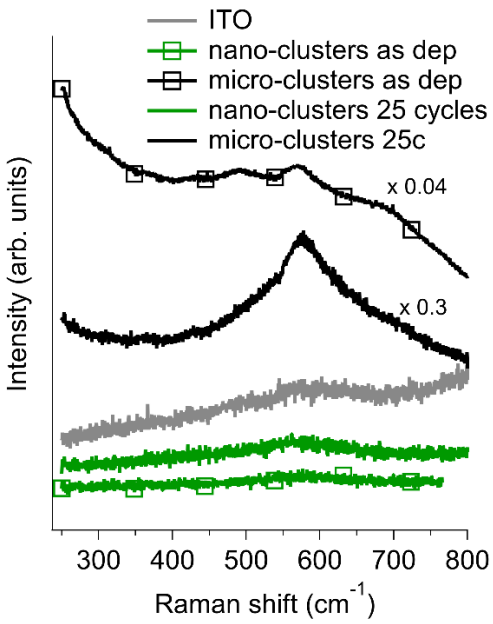

Figure 6-15. Comparison of Raman spectra for a freshly deposited NiFe electrode and after 25 cycles CV

The modification of the film morphology was carried out by acquiring AFM images after 5, 15 and 25 electrochemical (Figure 6-16a-d). These showed that, during the CV cycling, no significant variations in the grain height occurred, while the shape of the cluster was changing from a spherical morphology to a more elongated and thinner configuration. In order to quantify these modifications, the images were analyzed through the Gwyddion software [180] as explained more in detail in section 5.6.1. A watershed mask was applied to identify separated domains corresponding to the individual grains, whose area (projected on the x-y plane parallel to the substarte) is reported in Figure 6-16f. Then, for each grain, its size in the z direction (Figure 6-16e) was computed as the maximum height of the domain with respect to the minimum height at the domain boundary.

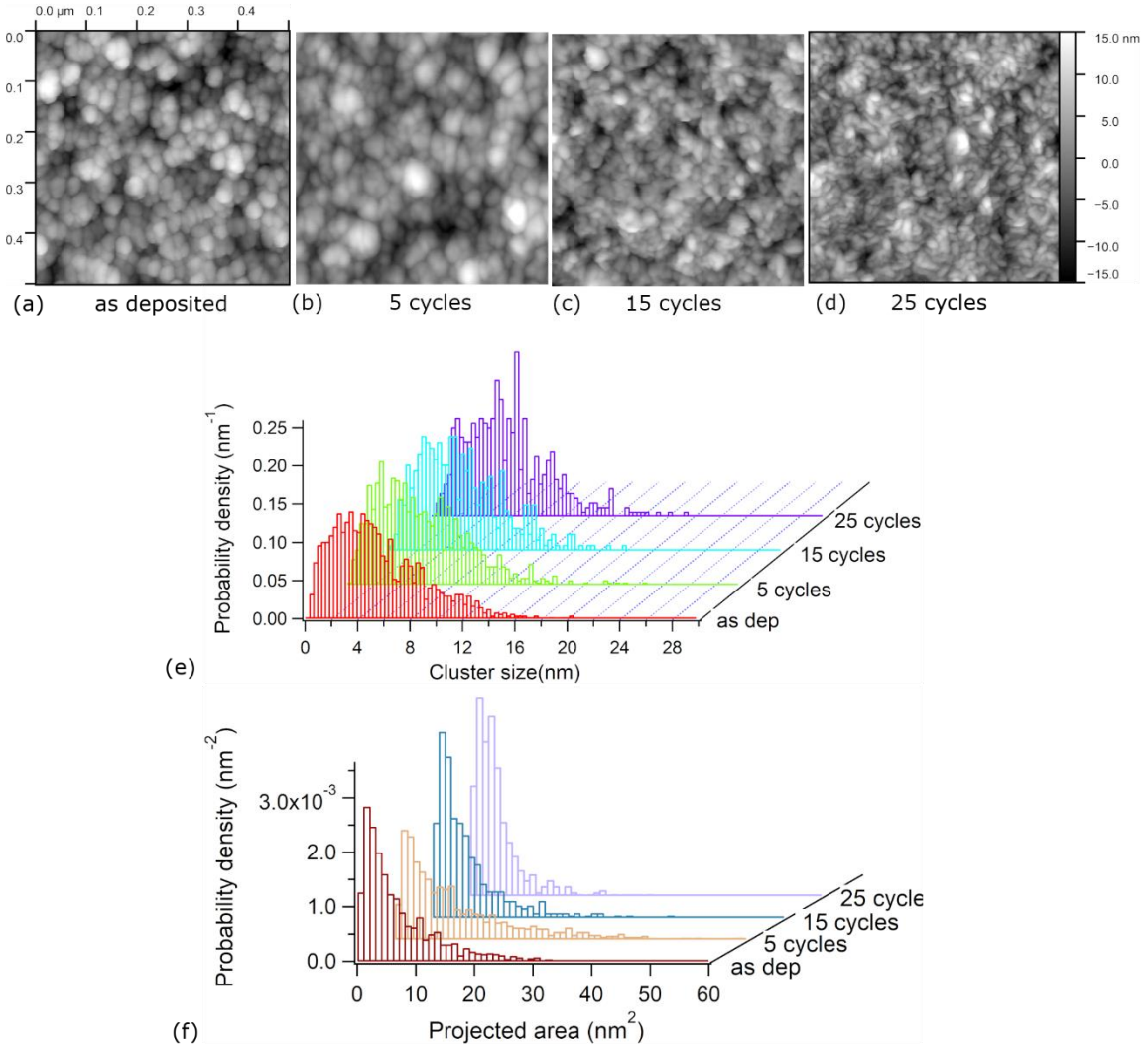

Figure 6-16. AFM images of a NiFe electrode, right after the deposition (a), and after 5 (b), 15 (c) and 25 (d) cycles. Associated nanograin height (e) and projected area (f) distributions.

The nano-cluster's height in the direction z does not show any significant variation along the CV test, with a peak maximum at 4 nm and a tail reaching 12 nm, resulting from the individual nanoparticle aggregation in the porous film. This also implies a nearly constant nanogranular surface roughness, slightly oscillating between 4.3 and 4.7 nm in the different images. Conversely, the cluster projected areas (Figure 6-16f) are uniformly overestimated due to the AFM tip convolution effect, while a relative variation of the distributions reflects a modification of the real nano-clusters morphology. In the histogram, the maximum remains unchanged, while a reduction of the tail is observed for the electrochemically treated films. The peak maximum region is distorted by the contribution of partially covered nanoclusters, that offer a reduced detectable projected area and are not representative of the real lateral dimensions. Instead, the reduction of the tail after 15-25 cycles reflects a global decrease of the real projected area of the nanoclusters after the electrochemical treatment. These modifications may be ascribed to the formation of hydroxides in the grains.

In order to confirm this assumption, XRD analysis was carried out after 25 cycles and compared to the as synthesized film in Figure 6-17. The peak appearing in the fresh electrode at 44.5 ° is widened after 25 cycles, with a width increasing from 1° to 2.5 °. According to the Scherrer formula (2-5), this corresponds to a decrease of the Ni crystalline domain radius from 1.6 nm to 1.1 nm. As a consequence, just the 30% of the metal content of the crystalline grains is not altered by the electrochemical treatment, while the 70% of the crystalline metal phase might be converted into hydroxides. Moreover, the absence of further peaks in the region between 30 and 40° indicates that the hydroxide and oxides growth may be amorphous.

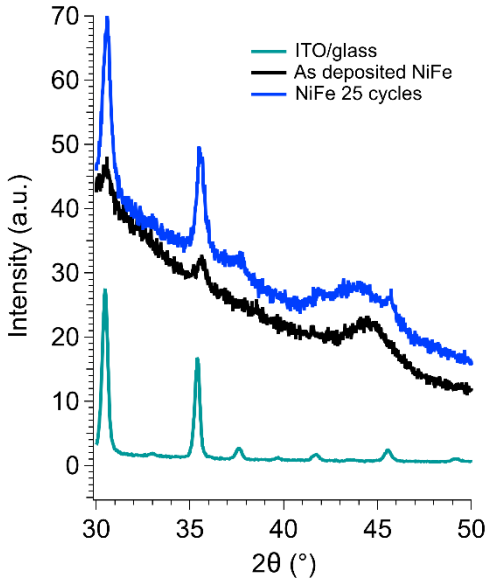

Figure 6-17. Comparison of XRD spectra obtained for an as deposited film and after 25 CV cycles.

The SEM images (Figure 6-18a-b) show that the well-defined nano-cluster arrangement is lost after the electrochemical treatment, in favor of a blurred profile, that may arise from the formation of an oxide and hydroxide coating.

At the micrometer length scale, a process of exfoliation of the film is shown in the SEM image in Figure 6-18c. The exfoliated film regions show a spherical shape with few tens of nanometers diameter, with the lifted film curling and laying on the side. This type of electrode degradation could be ascribed to the exposure of the film to the solution, while the spherical shape of the exfoliations may be a consequence of the film mechanical stress caused by the oxygen bubbles formation during the electrochemical treatment.

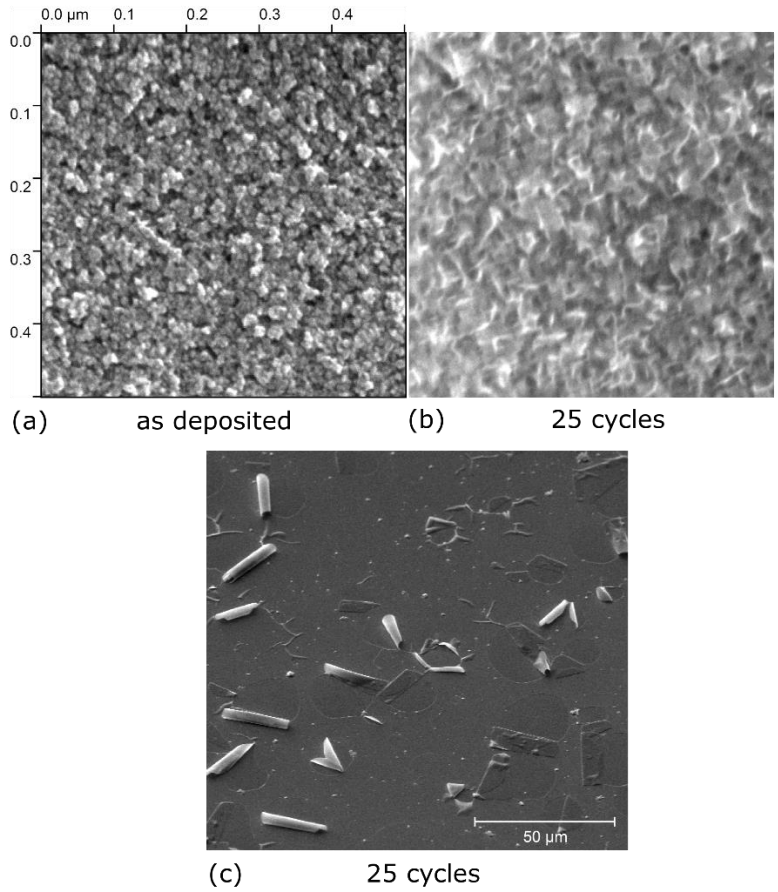

Figure 6-18. SEM images of the nanogranular morphology of a NiFe electrode before (a) and after (b) the 25 cycles CV test. Microscale view of the exfoliation process after 25 cycles (c).

6.6.7.2 Film bulk transformation and modelling

A further insight on the film modification can be provided directly by the electrochemical measurements. The redox peak area in the I/V curves is proportional to the total amount of electrochemically active $Ni(OH)_2$, trough equation (6-9). Therefore, assuming that just a $Ni(OH)_2$ surface monolayer undergoes the redox process, it is possible to estimate the electrochemically active surface area (ECSA) [16] that participates to the

redox transformations. In Figure 6-19a, the ECSA per unit of the electrode geometrical area, also known as roughness factor (RF), is reported. It is possible to notice how the ECSA increases during the electrochemical treatment, reaching for 25 cycles a value 4 times higher than the starting one, with an active surface 9 times higher than the geometrical surface. In the same figure the roughness factor deriving from the AFM images is plotted, obtained by calculating the total surface probed by the AFM tip and normalized by the geometrical area. The AFM values, initially around 1.1, are characterized by a slightly increasing trend, reaching the value 1.23 after 25 cycles. These values could be underestimated due to the finite tip size (10 nm) and the surface/tip convolution effect during the image acquisition. However, the significant difference between the electrochemical and the morphological surface areas as a function of the electrochemical cycles suggest that, during the CV test, the formation of hydroxides involves not only the film surface but also deeper regions.

In order to quantify the modification and oxidation degree in the deeper regions, the film thickness was measured by AFM at the film edge after 5, 15 and 25 electrochemical cycles, registering a linear increase from the 38 nm starting value to 63 nm, as shown in Figure 6-19b. The effect may be associated to the conversion of the metal components into oxides and hydroxides or, in a lesser extent not exceeding 20% (according to the XPS results), to a diffusion inside the film of other compounds [171] such as water present in the electrolyte. This furtherly supports that the chemical transformation of the electrode does not involve just the film surface, but also the bulk volume.

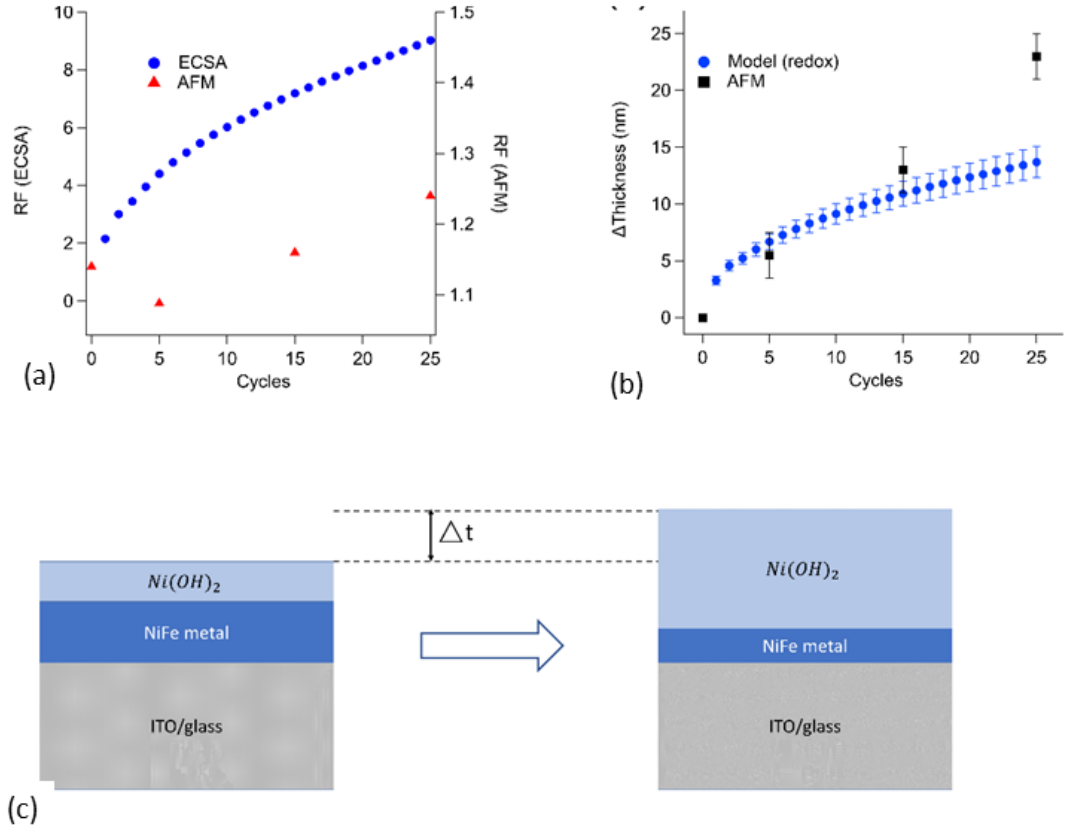

Figure 6-19. (a) Roughness factor computed from the AFM images or calculated directly from the j/V curves. (b) AFM measurement (ex situ) of the thickness increase during 25 cycles CV and prediction from the model in (c).

The growth of the nano-cluster region thickness occurring can be interpreted as a function of the j/V electrochemical curves and chemical modification resulting from XRD, XPS and optical spectroscopy analyses.

We elaborate here a model that can predict the film thickness modification starting from the cyclic voltammetry curve under the following assumptions:

- the film growth is ascribed completely just to the conversion of Ni metal phase to hydroxides $Ni(OH)_2$

- all the $Ni(OH)_2$ amount in the film is electrochemically active i.e. contributes to the redox current.
  In these assumptions, the following steps describe quantitatively the film growth.

The initial volume occupied by a mole of metal Ni is given by:

$$\frac{M_{Ni}}{\rho_{Ni}} = 6.6\ cm^3/mol \tag{6-30}$$

where $M_{Ni} = 58.7\ g/mol$ and $\rho_{Ni} = 8.9\ g/cm^3$ are the metal Ni molar mass and density.

Similarly, for Ni hydroxide phases we have:

$$\frac{M_{Ni(OH)_2}}{\rho_{Ni(OH)_2}} = 22.7\ cm^3/mol \tag{6-31}$$

with $M_{Ni(OH)_2} = 93\ g/mol$ and $\rho_{Ni(OH)_2} = 4.1\ g/cm^3$.

As a consequence, the absorption of OH^- ions by a Ni mole to form an hydroxide mole, determines an increase in the volume (per Ni mole) of:

$$\frac{\Delta V}{mol} = \frac{S\Delta t}{mol} = \left(\frac{M_{Ni(OH)_2}}{\rho_{Ni(OH)_2}} - \frac{M_{Ni}}{\rho_{Ni}}\right) \tag{6-32}$$

where S is the electrode geometrical area and Δt is the increase of the film thickness. This film transformation is represented schematically in Figure 6-19c, where a part of the film is converted into hydroxides, determining an increase in thickness. Despite the scheme is reporting the $Ni(OH)_2$ material adding as a top layer, the model is also valid in case the metal and hydroxide compounds are mixed in the film bulk. The thickness increase is directly proportional to the moles of hydroxide forming in the electrode during CV, that can be calculated from each j/V cycle in Figure 6-14a. If $A_{red+ox}(k)$ is the redox peak

area for the kth CV cycle computed according to (6-8), the moles of $Ni(OH)_2$ molecules per unit of surface (S), formed in addition to the ones existing at the beginning of the test, are:

$$\frac{mol}{S} = \frac{A_{red+ox}(k) - A_{red+ox}(1)}{2N_A ev} \tag{6-33}$$

where $v = 10mV/s$ is the CV potential scan rate.

By multiplying the volume increase per unit of mole (6-32) by the number of moles (6-33), one obtains:

$$\Delta t(k) = \frac{A_{red+ox}(k) - A_{red+ox}(1)}{2N_A ev}\left(\frac{M_{Ni(OH)_2}}{\rho_{Ni(OH)_2}} - \frac{M_{Ni}}{\rho_{Ni}}\right) \tag{6-34}$$

Formula (6-34) directly relates the film thickness increase prediction $\Delta t(k)$ to the redox peak area in the j/V curve ($A_{red+ox}(k)$).

Figure 6-19b shows the model output based on the j/V curves (Figure 6-14a), for each CV cycle. The film growth prediction shows an increasing trend, matching the AFM values for 5 and 15 cycles, and reaching a maximum of 13 nm after 25 cycles. This confirms that, in the early stages of the CV test, the thickness increases arises from the OH^- ions absorption to form hydroxide compounds in the film. Conversely, the predicted value at 25 cycles underestimates the AFM measured thickness. This discrepancy can be partly associated to the presence of other elements such as oxides or water phases contributing to the film volume but not visible in the j/V curves. However, this effect cannot influence the thickness growth for more than 20 % (according to XPS). As a consequence, the most plausible cause for the 13 nm underestimation of the thickness

growth stems from the fact that only a part of the overall hydroxide amount is electrochemically active and detectable by the j/V curve analysis, while the remaining fraction is contributing to the film growth without being accounted in the calculation (6-34). In order to support this hypothesis two further estimations were made, based on spectroscopy in the UV-VIS range and XRD spectrum in Figure 6-17.

In the UV-VIS wavelength range, the impinging light can probe all the film volume, as proven by a non-vanishing transmittance, providing an average of the chemical properties across all the film depth. Furthermore, the major influences on the optical response are assumed to be determined by the metal to hydroxide conversion, while the absorption of other molecules such as water is not expected to play a determinant role. The spectra are affected by a 5% uncertainty offset, due to the instrumental inaccuracy. The reflection spectrum (Figure 6-20a) shows after 25 cycles a 10 ± 5 % decrease with respect to the fresh electrode, uniformly in the spectrum. An overall shift is also reported in the transmittance (Figure 6-20b), with a 15 ± 5% uniform increase. The higher transmittance and lower reflection confirm a decrease in metallicity. In order to quantify this effect, the spectra can be compared the 25 CV spectra with the ones acquired for freshly deposited electrodes (Figure 5-5) of different thicknesses. A similar variation of 10 and 20% in R and T curves occurs between the 15 nm and 38 nm thick films in this dataset. This suggests that a fraction $f_{converted} = 50 \pm 20$ % of the metal Ni species is converted into hydroxide after 25 cycles. The associated moles per unit of surface are:

$$\frac{N_{converted}}{S} = f_{converted} \cdot \frac{\mu_0^{Ni}}{M_{Ni}} \tag{6-35}$$

where $\mu_0^{Ni} = 11\ \mu g/cm^2$ is the initial Ni mass loading equal to the 90% of the total NiFe mass loading and M_{Ni} the Ni molar mass.

By multiplying this result by equation (6-32) one obtains

$$\Delta t_{UV-VIS} = f_{converted} \cdot \frac{\mu_0^{Ni}}{M_{Ni}} \left(\frac{M_{Ni(OH)_2}}{\rho_{Ni(OH)_2}} - \frac{M_{Ni}}{\rho_{Ni}} \right) = 15 \pm 6\ nm \tag{6-36}$$

Due to its large uncertainty, this result is comparable with both the direct measurement of the thickness increase by AFM and the prediction from the electrochemical model (Figure 6-19b).

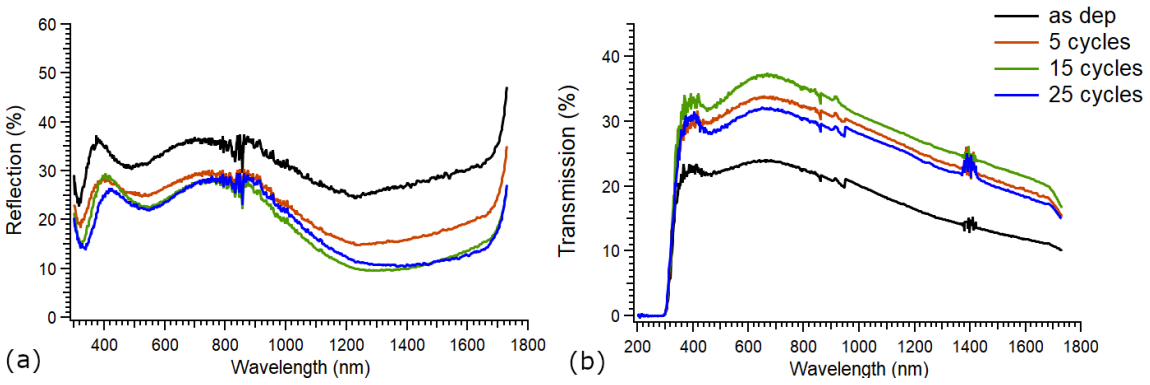

Figure 6-20. Reflectance (a) and transmission (b) optical spectra for an as deposited film and evolution over 25 cycles.

A further estimation of the thickness increase can be provided by XRD, that indicates a $f_{converted}$ =70% metal conversion into hydroxides (Figure 6-17). By plugging this value in formula (6-36), the predicted thickness increase would be:

$$\Delta t_{XRD} = 21\ nm \tag{6-37}$$

completely agreeing with the AFM direct measurement, suggesting that the film growth can be predominantly determined by the metal hydroxidation process. This implies that the thickness underestimation of the electrochemical model (13 nm prediction instead of 21 nm) is determined by fraction around 40% of $Ni(OH)_2$ species not participating to the redox

6.6.7.3 Conclusion

Microscopy techniques (AFM and SEM) show that the film morphology changes during CV cycling, with the formation of more elongated structures at the nanoscale and the exfoliation of the film at the micro-scale. Furthermore, the film thickness increases during the electrochemical test. These morphological transformations are determined by the conversion of the Ni (and Fe) metal species into hydroxides (as shown by XPS, XRD and optical spectroscopy). In particular the film growth can be directly related to the chemical transformation, as provided by the different spectroscopy techniques, through a new model presented in this work. Furthermore, a quantitative analysis of the increasing redox peaks in the electrochemical response indicates that about 40% of the total Ni hydroxide species participate to the NiOOH rfedox reactions, involving not only the film surface but also some deeper regions in the bulk.

CHAPTER 7:

NIFE ULTRA-THIN FILMS AND SINGLE NANOPARTICLE OER CATALYSIS

This chapter is based on:

L. Ciambriello, I. Alessandri, L. Gavioli, and I. Vassalini, "NiFe Catalysts for Oxygen Evolution Reaction: Is There an Optimal Thickness for Generating a Dynamically Stable Active Interface?", Submitted to ChemCatChem (Chemistry Europe)

7.1 Abstract

In this chapter, the electrochemical efficiency and stability of the NiFe nanogranular catalyst is investigated as a function of the mass loading in the 10 ng/cm^2-30 $\mu g/cm^2$ range.

Firstly, by varying the NiFe deposited density, different morphologies were explored as a result of the nanoparticle arrangement on the electrode surface. Below 300 ng/cm^2 the structures lay sparsely on the substrate revealing their individual electrochemical properties and interaction with the underlying material, while for higher loadings they aggregate and show collective catalytic properties. Above 1 $\mu g/cm^2$ continuous nanogranular films are formed, recovering the behavior described in section 5.4.

Secondly, the OER stability over 1000 potential sweep cycles was evaluated for the different morphologies, as a function of the mass loading. The electrochemical data suggest a chemical and morphological transformation of the structures, that induces a mass loading-dependent evolution during the prolonged test, before reaching a stable steady state. Upon prolonged potential sweeps the electrocatalytic performances of films decreased, while those of sparse nanoparticles were significantly improved.

This analysis provided a crucial insight on the mechanisms underlying the electrode stabilization procedure (proposed in chapter 6.4), and identifies in the 0.2-1 $\mu g/cm^2$ range the best balance in terms of catalytic efficiency and stability. These results can be considered helpful guidelines in the design and fabrication of OER electrodes form the viewpoint of large-scale production.

7.2 Introduction

In order to apply the OER technology to the industry world, a big effort was made to decrease the catalyst synthesis cost by optimizing the electrode chemical composition. The benchmark noble metal based materials [15] were replaced by mixed noble/non noble metal compounds [22], [53] or transition metal electrodes [62]. Nonetheless, the state-of-the-art catalysts are still not affordable from an industrial viewpoint, due to the still high synthesis cost and poor stability [2], [58], [61]. In this framework, two main improvements are required to make an OER large-scale development possible: 1) a further decrease in the synthesis costs through the optimization of the material morphology 2) the identification of an efficient stabilization mechanism.

From the morphological viewpoint, a wide range of micro- [43], [44] and nano- [45], [46] structures revealed promising catalytic properties arising from an enhanced electrochemical surface area (ECSA). However, no systematic study was carried out to determine the morphology/catalysis correlation. Furthermore, this issue becomes also more important if the morphological variations depend on the catalyst mass loading, since the optimization of the active material density can easily imply the reduction of the synthesis costs. Mass loading dependent investigations have been rarely addressed, involving mainly noble metal active sites. In case of transition metals, the dependence of the catalytic efficiency on the active species density [55] and on the substrate type [56] was proven, though not implying the identification of an optimized mass loading.

From the stability viewpoint, some investigations characterized and classified the different possible mechanisms leading to the electrode deactivation under prolonged activity. These range from the delamination, corrosion [27], leaching [39] and surface

capping due to O_2 bubble formation [61], [64]. In particular, it has been shown that the electrode transformation under OER activity is also determined by the equilibrium with the chemical composition of the electrolyte. It is the case of cyclic voltammetry stability test, where a process of NiFe leaching in the electrolyte is alternated with a recovery stage due to the redeposition of the metal species on the electrode surface [39], [215].

Despite these characterizations, very few remedies to the degradation have been proposed, mainly limited to spontaneous chemical modification of the material under operation [70] or to C-coatings [31], [71], that however have the drawbacks of being not controllable or limiting the electrode conductivity respectively.

In this framework, we employ supersonic cluster beam deposition (SCBD) to synthesize NiFe nanoalloyed materials of variable morphology and apply them as OER catalysts under prolonged stability tests. The electrodes morphology variability results from different nanostructures aggregation as a function of the NiFe mass loading in the 10 ng/cm^2 - 30 $\mu g/cm^2$ range. The morphology/catalysis correlation carried out in this work allowed to identify the optimized mass loading in nanogranular materials through the maximization of the TOF.

Furthermore, the prolonged OER operation revealed a mass loading-dependent electrode evolution that was correlated to a chemical and morphological transformation in the electrode. This allowed not only to interpret the mechanism underlying the stabilization procedure presented in chapter 6.4, but also to determine the most stable electrode morphology.

This work opens new insights in the development of stable and efficient OER catalysis that, thanks to the optimized mass loading and morphology, represents a promising candidate in real industrial applications.

7.3 Materials and methods

7.3.1 Preparation of NiFe electrodes at different mass loading

The electrodes consist of NiFe alloyed (90%/10% weight fraction) nanoparticles deposited through the SCBD technique on Indium/Tin oxide (ITO) conductive substrates. SCBD consists in the ablation of a bulk NiFe metal source by means of an arc discharge synchronized with a He gas pulse, followed by the condensation of nanoparticles, then ballistically deposited in vacuum (10^{-6} mbar base pressure) onto the substrate. The as deposited individual nanoparticles are characterized by a trimodal size distribution, ranging from 0.4 to 3.8 nm (see section 5.4.1). By tuning the deposition time, a set of electrodes with NiFe mass loading (μ) ranging from 10 ng/cm^2 to 30 μg/cm^2 were obtained.

7.3.2 Determination of mass loading

For values higher than 150 ng/cm^2, the determination of the mass loading in each electrode was achieved in situ during the deposition through a quartz microbalance. Due to the limited microbalance resolution, a different method was employed to determine lower mass loadings, in which the deposited nanoparticle number density was measured

by AFM and converted into mass density as described in supplementary section 7.6.1. To this aim, a Park NX10 AFM instrument with a PPP-NCSTR tip (Nanosensor, resonance frequency 120-250 Hz) was used and the images were processed through the Gwyddion software.

Since the detection of individual nanoparticles was not possible on ITO substrate due to its surface roughness (3.5 nm), for each electrode the NiFe material was also deposited simultaneously on flat (<0.1 nm roughness) Si wafers, in which the NP density was determined from the AFM images.

7.3.3 Electrochemical characterization

The NiFe electrodes were tested as OER electrocatalysts in an alkaline electrolyte (1M KOH), by employing a Pt counter electrode and a standard calomel reference electrode (SCE). The SCE electrode was calibrated before and after each use, measuring the value of the open circuit potential in a two electrode-cell using as reference electrode a new and recently calibrated (from the seller) Ag/AgCl reference electrode. The potential of SCE electrode was stable and did not show any drift under these conditions. Electrochemical impedance spectroscopy in the 600 Hz-80 kHz was performed at equilibrium potential and the ohmic drop (-iR) in the cell was calculated on the basis of the resistance value measured at 80 kHz. Cyclic voltammetry (CV) was carried out at 10 mV/s or 100 mV/s scan rates ranging from -0.5 V to +0.8 V or +1.34 V (vs SCE), respectively. The lower scan rate test was used to characterize the electrode efficiency as a function of different mass loadings for 5 cycles, while the higher scan rate was employed in 1000 cycles stability tests. For

each CV curve the current (I) was normalized by the electrode geometrical surface (S) and the potential was rescaled by subtracting the ohmic drop according to:

$$V = V_{applied} - iR \tag{7-1}$$

and referred to the reversible hydrogen reference electrode (RHE).

For each CV cycle, the overpotential η at 1 mA/cm^2 was calculated as the iR corrected potential exceeding 1.228 V (vs RHE) needed to achieve such current density. For each electrode the turnover frequency (TOF), defined here as the O_2 mole production rate normalized by the Ni+Fe deposited moles was calculated at 350 mV overpotential, as according to:

$$TOF = \frac{j}{4nF} \tag{7-2}$$

where n is the density of Ni+ Fe moles per unit of surface as calculated from the mass loading, F the Faraday constant and j the current density at η=350 mV.

The number of active sites on the electrode was estimated for each CV cycle as the number of $Ni(OH)_2$ species participating to the $Ni(OH)_2 \leftrightarrow NiOOH$ redox reaction corresponding to the electrochemical surface area (ECSA), calculated as:

$$ECSA = \frac{A_{red+ox}}{2v\sigma} \tag{7-3}$$

where $A_{(red+ox)}$ is the reduction + oxidation peak area enclosed between the forward and backward j/V curves in the 0.8-1.8 V (vs RHE) range, v is the scan rate and σ=514 μC/cm^2 is the $Ni(OH)_2$ surface charge density (assuming a single molecular layer coating). The

factor ½ is included since each single active site participate to both reduction and oxidation. The correspondent roughness factor defined as the ECSA normalized by the electrode geometrical surface (ECSA/S) was calculated for each electrode.

7.4 Results and discussions

22 thin films, with a mass loading (μ) of NiFe nanoparticles (NPs) in the 10 ng/cm^2-30 μg/cm^2 range, were deposited by SCBD on ITO substrates. SCBD was chosen for this study as it allows for depositing individual nanograins with a fine control of the surface density of the final electrode. In this way, it is possible to precisely evaluate the critical mass loading of NiFe needed to establish dynamic stability during OER.

Figure 7-1a-e show six representative AFM images of five substrates on which NiFe NPs (with a diameter of ~ 2.8 nm, in accordance with the previous results reported in section 5.4) have been deposited with increasing mass loadings, showing that they are characterized by a progressive increase of surface coverage. The two examples of low mass loadings (μ= 29±4 and μ= 75±15 ng/cm^2) show a sparse distribution of individual nanoparticles (NPs), with a surface density of 800±100 NP/μm^2 and 2000±400 NP/μm^2, respectively.

Increasing the mass loading results in a progressive coverage of the substrate and for mass loadings higher than μ=1.0 μg/cm^2 individual NPs start to stack forming a nanogranular film. In fact, μ=1.0 μg/cm^2 corresponds to the mass density ideally needed to coat completely the substrate with a monolayer composed of 2.8 nm-sized NPs. The thickness of the film increases as function of mass loading, reaching 88 nm at the maximum

value of investigated mass loadings (μ= 30 μg/cm^2). SCBD is characterized by ballistic deposition, thus an irregular NP stacking can occur, leading to an increase of surface roughness with film thickening, reaching 6 nm at 30 μg/cm^2 (see section 5.4).

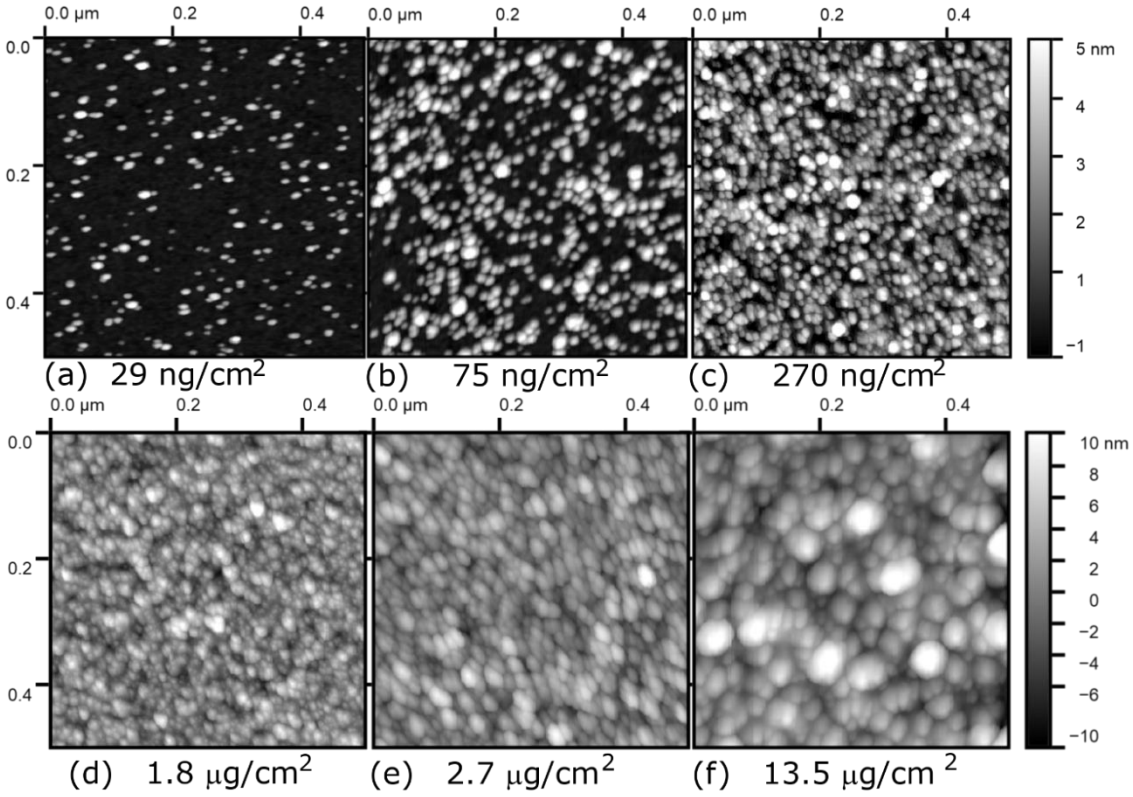

Figure 7-1. a-f) AFM images of six representative NiFe nanoparticles samples (deposited onto crystalline Si simultaneously with ITO electrodes). A progressive substrate surface coverage can be noticed.

The NiFe deposited onto conductive (ITO) substrates, were tested as OER catalysts as working electrodes in CV sweeps carried out at 10 mV/s scan rate in alkaline (KOH 1M) electrolyte. Figure 7-2a shows the j/V curves of the 1st CV cycle for five representative samples and compared to a bare ITO substrate. For potentials lower than 1.5 V vs RHE the

$Ni(OH)_2$ oxidation and reduction peaks are associated with the reversible transformation into $Ni(Fe)O_xH_y$ species.

Above 1.5 V vs RHE an exponential increase of the current density occurs, indicating the occurrence of OER. Interestingly, the onset voltage of OER current strongly depends on mass loading. At the lowest mass loading (μ=20 ng/cm^2) the OER current is 100 times higher than a pure ITO substrate, indicating that even a so limited amount of catalyst has a significant effect on the electrochemical activity of the electrode. At the lowest mass loading, the onset potential for OER is around 1.6 V vs RHE, reaching a current density of 0.5 mA/cm^2 at 1.8 V vs RHE. By increasing the mass loading, we observed a significant decrease of the onset potential for OER, passing to 1.58 V vs RHE for μ= 130 ng/cm^2 and 1.55 V for μ=270 ng/cm^2, and reaching 1.52 above 1 μg/cm^2. The onset potential did not furtherly decrease with further increase of mass loading and thickening of the film, setting at 1.5 V vs RHE for any mass loading higher than1 μg/cm^2. (Figure 7-2b)

The associated roughness factor ECSA/S was reported in Figure 7-2c as a function of the mass loading. It increased from 0.1 to 10 in correspondence of a mass loading increase from 10 ng/cm^2 to 30 μg/cm^2. This trend in ECSA/S values, which had been calculated from the area corresponding to the redox peaks related to Ni species, suggests that, when the mass loading of NiFe films exceeds the critical value of monolayer (μ>1.0 μg/cm^2), the reaction of oxy-hydroxylation is not limited to a surface layer but also involves deeper regions of the nanogranular catalyst.

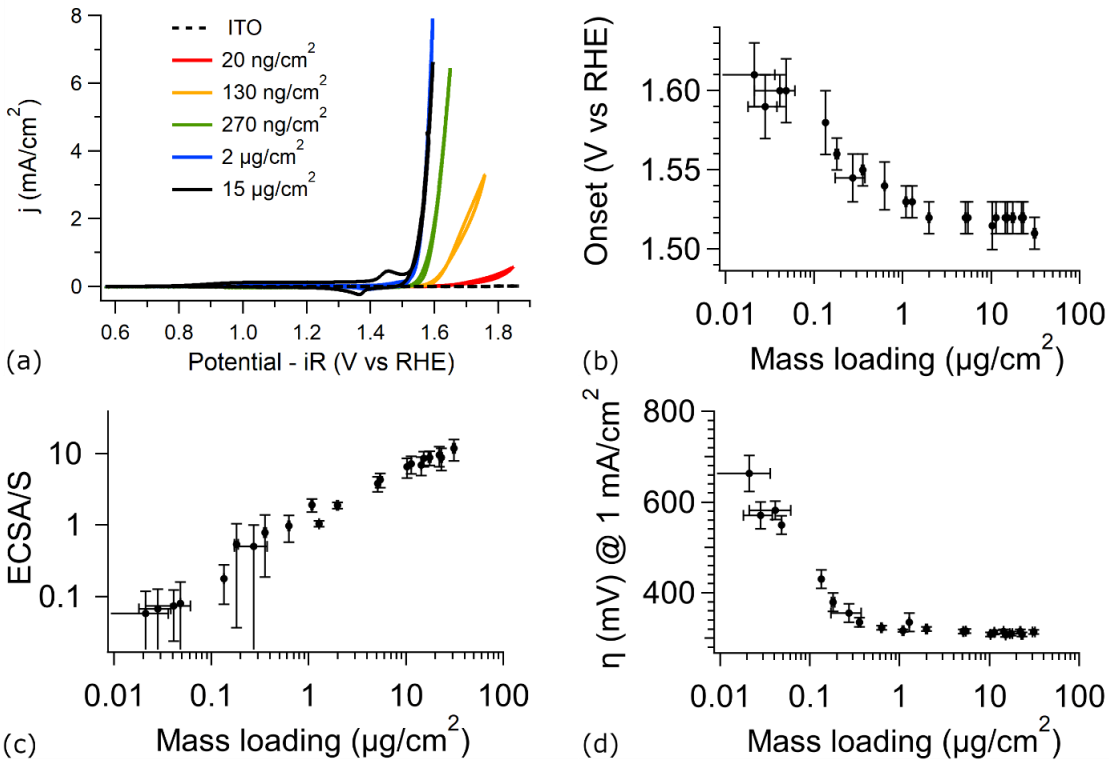

Figure 7-2. (a) j/V curves of five representative NiFe electrodes for different mass loadings. The current increases with mass loading, but it stabilizes above 1 μg/cm^2; (b) Variation of the OER onset as a function of mass loading; (c) ECSA/S (calculated as the redox peak area in the j/V curves), showing an increasing trend vs mass loading; (d) Overpotential (at 1 mA/cm^2), decreasing to reach a constant minimum value of 320 mV above 1 μg/cm^2 mass loading.

The OER efficiency of the electrodes can be quantified through the estimation of the overpotential at 1 mA/cm^2, whose trend as a function of mass loading is shown in Figure 7-2d. It is clearly visible that for very small mass loadings, very high value of overpotential were obtained (i.e 660 mV for µ= 20 ng/cm^2). However, the overpotential rapidly decreased reaching a plateau value of 320 mV for mass loadings equal to or higher than those foreseen for the formation of a monolayer (1.0 µg/cm^2). For higher values of mass loading the overpotential is stable and the OER efficiency was not affected by further increase of the NiFe deposited.

This observation is in contrast with the continuously increasing trend previously observed in relation to the roughness factor (ECSA/S) as a function of mass loading, suggesting that even if Ni(Fe) oxyhydroxide species under the surface of a multilayered electrode are effectively oxidized and reduced during CV cycles, only the species on the external surface can participate to OER. It seems that the stacking of more layers of nanoparticles prevents the catalytic activity of the regions below the surface layer.

A constant OER efficiency above $\mu = 1.0\ \mu g/cm^2$ is confirmed by the analysis of the turnover frequency (TOF), calculated at 350 mV overpotential and reported in Figure 7-3a for the 1st cycle. As discussed in supplementary section 7.6.5, the mass loading independent OER response of the electrodes results in a decreasing trend for the TOF. These data confirm what previously observed in relation to the overpotential at 1 mA (Figure 7-2d), i.e. there is no correlation between OER activity and mass loading increase for electrodes made of NiFe NPs with a thickness exceeding that of a monolayer. However, interestingly, this is valid only for mass loadings above $\mu = 1.0\ \mu g/cm^2$

At lower values of mass loadings, instead, a completely different behavior was observed. When μ ranges from 10 to 100 ng/cm^2, a very small and almost constant value of TOF ($\sim 0.05\ s^{-1}$) is obtained, probably as a consequence of the very strong interaction occurring between sparse single NiFe NPs and the substrate [56] and the poor conductivity between different catalyst NPs. These facts can negatively affect OER activity. When μ= 200 ng/cm^2 the TOF value starts to increase and reaches a maximum value of 0.9 s^{-1} for mass loadings in the 0.2-1 μg/cm^2 range. This behavior was discussed in supplementary section 7.6.5 through the elaboration of a new model to describe the catalytic response of NP assembled catalysts. These simulations support that, when the NPs are sparsely

distributed on the ITO substrate, the limited activity could be due to the NP/ITO substrate interaction. Conversely, above 300 ng/cm^2, a progressive NP stacking could occur in the ballistic deposition, resulting in a limitation of the NP/substrate interaction and in the improvement of the single particle OER activity, in agreement with the experimentally measured values.

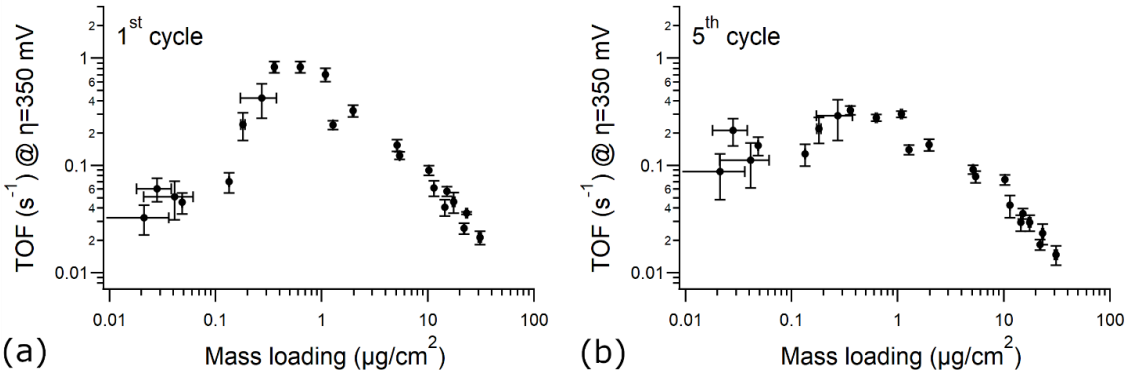

Figure 7-3. TOF values calculated from the 1st (a) and the 5th (b) cycle of CV tests (10 mV/s scan rate) as a function of the Ni+Fe mass loading.

This TOF/mass loading trend would suggest the 0.2-1 μg/cm^2 as the best morphology for the OER catalysts, in which the catalytic efficiency per unit of NiFe active sites is maximized. However, the characterization of TOF of as deposited NPs represents just an initial quality check of the catalysts. More important is the evolution of the catalytic properties as a function of electrochemical cycles. Figure 7-3b shows TOF of the catalysts after few (5) cycles.

The same decreasing TOF/loading trend observed in the case of the first CV cycle is retained for mass loadings above 1 μg/cm^2, while in the 0.3-1 μg/cm^2 region the TOF decreases of a factor 3 (0.3 s^{-1}) with respect to the first cycle. Conversely, an opposite

evolution is shown for μ<200 ng/cm^2, where an increase from 0.05 s^{-1} to 0.15 s^{-1} is observed on moving from the first to the fifth cycle. This fact suggests an improvement over cycling of their OER efficiency.

To better investigate the electrode evolution and stability, Figure 7-4a-d shows the results of 1000 cycle CV tests carried out at 100 mV/s scan rate for mass loadings of 15, 1.3, 0.09 and 0.015 μg/cm^2. The evolution over cycling of the associated overpotential at 1 mA/cm2 and roughness factor (ECSA/S) were directly calculated from the j/V curves and shown in Figure 7-4e-f. At the highest mass loading (15 μg/cm^2 in Figure 7-4a) a decrease in the OER activity occurs in the first 600 cycles, resulting in a shift of the onset potential from 1.5 to 1.65 V vs RHE, which means an increase of the overpotential at 1 mA/cm^2 from 300 to 470 mV (Figure 7-4e). The trend of the roughness factor (Figure 7-4f), which increases from 3 to 11 during the first 400 cycles and experiences a rapid drop to almost 0 around 500 CV cycles, suggests that oxidation yields an initial gradual increase of the amount of Ni-Fe hydroxide species, followed by the occurrence of an exfoliation/dissolution process. Between 400 and 500 cycles an increasing amount of electrocatalyst was transferred from to the electrode surface to the electrolyte. After 600 cycles, the OER activity did not show significant variations, setting up to a behavior similar to that obtained for an electrode with an initial mass loading of 80±10 ng/cm^2 NiFe. This residual mass is compatible with a NiFe hydroxide monolayer coating the electrode after the stability test.

Similar trends were also shown for the 1.3 μg/cm^2 electrode (around NP monolayer), even though variations are limited to a 50 mV shift in the OER onset and overpotential (Figure 7-4b).

An opposite behavior, in agreement with the 5 cycles CV tests shown in Figure 7-3b, was observed for mass loadings below 200 ng/cm^2. Figure 7-4e shows a remarkable increase in the OER efficiency, corresponding to a lowering of the overpotential for both the mass loadings of 15 and 90 ng/cm^2. In particular, in the case of μ= 15 ng/cm^2 the overpotential at 1 mA/cm^2 decreased of 300 mV, from about 900 to 600 mV, while it was limited to 50 mV in the case of μ=90 ng/cm^2. Conversely, the roughness factor maintains an almost constant value (Figure 7-4f), unlike what happens for higher mass loadings. Actually, for these low values of mass loading is very difficult to evaluate accurately the variation of the ECSA value and the related roughness factor, since no peaks ascribable to Ni(Fe) hydroxide or Ni(Fe) oxyhydroxide were clearly visible in the CV curve, since they are below the detection limit, however from the complete CV curves (Figure 7-4c and d) no insight about any material leaching from electrode can be deduced.

These results further confirm that a mechanism of dissolution/redeposition (Figure 7-4g) is at the basis of OER of NiFe electrodes in alkaline medium [67], [215], revealing the role of film morphology and mass loading.

These data allowed to obtain a detailed model that enables to estimate and quantify the electrode stability at a fixed value of overpotential as a function of mass loading (supplementary section 7.6.5). According to the models proposed in supplementary section 7.6.5, the TOF variation along CV test could be ascribed to the morphological transformation of the NiFe nanostructures from a NP shape into a monolayer (oxy)hydroxide coating of the ITO substrate. This transformation, arising from the dissolution/redeposition process (Figure 7-4g), would result in an increase of the OER active surface exposed to the electrolyte for $\mu < 200\ ng/cm^2$, and in a decrease of the

exposed surface for $\mu > 200\ ng/cm^2$. This explains the mass loading dependent variation of the catalytic response in agreement with experimental results in Figure 7-3 and Figure 7-4.

The results presented here, allow to identify in the 0.2-1 $\mu g/cm^2$ the ideal OER nanogranular catalyst, corresponding to the highest TOF (i.e. maximum OER current achieved with a minimized NiFe deposited mass) and solid stability under prolonged working conditions. In this mass loading range, in which the NPs are sparsely coating the electrode, a maximum TOF of 0.9 s^{-1} is reported, reaching a minimum overpotential of 320 mV at 1 mA/cm^2. This maximized efficiency is also accompanied by an improved stability with respect to nanogranular films, resulting even an increase in efficiency in the lowest mass loading regime upon CV tests.

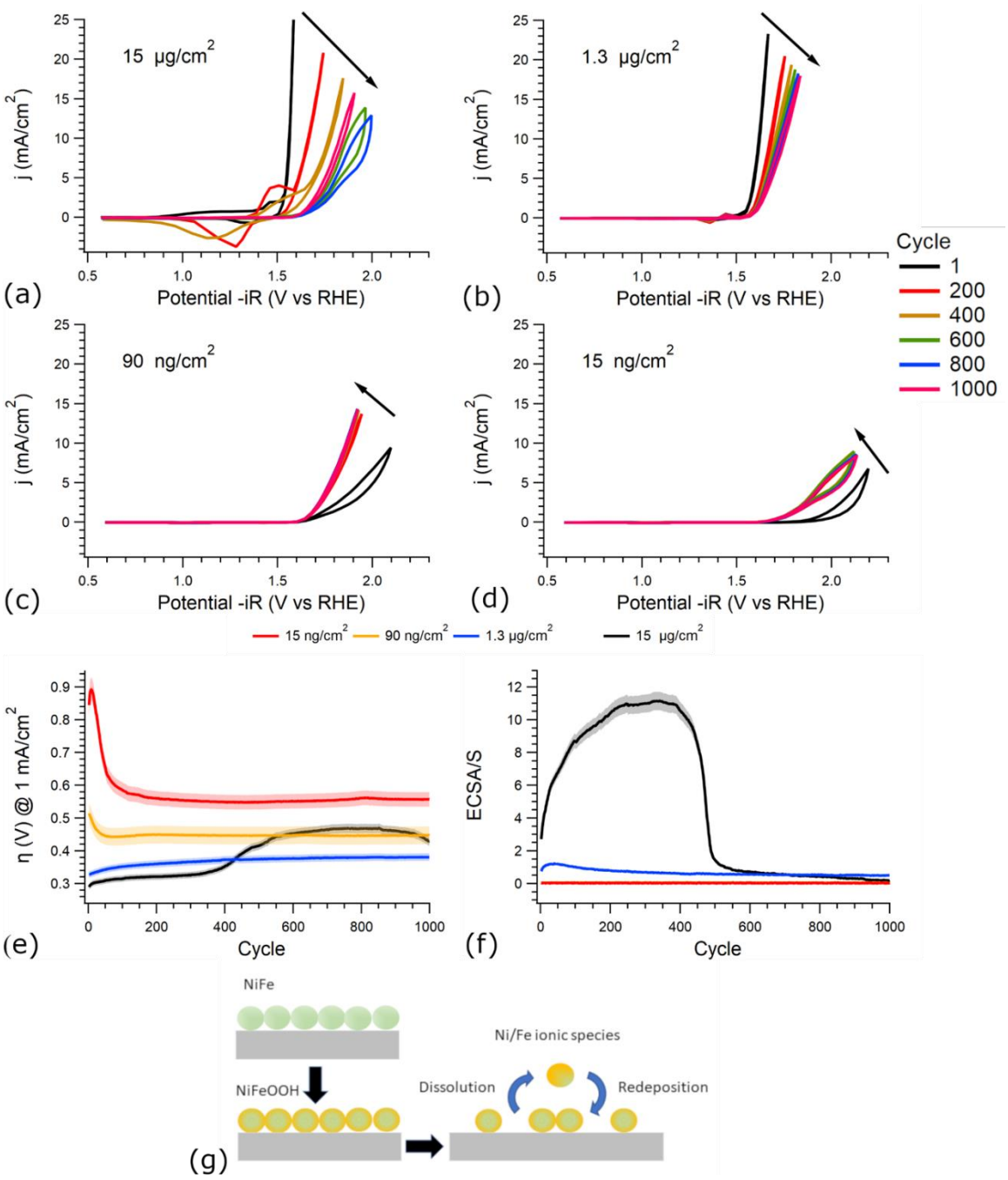

Figure 7-4. (a-d) Accelerated stability test (1000 cycles at 100 mV/s scan rate); (e-f) Trends of the overpotential (at 1 mA/cm^2) and ECSA, calculated directly from the j/V curves reported above; (g) General scheme of the dissolution/redeposition mechanism (see the main text for details).

7.5 Conclusions

This study investigated the dynamics of OER activity of NiFe (90/10) catalysts with 22 different values of mass loading, over 1000 potential sweep cycles. A wide range of morphologies were investigated by varying the mass loading in the 10 ng/cm^2-30 μg/cm^2. Below 200 ng/cm^2 the NPs are sparsely distributed on the electrode substrate (sub-monolayer distribution), whereas they aggregate above 200 ng/cm^2 and evolve into multilayers made of stacked aggregates above 1.0 μg/cm^2, giving rise to continuous porous films and reaching up to 90 nm in thickness at 30 μg/cm^2. The OER activity/morphology correlation was in depth investigated through the experimental measurement and modelling of the TOF.

In the freshly synthesized electrodes, the values of OER current of multilayered NiFe structures are higher than those of sub-monolayers, corresponding respectively to a overpotentials of 300 mV and 900 mV. However, upon prolonged potential sweeps the electrocatalytic performances of multilayers decrease, while those of monolayers are significantly improved. The experimental investigations and modelling, proposed in this work, suggest that this mass loading dependent OER evolution along prolonged test can be ascribed to a morphological transformation of the NiFe structures form nanogranular to (oxy)hydroxide coating.

These results agree with the model of dynamic dissolution/redeposition of the catalyst recently proposed in literature and, most importantly, reveal that the most stable and efficient OER catalysts can be achieved for ultrathin films with a mass loading in the

0.2-1 $\mu g/cm^2$ range. These results will allow to reduce the cost of production and environmental footprint, which are key points in view of scaling up of electrolyzers.

7.6 Supplementary

7.6.1 Mass loading determination

The quartz microbalance (employed in situ during the SCBD process) has been used to determine the Ni+Fe mass loading on the electrode through the Sauerbrey equation [216]:

$$\Delta f = -\frac{2f_0^2}{(\rho_q \mu_q)^{\frac{1}{2}}} \cdot \mu_{NiFe} \implies \mu_{NiFe} = -0.0123 \cdot \frac{\mu g}{cm^2 Hz} \Delta f \tag{7-4}$$

where Δf is the frequency variation of the quartz oscillation at the end of the deposition with respect to the initial value, $f_0 \sim 6\,MHz$ is the quartz oscillation frequency, $\rho_q = 2.648\,g/cm^3$ is the quartz density, $\mu_q = 2.95 \cdot 10^{11} g\,cm^{-1}\,s^{-2}$ is the quartz Shear modulus, and μ_{NiFe} is the Ni+Fe mass loading. This approach was considered reliable for $\Delta f > 10\,Hz$, as far as the frequency shift was considerably higher than the quartz resolution ($\sim 1\,Hz$). This case corresponds to mass loadings higher than 120 ng/cm^2.

For values lower than 120 ng/cm^2 (Δf<10 Hz), the quartz reading is characterized by a large uncertainty and a different technique was employed for the mass loading calibration. The NiFe structures were deposited simultaneously on a crystalline Si substrate, whose surface was scanned by AFM. The NiFe nanoparticle density per unit of area was then computed by processing the AFM image according to the following procedure by using the Gwyddion software [180]:

1. After flattening the Si substrate background signal, the background height profile was fitted through a gaussian distribution to identify its standard deviation (typical values are of the order of 0.1 nm)

2. A watershed mask is applied to the image. This process consists in reversing the height profile, placing virtual water drops uniformly on the surface, let the drops evolve towards local minima to form connected domains (grain location step), and finally fill each domain separately to increase their size (segmentation). The parameters employed in this process are reported in Table 7-1. Each domain is identified as a single particle.

3. To distinguish the NiFe NP from the Si background fluctuations, a selection is applied to the domains in the step 2. The domains characterized by a maximum heigh lower than three times the background standard deviation (calculated in the step 1), were ascribed to the Si substrate and excluded from the nanoparticle counting.

4. In the nanoparticle identification, the structures with a height smaller than 1.5 nm were discarded, since their detection could be variably affected by the AFM tip size and nanoparticle density on the substrate surface. This means that when a 3 nm nanoparticle and a nanoparticle with diameter<1.5 nm lay on the substrate at a distance lower than the AFM tip size, the smaller structure cannot be resolved.

TABLE 7-1:

WATERSHED PARAMETERS IN THE NANOPARTICLE DETECTION

Grain location			Segmentation	
N° steps	Drop size	Threshold	N° steps	Drop size
104	0.067%	1 px^2	9	1.677 %

Watershed parameters employed in the nanoparticle detection for the mass loading determination.

Figure 7-5 shows an example of a $1\mu m^2$ AFM image with the associated identification of NP, marked with a blue mask.

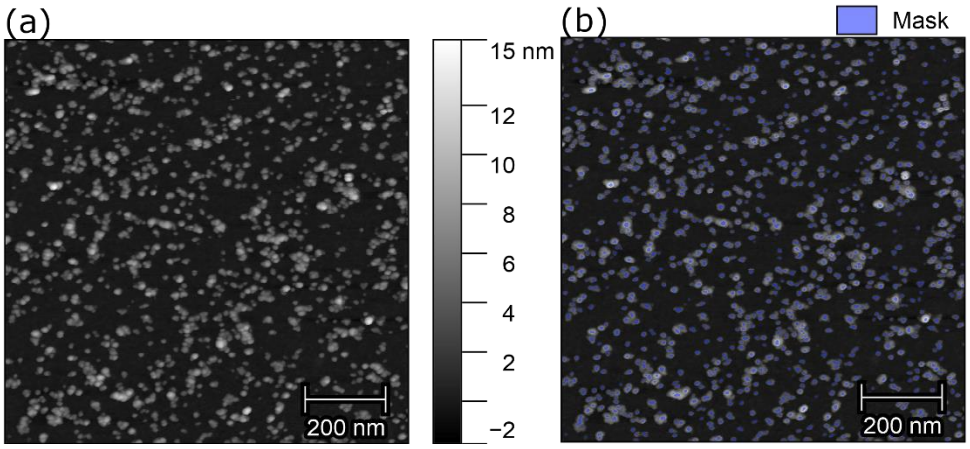

Figure 7-5. AFM image of a Si substrate with a NiFe NP distribution (a) and associated NP identification by means of the multistep process described above (b). NP are marked as blue domains.

To establish a direct correlation between the NP density (for size >1.5 nm) and the mass loading, the NP density obtained from AFM analysis was plotted as a function of the quartz frequency shift for a set of samples (Figure 7-6). For each sample a 1x1 μm^2 AFM image was analyzed, while the error bar on the NP counts is determined by the variability in the nanostructure identification upon modification of the parameters in the image masking process (Table 7-1). A linear fit was performed for $\Delta f < 10\,Hz$. The slope resulting from the fit is:

$$\frac{NP\ density}{Quartz\ \Delta f} = 337 \pm 30\ \frac{NP \cdot \mu m^{-2}}{Hz} \tag{7-5}$$

that, if opportunely converted into mass loading through (7-4) becomes:

$$\frac{Mass\ loading}{NP\ density} = (3.65 \pm 0.4) \cdot 10^{-5}\ \frac{\mu g \cdot cm^{-2}}{NP \cdot \mu m^{-2}} \tag{7-6}$$

This method allowed to reduce considerably the uncertainty on the mass loading with respect to a simple quartz microbalance output if $\Delta f < 5\ Hz$ ($\mu_{NiFe} < 60\ ng/cm^2$). Indeed, from (7-6), the mass loading was calculated with an uncertainty of 10-20 %, after obtaining the NP density from an AFM image. It should be noted that the calibrating fit in Figure 7-6 cannot be extended to $\Delta f > 10\ Hz$, since for increasingly high mass loadings the NP are sufficiently close to each other to prevent the detection of the individual structures.

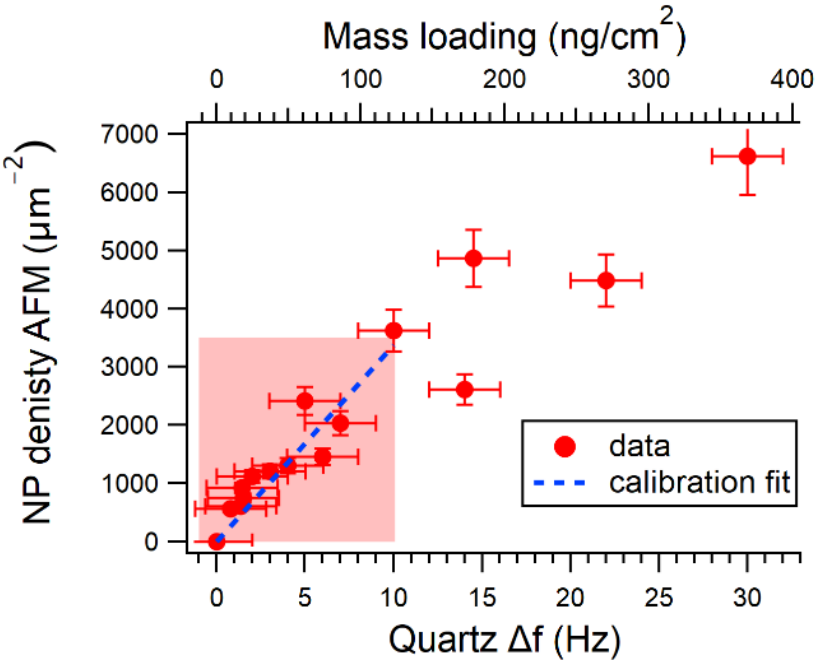

Figure 7-6. NP density measured through AFM vs the Δf frequency shift from the quartz microbalance. The dashed line is the calibration fit used to determine the mass loading/ NP density correspondence. The linear dependence between mass loading and NP density (detected by AFM) is valid in the range 0-120 ng/cm^2 (red area), where the linear fit is performed. In this range the NP number, measured directly through AFM, is converted into mass loading through the linear dependence. For higher values of the mass loading, the NP density is underestimated by the AFM, since the tip cannot resolve adjacent structures, resulting in a deviation from the linear dependence.

7.6.2 Supporting morphological characterization

The AFM images processing allowed not only to identify the number of NP per unit of surface, but also to determine the distribution of the NP size (only structures of height greater than 1.5 nm were considered, as discussed above). Figure 7-7a shows a representative NP height distribution (obtained from a 180 ng/cm^2 electrode) fitted through a gaussian curve. The same analysis was carried out for all the set of NiFe mass loadings in the $10 - 250\ ng/cm^2$ range deposited on Si. The gaussian fit was performed with the aim of just identifying the average NP size (peak maximum), while a more accurate description of the entire distribution would require a log normal modelling (as reported in section 5.4.1). The average heights are reported, with the standard deviation of the gaussian fit as error bar, in Figure 7-7b, showing a flat behavior as a function of the NP density (i.e. mass loading). This suggests no significant stacking along the z-axis. For higher mass loadings, since the AFM tip did not detect the substrate due to the higher NP density, the evaluation of the height of the individual NiFe structure was not possible. In such case, however, an average NiFe film thickness was measured, as discussed in the next section and shown in Figure 7-8.

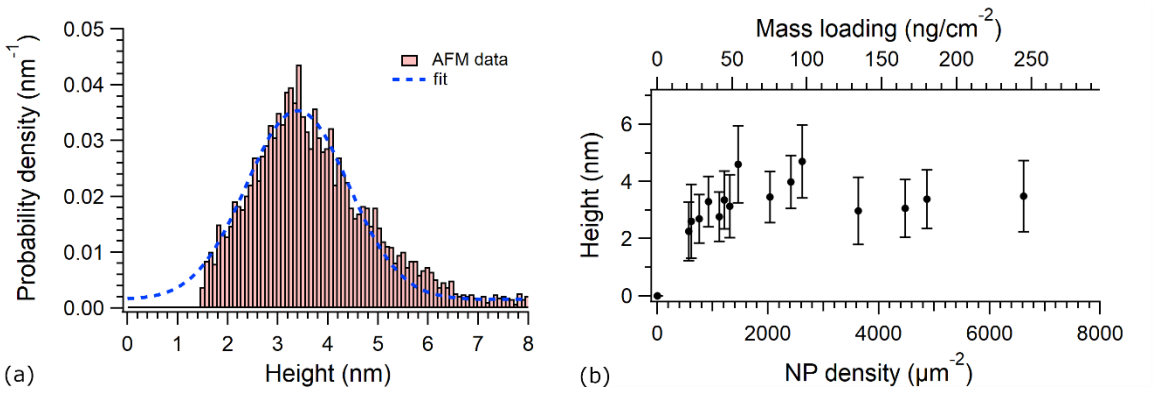

Figure 7-7. Representative histogram of the NP height distribution, fitted through a gaussian curve (a). Average NP height as a function of the mass loading (the error bar is the standard deviation from the gaussian fit) (b)

7.6.3 Film thickness and surface roughness

The NiFe NPs deposited on the electrode surface assembly and build up NiFe films resulting from the aggregation of the individual structures. As discussed in section 5.4, the film is characterized by a porous morphology, while its thickness and surface roughness increase with the mass loading. AFM allowed to directly measure the film thickness and surface roughness, reported in Figure 7-8 as a function of the mass loading.

Above 1.0 µg/cm^2, the nanogranular film coats completely the electrode surface (see Figure 7-1, main text) and the thickness is defined as the average height of the film top surface with respect to the underlying substrate. This was measured by scanning the electrode profile at the film edge, where it was possible to compare the NiFe profile with the one of the bare substrate. Conversely, below 1.0 µg/cm^2, the NiFe structures are sparse and do not cover completely the substrate, as shown in Figure 7-1 (main text). In this case, the thickness, reported in Figure 7-8a, was defined from an AFM image acquired on Si substrates as the average tip/substrate distance. From this viewpoint, uncovered regions

account as a 0 nm thick coating, while a single nanostructure as a thickness equal to the NP height. The average thickness, reported from the sparse regime to the thick films in Figure 7-8a, shows an increasing behavior as a function of mass loading.

In Figure 7-8b, the roughness was evaluated as the RMS deviation of the surface profile with respect to its average height. An increasing behavior is shown from the value of 0.8 nm recorded for sparse NPs at 30 ng/cm^2 to reach 5 nm at 30 µg/cm^2. As discussed in section 5.4, this increasing trend is expected in ballistic deposition, where the NPs arrange randomly on the electrode. The roughness reported in Figure 7-8b is calculated only for the NiFe coating, excluding the contribution of the substrate, differently from what reported in section 5.4.

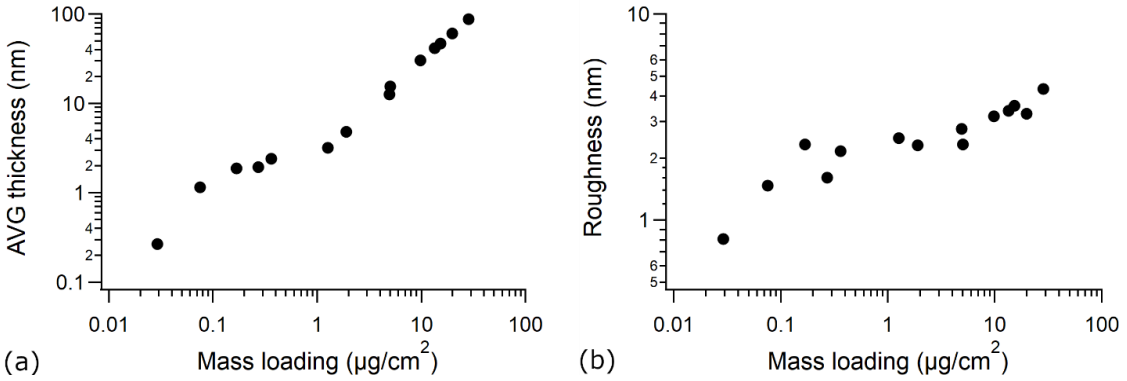

Figure 7-8. Average film thickness (a) and surface roughness (b), calculated from the AFM images.

7.6.4 Supporting electrochemical data

The electrochemical cell resistance was measured for each NiFe electrode before performing the 5 cycles CV experiments. In Figure 7-9, the measured resistance is reported as a function of the mass loading, showing a flat behavior and ruling out a dependence of the electrochemical efficiency and TOF on the ohmic drop.

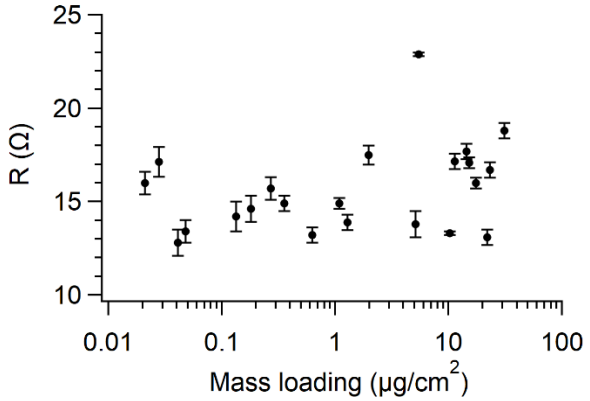

Figure 7-9. Cell resistance measured as a function of the mass loading.

The roughness factor (ECSA/S) was computed for each electrode at the 1st and 5th CV cycles (10 mV/s scan rate), by evaluating the $Ni(OH)_2$ redox peak area in the j/V curves (0.5-1.8 V vs RHE range) according to section 6.6.1. The computed values are reported as a function of the mass loading in Figure 7-10. For both the 1st and the 5th cycle, the ECSA/S values show exactly the same trend below 5 μg/cm^2. Conversely, for thicker electrodes, despite the 1st cycle data persist in the increasing behavior, in the 5th cycle the ECSA/S values stabilize around 7 with no significant dependence on the mass loading.

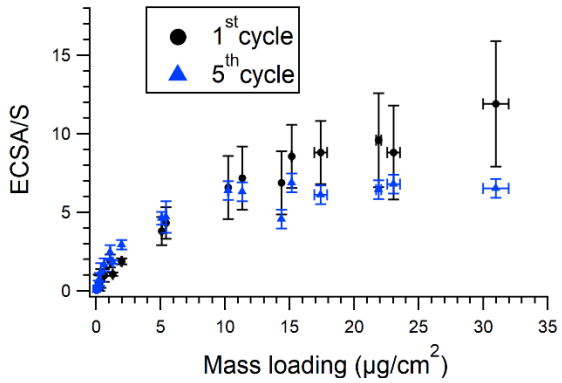

Figure 7-10. Roughness factor (ECSA/S) calculated form the $Ni(OH)_2$ redox peaks and reported as a function of the NiFe mass loading.

Figure 7-11 reports, for the 1st and the 5th CV cycles, a comparison between the TOF value at $\eta = 350\ mV$ and $\eta = 450\ mV$. Even though the values reached at 450 mV are 50 times higher than for the lower overpotential, in agreement with a 50-60 mV/dec Tafel slope (in section 6.6.1), the trends are identical.

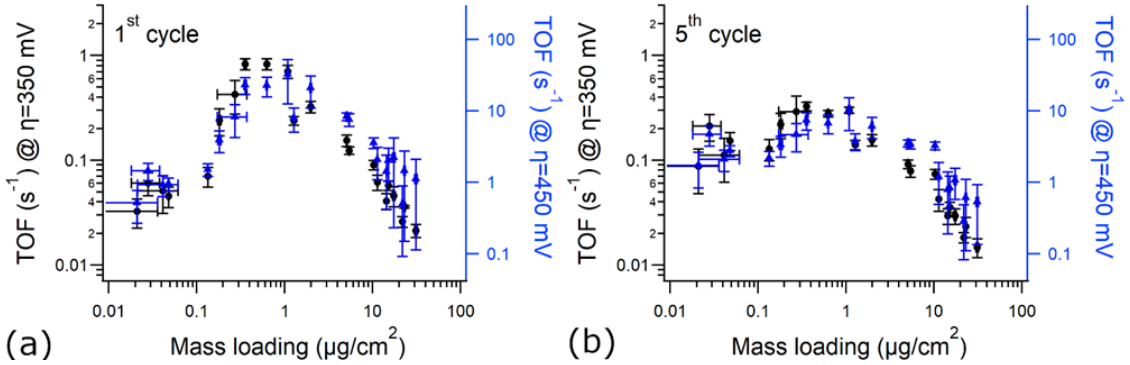

Figure 7-11. Comparison of TOF values measured at 350 and 450 mV overpotential for the 1st (a) and the 5th (b) CV cycle.

7.6.5 Modelling evolution of OER current and TOF vs mass loading

7.6.5.1 Preliminary determination of relevant quantities

In the case of a uniform and homogeneous NiFe coating of thickness h, which covers the entire electrode surface S, the total NiFe mass would be:

$$\rho_{NiFe} h S \tag{7-7}$$

where ρ_{NiFe} is the NiFe volume density. The associated mass loading would be:

$$\mu_{homogenous} = \rho_{NiFe} h \tag{7-8}$$

In case of NP assembly, instead of a homogenous morphology, the height is identified as the single NP height ($h=2r_{NP}$). Furthermore, the mass loading should be rescaled by a factor $(4/3\ \pi)/2^3$, since an ideal cube of volume $(2r_{NP})^3$ would be filled completely by a homogenous film, while just $4/3\ \pi r_{NP}^3$ volume would be occupied by a NP due to the spherical shape. The mass loading associated to an ideal NP monolayer coverage is therefore:

$$\mu_{ML} = \frac{\left(\frac{4}{3}\pi\right)}{2^3} \cdot \rho_{NP} \cdot 2 \cdot r_{Np} = 1.0\ \mu g/cm^2 \tag{7-9}$$

where a radius of r_{NP}=1.4 nm was considered for the NPs, according to the predominant size found in section 5.4.1, and ρ_{NP} corresponds to the NiFe density defined as the as deposited average density of the Ni and Fe species according to the relative stoichiometry (as reported in section 5.4) $\rho_{NP} = 37\% \cdot \rho_{Ni} + 38\% \cdot \rho_{NiO} + 25\% \cdot \rho_{Ni(OH)2} = 6.9\ g/cm^3$.

On the other hand, in view of establishing practical guidelines for film depositions, which utilizes Ni0.9Fe0.1 alloyed targets, we can also estimate the mass loading of an ideal, as deposited single NiFe homogeneous monolayer, before the occurrence of any oxidation process:

$$\mu_{ML} = \rho_{NiFe} \cdot 2r_{NP} = 2.46\,\mu g/cm^2 \tag{7-10}$$

where, $\rho_{NiFe} = 8.8\frac{g}{cm^3} = 90\% \cdot 8.9\frac{g}{cm^3} + 10\%\ 7.8\frac{g}{cm^3}$ is the average Ni+Fe mass density.

Since the layer would not be homogeneous but nanogranular the spherical shape of the grains can be taken into account by rescaling the result for the sphere/cube volume ratio

$$\mu_{ML} = \frac{\frac{4}{3}\pi}{2^3} \cdot 2.46\frac{\mu g}{cm^2} = 1.29\,\mu g/cm^2 \tag{7-11}$$

7.6.5.2 Model for the TOF evolution

In this section we present a model to interpret the variation of the current along the CV test in terms of the modification of the NP morphology. The OER current and TOF evolution over cyclic voltammetry test was modelled as a function of the morphological transformation of the NiFe structures. In particular, the NiFe mass is assumed to dissolve completely in the electrolyte and redeposit on the electrode surface as a $Ni - Fe$ hydroxide or oxyhydroxide homogenous layer. The modification in the OER current (and then in the

TOF) is determined by the variation of the surface of the NPs exposed to the electrolyte, from spherical to planar.

7.6.5.2.1 Before the CV treatment

If N is the number of NP in a geometrical surface S and μ is the mass loading, the following relation can be written (by expressing the individual NP mass as $\rho_{NP}\frac{4}{3}\pi r_{NP}^3$):

$$\mu = \frac{N}{S}\rho_{NP}\frac{4}{3}\pi r_{NP}^3$$

(7-12)

where $\rho_{NP} = 6.9\ g/cm^3$ is the effective NP mass density (combination of metal, oxide and hydroxides) and $r_{NP} = 1.4\ nm$ is the NP radius (according to section 5.4.1). By inverting equation (7-12) one obtains:

$$N = \frac{S\mu}{\rho_{NP} r_{NP}^3}\frac{3}{4\pi}$$

(7-13)

The total NiFe surface S_0 exposed to the electrolyte is obtained by multiplying the number of NP by the individual surface ($4\pi r_{NP}^2$):

$$\frac{S_0}{S} = \frac{N}{S}4\pi r_{NP}^2 = 3\frac{\mu}{\rho_{NP} r_{NP}}$$

(7-14)

Furthermore, the number of Ni moles in each NP is:

$$n_{NP} = \frac{\rho_{NP}}{m_{NP}}\frac{4}{3}\pi r_{NP}^3$$

(7-15)

where $m_{NP} = 37\% \cdot 59\frac{g}{mol} + 33\% \cdot (59+16)\frac{g}{mol} + 25\% \cdot (59+34)\frac{g}{mol} + 5\% \cdot (59+56+16)\frac{g}{mol} = 76.38\ g/mol$ is the as deposited nanoparticle averaged molar mass (considering Ni metal, NiO, $Ni(OH)_2$ and NiFeOx fractions as found in section 5.4).

7.6.5.2.2 After the CV treatment

After the CV treatment, we assume that the total amount (moles) of Ni enclosed in each single NP (in equation (7-15)) is completely dissolved in the electrolyte and redeposited on the electrode as a hydroxide or oxyhydroxide monolayer of volume V_f. If S_f^{NP} is the electrode surface covered by this monolayer structure, its volume can be expressed as $V_f = S_f^{NP} t_f$, where t_f is the thickness. In such volume, the number of Ni (oxy)hydroxide molecules is:

$$\frac{\rho_f V_f N_A}{m_f} \tag{7-16}$$

where m_f and ρ_f are the Ni hydroxide or oxyhydroxide molar mass and density and N_A is the Avogadro number.

Then, the volume of a single Ni (oxy)hydroxide molecule can be calculated by dividing V_f by the number of molecules in eq. (7-16):

$$\frac{m_f}{\rho_f N_A} \tag{7-17}$$

The average Ni (oxy)hydroxide diameter, i.e. the thickness of a monolayer, is then:

$$t_f = \left(\frac{m_f}{\rho_f N_A}\right)^{\frac{1}{3}}$$

(7-18)

The volume V_f of the monolayer (formed after the CV) can be also expressed in terms of the initial volume (or number of Ni moles) of the as deposited NP (eq. (7-15)):

$$V_f = \frac{n_{NP} m_f}{\rho_f} = \frac{4}{3}\pi r_{NP}^3 \frac{\rho_{NP}}{\rho_f}\frac{m_f}{m_{NP}}$$

(7-19)

where the first equality is due to the fact that the as deposited NP and the final structure contain the same Ni moles, while the second one was obtained through eq. (7-15).

From eq. (7-19) we can then calculate the monolayer surface S_f^{NP}, that corresponds also to the surface exposed to the electrolyte in the final structure:

$$S_f^{NP} t_f = V_f = \frac{4}{3}\pi r_{NP}^3 \frac{\rho_{NP}}{\rho_f}\frac{m_f}{m_0}$$

(7-20)

that implies:

$$S_f^{NP} = \frac{4}{3}\pi r_{NP}^3 \frac{\rho_{NP}}{\rho_f}\frac{m_f}{m_{NP}}\frac{1}{t_f}$$

(7-21)

The final total surface S_f exposed to the electrolyte is obtained by multiplying the result for the total number of nanostructures:

$$\frac{S_f}{S} = \frac{N}{S} S_f^{NP} = \frac{\mu}{\rho_f}\frac{m_f}{m_{NP}}\frac{1}{t_f}$$

(7-22)

In this equation the final surface is linearly increasing with the mass loading. However, since the final structure is a planar, the total surface cannot exceed the electrode geometrical surface. In this assumption, in case the total active sites exceed the monolayer coverage, the excess mass will be either added to the monolayer as an additional layer or dissolved in the electrolyte, without determining an increase in the exposed surface. Therefore, the final surface should be corrected by imposing a maximum of 100% of the electrode geometrical surface coverage:

$$\frac{S_f}{S} = \min\left\{1, \frac{\mu}{\rho_f}\frac{m_f}{m_{NP}}\frac{1}{t_f}\right\} \tag{7-23}$$

The current relative change with respect to the initial value is then computed as the ratio of the final/initial exposed surfaces:

$$\frac{S_f}{S_0} = \min\left\{\frac{\rho_{NP} r_{NP}}{3\mu}, \frac{\rho_{NP} r_{NP}}{3\rho_f}\frac{m_f}{m_{NP}}\frac{1}{t_f}\right\} \tag{7-24}$$

where t_f is defined in eq. (7-18).

7.6.5.3 Results

Figure 7-12a shows the experimental relative variation of OER current density at η=350 mV (Δj/j) over 1000 CV cycles (100 mV/s) as a function of mass loading. As discussed in the main text, since the electrochemical activity is still observed even for prolonged cycles of potential sweeps, part of the NiFe NPs that had been leached in the electrolyte are expected to dynamically redeposit on the electrode surface. This mechanism

is expected to determine the experimentally measured $\Delta j/j$ behavior in Figure 7-12a. The experimental data show a flat behavior around 2, for mass loadings lower than 100 ng/cm^2, corresponding to an increase of OER efficiency as discussed in the main text. An opposite trend was instead found for higher mass loadings, where around 1 and 10 $\mu g/cm^2$ a $\frac{\Delta j}{j} \sim -1$ is reported, as a consequence of a decrease in efficiency.

To interpret these experimental results, we employed the model described above in eq. (7-24), in which we calculated the expected OER current variation in the assumption that the redeposition occurs as a single layer of Ni(Fe) (xoy)hydroxide. Under this hypothesis, any modification in the OER efficiency, expressed as Δj/j, was extrapolated by calculating and modelling the variations of the exposed NiFe surface area from the initial (nanogranular) to a final (flat) morphology, consisting of a monolayer of Ni(Fe) (oxy)hydroxide, which can be further approximated as a monolayer of Ni (oxy)hydroxide.

Figure 7-12a shows the $\Delta j/j$ curve (black dashed line) calculated through the model, in which a complete $Ni(OH)_2$ final composition is considered, corresponding to the parameters $\rho_f = 4.1\ g/cm^3$, and $m_f = 93\ g/mol$ (implying $t_f = 0.34\ nm$) in eq. (7-24). This mass loading dependent trend is completely reproduced by the model, identifying the threshold value of 200 ng/cm^2 as the transition point (at which $\Delta j/j \sim 0$) between the improvement ($\Delta j/j > 0$) and the deterioration ($\Delta j/j < 0$) of the electrode efficiency along CV. According to the model, below this critical mass loading the final NiFe monolayer rearrangement is characterized by a greater exposed surface with respect to the initial NP configuration, due to the change of the morphology. Conversely for higher mass loadings, a denser initial NP density corresponds to a higher initial exposed surface with respect to a complete monolayer coating.

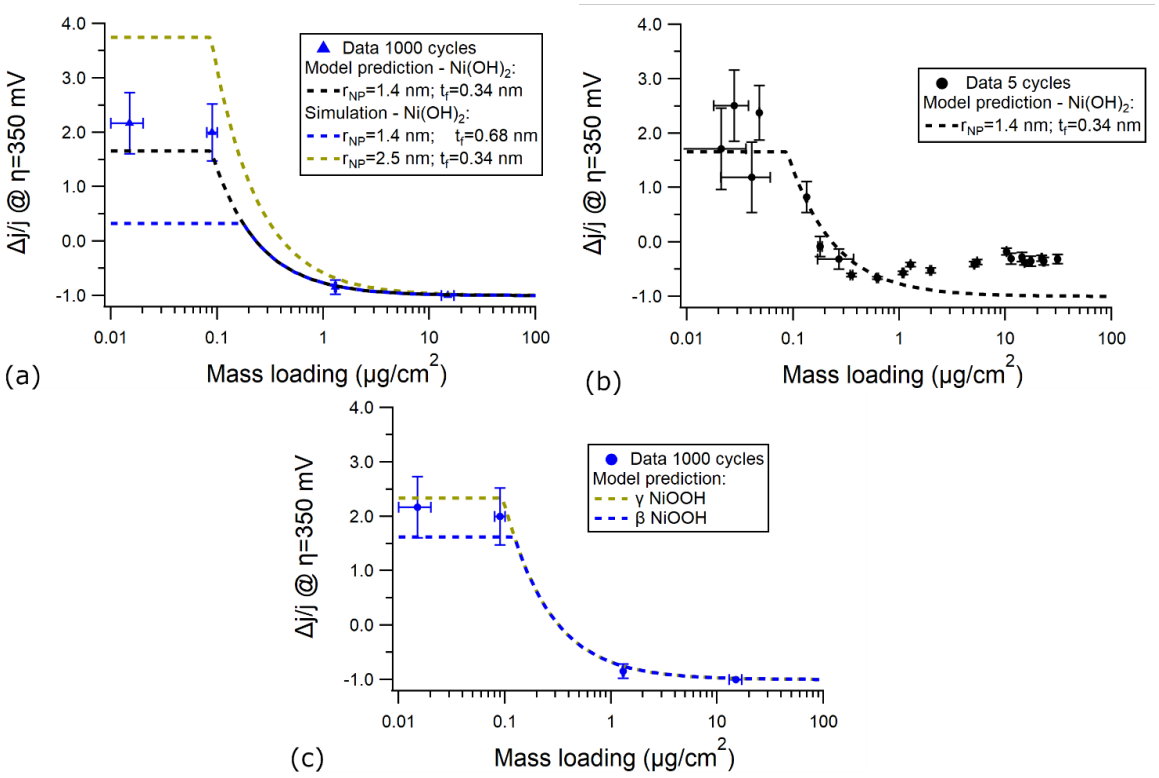

Figure 7-12 a) Comparison of experimental data (triangles with error bars) and model predictions under different assumptions for Δj/j at η=350 mV for the films with four different mass loadings after 1000 CV cycles; b) comparison of experimental data (dots with error bars) and model predictions for Δj/j at η=350 mV for films with different mass loadings after 5 CV cycles. In a) and b) a $Ni(OH)_2$ chemical composition post CV is assumed in the simulation. c) Model prediction considering NiOOH in the final monolayer.

The same model also enables the extrapolation of a mass loading μ= 100 ng/cm^2, for which it is possible to differentiate between the flat and the decreasing trend. For μ<100 ng/cm^2, each original nanoparticle is dissolved in the electrolyte and all the leached material is completely redeposited on the ITO substrate, forming a single Ni(Fe) hydroxide monolayer and coating partially the electrode surface. Conversely, for μ> 100 ng/cm^2 the electrode is completely covered by the hydroxide monolayer and the mass deriving from

original NiFe is higher than the one that is redeposited, with a fraction of material remaining dissolved in the electrolyte.

It should be noticed that the prediction is highly affected by the NP initial radius and the final coating thickness, input parameters in the model, since the modification of such values (increasing $r_{NP}$to 2.5 nm or t_f to 0.68 nm) lead to significant differences in the prediction (dashed yellow and blue lines in Figure 7-12a). In Figure 7-12b, the same relative current variation is instead reported after 5 CV cycles (10 mV/s). The flat behavior around 2 is confirmed below $100\ ng/cm^2$, while a decrease is reported for higher mass loadings. Despite the model qualitatively agrees with the measured points, a deviation above 1 $\mu g/cm^2$ can be ascribed to an incomplete process of stabilization of the electrode after such short CV test.

In Figure 7-12c, we also report the model prediction in case NiOOH is assumed to compose the monolayer coating instead of $Ni(OH)_2$. In eq. (7-24), a value $m_f = 92\ g/mol$ is considered, while two possible values for the oxyhydroxide density, $\rho_f = 3.2\ g/cm^3$ or $\rho_f = 4.6\ g/cm^3$, are taken into account, associated respectively to the γ and β phases ($t_f = 0.36$ nm or 0.32 nm). This lead to two predicted $\Delta j/j$ curves, both characterized by the initially flat and then decreasing trend. The two curves are coincident above 100 -200 ng/cm^2, while a 0.8 shift between the two occurs in the flat region. Nonetheless both the predictions remain compatible with experimental data, compatibly with the presence of NiOOH.

7.6.5.4 Model for the freshly deposited electrode TOF

In this section a new model is presented to quantify the TOF of freshly deposited NiFe nanogranular electrodes obtained through ballistic deposition techniques, as a function of the mass loading. The parameters involved in the model are listed in Table 7-2.

Let σ_{NP} be the geometrical surface covered by a single nanostructure when deposited on the substrate, i.e. the projection of the volume of the nanostructure on the horizontal plane. For instance, in case of spherical nanoparticles $\sigma_{NP} = \pi r_{NP}^2$, where r_{NP} is the NP radius. Furthermore, let us imagine depositing a number of n of nanostructures on a geometrical electrode surface S. In a ballistic process, the NPs have a uniformly distributed probability of being deposited on each point of the surface S. When an individual NP lands on a certain point of the electrode surface, it can either become in contact with the substrate, if there are no other structures in that point, or either stack on other NPs. After the deposition the electrode profile is then characterized by randomly distributed empty regions or NPs clusters and stacks.

For a given number n of NPs, let $\theta_1(n)$, $\theta_2(n)$ and $\theta_{3+}(n)$ be defined as the fraction of the surface S covered by respectively just one NP, a stack of two NPs or a stack of three or more NPs. If in such system of n nanostructures one further NP is ballistically deposited, the θ_1 coverage will increase by σ_{NP}/S only if the NP hits an empty region (with probability $1 - \theta_1 - \theta_2 - \theta_{3+}$), while θ_1 decreases by σ_{NP}/S if the NP stacks with another structure (with probability θ_1). This leads to the equation:

$$\theta_1(n+1) - \theta_1(n) = \frac{\sigma_{NP}}{S}[1 - \theta_1(n) - \theta_2(n) - \theta_{3+}(n)] - \frac{\sigma_{NP}}{S}\theta_1(n) \quad (7\text{-}25)$$

A similar equation can be written for θ_2: an increase of σ_{NP}/S occurs if the NP stacks with another structure (probability θ_1) or a decrease occurs if the NP hits a region with two layers of NSs (probability θ_2):

$$\theta_2(n+1) - \theta_2(n) = \frac{\sigma_{NP}}{S}\theta_1(n) - \frac{\sigma_{NP}}{S}\theta_2(n)$$

(7-26)

Finally, the θ_{3+} coverage increases only if the NP lands on a two-layer stack:

$$\theta_{3+}(n+1) - \theta_{3+}(n) = \frac{\sigma_{NP}}{S}\theta_2(n)$$

(7-27)

These three equations can be rewritten as a third-order Cauchy problem:

$$\begin{cases} \frac{d\theta_1}{dn} = \frac{\sigma_{NP}}{S}[1 - 2\theta_1 - \theta_2 - \theta_{3+}] & (a) \\ \frac{d\theta_2}{dn} = \frac{\sigma_{NP}}{S}[\theta_1 - \theta_2] & (b) \\ \frac{d\theta_{3+}}{dn} = \frac{\sigma_{NP}}{S}\theta_2 & (c) \\ \theta_1(0) = 0 & (e) \\ \theta_2(0) = 0 & (f) \\ \theta_3(0) = 0 & (g) \end{cases}$$

(7-28)

By plugging eq. (7-28)c and (7-28)b in eq. (7-28)a, a third order linear differential equation in θ_{3+} can be found, with associated boundary conditions:

$$\begin{cases} \left(\frac{S}{\sigma_{NP}}\right)^3 \frac{d^3\theta_{3+}}{dn^3} + 3\left(\frac{S}{\sigma_{NP}}\right)^2 \frac{d^2\theta_{3+}}{dn^3} + \left(\frac{S}{\sigma_{NP}}\right)\frac{d\theta_{3+}}{dn} + \theta_{3+} = 1 & (a) \\ \theta_{3+} = \frac{d\theta_{3+}}{dn} = \frac{d^2\theta_{3+}}{dn^2} = 0 & (b) \end{cases}$$

(7-29)

The solution of the system in eq. (7-29) is $\theta_{3+} = 1 - \left(1 + \frac{\sigma_{NP}}{S} n + \frac{1}{2}\left(\frac{\sigma_{NP}}{S}\right)^2 n^2\right) e^{-\frac{\sigma_{NP}}{S} n}$, while θ_1 and θ_2 can be found by plugging the result in eq. (7-28)b-c. The overall solution of the system in eq. (7-28) is:

$$\begin{cases} \theta_{3+} = 1 - \left(1 + \dfrac{\sigma_{NP}}{S} n + \dfrac{1}{2}\left(\dfrac{\sigma_{NP}}{S}\right)^2 n^2\right) e^{-\frac{\sigma_{NP}}{S} n} \\ \theta_2 = \dfrac{1}{2}\left(\dfrac{\sigma_{NP}}{S}\right)^2 n^2 e^{-\frac{\sigma_{NP}}{S} n} \\ \theta_1 = \dfrac{\sigma_{NP}}{S} n e^{-\frac{\sigma_{NP}}{S} n} \end{cases}$$

(7-30)

Furthermore, the factor $\frac{\sigma_{NP}}{S} n$ can be rewritten as:

$$\frac{\sigma_{NP}}{S} n = \frac{\mu}{\mu_0}$$

(7-31)

where the mass loading is expressed as $\mu = \frac{V_{NP} \rho_{NP} n}{S}$ (with V_{NP} and ρ_{NP} the as deposited NP volume and volume density), while μ_0 is defined as:

$$\mu_0 = \frac{V_{NP}}{\sigma_{NP}} \rho_{NP}$$

(7-32)

It should be noted that the μ_0 variable depends on the ratio between NP volume and projected surface, that depends on the structure morphology. By using eq. (7-31), the result in (7-30) can be rewritten as

$$\begin{cases} \theta_{3+} = 1 - \left(1 + \frac{\mu}{\mu_0} + \frac{1}{2}\left(\frac{\mu}{\mu_0}\right)^2\right) e^{-\frac{\mu}{\mu_0}} \\ \theta_2 = \frac{1}{2}\left(\frac{\mu}{\mu_0}\right)^2 e^{-\frac{\mu}{\mu_0}} \\ \theta_1 = \frac{\mu}{\mu_0} e^{-\frac{\mu}{\mu_0}} \end{cases}$$

(7-33)

More generally, one can find that, in case of a stack of k NPs, the result is $\theta_k = \frac{1}{k!}\left(\frac{\mu}{\mu_0}\right)^k e^{-\frac{\mu}{\mu_0}}$.

The TOF value can be calculated from eq. (7-33), according to the following steps:

- If j_0 is the OER current per unit of NP surface area, each single NP produces:

$$I_{NP} = S_{NP} j_0$$

(7-34)

  where S_{NP} is the NP surface exposed to the electrolyte. We assume that in each point of the electrode surface just the top NP of the stack is participating to the OER current. Therefore, in each point of the electrode, the current density is obtained by normalizing the single particle current in eq. (7-34) (generated by the top NP in the stack) by the projected geometrical area occupied by the NP stack (σ_{NP}).

$$j = \frac{S_{NP}}{\sigma_{NP}} \cdot j_0$$

(7-35)

- The current density in eq. (7-35) should be then corrected considering that only the fraction of the electrode surface covered by at least one NP ($\theta_1 + \theta_2 + \theta_{3+}$) contributes to the current:

$$j = \frac{S_{NP}}{\sigma_{NP}} \cdot j_0(\theta_1 + \theta_2 + \theta_{3+})$$

(7-36)

- Furthermore, we assume that the contribution of NPs that lay in contact with the ITO substrate or in a 2 NPs stack is attenuated by a factor α. This can be ascribed to a NP/substrate interaction. This leads to a correction of the current as:

$$j(\mu) = \frac{S_{NP}}{\sigma_{NP}} \cdot j_0 \cdot (\alpha\theta_1 + \alpha\theta_2 + \theta_{3+}) = \\ = \frac{S_{NP}}{\sigma_{NP}} \cdot j_0 \\ \cdot \left[\alpha \frac{\mu}{\mu_0} e^{-\frac{\mu}{\mu_0}} + \alpha \frac{1}{2} \left(\frac{\mu}{\mu_0}\right)^2 e^{-\frac{\mu}{\mu_0}} + \left(1 - \frac{\mu}{\mu_0} e^{-\frac{\mu}{\mu_0}} - \frac{1}{2} \left(\frac{\mu}{\mu_0}\right)^2 e^{-\frac{\mu}{\mu_0}}\right)\right] \tag{7-37}$$

- The TOF value is then found as:

$$TOF(\mu) = \frac{M_{NiFe}}{4eN_A} \cdot \frac{j(\mu)}{\mu} \tag{7-38}$$

with $j(\mu)$ defined in eq. 35 and $M_{NiFe} = 58.4\ g/mol$ is the average Ni+Fe molar mass (considering 90/10 relative fraction).

Figure 7-13 shows that the model in eq. (7-38) correctly describes the trend of TOF for the as deposited electrodes. The lower OER efficiency below 200 ng/cm^2 can be ascribed to the strong NP/ITO interaction that reduces of 98% (see value for α in Table 7-2) the single NP activity. Furthermore, when the NPs start to stack for higher mass loadings, this attenuation progressively disappear, leading to the maximum OER efficiency. Then, above 1 $\mu g/cm^2$, the NPs reach an average monolayer coverage of the substrate and the addition of further structures to the continuous film does not determine an improvement of the OER current, confirming that just the NP at the film surface participate to the catalysis. In the logarithmic TOF plot, this correctly results in a linearly decreasing trend that can be easily predicted from eq. (7-38). Indeed, for a complete coverage of multiple NP stack, $\theta_1 = \theta_2 = 0$, θ_{3+}=1 and eq. (7-38) becomes:

$$TOF(\mu) = \frac{M_{NiFe}}{4eN_A} \cdot \frac{S_{NP}}{\sigma_{NP}} \cdot \frac{j_0}{\mu} \tag{7-39}$$

It should be noted that the experimental TOF trend is reproduced if the geometrical factors $\frac{V_{NP}}{\sigma_{NP}} \sim 0.43\ nm$ and $\frac{S_{NP}}{\sigma_{NP}} \sim 1.4$ are assumed. This values, deviating the values of $\frac{4}{3} r_{NP} = 1.8\ nm$ and $4\pi r_{NP}^2 / \pi r_{NP}^2 = 4$, suggest that the NPs are characterized by a non-spherical shape, also confirmed in section 5.4.1.

TABLE 7-2:

PARAMETERS INVOLVED IN THE TOF MODEL

Parameter	Value in the simulation	Description
$\frac{S_{NP}}{\sigma_{NP}}$	1.4	Geometrical factor accounting for the NP exposed surface/projected surface
$\frac{V_{NP}}{\sigma_{NP}}$	0.43 nm	Geometrical factor accounting for the NP volume/projected surface
α	0.02	Attenuation factor in the OER activity for particles in contact with the substrate
j_0	4 mA/cm^2	Current density per unit of nanostructure area at η=350 mV

Parameters involved in the model.

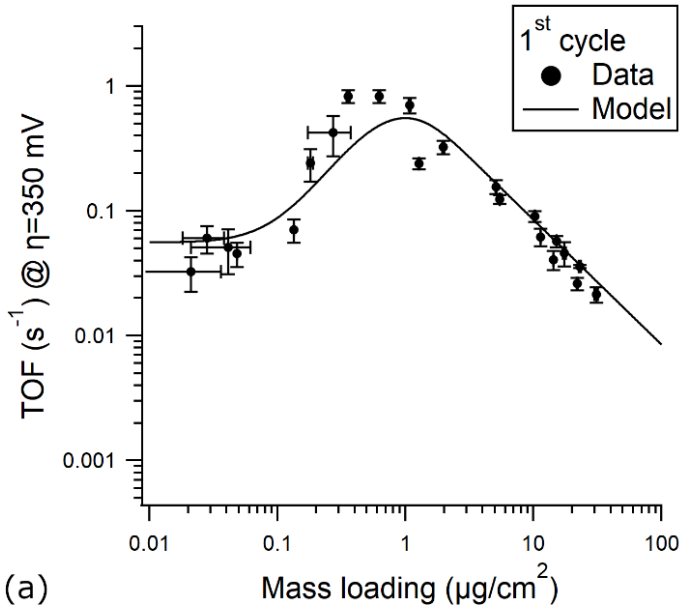

Figure 7-13. TOF behavior simulated according to eq. (7-38) and compared to experimental data.

7.6.5.5 Model for the TOF after CV

After the CV tests, the NP material is assumed to completely rearrange in a uniform and homogenous hydroxide or oxyhydroxide monolayer coating the electrode surface. In order to compute the fraction of the electrode covered by the redeposited hydroxide, a critical mass loading value $\mu_c = \rho_f \cdot t_f$ can be defined (where ρ_f and t_f are the hydroxide or oxyhydroxide density and molecular monolayer thickness defined in eq. (7-18)), so that:

- If $\mu > \mu_c$ the initial NiFe mass loading in the as deposited electrode exceeds the minimum value needed to cover completely the electrode surface, after the redeposition as hydroxide monolayer. In this case we assume that, after the CV test, 100 % of the surface is coated by the hydroxide monolayer. Excess NiFe mass can either be dispersed in the electrolyte or redeposit on the electrode surface as additional layers, without increasing the surface coverage and the number of active sites exposed to the electrolyte.

- If $\mu < \mu_c$, in the assumption that all the NiFe mass is redeposited as hydroxide monolayer, the electrode surface would result partially coated. The fraction of covered surface would be μ/μ_c.

The surface coverage in both the cases above can be expressed through the equation:

$$coverage = \min\left(\frac{\mu}{\mu_c}, 1\right)$$

(7-40)

The current density can be then deduced by multiplying the covered surface by the current density per unit of active area j_0 (defined in (7-34)):

$$j^{CV}(\mu) = \alpha \cdot j_0 \cdot \min\left(\frac{\mu}{\mu_c}, 1\right)$$

(7-41)

where the attenuation factor $\alpha = 0.02$ is considered in order to account for the active site/ITO interaction, similarly to the NPs in contact with the substrate for the as deposited electrodes.

The TOF can be then expressed as:

$$TOF^{CV}(\mu) = \frac{M_{NiFe}}{4eN_A} \cdot \frac{j^{CV}(\mu)}{\mu}$$

(7-42)

Figure 7-14a reports the experimentally measured TOF at the end of a 1000 CV cycle, compared to the model output from eq. (7-42), calculated in the assumption of $Ni(OH)_2$ chemical composition of the monoloayer. In the model parameters, this corresponds to $\rho_f = 4.1\ g/cm^3$, $t_f = 0.34\ nm$ and $\mu_c = 140\ ng/cm^2$. The model, consistently with experimental data, predicts a constant TOF value around 0.1 Hz for $\mu < 140\ ng/cm^2$, while for higher mass loading the prediction agrees with the measured

decreasing trend to reach 0.001 Hz at 15 $\mu g/cm^2$. According to the interpretation in the model, below 140 ng/cm^2 the surface coverage (and then the OER current) is proportional to the mass loading and the current/mass loading ratio appearing in the TOF is then constant (see eq. (7-42), where $TOF^{CV} = \frac{M_{NiFe}}{4eN_A} \cdot \alpha \cdot \frac{j_0}{\mu_c}$ results independent of μ). Conversely, above 140 ng/cm^2, a constant 100% coverage (and constant OER current) is independent of the mass loading and the TOF decreasing trend is expressed as:

$$TOF^{CV}(\mu) = \frac{M_{NiFe}}{4eN_A} \cdot \frac{\alpha \cdot j_0}{\mu} \tag{7-43}$$

In Figure 7-14b, we also report the model prediction in case NiOOH (in γ and β phases) is assumed as post CV chemical composition. For both oxyhydroxide phases (with parameters $\rho_f = 3.12\ g/cm^3$ and $\mu_c = 120\ ng/cm^2$ for the γ compound, $\rho = 4.6\ g/cm^3$ and $\mu_c = 150\ ng/cm^2$ for the β type), the two predictions are coincident above 150 ng/cm^2. Conversely, despite for lower mass loadings these are characterized by a 20% difference in the flat region, in both cases the simulated curves agree with the experimental values, compatibly with the presence of NiOOH.

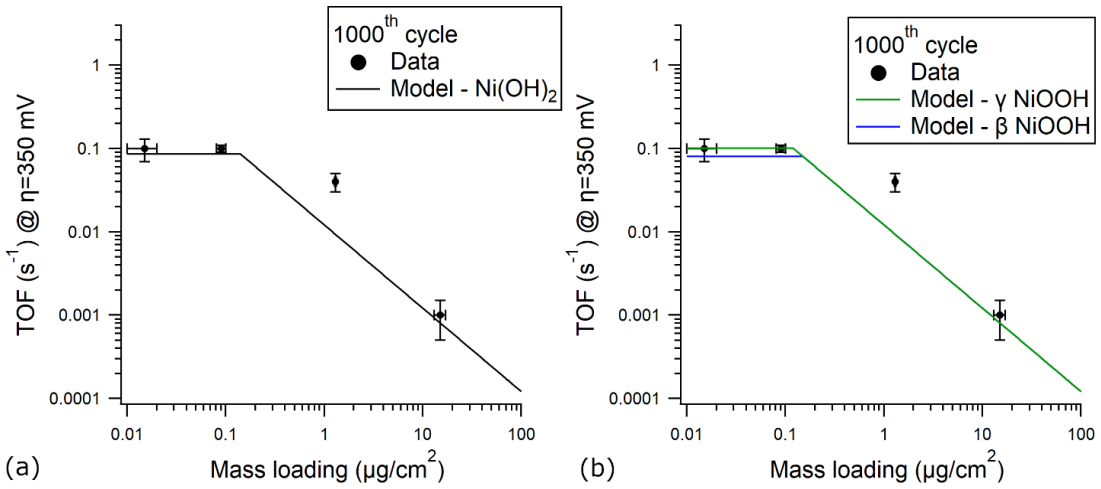

Figure 7-14. TOF behavior simulated according to (7-42) and compared to experimental data. In the simulation a $Ni(OH)_2$ (a) or NiOOH final composition is assumed.

CONCLUSIONS

In this dissertation a novel NiFe nanoalloyed electrode was synthesized through supersonic cluster beam deposition in order to face the two main challenges in the OER catalysis: 1) the optimization of the material morphology and 2) the achievement of a stability under prolonged activity.

The freshly synthesized material and its efficiency as OER catalyst were characterized through many spectroscopy and microscopy techniques as a function of the NiFe mass loading in the 10 ng/cm^2 – 30 $\mu g/cm^2$. The catalyst was composed by individual nanoparticle of size between 0.3 and 3 nm, in which the Ni and Fe species (90/10 % alloying fraction) were partially oxy-hydroxidized as a result of a high reactivity in ambient air and in the electrochemical cell. The nanoparticles aggregation resulted in a variable morphology depending on the NiFe mass loading on the electrode surface. Below 1 $\mu g/cm^2$ the structures were sparse, revealing their individual electrocatalytic response resulting from a combined electrolyte/NiFe/electrode interaction. Conversely for higher densities they aggregated to form continuous porous and nanogranular films to reach 90 nm thickness at 30 $\mu g/cm^2$, in which a mass loading independent OER activity involves just the electrode surface. This allowed to identify an optimal electrode morphology, corresponding to the 0.2-1 $\mu g/cm^2$ mass loading range, in which the best catalytic activity

could be reached (380 mV overpotential at 10 mA/cm^2 and 1 s^{-1} TOF at 350 mV overpotential).

Furthermore, the electrode stability under prolonged OER activity was tested as a function of the mass loading, revealing a progressive oxy-hydroxylation and NiFe material rearrangement on the electrode surface. Below 0.2 $\mu g/cm^2$ the nanoparticles increase their individual OER activity, while for continuous films a decrease in efficiency results from the NiFe species leaching in the electrolyte. More importantly, it was possible to define an electrochemical procedure to achieve a very stable OER efficiency.

The optical spectroscopy played a crucial role in the electrode characterization. To this aim a new home-made software (DEMON) was developed to simulate and fit the optical response of nanostructured materials as a function of the morphology and chemical composition. In this framework a detailed optical investigation was also performed for Au based plasmonic systems. These were synthesized through an advanced nanofabrication technique, the dynamic templating followed by the liquid/sold interface growth, that allowed to obtain arrays of 2D Au crystalline plates. This dissertation delved into the optimization of the synthesis process, achieved by tuning the chemical composition of the solution employed in the liquid/solid growth and the exposure to variable wavelength light. The results provided insightful information on the reduction process taking place during the crystal growth, as well as its enhancement under light exposure due to the plasmonic excitations or the Au intermediates formation.

Then, the optimized synthesis process was applied to fabricate specific structures, whose plasmonic and optical properties were characterized in detail. Large area films were obtained by growing and merging adjacent hexagons, revealing promising conductivity

properties for the application in nanoelectronics devices. Furthermore, the combination of the synthesis technique with subsequent atomic layer deposition and etching allowed to obtain nanostructures with embedded nanogaps, useful for the advancement in the molecular sensing. Finally, a new alternative synthesis method to obtain plasmonic structures was proposed.

LIST OF PUBLICATIONS

As first author:

- L. Ciambriello, E. Cavaliere, and L. Gavioli, “Influence of roughness, porosity and grain morphology on the optical properties of ultrathin Ag films,” Applied Surface Science, vol. 576, p. 151885, Feb. 2022, doi: 10.1016/j.apsusc.2021.151885.

- L. Ciambriello, E. Cavaliere, I. Vassalini, I. Alessandri, M. Ferroni, L. Leoncino, R. Brescia, L. Gavioli, "Role of electrode thickness in NiFe nanogranular films for oxygen evolution reaction". Journal of Physical Chemistry C, December 2022, 126, 51, 21759- 21770, DOI: 10.1021/acs.jpcc.2c06669

- L. Ciambriello, I. Alessandri, M. Ferroni, L. Gavioli, and I. Vassalini, “Unexpected resilience of NiFe Catalysts for alkaline Oxygen Evolution Reaction”, submitted to American Chemical Society – Applied Energy Materials (Feb 2024)

- L. Ciambriello, I. Alessandri, L. Gavioli, and I. Vassalini, “NiFe Catalysts for Oxygen Evolution Reaction: Is There an Optimal Thickness for Generating a Dynamically Stable Active Interface?”, Submitted to ChemCatChem -Chemistry Europe (Feb 2024)

As coauthor:

- D. Valerini, L. Tammaro, G. Vigliotta, E. Picariello, F. Banfi, E. Cavaliere, L. Ciambriello, L. Gavioli, “Ag Functionalization of Al-Doped ZnO Nanostructured Coatings on PLA Substrate for Antibacterial Applications,” Coatings, vol. 10, no. 12, Art. no. 12, Dec. 2020, DOI: 10.3390/coatings10121238

- M. Bottagisio, V. Balzano, L. Ciambriello, L. Rosa, G.Talò, A.B. Lovati, E. De Vecchi and L. Gavioli, “Exploring multielemental nanogranular coatings to forestall implant related infections” Frontiers in Cellular and

Infection Microbiology, Vol 13, Feb 2023, Sec. Biofilms. DOI: 10.3389/fcimb.2023.1128822

- W.J. Tuff, R.A. Hughes, B.D. Nieukirk, L. Ciambriello, R.D. Neal, S.D. Golze, L. Gavioli, and S. Neretina, "Periodic arrays of structurally complex oxide Nanoshells and their use as substrate-confined nanoreactors" Nanoscale 2023, 15, 17609-17620. DOI: 10.1039/D3NR04345B.

BIBLIOGRAPHY

[1] "International Energy Outlook 2023 - U.S. Energy Information Administration (EIA)." Accessed: Oct. 31, 2023. [Online]. Available: https://www.eia.gov/outlooks/ieo/index.php

[2] H. Ishaq, I. Dincer, and C. Crawford, "A review on hydrogen production and utilization: Challenges and opportunities," *International Journal of Hydrogen Energy*, vol. 47, no. 62, pp. 26238–26264, Jul. 2022, doi: 10.1016/j.ijhydene.2021.11.149.

[3] D. Gielen, F. Boshell, D. Saygin, M. D. Bazilian, N. Wagner, and R. Gorini, "The role of renewable energy in the global energy transformation," *Energy Strategy Reviews*, vol. 24, pp. 38–50, Apr. 2019, doi: 10.1016/j.esr.2019.01.006.

[4] F. Dawood, M. Anda, and G. M. Shafiullah, "Hydrogen production for energy: An overview," *International Journal of Hydrogen Energy*, vol. 45, no. 7, pp. 3847–3869, Feb. 2020, doi: 10.1016/j.ijhydene.2019.12.059.

[5] I. Staffell *et al.*, "The role of hydrogen and fuel cells in the global energy system," *Energy & Environmental Science*, vol. 12, no. 2, pp. 463–491, 2019, doi: 10.1039/C8EE01157E.

[6] J. Kibsgaard and I. Chorkendorff, "Considerations for the scaling-up of water splitting catalysts," *Nat Energy*, vol. 4, no. 6, Art. no. 6, Jun. 2019, doi: 10.1038/s41560-019-0407-1.

[7] Y. Khojasteh Salkuyeh, B. A. Saville, and H. L. MacLean, "Techno-economic analysis and life cycle assessment of hydrogen production from natural gas using current and emerging technologies," *International Journal of Hydrogen Energy*, vol. 42, no. 30, pp. 18894–18909, Jul. 2017, doi: 10.1016/j.ijhydene.2017.05.219.

[8] N. Muradov, "Low to near-zero CO2 production of hydrogen from fossil fuels: Status and perspectives," *International Journal of Hydrogen Energy*, vol. 42, no. 20, pp. 14058–14088, May 2017, doi: 10.1016/j.ijhydene.2017.04.101.

[9] Y. Yan, B. Yu Xia, B. Zhao, and X. Wang, "A review on noble-metal-free bifunctional heterogeneous catalysts for overall electrochemical water splitting,"

Journal of Materials Chemistry A, vol. 4, no. 45, pp. 17587–17603, 2016, doi: 10.1039/C6TA08075H.

[10] D. Pletcher and X. Li, "Prospects for alkaline zero gap water electrolysers for hydrogen production," *International Journal of Hydrogen Energy*, vol. 36, no. 23, pp. 15089–15104, Nov. 2011, doi: 10.1016/j.ijhydene.2011.08.080.

[11] F. Lyu, Q. Wang, S. M. Choi, and Y. Yin, "Noble-Metal-Free Electrocatalysts for Oxygen Evolution," *Small*, vol. 15, no. 1, p. 1804201, 2019, doi: 10.1002/smll.201804201.

[12] Y. Jiao, Y. Zheng, M. Jaroniec, and S. Z. Qiao, "Design of electrocatalysts for oxygen- and hydrogen-involving energy conversion reactions," *Chem. Soc. Rev.*, vol. 44, no. 8, pp. 2060–2086, Apr. 2015, doi: 10.1039/C4CS00470A.

[13] I. C. Man *et al.*, "Universality in Oxygen Evolution Electrocatalysis on Oxide Surfaces," *ChemCatChem*, vol. 3, no. 7, pp. 1159–1165, 2011, doi: 10.1002/cctc.201000397.

[14] Z. W. Seh, J. Kibsgaard, C. F. Dickens, I. Chorkendorff, J. K. Nørskov, and T. F. Jaramillo, "Combining theory and experiment in electrocatalysis: Insights into materials design," *Science*, vol. 355, no. 6321, p. eaad4998, Jan. 2017, doi: 10.1126/science.aad4998.

[15] Q. Shi, C. Zhu, D. Du, and Y. Lin, "Robust noble metal-based electrocatalysts for oxygen evolution reaction," *Chem. Soc. Rev.*, vol. 48, no. 12, pp. 3181–3192, Jun. 2019, doi: 10.1039/C8CS00671G.

[16] C. C. L. McCrory, S. Jung, J. C. Peters, and T. F. Jaramillo, "Benchmarking Heterogeneous Electrocatalysts for the Oxygen Evolution Reaction," *J. Am. Chem. Soc.*, vol. 135, no. 45, pp. 16977–16987, Nov. 2013, doi: 10.1021/ja407115p.

[17] H. Zhong *et al.*, "Template-free synthesis of three-dimensional NiFe-LDH hollow microsphere with enhanced OER performance in alkaline media," *Journal of Energy Chemistry*, vol. 33, pp. 130–137, Jun. 2019, doi: 10.1016/j.jechem.2018.09.005.

[18] T. Noor, L. Yaqoob, and N. Iqbal, "Recent Advances in Electrocatalysis of Oxygen Evolution Reaction using Noble-Metal, Transition-Metal, and Carbon-Based Materials," *ChemElectroChem*, vol. 8, no. 3, pp. 447–483, 2021, doi: 10.1002/celc.202001441.

[19] Z. Wang *et al.*, "Influence of the MnO2 Phase on Oxygen Evolution Reaction Performance for Low-Loading Iridium Electrocatalysts," *ChemElectroChem*, vol. 8, no. 2, pp. 418–424, 2021, doi: 10.1002/celc.202001513.

[20] H. Yu *et al.*, “Nano-size IrOx catalyst of high activity and stability in PEM water electrolyzer with ultra-low iridium loading,” *Applied Catalysis B: Environmental*, vol. 239, pp. 133–146, Dec. 2018, doi: 10.1016/j.apcatb.2018.07.064.

[21] M. Liu, F. Hof, M. Moro, G. Valenti, F. Paolucci, and A. Pénicaud, “Carbon supported noble metal nanoparticles as efficient catalysts for electrochemical water splitting,” *Nanoscale*, vol. 12, no. 39, pp. 20165–20170, 2020, doi: 10.1039/D0NR05659F.

[22] J. Ruiz Esquius, G. Algara-Siller, I. Spanos, S. J. Freakley, R. Schlögl, and G. J. Hutchings, “Preparation of Solid Solution and Layered IrOx–Ni(OH)2 Oxygen Evolution Catalysts: Toward Optimizing Iridium Efficiency for OER,” *ACS Catal.*, vol. 10, no. 24, pp. 14640–14648, Dec. 2020, doi: 10.1021/acscatal.0c03866.

[23] Z.-P. Wu, X. F. Lu, S.-Q. Zang, and X. W. (David) Lou, “Non-Noble-Metal-Based Electrocatalysts toward the Oxygen Evolution Reaction,” *Advanced Functional Materials*, vol. 30, no. 15, p. 1910274, 2020, doi: 10.1002/adfm.201910274.

[24] W. Schmickler and R. Guidelli, “The partial charge transfer,” *Electrochimica Acta*, vol. 127, pp. 489–505, May 2014, doi: 10.1016/j.electacta.2014.02.057.

[25] R. D. L. Smith, M. S. Prévot, R. D. Fagan, S. Trudel, and C. P. Berlinguette, “Water Oxidation Catalysis: Electrocatalytic Response to Metal Stoichiometry in Amorphous Metal Oxide Films Containing Iron, Cobalt, and Nickel,” *J. Am. Chem. Soc.*, vol. 135, no. 31, pp. 11580–11586, Aug. 2013, doi: 10.1021/ja403102j.

[26] M. W. Louie and A. T. Bell, “An Investigation of Thin-Film Ni–Fe Oxide Catalysts for the Electrochemical Evolution of Oxygen,” *J. Am. Chem. Soc.*, vol. 135, no. 33, pp. 12329–12337, Aug. 2013, doi: 10.1021/ja405351s.

[27] J. Mohammed-Ibrahim, “A review on NiFe-based electrocatalysts for efficient alkaline oxygen evolution reaction,” *Journal of Power Sources*, vol. 448, p. 227375, Feb. 2020, doi: 10.1016/j.jpowsour.2019.227375.

[28] S. Anantharaj, S. Kundu, and S. Noda, “‘The Fe Effect’: A review unveiling the critical roles of Fe in enhancing OER activity of Ni and Co based catalysts,” *Nano Energy*, vol. 80, p. 105514, Feb. 2021, doi: 10.1016/j.nanoen.2020.105514.

[29] D. Friebel *et al.*, “Identification of Highly Active Fe Sites in (Ni,Fe)OOH for Electrocatalytic Water Splitting,” *J. Am. Chem. Soc.*, vol. 137, no. 3, pp. 1305–1313, Jan. 2015, doi: 10.1021/ja511559d.

[30] M. Gong and H. Dai, “A mini review of NiFe-based materials as highly active oxygen evolution reaction electrocatalysts,” *Nano Res.*, vol. 8, no. 1, pp. 23–39, Jan. 2015, doi: 10.1007/s12274-014-0591-z.

[31] L. Gong, H. Yang, A. I. Douka, Y. Yan, and B. Y. Xia, “Recent Progress on NiFe-Based Electrocatalysts for Alkaline Oxygen Evolution,” *Advanced Sustainable Systems*, vol. 5, no. 1, p. 2000136, 2021, doi: 10.1002/adsu.202000136.

[32] J. Zhao, J.-J. Zhang, Z.-Y. Li, and X.-H. Bu, “Recent Progress on NiFe-Based Electrocatalysts for the Oxygen Evolution Reaction,” *Small*, vol. 16, no. 51, p. 2003916, 2020, doi: 10.1002/smll.202003916.

[33] S. Klaus, Y. Cai, M. W. Louie, L. Trotochaud, and A. T. Bell, “Effects of Fe Electrolyte Impurities on Ni(OH)2/NiOOH Structure and Oxygen Evolution Activity,” *J. Phys. Chem. C*, vol. 119, no. 13, pp. 7243–7254, Apr. 2015, doi: 10.1021/acs.jpcc.5b00105.

[34] A. S. Batchellor and S. W. Boettcher, “Pulse-Electrodeposited Ni–Fe (Oxy)hydroxide Oxygen Evolution Electrocatalysts with High Geometric and Intrinsic Activities at Large Mass Loadings,” *ACS Catal.*, vol. 5, no. 11, pp. 6680–6689, Nov. 2015, doi: 10.1021/acscatal.5b01551.

[35] M. Gao *et al.*, “Efficient Water Oxidation Using Nanostructured α-Nickel-Hydroxide as an Electrocatalyst,” *J. Am. Chem. Soc.*, vol. 136, no. 19, pp. 7077–7084, May 2014, doi: 10.1021/ja502128j.

[36] H. Li, X. Wang, T. Wang, and F. Xiao, “A facile, green and time-saving method to prepare partially crystalline NiFe layered double hydroxide nanosheets on nickel foam for superior OER catalysis,” *Journal of Alloys and Compounds*, vol. 844, p. 156224, Dec. 2020, doi: 10.1016/j.jallcom.2020.156224.

[37] B. J. Trześniewski *et al.*, “In Situ Observation of Active Oxygen Species in Fe-Containing Ni-Based Oxygen Evolution Catalysts: The Effect of pH on Electrochemical Activity,” *J. Am. Chem. Soc.*, vol. 137, no. 48, pp. 15112–15121, Dec. 2015, doi: 10.1021/jacs.5b06814.

[38] R. Subbaraman *et al.*, “Trends in activity for the water electrolyser reactions on 3d M(Ni,Co,Fe,Mn) hydr(oxy)oxide catalysts,” *Nature Mater*, vol. 11, no. 6, Art. no. 6, Jun. 2012, doi: 10.1038/nmat3313.

[39] F. Bao *et al.*, “Host, Suppressor, and Promoter—The Roles of Ni and Fe on Oxygen Evolution Reaction Activity and Stability of NiFe Alloy Thin Films in Alkaline Media,” *ACS Catal.*, vol. 11, no. 16, pp. 10537–10552, Aug. 2021, doi: 10.1021/acscatal.1c01190.

[40] F. Song and X. Hu, “Exfoliation of layered double hydroxides for enhanced oxygen evolution catalysis,” *Nat Commun*, vol. 5, no. 1, p. 4477, Jul. 2014, doi: 10.1038/ncomms5477.

[41] P. Zhang *et al.*, “Dendritic core-shell nickel-iron-copper metal/metal oxide electrode for efficient electrocatalytic water oxidation,” *Nat Commun*, vol. 9, no. 1, p. 381, Jan. 2018, doi: 10.1038/s41467-017-02429-9.

[42] H. Zhou *et al.*, “Water splitting by electrolysis at high current densities under 1.6 volts,” *Energy Environ. Sci.*, vol. 11, no. 10, pp. 2858–2864, Oct. 2018, doi: 10.1039/C8EE00927A.

[43] F. Yu *et al.*, “High-performance bifunctional porous non-noble metal phosphide catalyst for overall water splitting,” *Nat Commun*, vol. 9, no. 1, p. 2551, Jun. 2018, doi: 10.1038/s41467-018-04746-z.

[44] J. Jin *et al.*, “Exceptional electrocatalytic oxygen evolution efficiency and stability from electrodeposited NiFe alloy on Ni foam,” *Electrochimica Acta*, vol. 299, pp. 567–574, Mar. 2019, doi: 10.1016/j.electacta.2019.01.026.

[45] C. Deng, K.-H. Wu, J. Scott, S. Zhu, R. Amal, and D.-W. Wang, “Core/Shell NiFe Nanoalloy with a Discrete N-doped Graphitic Carbon Cover for Enhanced Water Oxidation,” *ChemElectroChem*, vol. 5, no. 5, pp. 732–736, 2018, doi: 10.1002/celc.201701285.

[46] A. Kumar and S. Bhattacharyya, “Porous NiFe-Oxide Nanocubes as Bifunctional Electrocatalysts for Efficient Water-Splitting,” *ACS Appl. Mater. Interfaces*, vol. 9, no. 48, pp. 41906–41915, Dec. 2017, doi: 10.1021/acsami.7b14096.

[47] K. Ho Kim, J. You Zheng, W. Shin, and Y. Soo Kang, “Preparation of dendritic NiFe films by electrodeposition for oxygen evolution,” *RSC Advances*, vol. 2, no. 11, pp. 4759–4767, 2012, doi: 10.1039/C2RA20241G.

[48] K. Sliozberg, Y. Aniskevich, U. Kayran, J. Masa, and W. Schuhmann, “CoFe–OH Double Hydroxide Films Electrodeposited on Ni-Foam as Electrocatalyst for the Oxygen Evolution Reaction,” *Zeitschrift für Physikalische Chemie*, vol. 234, no. 5, pp. 995–1019, May 2020, doi: 10.1515/zpch-2019-1466.

[49] M. Koj, T. Gimpel, W. Schade, and T. Turek, “Laser structured nickel-iron electrodes for oxygen evolution in alkaline water electrolysis,” *International Journal of Hydrogen Energy*, vol. 44, no. 25, pp. 12671–12684, May 2019, doi: 10.1016/j.ijhydene.2019.01.030.

[50] S. Anantharaj and S. Kundu, “Do the Evaluation Parameters Reflect Intrinsic Activity of Electrocatalysts in Electrochemical Water Splitting?,” *ACS Energy Lett.*, vol. 4, no. 6, pp. 1260–1264, Jun. 2019, doi: 10.1021/acsenergylett.9b00686.

[51] H. Kim *et al.*, “Dendritic gold-supported iridium/iridium oxide ultra-low loading electrodes for high-performance proton exchange membrane water electrolyzer,” *Applied Catalysis B: Environmental*, vol. 283, p. 119596, Apr. 2021, doi: 10.1016/j.apcatb.2020.119596.

[52] J. Zhu *et al.*, “Facile Synthesis and Characterization of Pd@IrnL (n = 1–4) Core–Shell Nanocubes for Highly Efficient Oxygen Evolution in Acidic Media,” *Chem. Mater.*, vol. 31, no. 15, pp. 5867–5875, Aug. 2019, doi: 10.1021/acs.chemmater.9b02011.

[53] M. Bernt *et al.*, “Current Challenges in Catalyst Development for PEM Water Electrolyzers,” *Chemie Ingenieur Technik*, vol. 92, no. 1–2, pp. 31–39, 2020, doi: 10.1002/cite.201900101.

[54] R. D. McKerracher *et al.*, “A Comparison of Pd/C, Perovskite, and Ni-Fe Hexacyanoferrate Bifunctional Oxygen Catalysts, at Different Loadings and Catalyst Layer Thicknesses on an Oxygen Gas Diffusion Electrode,” *J. Electrochem. Soc.*, vol. 165, no. 7, p. A1254, Apr. 2018, doi: 10.1149/2.0321807jes.

[55] C. G. Morales-Guio, L. Liardet, and X. Hu, “Oxidatively Electrodeposited Thin-Film Transition Metal (Oxy)hydroxides as Oxygen Evolution Catalysts,” *J. Am. Chem. Soc.*, vol. 138, no. 28, pp. 8946–8957, Jul. 2016, doi: 10.1021/jacs.6b05196.

[56] X. Deng, D. C. Sorescu, I. Waluyo, A. Hunt, and D. R. Kauffman, “Bulk vs Intrinsic Activity of NiFeOx Electrocatalysts in the Oxygen Evolution Reaction: The Influence of Catalyst Loading, Morphology, and Support Material,” *ACS Catal.*, vol. 10, no. 20, pp. 11768–11778, Oct. 2020, doi: 10.1021/acscatal.0c03109.

[57] M. Görlin *et al.*, “Tracking Catalyst Redox States and Reaction Dynamics in Ni–Fe Oxyhydroxide Oxygen Evolution Reaction Electrocatalysts: The Role of Catalyst Support and Electrolyte pH,” *J. Am. Chem. Soc.*, vol. 139, no. 5, pp. 2070–2082, Feb. 2017, doi: 10.1021/jacs.6b12250.

[58] M. E. C. Pascuzzi, A. J. W. Man, A. Goryachev, J. P. Hofmann, and E. J. M. Hensen, “Investigation of the stability of NiFe-(oxy)hydroxide anodes in alkaline water electrolysis under industrially relevant conditions,” *Catal. Sci. Technol.*, vol. 10, no. 16, pp. 5593–5601, Aug. 2020, doi: 10.1039/D0CY01179G.

[59] K. Zhu, X. Zhu, and W. Yang, “Application of In Situ Techniques for the Characterization of NiFe-Based Oxygen Evolution Reaction (OER) Electrocatalysts,” *Angewandte Chemie International Edition*, vol. 58, no. 5, pp. 1252–1265, 2019, doi: 10.1002/anie.201802923.

[60] H. Sun, X. Xu, H. Kim, W. Jung, W. Zhou, and Z. Shao, “Electrochemical Water Splitting: Bridging the Gaps Between Fundamental Research and Industrial Applications,” *ENERGY & ENVIRONMENTAL MATERIALS*, vol. 6, no. 5, p. e12441, 2023, doi: 10.1002/eem2.12441.

[61] F. Zeng, C. Mebrahtu, L. Liao, A. K. Beine, and R. Palkovits, “Stability and deactivation of OER electrocatalysts: A review,” *Journal of Energy Chemistry*, vol. 69, pp. 301–329, Jun. 2022, doi: 10.1016/j.jechem.2022.01.025.

[62] M. I. Jamesh, “Recent progress on earth abundant hydrogen evolution reaction and oxygen evolution reaction bifunctional electrocatalyst for overall water splitting in alkaline media,” *Journal of Power Sources*, vol. 333, pp. 213–236, Nov. 2016, doi: 10.1016/j.jpowsour.2016.09.161.

[63] W. Cai *et al.*, “Amorphous versus Crystalline in Water Oxidation Catalysis: A Case Study of NiFe Alloy,” *Nano Letters*, May 2020, doi: 10.1021/acs.nanolett.0c00840.

[64] N. Trogisch, M. Koch, E. N. El Sawy, and H. A. El-Sayed, “Microscopic Bubble Accumulation: The Missing Factor in Evaluating Oxygen Evolution Catalyst Stability during Accelerated Stress Tests,” *ACS Catal.*, vol. 12, no. 21, pp. 13715–13724, Nov. 2022, doi: 10.1021/acscatal.2c03881.

[65] A. Angulo, P. van der Linde, H. Gardeniers, M. Modestino, and D. Fernández Rivas, “Influence of Bubbles on the Energy Conversion Efficiency of Electrochemical Reactors,” *Joule*, vol. 4, no. 3, pp. 555–579, Mar. 2020, doi: 10.1016/j.joule.2020.01.005.

[66] L. Trotochaud, S. L. Young, J. K. Ranney, and S. W. Boettcher, “Nickel–Iron Oxyhydroxide Oxygen-Evolution Electrocatalysts: The Role of Intentional and Incidental Iron Incorporation,” *J. Am. Chem. Soc.*, vol. 136, no. 18, pp. 6744–6753, May 2014, doi: 10.1021/ja502379c.

[67] D. Y. Chung *et al.*, “Dynamic stability of active sites in hydr(oxy)oxides for the oxygen evolution reaction,” *Nat Energy*, vol. 5, no. 3, Art. no. 3, Mar. 2020, doi: 10.1038/s41560-020-0576-y.

[68] F.-Y. Chen, Z.-Y. Wu, Z. Adler, and H. Wang, “Stability challenges of electrocatalytic oxygen evolution reaction: From mechanistic understanding to reactor design,” *Joule*, vol. 5, no. 7, pp. 1704–1731, Jul. 2021, doi: 10.1016/j.joule.2021.05.005.

[69] Y. Zhou *et al.*, “Fe-leaching induced surface reconstruction of Ni-Fe alloy on N-doped carbon to boost oxygen evolution reaction,” *Chemical Engineering Journal*, vol. 394, p. 124977, Aug. 2020, doi: 10.1016/j.cej.2020.124977.

[70] N. Hashemi, S. Nandy, K. H. Chae, and M. M. Najafpour, “Anodization of a NiFe Foam: An Efficient and Stable Electrode for Oxygen-Evolution Reaction,” *ACS Appl. Energy Mater.*, vol. 5, no. 9, pp. 11098–11112, Sep. 2022, doi: 10.1021/acsaem.2c01707.

[71] J. Lu, S. Yin, and P. K. Shen, “Carbon-Encapsulated Electrocatalysts for the Hydrogen Evolution Reaction,” *Electrochem. Energ. Rev.*, vol. 2, no. 1, pp. 105–127, Mar. 2019, doi: 10.1007/s41918-018-0025-9.

[72] K. Wegner, P. Piseri, H. V. Tafreshi, and P. Milani, “Cluster beam deposition: a tool for nanoscale science and technology,” *J. Phys. D: Appl. Phys.*, vol. 39, no. 22, pp. R439–R459, Nov. 2006, doi: 10.1088/0022-3727/39/22/R02.

[73] P. Milani, P. Piseri, E. Barborini, A. Podesta, and C. Lenardi, “Cluster beam synthesis of nanostructured thin films,” *Journal of Vacuum Science & Technology A*, vol. 19, no. 4, pp. 2025–2033, Jul. 2001, doi: 10.1116/1.1331289.

[74] K. M. McPeak *et al.*, “Plasmonic Films Can Easily Be Better: Rules and Recipes,” *ACS Photonics*, vol. 2, no. 3, pp. 326–333, Mar. 2015, doi: 10.1021/ph5004237.

[75] A. S. Baburin, A. M. Merzlikin, A. V. Baryshev, I. A. Ryzhikov, Y. V. Panfilov, and I. A. Rodionov, “Silver-based plasmonics: golden material platform and application challenges [Invited],” *Opt. Mater. Express, OME*, vol. 9, no. 2, pp. 611–642, Feb. 2019, doi: 10.1364/OME.9.000611.

[76] J. Gong, R. Dai, Z. Wang, and Z. Zhang, “Thickness Dispersion of Surface Plasmon of Ag Nano-thin Films: Determination by Ellipsometry Iterated with Transmittance Method,” *Sci Rep*, vol. 5, no. 1, Art. no. 1, Mar. 2015, doi: 10.1038/srep09279.

[77] J. Choi *et al.*, “Optical dielectric constants of single crystalline silver films in the long wavelength range,” *Opt. Mater. Express, OME*, vol. 10, no. 2, pp. 693–703, Feb. 2020, doi: 10.1364/OME.385723.

[78] B. K. Kim and S. Y. Lee, “Optimized Design of SiInZnO/Ag/SiInZnO Transparent Conductive Electrode by Using Optical Admittance Simulation,” *Trans. Electr. Electron. Mater.*, vol. 21, no. 3, pp. 324–328, Jun. 2020, doi: 10.1007/s42341-020-00178-z.

[79] P. B. Johnson and R. W. Christy, “Optical Constants of the Noble Metals,” *Phys. Rev. B*, vol. 6, no. 12, pp. 4370–4379, Dec. 1972, doi: 10.1103/PhysRevB.6.4370.

[80] E. Fontana, “Thickness optimization of metal films for the development of surface-plasmon-based sensors for nonabsorbing media,” *Appl. Opt., AO*, vol. 45, no. 29, pp. 7632–7642, Oct. 2006, doi: 10.1364/AO.45.007632.

[81] Y. Pan, Y. Fan, and J. Niu, “Optical properties of ultra-thin silver films deposited by thermal evaporation and its application in optical filters,” *Infrared Physics & Technology*, vol. 104, p. 103123, Jan. 2020, doi: 10.1016/j.infrared.2019.103123.

[82] T. C. Choy, *Effective Medium Theory: Principles and Applications*. Oxford University Press, 2015.

[83] S. D. Golze, R. A. Hughes, S. Rouvimov, R. D. Neal, T. B. Demille, and S. Neretina, “Plasmon-Mediated Synthesis of Periodic Arrays of Gold Nanoplates Using Substrate-Immobilized Seeds Lined with Planar Defects,” *Nano Lett.*, vol. 19, no. 8, pp. 5653–5660, Aug. 2019, doi: 10.1021/acs.nanolett.9b02215.

[84] R. D. Neal *et al.*, “Large-Area Periodic Arrays of Atomically Flat Single-Crystal Gold Nanotriangles Formed Directly on Substrate Surfaces,” *Small*, vol. 18, no. 52, p. 2205780, 2022, doi: 10.1002/smll.202205780.

[85] T. B. Demille *et al.*, “Large-area periodic arrays of gold nanostars derived from HEPES-, DMF-, and ascorbic-acid-driven syntheses,” *Nanoscale*, vol. 12, no. 31, pp. 16489–16500, 2020, doi: 10.1039/D0NR04141F.

[86] S. D. Golze *et al.*, “Sequential Symmetry-Breaking Events as a Synthetic Pathway for Chiral Gold Nanostructures with Spiral Geometries,” *Nano Lett.*, vol. 21, no. 7, pp. 2919–2925, Apr. 2021, doi: 10.1021/acs.nanolett.0c05105.

[87] W. J. Tuff, R. A. Hughes, S. D. Golze, and S. Neretina, “Ion Beam Milling as a Symmetry-Breaking Control in the Synthesis of Periodic Arrays of Identically Aligned Bimetallic Janus Nanocrystals,” *ACS Nano*, vol. 17, no. 4, pp. 4050–4061, Feb. 2023, doi: 10.1021/acsnano.3c00149.

[88] G. A. Vinnacombe-Willson, Y. Conti, A. Stefancu, P. S. Weiss, E. Cortés, and L. Scarabelli, “Direct Bottom-Up In Situ Growth: A Paradigm Shift for Studies in Wet-Chemical Synthesis of Gold Nanoparticles,” *Chem. Rev.*, vol. 123, no. 13, pp. 8488–8529, Jul. 2023, doi: 10.1021/acs.chemrev.2c00914.

[89] V. Dubois, S. J. Bleiker, G. Stemme, and F. Niklaus, “Scalable Manufacturing of Nanogaps,” *Advanced Materials*, vol. 30, no. 46, p. 1801124, 2018, doi: 10.1002/adma.201801124.

[90] G. Benetti *et al.*, “Bottom-Up Mechanical Nanometrology of Granular Ag Nanoparticles Thin Films,” *J. Phys. Chem. C*, vol. 121, no. 40, pp. 22434–22441, Oct. 2017, doi: 10.1021/acs.jpcc.7b05795.

[91] V. Mironov, *Fundamentals of Scanning Probe Microscopy*. 2014.

[92] B. Cappella and G. Dietler, “Force-distance curves by atomic force microscopy,” *Surface Science Reports*, vol. 34, no. 1, pp. 1–104, Jan. 1999, doi: 10.1016/S0167-5729(99)00003-5.

[93] G. Greczynski and L. Hultman, “X-ray photoelectron spectroscopy: Towards reliable binding energy referencing,” *Progress in Materials Science*, vol. 107, p. 100591, Jan. 2020, doi: 10.1016/j.pmatsci.2019.100591.

[94] G. Greczynski and L. Hultman, “A step-by-step guide to perform x-ray photoelectron spectroscopy,” *Journal of Applied Physics*, vol. 132, no. 1, p. 011101, Jul. 2022, doi: 10.1063/5.0086359.

[95] J. F. Moulder, *Handbook of X-ray Photoelectron Spectroscopy: A Reference Book of Standard Spectra for Identification and Interpretation of XPS Data*. Physical Electronics Division, Perkin-Elmer Corporation, 1992.

[96] H. Förster, “UV/VIS Spectroscopy,” in *Characterization I: -/-*, H. G. Karge and J. Weitkamp, Eds., in Molecular Sieves – Science and Technology. , Berlin, Heidelberg: Springer, 2004, pp. 337–426. doi: 10.1007/b94239.

[97] H.-H. Perkampus, *UV-VIS Spectroscopy and Its Applications*. Springer Science & Business Media, 2013.

[98] J. W. Jr and A. Springsteen, *Applied Spectroscopy: A Compact Reference for Practitioners*. Academic Press, 1998.

[99] G. Gauglitz and D. S. Moore, *Handbook of Spectroscopy*. John Wiley & Sons, 2014.

[100] J. Epp, “4 - X-ray diffraction (XRD) techniques for materials characterization,” in *Materials Characterization Using Nondestructive Evaluation (NDE) Methods*, G. Hübschen, I. Altpeter, R. Tschuncky, and H.-G. Herrmann, Eds., Woodhead Publishing, 2016, pp. 81–124. doi: 10.1016/B978-0-08-100040-3.00004-3.

[101] B. E. Warren, *X-ray Diffraction*. Courier Corporation, 1990.

[102] N. Elgrishi, K. J. Rountree, B. D. McCarthy, E. S. Rountree, T. T. Eisenhart, and J. L. Dempsey, “A Practical Beginner’s Guide to Cyclic Voltammetry,” *J. Chem. Educ.*, vol. 95, no. 2, pp. 197–206, Feb. 2018, doi: 10.1021/acs.jchemed.7b00361.

[103] E. Menumerov, S. D. Golze, R. A. Hughes, and S. Neretina, “Arrays of highly complex noble metal nanostructures using nanoimprint lithography in combination with liquid-phase epitaxy,” *Nanoscale*, vol. 10, no. 38, pp. 18186–18194, Oct. 2018, doi: 10.1039/C8NR06874G.

[104] A. S. Baburin, A. M. Merzlikin, A. V. Baryshev, I. A. Ryzhikov, Y. V. Panfilov, and I. A. Rodionov, “Silver-based plasmonics: golden material platform and application challenges [Invited],” *Opt. Mater. Express*, vol. 9, no. 2, p. 611, Feb. 2019, doi: 10.1364/OME.9.000611.

[105] K. M. McPeak *et al.*, “Plasmonic Films Can Easily Be Better: Rules and Recipes,” *ACS Photonics*, vol. 2, no. 3, pp. 326–333, Mar. 2015, doi: 10.1021/ph5004237.

[106] A. S. Baburin *et al.*, “Epitaxial Silver Films Morphology and Optical Properties Evolution over Two Years,” *Coatings*, vol. 10, no. 10, Art. no. 10, Oct. 2020, doi: 10.3390/coatings10100911.

[107] M. Zhou, Y.-P. Li, S. Zhou, and D.-Q. Liu, “Optical Properties and Surface Morphology of Thin Silver Films Deposited by Thermal Evaporation*,” *Chinese Phys. Lett.*, vol. 32, no. 7, p. 077802, Jul. 2015, doi: 10.1088/0256-307X/32/7/077802.

[108] J. Gong, R. Dai, Z. Wang, and Z. Zhang, “Thickness Dispersion of Surface Plasmon of Ag Nano-thin Films: Determination by Ellipsometry Iterated with Transmittance Method,” *Sci Rep*, vol. 5, no. 1, p. 9279, Aug. 2015, doi: 10.1038/srep09279.

[109] J. A. Sánchez-Gil, J. V. García-Ramos, and E. R. Méndez, “Electromagnetic mechanism in surface-enhanced Raman scattering from Gaussian-correlated randomly rough metal substrates,” *Opt. Express*, vol. 10, no. 17, p. 879, Aug. 2002, doi: 10.1364/OE.10.000879.

[110] R. Gupta, M. J. Dyer, and W. A. Weimer, “Preparation and characterization of surface plasmon resonance tunable gold and silver films,” *Journal of Applied Physics*, vol. 92, no. 9, pp. 5264–5271, Oct. 2002, doi: 10.1063/1.1511275.

[111] W. A. Weimer and M. J. Dyer, “Tunable surface plasmon resonance silver films,” *Appl. Phys. Lett.*, vol. 79, no. 19, pp. 3164–3166, Nov. 2001, doi: 10.1063/1.1416473.

[112] D. G. Gromov *et al.*, “Investigation of condensation of small portions of Ag at thermal evaporation in vacuum,” *J. Phys.: Conf. Ser.*, vol. 643, p. 012014, Nov. 2015, doi: 10.1088/1742-6596/643/1/012014.

[113] S. K. Sharma, S. U. M. Rao, and N. Kumar, “Hillock formation and agglomeration in silver films prepared by thermal evaporation,” *Thin Solid Films*, vol. 142, no. 1, pp. L95–L98, Aug. 1986, doi: 10.1016/0040-6090(86)90311-1.

[114] K. Khurana, N. Rathee, and N. Jaggi, “Deposition of uniform plasmonic Ag nanoparticles by in-situ substrate heating using thermal evaporator,” *AIP Conference Proceedings*, vol. 2220, no. 1, p. 090006, May 2020, doi: 10.1063/5.0001691.

[115] H. U. Yang, J. D’Archangel, M. L. Sundheimer, E. Tucker, G. D. Boreman, and M. B. Raschke, “Optical dielectric function of silver,” *Phys. Rev. B*, vol. 91, no. 23, p. 235137, Jun. 2015, doi: 10.1103/PhysRevB.91.235137.

[116] J. Choi *et al.*, “Optical dielectric constants of single crystalline silver films in the long wavelength range,” *Opt. Mater. Express*, vol. 10, no. 2, p. 693, Feb. 2020, doi: 10.1364/OME.385723.

[117] B. K. Kim and S. Y. Lee, “Optimized Design of SiInZnO/Ag/SiInZnO Transparent Conductive Electrode by Using Optical Admittance Simulation,” *Trans. Electr. Electron. Mater.*, vol. 21, no. 3, pp. 324–328, Jun. 2020, doi: 10.1007/s42341-020-00178-z.

[118] P. B. Johnson and R. W. Christy, “Optical Constants of the Noble Metals,” *Phys. Rev. B*, vol. 6, no. 12, pp. 4370–4379, Dec. 1972, doi: 10.1103/PhysRevB.6.4370.

[119] J. E. Nestell and R. W. Christy, “Derivation of Optical Constants of Metals from Thin-Film Measurements at Oblique Incidence,” *Appl. Opt., AO*, vol. 11, no. 3, Art. no. 3, Mar. 1972, doi: 10.1364/AO.11.000643.

[120] W. P. Chen and J. M. Chen, “Use of surface plasma waves for determination of the thickness and optical constants of thin metallic films,” *J. Opt. Soc. Am., JOSA*, vol. 71, no. 2, Art. no. 2, Feb. 1981, doi: 10.1364/JOSA.71.000189.

[121] E. Fontana, “Thickness optimization of metal films for the development of surface-plasmon-based sensors for nonabsorbing media,” *Appl. Opt., AO*, vol. 45, no. 29, Art. no. 29, Oct. 2006, doi: 10.1364/AO.45.007632.

[122] Y. Pan, Y. Fan, and J. Niu, “Optical properties of ultra-thin silver films deposited by thermal evaporation and its application in optical filters,” *Infrared Physics & Technology*, vol. 104, p. 103123, Jan. 2020, doi: 10.1016/j.infrared.2019.103123.

[123] M. N. M. N. Perera, D. Schmidt, W. E. K. Gibbs, S. Juodkazis, and P. R. Stoddart, “Influence of the dielectric substrate on the effective optical constants of silver plasmonic films,” *Applied Optics*, vol. 58, no. 22, p. 6038, Aug. 2019, doi: 10.1364/AO.58.006038.

[124] G. Rizzi, G. Benetti, C. Giannetti, L. Gavioli, and F. Banfi, “Analytical model of the acoustic response of nanogranular films adhering to a substrate,” *Phys. Rev. B*, vol. 104, no. 3, p. 035416, Jul. 2021, doi: 10.1103/PhysRevB.104.035416.

[125] N. Bontempi, E. Cavaliere, V. Cappello, P. Pingue, and L. Gavioli, “Ag@TiO_2 nanogranular films by gas phase synthesis as hybrid SERS platforms,” *Physical Chemistry Chemical Physics*, vol. 21, no. 45, pp. 25090–25097, 2019, doi: 10.1039/C9CP03998H.

[126] T. C. Choy, *Effective Medium Theory: Principles and Applications*. Oxford University Press, 2015.

[127] D. Lehmann, F. Seidel, and D. Zahn, “Thin films with high surface roughness: Thickness and dielectric function analysis using spectroscopic ellipsometry,” *SpringerPlus*, vol. 3, p. 82, Feb. 2014, doi: 10.1186/2193-1801-3-82.

[128] D. E. Aspnes, “Optical properties of thin films,” *Thin Solid Films*, vol. 89, no. 3, pp. 249–262, Mar. 1982, doi: 10.1016/0040-6090(82)90590-9.

[129] B. K. Juluri, Y. B. Zheng, D. Ahmed, L. Jensen, and T. J. Huang, “Effects of Geometry and Composition on Charge-Induced Plasmonic Shifts in Gold Nanoparticles,” *J. Phys. Chem. C*, vol. 112, no. 19, pp. 7309–7317, May 2008, doi: 10.1021/jp077346h.

[130] E. Cavaliere, G. Benetti, M. Van Bael, N. Winckelmans, S. Bals, and L. Gavioli, “Exploring the Optical and Morphological Properties of Ag and Ag/TiO2 Nanocomposites Grown by Supersonic Cluster Beam Deposition,” *Nanomaterials*, vol. 7, no. 12, Art. no. 12, Dec. 2017, doi: 10.3390/nano7120442.

[131] C. Noguez, “Surface Plasmons on Metal Nanoparticles: The Influence of Shape and Physical Environment,” *J. Phys. Chem. C*, vol. 111, no. 10, pp. 3806–3819, Mar. 2007, doi: 10.1021/jp066539m.

[132] F. Bisio *et al.*, “Optical properties of cluster-assembled nanoporous gold films,” *Phys. Rev. B*, vol. 80, no. 20, p. 205428, Nov. 2009, doi: 10.1103/PhysRevB.80.205428.

[133] H. Monard and F. Sabary, “Optical properties of silver, gold and aluminum ultra-thin granular films evaporated on oxidized aluminum,” *Thin Solid Films*, vol. 310, no. 1, pp. 265–273, Nov. 1997, doi: 10.1016/S0040-6090(97)00331-3.

[134] P. Gnanadurai, N. Sivaraja, N. Soundrarajan, and C. Vijayan, “Influence of annealing on the optical properties of vacuum deposited silver thin films,” *AIP Conference Proceedings*, vol. 1665, no. 1, p. 080071, Jun. 2015, doi: 10.1063/1.4917975.

[135] K. Aslan, S. N. Malyn, Y. Zhang, and C. D. Geddes, “Conversion of just-continuous metallic films to large particulate substrates for metal-enhanced fluorescence,” *Journal of Applied Physics*, vol. 103, no. 8, p. 084307, Apr. 2008, doi: 10.1063/1.2905319.

[136] M. M. Rahman *et al.*, “Preparation and characterization of silver nanoparticles on localized surface plasmon-enhanced optical absorption,” *Jpn. J. Appl. Phys.*, vol. 53, no. 11S, p. 11RE01, Sep. 2014, doi: 10.7567/JJAP.53.11RE01.

[137] S. Yamaguchi, “Theory of the Optical Properties of Very Thin Inhomogeneous Films,” *J. Phys. Soc. Jpn.*, vol. 17, no. 1, pp. 184–193, Jan. 1962, doi: 10.1143/JPSJ.17.184.

[138] J. Toudert, D. Babonneau, L. Simonot, S. Camelio, and T. Girardeau, "Quantitative modelling of the surface plasmon resonances of metal nanoclusters sandwiched between dielectric layers: the influence of nanocluster size, shape and organization," *Nanotechnology*, vol. 19, no. 12, p. 125709, Feb. 2008, doi: 10.1088/0957-4484/19/12/125709.

[139] V. V. Truong and G. D. Scott, "Optical properties of aggregated noble metal films*," *J. Opt. Soc. Am., JOSA*, vol. 67, no. 4, pp. 502–510, Apr. 1977, doi: 10.1364/JOSA.67.000502.

[140] A. Mejdoubi and C. Brosseau, "Finite-Element Simulation of the Depolarization Factor of Arbitrarily Shaped Inclusions," *Physical review. E, Statistical, nonlinear, and soft matter physics*, vol. 74, p. 031405, Oct. 2006, doi: 10.1109/TMAG.2007.916492.

[141] K.-P. Chen, V. P. Drachev, J. D. Borneman, A. V. Kildishev, and V. M. Shalaev, "Drude Relaxation Rate in Grained Gold Nanoantennas," *Nano Lett.*, vol. 10, no. 3, pp. 916–922, Mar. 2010, doi: 10.1021/nl9037246.

[142] S. Norrman, T. Andersson, C. G. Granqvist, and O. Hunderi, "Optical properties of discontinuous gold films," *Phys. Rev. B*, vol. 18, no. 2, pp. 674–695, Jul. 1978, doi: 10.1103/PhysRevB.18.674.

[143] E. Anno and R. Hoshino, "Size Effect on the Width of Plasma Resonance Absorption of Silver Island Films," *J. Phys. Soc. Jpn.*, vol. 51, no. 4, pp. 1185–1192, Apr. 1982, doi: 10.1143/JPSJ.51.1185.

[144] A. Kawabata and R. Kubo, "Electronic Properties of Fine Metallic Particles. II. Plasma Resonance Absorption," *J. Phys. Soc. Jpn.*, vol. 21, no. 9, pp. 1765–1772, Sep. 1966, doi: 10.1143/JPSJ.21.1765.

[145] U. Kreibig and L. Genzel, "Optical absorption of small metallic particles," *Surface Science*, vol. 156, pp. 678–700, Jun. 1985, doi: 10.1016/0039-6028(85)90239-0.

[146] E. A. Coronado and G. C. Schatz, "Surface plasmon broadening for arbitrary shape nanoparticles: A geometrical probability approach," *The Journal of Chemical Physics*, vol. 119, no. 7, p. 3926, Jul. 2003, doi: 10.1063/1.1587686.

[147] G. Torrisi *et al.*, "Ag cluster beam deposition for TCO/Ag/TCO multilayer," *Solar Energy Materials and Solar Cells*, vol. 199, pp. 114–121, Sep. 2019, doi: 10.1016/j.solmat.2019.04.025.

[148] H. A. MacLeod and H. A. Macleod, *Thin-Film Optical Filters*, 0 ed. CRC Press, 2010. doi: 10.1201/9781420073034.

[149] J. E. Nestell and R. W. Christy, “Derivation of Optical Constants of Metals from Thin-Film Measurements at Oblique Incidence,” *Appl. Opt., AO*, vol. 11, no. 3, pp. 643–651, Mar. 1972, doi: 10.1364/AO.11.000643.

[150] A. V. Tikhonravov, M. K. Trubetskov, A. A. Tikhonravov, and A. Duparré, “Effects of interface roughness on the spectral properties of thin films and multilayers,” *Appl. Opt., AO*, vol. 42, no. 25, pp. 5140–5148, Sep. 2003, doi: 10.1364/AO.42.005140.

[151] I. H. Malitson, “Interspecimen Comparison of the Refractive Index of Fused Silica*,†,” *J. Opt. Soc. Am., JOSA*, vol. 55, no. 10, pp. 1205–1209, Oct. 1965, doi: 10.1364/JOSA.55.001205.

[152] P. G. Etchegoin, E. C. Le Ru, and M. Meyer, “An analytic model for the optical properties of gold,” *J. Chem. Phys.*, vol. 125, no. 16, p. 164705, Oct. 2006, doi: 10.1063/1.2360270.

[153] A. Kossoy, V. Merk, D. Simakov, K. Leosson, S. Kéna-Cohen, and S. A. Maier, “Optical and Structural Properties of Ultra-thin Gold Films,” *Advanced Optical Materials*, vol. 3, no. 1, pp. 71–77, 2015, doi: https://doi.org/10.1002/adom.201400345.

[154] P. Gadenne, “Modifications of the optical and electrical properties of thin gold films as a function of structure during deposition,” *Thin Solid Films*, vol. 57, no. 1, pp. 77–81, Feb. 1979, doi: 10.1016/0040-6090(79)90408-5.

[155] M. Rosete-Aguilar, F. C. Estrada-Silva, N. C. Bruce, C. J. Roman-Moreno, and R. Ortega-Martınez, “Calculation of temporal spreading of ultrashort pulses propagating through optical glasses,” p. 8, 2008.

[156] Z. R. Lawson *et al.*, “Plasmonic Gold Trimers and Dimers with Air-Filled Nanogaps,” *ACS Appl. Mater. Interfaces*, vol. 14, no. 24, pp. 28186–28198, Jun. 2022, doi: 10.1021/acsami.2c04800.

[157] “Direct Bottom-Up In Situ Growth: A Paradigm Shift for Studies in Wet-Chemical Synthesis of Gold Nanoparticles | Chemical Reviews.” Accessed: Jun. 23, 2023. [Online]. Available: https://pubs.acs.org/doi/10.1021/acs.chemrev.2c00914?ref=pdf

[158] S. Naghdi, K. Y. Rhee, D. Hui, and S. J. Park, “A Review of Conductive Metal Nanomaterials as Conductive, Transparent, and Flexible Coatings, Thin Films, and Conductive Fillers: Different Deposition Methods and Applications,” *Coatings*, vol. 8, no. 8, Art. no. 8, Aug. 2018, doi: 10.3390/coatings8080278.

[159] Z. Lu *et al.*, “Application of Micro/Nanofabrication Techniques to On-Chip Molecular Electronics,” *Small Methods*, vol. 5, no. 3, p. 2001034, 2021, doi: 10.1002/smtd.202001034.

[160] T. Adam, Th. S. Dhahi, S. C. B. Gopinath, U. Hashim, and M. N. A. Uda, "Recent advances in techniques for fabrication and characterization of nanogap biosensors: A review," *Biotechnology and Applied Biochemistry*, vol. 69, no. 4, pp. 1395–1417, 2022, doi: 10.1002/bab.2212.

[161] J. Dong, P. L. Carpinone, G. Pyrgiotakis, P. Demokritou, and B. M. Moudgil, "Synthesis of Precision Gold Nanoparticles Using Turkevich Method," *KONA Powder and Particle Journal*, vol. 37, pp. 224–232, 2020, doi: 10.14356/kona.2020011.

[162] T. B. Demille *et al.*, "Epitaxially aligned single-crystal gold nanoplates formed in large-area arrays at high yield," *Nano Res.*, vol. 15, no. 1, pp. 296–303, Jan. 2022, doi: 10.1007/s12274-021-3473-1.

[163] S. Shan *et al.*, "Nanoalloy catalysts for electrochemical energy conversion and storage reactions," *RSC Advances*, vol. 4, no. 80, pp. 42654–42669, 2014, doi: 10.1039/C4RA05943C.

[164] A. K. Sharma and B. D. Gupta, "Fibre-optic sensor based on surface plasmon resonance with Ag–Au alloy nanoparticle films," *Nanotechnology*, vol. 17, no. 1, pp. 124–131, Dec. 2005, doi: 10.1088/0957-4484/17/1/020.

[165] G. Benetti *et al.*, "Tailored Ag–Cu–Mg multielemental nanoparticles for wide-spectrum antibacterial coating," *Nanoscale*, vol. 11, no. 4, pp. 1626–1635, 2019, doi: 10.1039/C8NR08375D.

[166] K. McNamara and S. A. M. Tofail, "Nanosystems: the use of nanoalloys, metallic, bimetallic, and magnetic nanoparticles in biomedical applications," *Phys. Chem. Chem. Phys.*, vol. 17, no. 42, pp. 27981–27995, Oct. 2015, doi: 10.1039/C5CP00831J.

[167] Z.-P. Wu *et al.*, "Revealing the Role of Phase Structures of Bimetallic Nanocatalysts in the Oxygen Reduction Reaction," *ACS Catal.*, vol. 8, no. 12, pp. 11302–11313, Dec. 2018, doi: 10.1021/acscatal.8b03106.

[168] I. Vassalini *et al.*, "Enhanced Electrocatalytic Oxygen Evolution in Au–Fe Nanoalloys," *Angewandte Chemie International Edition*, vol. 56, no. 23, pp. 6589–6593, 2017, doi: 10.1002/anie.201703387.

[169] J. Zhao, J.-J. Zhang, Z.-Y. Li, and X.-H. Bu, "Recent Progress on NiFe-Based Electrocatalysts for the Oxygen Evolution Reaction," *Small*, vol. 16, no. 51, p. 2003916, 2020, doi: 10.1002/smll.202003916.

[170] Z. Qiu, C.-W. Tai, G. A. Niklasson, and T. Edvinsson, "Direct observation of active catalyst surface phases and the effect of dynamic self-optimization in NiFe-layered double hydroxides for alkaline water splitting," *Energy Environ. Sci.*, vol. 12, no. 2, pp. 572–581, Feb. 2019, doi: 10.1039/C8EE03282C.

[171] S. L. Medway, C. A. Lucas, A. Kowal, R. J. Nichols, and D. Johnson, “In situ studies of the oxidation of nickel electrodes in alkaline solution,” *Journal of Electroanalytical Chemistry*, vol. 587, no. 1, pp. 172–181, Feb. 2006, doi: 10.1016/j.jelechem.2005.11.013.

[172] X. Zhang, Y. Zhao, Y. Zhao, R. Shi, G. I. N. Waterhouse, and T. Zhang, “A Simple Synthetic Strategy toward Defect-Rich Porous Monolayer NiFe-Layered Double Hydroxide Nanosheets for Efficient Electrocatalytic Water Oxidation,” *Advanced Energy Materials*, vol. 9, no. 24, p. 1900881, 2019, doi: 10.1002/aenm.201900881.

[173] S. Anantharaj and S. Kundu, “Do the Evaluation Parameters Reflect Intrinsic Activity of Electrocatalysts in Electrochemical Water Splitting?,” *ACS Energy Lett.*, vol. 4, no. 6, pp. 1260–1264, Jun. 2019, doi: 10.1021/acsenergylett.9b00686.

[174] B. S. Yeo and A. T. Bell, “In Situ Raman Study of Nickel Oxide and Gold-Supported Nickel Oxide Catalysts for the Electrochemical Evolution of Oxygen,” *J. Phys. Chem. C*, vol. 116, no. 15, pp. 8394–8400, Apr. 2012, doi: 10.1021/jp3007415.

[175] A. Touni, A. Papaderakis, D. Karfaridis, G. Vourlias, and S. Sotiropoulos, “Oxygen Evolution Reaction at IrO2/Ir(Ni) Film Electrodes Prepared by Galvanic Replacement and Anodization: Effect of Precursor Ni Film Thickness,” *Molecules*, vol. 24, no. 11, Art. no. 11, Jan. 2019, doi: 10.3390/molecules24112095.

[176] P. Plate *et al.*, “On the Origin of the OER Activity of Ultrathin Manganese Oxide Films,” *ACS Appl. Mater. Interfaces*, vol. 13, no. 2, pp. 2428–2436, Jan. 2021, doi: 10.1021/acsami.0c15977.

[177] J. Lee *et al.*, “Contribution of the Sub-Surface to Electrocatalytic Activity in Atomically Precise La0.7Sr0.3MnO3 Heterostructures,” *Small*, vol. 17, no. 49, p. 2103632, 2021, doi: 10.1002/smll.202103632.

[178] E. Cavaliere, G. Benetti, M. Van Bael, N. Winckelmans, S. Bals, and L. Gavioli, “Exploring the Optical and Morphological Properties of Ag and Ag/TiO2 Nanocomposites Grown by Supersonic Cluster Beam Deposition,” *Nanomaterials*, vol. 7, no. 12, p. 442, Dec. 2017, doi: 10.3390/nano7120442.

[179] B. D. Fraters, E. Cavaliere, G. Mul, and L. Gavioli, “Synthesis of photocatalytic TiO2 nano-coatings by supersonic cluster beam deposition,” *Journal of Alloys and Compounds*, vol. 615, pp. S467–S471, Dec. 2014, doi: 10.1016/j.jallcom.2013.12.037.

[180] D. Nečas and P. Klapetek, “Gwyddion: an open-source software for SPM data analysis,” *Open Physics*, vol. 10, no. 1, pp. 181–188, Feb. 2012, doi: 10.2478/s11534-011-0096-2.

[181] “Copyright © 2005 Casa Software Ltd.” Accessed: Dec. 15, 2021. [Online]. Available: http://www.casaxps.com/

[182] L. Ciambriello, E. Cavaliere, and L. Gavioli, “Influence of roughness, porosity and grain morphology on the optical properties of ultrathin Ag films,” *Applied Surface Science*, vol. 576, p. 151885, Feb. 2022, doi: 10.1016/j.apsusc.2021.151885.

[183] J. C. H. Spence and J. C. H. Spence, *High-resolution electron microscopy*, 4th edition. Oxford ; New York: Oxford University Press, 2017. Accessed: Jun. 29, 2022. [Online]. Available: http://resolver.ebscohost.com/Redirect/PRL?EPPackageLocationID=9616.2266256.56793400&epcustomerid=s8491974&db=9616

[184] F. Borghi, A. Podestà, C. Piazzoni, and P. Milani, “Growth Mechanism of Cluster-Assembled Surfaces: From Submonolayer to Thin-Film Regime,” *Phys. Rev. Applied*, vol. 9, no. 4, p. 044016, Apr. 2018, doi: 10.1103/PhysRevApplied.9.044016.

[185] Y. Liu, Y. Chi, S. Shan, J. Yin, J. Luo, and C.-J. Zhong, “Characterization of magnetic NiFe nanoparticles with controlled bimetallic composition,” *Journal of Alloys and Compounds*, vol. 587, pp. 260–266, Feb. 2014, doi: 10.1016/j.jallcom.2013.10.203.

[186] N. Mironova-Ulmane, A. Kuzmin, I. Steins, J. Grabis, I. Sildos, and M. Pärs, “Raman scattering in nanosized nickel oxide NiO,” *J. Phys.: Conf. Ser.*, vol. 93, p. 012039, Dec. 2007, doi: 10.1088/1742-6596/93/1/012039.

[187] J. Desilvestro, D. A. Corrigan, and M. J. Weaver, “Characterization of Redox States of Nickel Hydroxide Film Electrodes by In Situ Surface Raman Spectroscopy,” *J. Electrochem. Soc.*, vol. 135, no. 4, p. 885, Apr. 1988, doi: 10.1149/1.2095818.

[188] M. C. Biesinger, B. P. Payne, A. P. Grosvenor, L. W. M. Lau, A. R. Gerson, and R. St. C. Smart, “Resolving surface chemical states in XPS analysis of first row transition metals, oxides and hydroxides: Cr, Mn, Fe, Co and Ni,” *Applied Surface Science*, vol. 257, no. 7, pp. 2717–2730, Jan. 2011, doi: 10.1016/j.apsusc.2010.10.051.

[189] N. S. McIntyre and D. G. Zetaruk, “X-ray photoelectron spectroscopic studies of iron oxides,” ACS Publications. Accessed: Dec. 15, 2021. [Online]. Available: https://pubs.acs.org/doi/pdf/10.1021/ac50019a016

[190] M. Fingerle, S. Tengeler, W. Calvet, T. Mayer, and W. Jaegermann, “Water Interaction with Sputter-Deposited Nickel Oxide on n-Si Photoanode: Cryo Photoelectron Spectroscopy on Adsorbed Water in the Frozen Electrolyte Approach,” *J. Electrochem. Soc.*, vol. 165, no. 4, p. H3148, Feb. 2018, doi: 10.1149/2.0191804jes.

[191] M. C. Biesinger, B. P. Payne, L. W. M. Lau, A. Gerson, and R. St. C. Smart, “X-ray photoelectron spectroscopic chemical state quantification of mixed nickel metal, oxide and hydroxide systems,” *Surface and Interface Analysis*, vol. 41, no. 4, pp. 324–332, 2009, doi: 10.1002/sia.3026.

[192] M. Rosete-Aguilar, F. C. Estrada-Silva, N. C. Bruce, C. J. Román-Moreno, and R. Ortega-Martínez, “http://www.scielo.org.mx/scielo.php?script=sci_abstract&pid=S0035-001X2008000200010&lng=es&nrm=iso&tlng=en,” *Revista mexicana de física*, vol. 54, no. 2, pp. 141–148, Apr. 2008.

[193] A. D. Rakić, A. B. Djurišić, J. M. Elazar, and M. L. Majewski, “Optical properties of metallic films for vertical-cavity optoelectronic devices,” *Appl. Opt., AO*, vol. 37, no. 22, pp. 5271–5283, Aug. 1998, doi: 10.1364/AO.37.005271.

[194] R. Solmaz and G. Kardaş, “Electrochemical deposition and characterization of NiFe coatings as electrocatalytic materials for alkaline water electrolysis,” *Electrochimica Acta*, vol. 54, no. 14, pp. 3726–3734, May 2009, doi: 10.1016/j.electacta.2009.01.064.

[195] E. Cossar, M. S. E. Houache, Z. Zhang, and E. A. Baranova, “Comparison of electrochemical active surface area methods for various nickel nanostructures,” *Journal of Electroanalytical Chemistry*, vol. 870, p. 114246, Aug. 2020, doi: 10.1016/j.jelechem.2020.114246.

[196] D. S. Hall, C. Bock, and B. R. MacDougall, “An Oxalate Method for Measuring the Surface Area of Nickel Electrodes,” *J. Electrochem. Soc.*, vol. 161, no. 12, p. H787, Sep. 2014, doi: 10.1149/2.0711412jes.

[197] H. Ehrenreich, H. R. Philipp, and D. J. Olechna, “Optical Properties and Fermi Surface of Nickel,” *Phys. Rev.*, vol. 131, no. 6, pp. 2469–2477, Sep. 1963, doi: 10.1103/PhysRev.131.2469.

[198] L. M. M. de Souza, F. P. Kong, F. R. McLarnon, and R. H. Muller, “Spectroscopic ellipsometry study of nickel oxidation in alkaline solution,” *Electrochimica Acta*, vol. 42, no. 8, pp. 1253–1267, Jan. 1997, doi: 10.1016/S0013-4686(96)00298-8.

[199] D. S. Hall, D. J. Lockwood, C. Bock, and B. R. MacDougall, “Nickel hydroxides and related materials: a review of their structures, synthesis and properties,” *Proceedings of the Royal Society A: Mathematical, Physical and Engineering*

Sciences, vol. 471, no. 2174, p. 20140792, Feb. 2015, doi: 10.1098/rspa.2014.0792.

[200] F. Dionigi and P. Strasser, "NiFe-Based (Oxy)hydroxide Catalysts for Oxygen Evolution Reaction in Non-Acidic Electrolytes," *Advanced Energy Materials*, vol. 6, no. 23, p. 1600621, 2016, doi: 10.1002/aenm.201600621.

[201] R. Chen *et al.*, "Layered Structure Causes Bulk NiFe Layered Double Hydroxide Unstable in Alkaline Oxygen Evolution Reaction," *Advanced Materials*, vol. 31, no. 41, p. 1903909, 2019, doi: 10.1002/adma.201903909.

[202] C. Kuai *et al.*, "Phase segregation reversibility in mixed-metal hydroxide water oxidation catalysts," *Nat Catal*, vol. 3, no. 9, Art. no. 9, Sep. 2020, doi: 10.1038/s41929-020-0496-z.

[203] A. E. Thorarinsdottir, S. S. Veroneau, and D. G. Nocera, "Self-healing oxygen evolution catalysts," *Nat Commun*, vol. 13, no. 1, Art. no. 1, Mar. 2022, doi: 10.1038/s41467-022-28723-9.

[204] L. Ciambriello *et al.*, "Role of Electrode Thickness in NiFe Nanogranular Films for Oxygen Evolution Reaction," *J. Phys. Chem. C*, vol. 126, no. 51, pp. 21759–21770, Dec. 2022, doi: 10.1021/acs.jpcc.2c06669.

[205] E. Cavaliere, G. Benetti, M. Van Bael, N. Winckelmans, S. Bals, and L. Gavioli, "Exploring the Optical and Morphological Properties of Ag and Ag/TiO2 Nanocomposites Grown by Supersonic Cluster Beam Deposition," *Nanomaterials*, vol. 7, no. 12, Art. no. 12, Dec. 2017, doi: 10.3390/nano7120442.

[206] B. D. Fraters, E. Cavaliere, G. Mul, and L. Gavioli, "Synthesis of photocatalytic TiO2 nano-coatings by supersonic cluster beam deposition," *Journal of Alloys and Compounds*, vol. 615, pp. S467–S471, Dec. 2014, doi: 10.1016/j.jallcom.2013.12.037.

[207] M. Bottagisio *et al.*, "Exploring multielement nanogranular coatings to forestall implant-related infections," *Frontiers in Cellular and Infection Microbiology*, vol. 13, 2023, Accessed: Nov. 16, 2023. [Online]. Available: https://www.frontiersin.org/articles/10.3389/fcimb.2023.1128822

[208] W. Lai *et al.*, "In situ Raman spectroscopic study towards the growth and excellent HER catalysis of Ni/Ni(OH)2 heterostructure," *International Journal of Hydrogen Energy*, vol. 46, no. 53, pp. 26861–26872, Aug. 2021, doi: 10.1016/j.ijhydene.2021.05.158.

[209] J. Ferreira de Araújo, F. Dionigi, T. Merzdorf, H.-S. Oh, and P. Strasser, "Evidence of Mars-Van-Krevelen Mechanism in the Electrochemical Oxygen Evolution on Ni-Based Catalysts," *Angewandte Chemie International Edition*, vol. 60, no. 27, pp. 14981–14988, 2021, doi: 10.1002/anie.202101698.

[210] R. Sander, “Compilation of Henry’s law constants (version 5.0.0) for water as solvent,” *Atmospheric Chemistry and Physics*, vol. 23, no. 19, pp. 10901–12440, Oct. 2023, doi: 10.5194/acp-23-10901-2023.

[211] K. Kishi and S. Ikeda, “X-Ray Photoelectron Spectroscopic Study for the Reaction of Evaporated Iron with O2 and H2O,” *BCSJ*, vol. 46, no. 2, pp. 341–345, Feb. 1973, doi: 10.1246/bcsj.46.341.

[212] D. Gall, “Electron mean free path in elemental metals,” *Journal of Applied Physics*, vol. 119, no. 8, p. 085101, Feb. 2016, doi: 10.1063/1.4942216.

[213] M. C. Biesinger, L. W. M. Lau, A. R. Gerson, and R. S. C. Smart, “The role of the Auger parameter in XPS studies of nickel metal, halides and oxides,” *Phys. Chem. Chem. Phys.*, vol. 14, no. 7, pp. 2434–2442, Jan. 2012, doi: 10.1039/C2CP22419D.

[214] A. N. Mansour and C. A. Melendres, “Characterization of Electrochemically Prepared γ-NiOOH by XPS,” *Surface Science Spectra*, vol. 3, no. 3, p. 271, Oct. 2021, doi: 10.1116/1.1247756.

[215] Q. Zhang *et al.*, “Unraveling the Mechanism of Self-Repair of NiFe-Based Electrocatalysts by Dynamic Exchange of Iron during the Oxygen Evolution Reaction,” *ACS Catal.*, vol. 13, no. 22, pp. 14975–14986, Nov. 2023, doi: 10.1021/acscatal.3c03804.

[216] G. Magna *et al.*, “Experimental determination of the mass sensitivity of quartz microbalances coated by an optical dye,” *Sensors and Actuators B: Chemical*, vol. 320, p. 128373, Oct. 2020, doi: 10.1016/j.snb.2020.128373.